

Studies on the Focusing Performance of a Gabor Lens Depending on Nonneutral Plasma Properties

Dissertation
submitted to attain the degree of
doctor of natural science

at the department of physics
of the Johann Wolfgang Goethe-University
in Frankfurt am Main

by
Kathrin Silvana Schulte
from Attendorn



Frankfurt am Main 2013
(D30)

by the department of physics of the
Johann Wolfgang Goethe-University accepted as dissertation.

faculty director:

Prof. Dr. J. Stroth

expert assessors:

Prof. Dr. U. Ratzinger

Prof. Dr. O. Kester

date of disputation: 11/22/2013

Untersuchung der
Fokussiereigenschaften einer
Gabor-Linse in Abhängigkeit von
den Parametern des
eingeschlossenen nichtneutralen
Plasmas

Dissertation
zur Erlangung des Doktorgrades
der Naturwissenschaften
vorgelegt beim Fachbereich Physik
der Johann Wolfgang Goethe-Universität
in Frankfurt am Main

von
Kathrin Silvana Schulte
aus Attendorn



Frankfurt am Main 2013
(D30)

**vom Fachbereich Physik der
Johann Wolfgang Goethe-Universität als Dissertation angenommen.**

Dekan:

Prof. Dr. J. Stroth

Gutachter:

Prof. Dr. U. Ratzinger

Prof. Dr. O. Kester

Datum der Disputation: 22.11.2013

Zusammenfassung

Die Gabor-Linse eröffnet eine Vielzahl an Möglichkeiten, das in ihr eingeschlossene nicht-neutrale Plasma und seine grundlegenden physikalischen Prinzipien zu untersuchen. Neben der Anwendung als Fokussierelement für intensive Ionenstrahlen in Beschleunigeranlagen können sowohl kollektive Phänomene als auch Wechselwirkungsprozesse des Elektronenensembles mit seiner Umgebung studiert werden. Insbesondere die Mechanismen, die zur Einstellung eines dynamischen Gleichgewichtszustandes des nichtneutralen Plasmas führen, sind dabei von Interesse.

1947 schlug Dennis Gabor erstmals das Konzept einer Elektronenfalle als effiziente Zerstreuungslinse für Elektronenstrahlen (bzw. Sammellinse für Ionenstrahlen) vor [Gab47]. Durch eine spezielle Konfiguration aus elektrischen und magnetischen Feldern werden in einer Gabor-Linse Elektronen eingeschlossen, deren Raumladungsfeld eine starke Fokussierwirkung auf einen durchlaufenden Ionenstrahl ausübt. Im Falle einer homogenen Ladungsträgerverteilung ist das elektrische Feld in radialer Richtung linear.

In der Niederenergiestrahlführung (LEBT - Low Energy Beam Transport Section) einer Beschleunigeranlage soll der aus der Quelle extrahierte Ionenstrahl über eine gewisse Strecke geführt und an die Akzeptanz eines nachfolgenden Beschleunigers (typischerweise ein RFQ - Radio Frequenz Quadrupol) angepasst werden. Dabei soll der Strahl idealerweise weder Transmissionsverluste noch eine Verschlechterung der Strahlqualität (letztere ist durch ein Emittanzwachstum gekennzeichnet) erfahren.

Vor allem intensive, raumladungsdominierte Strahlen leiden unter der starken Vergrößerung ihres Querschnitts. Diese führt häufig zur einer Minimierung, der für die Experimente bereitgestellten Intensität. Die abstoßenden Kräfte, die innerhalb des Strahls auf die Teilchen ausgeübt werden, können durch das Einbringen von Ladungsträgern gegensätzlicher Polarität kompensiert werden. Die Quelle dieser Ladungsträger sind zum

Zusammenfassung

einen Ionisierungsprozesse zwischen Strahl und Restgas. Aber auch durch Strahlverluste an den Vakuumwandungen der Strahlführung können Sekundärelektronen produziert werden.

Hierin zeigt sich der Vorteil des Einsatzes einer Gabor-Linse zur Fokussierung von Ionenstrahlen gegenüber konventionellen Linsensystem, wie beispielsweise Solenoiden, magnetischen Quadrupolen und elektrostatische Einzellinsen. Neben der wirksamen Fokussierung wird durch die elektrischen und magnetischen Felder der Gabor-Linse die Verteilung der Elektronen im Strahlvolumen gezielt beeinflusst. Dadurch wird der Transport von hochintensiven Ionenstrahlen bei im Vergleich nur geringen aufzuwendenden Feldstärken und guter Strahlqualität ermöglicht.

Trotz dieser theoretisch großen Vorteile blieben bei den Untersuchungen der Transporteigenschaften von unterschiedlichen Forschungsgruppen die Ergebnisse zunächst hinter den Erwartungen zurück [PMSY90], [Rei89]. Am Institut für Angewandte Physik (IAP) wurde das Design der Gabor-Linse seit den 1990er Jahren stetig weiterentwickelt. Zudem wurden numerische Modelle zur Beschreibung des nichtneutralen Plasmas erarbeitet sowie neuartige Diagnoseverfahren entwickelt. Durch das bessere Verständnis des Plasmaeinschlusses und Systemzustands in Abhängigkeit von den externen Parametern wurden zwei solcher Linsen auch sehr erfolgreich als Niederenergietransportsektion, allerdings bei vergleichsweise geringen Strahlströmen, getestet und befinden sich dort auch weiterhin im Einsatz. Außerdem wurde die Anwendung einer Hochfeldgaborlinse zur Strahlführung nach einem RFQ bei einer Strahlenergie von $W_b=436$ keV untersucht [Meu06].

Im Rahmen der vorliegenden Arbeit wurde die Anwendung einer Gabor-Linse erstmals im Bereich raumladungsdominierter Strahlen am Hochstromtestinjektor (HOSTI) der GSI Helmholtzzentrum für Schwerionenforschung GmbH, im Zusammenhang mit dem geplanten FAIR Projekt, untersucht.

Die Facility for Antiproton and Ion Research (FAIR) ist eine neue Beschleunigeranlage, die bei GSI errichtet wird. Die Forschung an FAIR umfasst ein weites Feld der Kern- und Hadronenphysik, der Plasma- und Atomphysik einschließlich Anwendungen im Feld kondensierter Materie sowie der Biologie [Ros07]. Eine Synchrotron-Doppelring-Anlage (SIS 100/300) wird dazu genutzt, um hochintensive Sekundärstrahlen aus Antiprotonen und kurzlebigen radioaktiven Nukleiden zu produzieren [SF06]. Aus diesem Grunde werden die Anforderungen an den existierenden Hochstrominjektor bezüglich Intensität

und Brillanz der erzeugten $^{238}\text{U}^{4+}$ -Ionenstrahlen steigen. Der Einsatz einer Gabor-Linse verspricht dabei eine Verbesserung der Qualität des injizierten Strahls und trägt somit zur Steigerung der Luminosität am Ende der Beschleunigeranlage bei.

Aus diesem Grund wurde ein Prototyp für den Test am HOSTI der GSI ausgelegt und gebaut. Ein homogener und zeitlich wie auch räumlich stabiler Plasmaeinschluss ist von großer Bedeutung, um eine gute Abbildungsqualität der Gabor-Linse zu gewährleisten. Daher wurden Diagnosemethoden entwickelt, um die Parameter der eingeschlossenen Plasmawolke zu bestimmen und die Abhängigkeit ihres Zustands von den externen Parametern zu untersuchen. Eine große Herausforderung stellte dabei die Entwicklung einer nicht-invasiven Temperaturmessung mithilfe optischer Spektroskopie dar, die eine dedizierte Untersuchung der atomaren Anregungsprozesse erforderte. Um nun zu untersuchen, welchen Einfluss die Plasmastrahlwechselwirkung auf das System hat, wurde die Elektronenwolke zunächst am IAP numerisch wie auch experimentell untersucht. Anschließend wurden diese Ergebnisse mit den Resultaten der Strahltransportmessungen und -rechnungen verglichen.

Die unterschiedlichen Aspekte werden in den nachfolgenden Abschnitten noch etwas genauer erläutert.

Gabor-Linse – Charakterisierung

Im zweiten Kapitel der Arbeit werden zunächst die grundlegenden Eigenschaften von nichtneutralen Plasmen und die theoretischen Grundlagen des Plasmaeinschlusses in der Gabor-Linse erklärt.

Ein nichtneutrales Plasma ist ein Vielteilchensystem von geladenen Partikeln, in dem keine ingesamte Ladungsneutralität besteht. Genau wie auch quasineutrale Plasmen weisen nichtneutrale Plasmen kollektive Effekte wie die Debye-Abschirmung und die Plasmafrequenz auf.

Die Gabor-Linse dient als Falle für Teilchen gleicher Ladung. Aufgrund eines an der zylindrischen Anode anliegenden positiven Potentials verbleiben die Elektronen in longitudinaler Richtung im Linsenvolumen, während ein homogenes Magnetfeld, erzeugt von einem Solenoiden oder Helmholtzspulenpaar, die Elektronen auf eine Kreisbahn zwingt und somit in transversaler Richtung einschließt. In beiden Einschlussrichtungen kann so für eine vorgegebene Feldstärke die theoretische Maximaldichte der Elektronen

Zusammenfassung

abgeleitet werden.

Es wird angenommen, dass sich ein Gleichgewichtszustand des Plasmas und somit eine homogene Elektronendichteverteilung einstellt, wenn die Einschlussbedingungen in beiden Ebenen gleich sind. Daraus ergibt sich eine Konfigurationsvorschrift für die externen Felder. Diese wird als Arbeitsfunktion der Linse bezeichnet.

In der vorliegenden Arbeit geht es neben der Performance der Linse als Fokussierelement auch um die Bestimmung der Plasmaparameter wie der Dichte, aber vor allem der Temperatur, um eine bessere Beschreibung des Elektronenensembles in Abhängigkeit der externen Parameter zu ermöglichen.

Um den Plasmazustand möglichst unbeeinflusst untersuchen zu können, wurde die Temperatur über ein spezielles Verfahren mithilfe der optischen Spektroskopie bestimmt. Dieses erfordert allerdings eine genaue Kenntnis über die atomaren Wechselwirkungen aller beteiligten Partikel. Darüberhinaus sind diese auch entscheidend für eine Kompensations- und Sekundärelektronenproduktion. Daher wurden mithilfe der Wirkungsquerschnitte die Stoßraten für jeden möglichen Wechselwirkungsprozess zwischen Elektronen, Ionen und Atomen abgeschätzt. Aufgrund der zu erwartenden Dichten ($n_e = 1 \cdot 10^{14} \text{ m}^{-3}$) und Temperaturen ($T_e \approx 100 \text{ eV}$) des eingeschlossenen, nichtneutralen Plasmas kann davon ausgegangen werden, dass die für die optische Spektroskopie relevanten An- und Abregungsprozesse sich auf die Elektronenstoßanregung und die spontane Emission beschränken. Insofern muss dem Elektronenplasma zur theoretischen Beschreibung das Koronamodell zugrunde gelegt werden. Dieses nutzt zur Intensitätsdefinition das Gleichgewicht zwischen Elektronenstoßanregung und spontaner Emission. Die produzierten Restgasionen werden aufgrund des anliegenden Potentials aus dem Linsenvolumen heraus beschleunigt und tragen somit - zumindest im Bereich kleinerer Anodenspannungen - nicht zum Emissionsspektrum bei.

Entscheidend für das Einstellen eines Gleichgewichtszustandes des Elektronenensembles und somit auch einer Temperatur, sind nicht nur die diskutierten Produktionsmechanismen, sondern auch die Verlustprozesse. Neben der Berechnung einer Zündkurve nach Paschen (äquivalent zu quasineutralen Plasmen) wurde auch eine Möglichkeit zur Charakterisierung und Bestimmung der Elektronenverluste vorgestellt.

Am IAP wurden im Laufe der Zeit zwei Computermodelle zur Beschreibung des nichtneutralen Plasmas entwickelt, mit denen im Rahmen der vorliegenden Arbeit der Einschluss der Elektronenwolke simuliert wurde. Das Programm GABOR-M [Meu06], [Poz97]

ist ein Hydrodynamik-Code, der die Gleichgewichtsdichteverteilung in Abhängigkeit von den externen Feldern und dem Elektronenverluststrom berechnet, während bei GAB_LENS [Dro] auf einen Particle-in-Cell Algorithmus zur Beschreibung der Teilchendynamik zurückgegriffen wird.

Am Ende des zweiten Kapitels wird die Fokussierwirkung der Linse auf einen Ionenstrahl theoretisch beschrieben und eine Formel für die Brechkraft hergeleitet. Darüber hinaus werden die grundlegenden Begriffe des Strahltransports erläutert.

Instabilitäten in nichtneutralen Plasmen

Eine mögliche Ursache für ein beobachtetes Emittanzwachstum ist das Auftreten von Instabilitäten im nichtneutralen Plasma, die sich im Parameterraum fern der Arbeitsfunktion ausbilden können.

Bespielsweise entwickelt sich bei der theoretisch sehr gut beschriebenen Diocotron-Instabilität ein Hohlprofil der Elektronendichteverteilung, das ein höchst nichtlineares, radiales Eigenfeld zur Folge hat.

Durch ein zu großes Magnetfeld im Verhältnis zum eingestellten Anodenpotential, werden die Elektronen an der Achse komprimiert. Somit kommt es lokal zu einer Überfüllung des Potentials und dadurch zu Elektronenverlusten auf der Achse. In Abbildung 1 ist die gerechnete zeitliche Entwicklung einer Diocotron-Instabilität exemplarisch dargestellt.

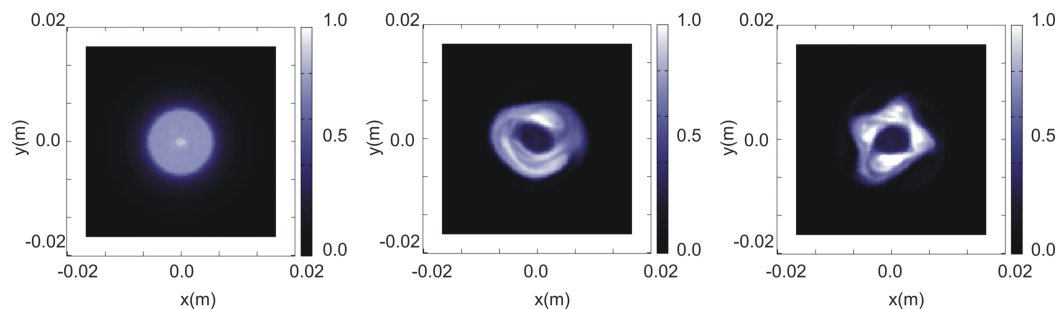


Abbildung 1: Exemplarische Darstellung der berechneten zeitlichen Entwicklung der Diocotronmoden (von links nach rechts). Der Farbcode kennzeichnet die über z integrierte und normierte Elektronendichte [MDS13].

Allerdings wird die Ausbildung eines Hohlprofils auch im Regime hoher Restgasdrücke beobachtet. Dies kann durch eine erhöhte Neutralisation des elektrischen Eigenfeldes der Elektronen durch produziert Restgasionen und die damit verbundene Verschiebung des

Zusammenfassung

Arbeitspunktes erklärt werden. Eine andere mögliche Erklärung ist die unausgeglichene Verteilung der kinetischen Energien in longitudinaler und transversaler Einschlussrichtung. Denn die nun größere Anzahl an Restgasatomen, mit denen die Elektronen vor allem in longitudinaler Richtung wechselwirken können, würde zu diesem beschriebenen Ungleichgewicht führen. Im Fall einer zu hohen Magnetfeldeinstellung wird dieses Ungleichgewicht der kinetischen Energien von der numerischen Simulation vorhergesagt.

Auslegung der Prototypelinse für GSI

Im vierten Kapitel geht es um die technische Auslegung der Prototypelinse für GSI (siehe Abbildung 2).

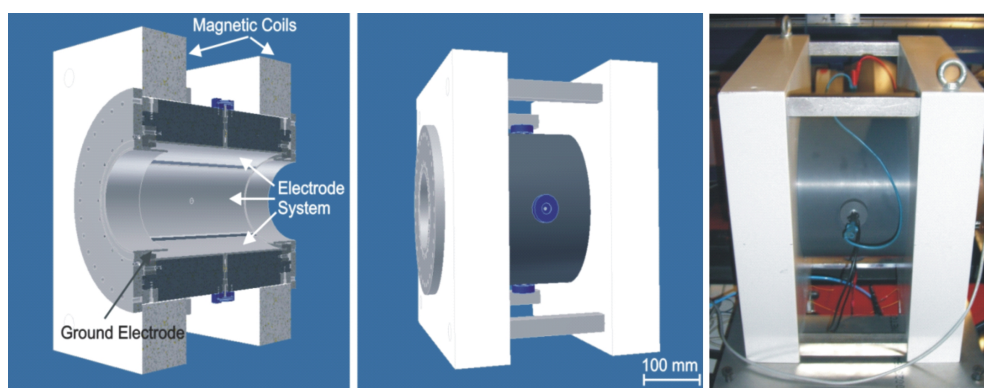


Abbildung 2: Schematische Darstellung der Gabor-Linse im Schnitt (links), in der Vollansicht (Mitte) und ein Foto der Prototypelinse (rechts).

Aufgrund des zu erwartenden hohen Strahlradius von $r_b=50$ mm musste die neue Linse gegenüber den Vorgängermodellen entsprechend skaliert werden. Bei Vergrößerung der Apertur wurde auch der Abstand von Erdelektrode zu Anode berücksichtigt, der die Effizienz des Elektroneneinschlusses stark beeinflusst. Zudem wurde auch die Anode verlängert, um das Potential auf der Achse zu erhalten. Die Optimierung des Plasmaeinschlusses und somit die Untersuchung der Linearität des erzeugten elektrischen Feldes wurde mit dem Programm GABOR-M durchgeführt.

Aus Gründen der technischen Flexibilität wurde bei dem magnetischen System auf ein Helmholtzspulenpaar zurückgegriffen. Aufgrund der nötigen Elektrodenlänge musste der Spulenabstand etwas größer, als für die Helmholtzkonfiguration nötig, gewählt werden. Insofern waren noch weitere Berechnungen durchzuführen, um zu prüfen, inwiefern sich

dieses nicht ganz homogene Feld auf die Elektronendichteverteilung auswirkt. Durch Strahltransportrechnungen konnte gezeigt werden, dass die Inhomogenität die Abbildungsqualität des Prototyps für die von GSI vorgegebenen Parameter nicht beeinflussen wird.

Diagnose des nichtneutralen Plasmas

Neben der Bestimmung der Plasmaparameter können über das Experiment auch Bedingungen für die Stabilität der Elektronenwolke abgeleitet werden. Nur durch ein erweitertes Verständnis der Dynamik des Systems kann die Linse auch für ihren Einsatz als Fokussierelement optimiert werden.

Da der Plasmazustand möglichst unbeeinflusst bleiben sollte, wurde neben den emittierten Restgasionen vor allem die Plasmaemission untersucht. Dazu wurde ein Experiment mit verschiedenen Diagnoseeinheiten aufgebaut. Eine Faraday Tasse, ein Impulsspektrometer und eine Pepperpotemittanzmessanlage sind zur Analyse der Restgasionen herangezogen worden, während die Plasmaemission mithilfe eines optischen Systems aus Monochromator und einer sensitiven CCD Kamera detektiert wurde, sowie einer CCD Kamera mit integriertem Verstärker zur schnellen, zeitaufgelösten Diagnose des Plasmazustandes.

Die Elektronendichte konnte mithilfe des Impulsspektrometers aus der gemessenen Energie der emittierten Restgasionen abgeleitet werden. Die zugrundeliegende Idee ist dabei, dass das angelegte Anodenpotential durch Elektroneneinschluss reduziert wird und daher die Ionen ihre Energie nur noch aus diesem reduzierten Potential gewinnen können. Darüber hinaus konnte auch das zeitliche Stromprofil mithilfe der Faraday Tasse und die Phasenraumverteilung der Restgasionen mithilfe der Pepperpotemittanzmessanlage detektiert werden. Im Falle der zeitlichen Strommessung durch die Faraday Tasse konnten somit Rückschlüsse auf die Stabilität des Plasmazustandes gezogen werden, wobei der Einsatz der Emittanzmessanlage zur zeitaufgelösten Diagnose noch zu prüfen ist. Eine ähnliche Analyse des Plasmazustandes erfolgte über die Vermessung der Leuchtdichteverteilung. Diese konnte durch einen speziellen Algorithmus auf Asymmetrien untersucht und auch klassifiziert werden.

Die Temperaturbestimmung erfolgte über die Untersuchung der emittierten Spektrallinien des Heliums. Dabei wurde der detektierte Photonfluss Φ_{ij} zweier Spektrallinien,

Zusammenfassung

der aus der Wechselwirkung des Restgases mit den eingeschlossenen Elektronen entsteht, ins Verhältnis gesetzt. Die Anregungswahrscheinlichkeit des spektralen Übergangs wird über den optischen Wirkungsquerschnitt $Q_{ij}(E)$ berücksichtigt, der abhängig ist von der Elektronenenergie. Unter der Annahme einer energetischen Maxwell-Verteilung der Elektronen kann über

$$\frac{\Phi_{ij}}{\Phi_{ab}} = \frac{\int_{E_1}^{\infty} Q_{ij} \exp[-E/kT_e] E dE}{\int_{E_2}^{\infty} Q_{ab} \exp[-E/kT_e] E dE} \quad (1)$$

die Elektronentemperatur bestimmt werden.

Allerdings war die bisherige Datenlage der optischen Wirkungsquerschnitte vor allem im Bereich höherer Energien von über 200 eV ungenügend oder auf einen kleinen Teil des optischen Spektrums beschränkt, so dass ein weiteres Experiment zur Vermessung der optischen Wirkungsquerschnitte aufgebaut wurde. Die optischen Wirkungsquerschnitte für die wichtigsten Anregungen im Helium, wurden im Energiebereich von 80-1830 eV ausgemessen.

Dadurch bot sich auch die Möglichkeit, die Wechselwirkungsprozesse von Elektronen definierter Energie mit Restgasatomen bestimmter Anzahl näher zu untersuchen und sie der Emission des nichtneutralen Plasmas direkt gegenüberzustellen.

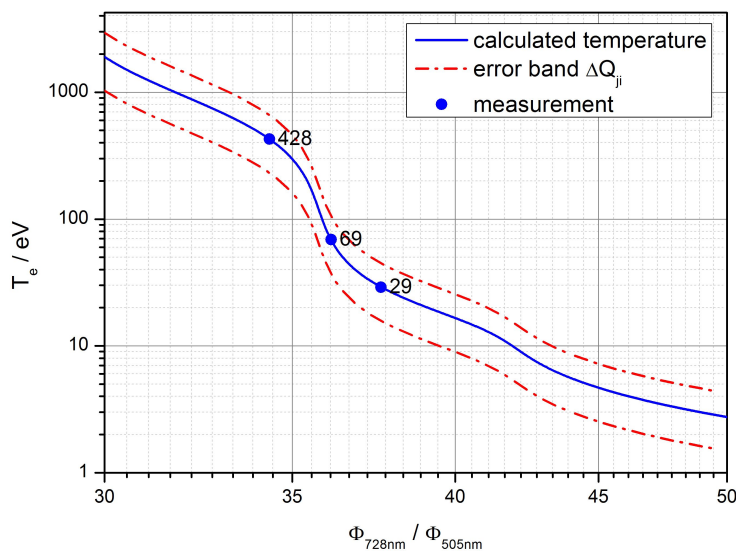


Abbildung 3: Messung der Elektronentemperatur für verschiedene Einstellungen der Gabor-Linse. Die Temperaturen von 29 eV und 69 eV wurden nahe des Arbeitspunktes der Linse bestimmt, während bei 428 eV die Linsenparameter stark vom Arbeitsbereich der Linse abweichen.

Es zeigte sich, dass sich das Anregungsspektrum des Gases durch Wechselwirkung mit der Elektronenwolke bei einigen der spektralen Übergänge zu dem des Elektronenstrahls unterscheidet. Es konnten aber auch Übergänge identifiziert werden, bei denen scheinbar der gleiche Anregungsprozess stattfindet. Diese wurden zur Bestimmung der Elektronentemperatur des nichtneutralen Plasmas verwendet.

In dieser Arbeit konnte somit die Temperatur des nichtneutralen Plasmas über eine optische Diagnose bestimmt werden (siehe Abbildung 3). Darüberhinaus erfolgte ein Vergleich der Plasmaparameter, d.h. Dichte und Temperatur, mit der numerischen Simulation. Zum ersten Mal wurde es möglich, den Zustand des nichtneutralen Plasmas numerisch an die experimentellen Befunde anzupassen.

Strahltransportexperimente bei GSI

Im sechsten und letzten Kapitel der vorliegenden Arbeit werden die Ergebnisse der Strahltransportexperimente am Hochstromtestinjektor der GSI vorgestellt. Dazu werden zunächst der experimentelle Aufbau und die einzelnen Komponenten erläutert. Bei der verwendeten Ionenquelle handelt es sich um eine MUCIS d.h. Multicusp Ion Source, die gepulst, bei einer Frequenz von 1 Hz und einer Pulslänge von 1.25 ms, betrieben wurde. Die Emittanzen wurden hinter der Linse mit einer Schlitzgitter-Emittanzmessanlage gemessen und der Strom mithilfe eines Strahltransformators direkt am Ausgang der Linse und vor dem Eingang der Emittanzmessanlage aufgenommen.

Die Messungen selbst waren in die Untersuchung eines emittanzdominierten Strahltransportes (He^+ , $I_b=3$ mA, $W_b=50$ keV) und eines raumladungsdominierten Strahltransportes (Ar^+ , $I_b=35$ mA, $W_b=124$ keV) unterteilt. In beiden Fällen wurde das magnetische Feld der Prototyplinse variiert, während das Anodenpotential konstant gehalten wurde. So konnte zum einen ein schnelles Anwachsen der eingeschlossenen Elektronendichte erzielt, zum anderen die Abhängigkeit der Fokussierperformance vom Arbeitspunkt der Linse untersucht werden. Über die gemessene Fokallänge ließ sich außerdem die in der Linse eingeschlossene Elektronendichte bestimmen. Für die unterschiedlichen Strahltransportmessungen konnte so Einschlusseffizienzen von $\kappa=0.14$ erreicht werden, die maximale Einschlusseffizienz lag dabei allerdings deutlich über $\kappa_{\text{max}}=0.20$.

Die Ergebnisse der Strahltransportmessungen konnten sodann den Ergebnissen der zuvor am IAP durchgeführten Plasmadiagnose und der Numerik gegenübergestellt werden.

Zusammenfassung

Für den Fall des emittanzdominierten Strahltransportes zeigte sich durch den Vergleich von Diagnose, Strahltransport und Numerik, dass sich der Zustand der Elektronenwolke unter Einfluss des Ionenstrahls von dem der unbeeinflussten Plasmawolke unterscheidet. In beiden Fällen wird deutlich, dass die Linse im Bereich ihrer Arbeitsfunktion eine sehr gute Abbildungsqualität hat, während sich fernab dieses Arbeitsbereiches Instabilitäten ausbilden, die zu einer Herabsetzung der Fokussierqualität führen.

Vielversprechend sind vor allem die Ergebnisse zum Transport des raumladungsdominierten Ar^+ Strahles. In Abbildung 4 wird die gemessene Phasenraumverteilung des gedrifteten Strahls derjenigen des fokussierten Strahls gegenübergestellt.

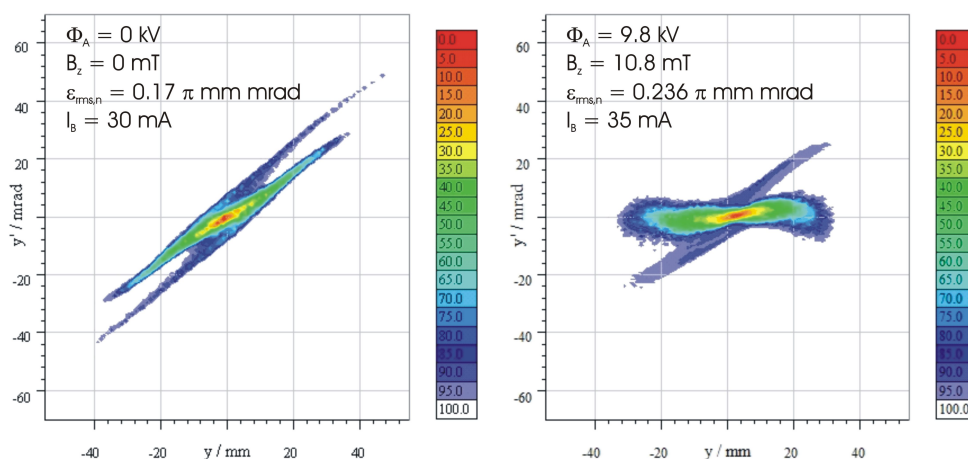


Abbildung 4: Gemessene Phasenraumverteilung des gedrifteten Ar^+ -Strahls (links) und des durch die Gabor-Linse transportierten Strahles (rechts). Beide Emittanzen wurden an derselben Stelle hinter der Linse aufgenommen.

Bei einer Strahlenergie von $W_b = 3.1$ keV/u wird bei einem Strom von $I_b = 35$ mA ein paralleler Strahl bei einer Einstellung der Linsenparameter von $\Phi_A = 9.8$ kV für das Anodenpotential und $B_z = 10.8$ mT für das Magnetfeld erreicht. Dabei wächst die normierte rms-Emittanz um etwa einen Faktor 1.38.

In Rahmen der vorliegenden Arbeit wurde die entwickelte Prototypinse erfolgreich am Hochstromtestinjektor der GSI, insbesondere für den Strahltransport intensiver, raumladungsdominierter Ionenstrahlen, getestet. Darüber hinaus konnte erstmals die Anwendung einer optischen Spektroskopie im Fall nichtneutraler Plasmen demonstriert werden.

In diesem Zusammenhang stellte sich der Einfluss einer geänderten Elektronenproduk-

tions- und Verlustrate auf die Fokussierkraft der Linse und den Plasmazustand des eingeschlossenen, nichtneutralen Plasmas als besonders wichtig und interessant dar. Im Regime eines erhöhten Restgasdrucks (im Bereich von $\approx 10^{-4}$ Pa), in dem Wechselwirkungsprozesse mit Restgasatomen an Bedeutung gewinnen, müssen insbesondere die Produktions- und Verlustraten, die den Gleichgewichtszustand des Systems definieren, genauer untersucht werden, um die Performance des gesamten Transportkanals zu steigern.

Zusammenfassung

Contents

Zusammenfassung	i
1 Introduction	1
2 Gabor Lens – Basic Principles	5
2.1 Fundamental Properties of Nonneutral Plasmas	6
2.2 Nonneutral Plasma Confinement	9
2.3 Thermal Equilibrium and Electron Temperature	17
2.4 Electron Production and Losses	32
2.5 Numerical Simulation of the Nonneutral Plasma State	39
2.6 Theory of Ion Beam Transport	41
2.7 Focusing Principle of the Gabor Lens	46
2.8 Numerical Simulation of the Beam Transport	48
3 Nonneutral Plasma Instabilities	49
3.1 Experimental Observation of Nonneutral Plasma Instabilities	49
3.2 Diocotron Instability	51
4 Design of the Prototype Gabor Lens for GSI	57
4.1 Gabor Lens Requirements and Design of the Electrode System	57
4.2 The Magnetic System	60
4.3 Technical Specifications	66
5 Nonneutral Plasma Diagnostics	69
5.1 Experimental Set-Up	70
5.2 Residual Gas Ion Current	73
5.3 Plasma Emission	80

CONTENTS

5.4	Time-Resolved Optical Diagnostics	84
5.5	Electron Temperature Measurement	88
6	Beam Transport Measurements at GSI	121
6.1	Experimental Set-Up	121
6.2	High-Voltage Conditioning and Commissioning of the Gabor Lens	125
6.3	Results of the Beam Transport Measurements and the Comparative Per- formed Nonneutral Plasma Diagnostics	128
7	Summary and Conclusion	147
	References	151
	List of Figures	163
	List of Tables	173

1

Introduction

The investigation of a nonneutral plasma confined in a Gabor lens opens up a wide area of fundamental research. Beside the application in accelerator physics as a focusing device, especially for intense ion beams, it is possible to study basic physical mechanisms involving interaction processes and the collective behavior of a particle ensemble. In this context, the physical mechanisms that lead to a dynamic equilibrium state of the nonneutral plasma attract special interest.

The concept of the Gabor lens goes back to an idea of Dennis Gabor, who proposed a magnetron-type trap as an effective diverging lens for electron beams (collecting lens for positive ion beams) [Gab47]. Electrons, which are confined inside the lens volume by orthogonal magnetic and electric fields, create an electric self-field that causes a radial symmetric focusing force on an ion beam passing through the lens volume. A homogeneous electron distribution results in a linear electric space charge field in radial direction.

In the low energy beam transport section (LEBT) of an accelerator facility, an extracted ion beam has to be guided and matched over a given distance to the acceptance of a following accelerator (typically a Radio Frequency Quadrupole - RFQ). Ideally, the ion beam is transported without any losses or a growth in the emittance, which represents the quality of the beam. High intensity ion beams often suffer from the transverse expansion as a result of the radial ion motion. This is due to a space charge blow-up [Gon13] and can lead to degradation of the beam current density needed for the experiments. The repulsing forces that act on the beam ions may be compensated by electrons. The primary sources of neutralizing electrons are ionization processes of the

1. INTRODUCTION

residual gas interacting with the beam and secondary electron production due to beam particles striking the chamber wall. With respect to the application of conventional focusing devices, the Gabor lens offers the advantage that the electron distribution within the beam potential is controlled by the external fields. This enables the transport of intense ion beams without aberrations at relatively low field strengths.

The application of a Gabor lens as a focusing device has been studied by several research groups since the beginning of the 1970s [Mob73], [PMSY90]. However, despite the theoretical advantage of this concept the performance of the lens has fallen short of expectations since the influence of the external parameters on the dynamics of the nonneutral plasma have not been sufficiently described to date. At the Institute for Applied Physics (IAP), a new conceptional design of this lens type as well as numerical models of the confined plasma cloud have been developed. Thanks to an improved understanding of the plasma confinement as a function of the external fields, two lenses have been successfully tested as a LEBT for small beam currents and remain in operation. Furthermore, the application of a high field Gabor lens behind an RFQ has also been studied in detail [Meu06].

In the context of the planned FAIR project, the application of the Gabor lens for focusing space charge dominated ion beams at the High Current Test Injector (HOSTI) has been investigated for the first time within the scope of this thesis.

The Facility for Antiproton and Ion Research, FAIR, is a new particle accelerator facility that will be built at the GSI Helmholtzzentrum für Schwerionenforschung GmbH in Germany. The research program at FAIR will cover a wide range of topics in nuclear and hadron physics, high density plasma and atomic physics and applications in condensed matter physics and biology [Ros07]. A two stage synchrotron concept will be used to produce high intensity secondary beams of antiprotons and short-lived radioactive nuclei [SF06].

As a part of the FAIR project, the requirements of the existing High Current Injector (HSI) [Rat01] concerning beam brightness and intensity, especially of the delivered $^{238}\text{U}^{4+}$ -beam, will be more challenging [AHS10]. For this reason, the application of a Gabor lens holds a lot of promise in terms of increasing the quality of the injected beam and consequently the luminosity at the end of the particle accelerator.

In this thesis, a prototype lens has been designed and constructed in order to investigate

its performance at the HOSTI, which allows to develop an optimized low energy beam transport for HSI. Due to large beam radii, a major issue in the design concerned the generation of a stably confined electron cloud with a radius of up to $r=50$ mm. If the lens is operated with respect to its operation function, the electron cloud is stably and homogeneously confined and the created linear electric self-field provides a rotationally symmetric focusing force on the beam ions. However, the electric field is strongly nonlinear at the edge of the plasma cloud, due to the Debye drop off. These nonlinear forces acting on the beam result in an emittance growth if its radius is larger than the plasma radius.

Other nonlinear forces are created by plasma instabilities whose occurrence is observed in the regime of unbalanced confinement conditions or at high residual gas pressures. Therefore, the investigation of instabilities and their dependency on the plasma parameters is a necessary requirement to ensure a beam transport without emittance growth.

In this context, non-invasive diagnostic techniques to determine the important plasma parameters were developed, given that conventional plasma diagnostics is not applicable to the nonneutral plasma in most cases. For the steady state of the electron ensemble the temperature can be determined by optical emission spectroscopy, since the lens is always operated in a regime of increased gas pressures right behind the ion source.

The investigation of the plasma emission produced by the interaction of confined particles with residual gas or ions reflects a common way of determining the electron density and temperature [Fan06]. Different plasma models describe the state of plasma from the number of interaction processes occurring within the system. If the energy is conserved, i.e. all possible interaction processes are balanced, the plasma may be described by a thermodynamic equilibrium. Since laboratory plasmas are optically thin, the application of a local thermal equilibrium excluding all process that involve a photon emission or absorption to the actual situation might be useful [Hut05a].

For a better description of the processes occurring in the solar corona, a plasma model was developed that balances between a collisional excitation from and a radiative decay to the ground level solely [Hut05b]. Since the parameters of the solar corona are comparable to the nonneutral plasma, i.e. high electron densities of 10^{14} m^{-3} and high plasma temperatures of $T_e \approx 100 \text{ eV}$, this model can be applied after a careful examination of the occurring atomic processes.

1. INTRODUCTION

Beside the plasma parameters, the dynamical behavior of the electron cloud was also investigated given that the plasma is required to be not only spatially but also temporally stable in order to achieve a good focusing performance.

In the first part of this work, the theoretical description of the nonneutral plasma confined in the Gabor lens is presented and the occurrence of plasma instabilities due to external parameters is described. The design and construction of the prototype lens as well as the diagnostics concepts are discussed in chapters 4 and 5. Finally, the results of the beam transport experiments at GSI and the nonneutral plasma diagnostics studied at IAP are presented in chapter 6.

2

Gabor Lens – Basic Principles

2.1	Fundamental Properties of Nonneutral Plasmas	6
2.1.1	Debye Shielding	6
2.1.2	Plasma Frequency	7
2.1.3	Nonneutral Plasma Definition	8
2.2	Nonneutral Plasma Confinement	9
2.2.1	Longitudinal Confinement	9
2.2.2	Radial Confinement	12
2.2.3	Operation Function	15
2.3	Thermal Equilibrium and Electron Temperature	17
2.3.1	Particle Collisions and Thermalization	18
2.3.2	Equilibrium States	26
2.4	Electron Production and Losses	32
2.4.1	Electron Production and Nonneutral Plasma Ignition	32
2.4.2	Electron Losses	35
2.4.3	Experimentally Investigated Particle Losses by X-Ray Spectroscopy	37
2.5	Numerical Simulation of the Nonneutral Plasma State	39
2.5.1	GABOR-M	39
2.5.2	GAB_LENS	40
2.6	Theory of Ion Beam Transport	41
2.6.1	Emittance	41
2.6.2	Kurtosis	42
2.6.3	Brightness	44

2. GABOR LENS – BASIC PRINCIPLES

2.6.4	Perveance	44
2.6.5	Envelope Equation	46
2.7	Focusing Principle of the Gabor Lens	46
2.8	Numerical Simulation of the Beam Transport	48

2.1 Fundamental Properties of Nonneutral Plasmas

A nonneutral plasma is defined as a many-body collection of charged particles in which there is not overall charge neutrality [Dav90a].

Nonneutral plasmas show a similar collective behavior as described for quasineutral plasmas, i.e. the Debye shielding, plasma frequency and appearance of plasma instabilities. In this connection, it should be pointed out that the quasineutrality is often adduced as a necessary criterion in the relevant plasma physics literature, in order to derive the concept of the Debye shielding. In case of a one-component plasma, the potential of the trap adopts the role of the neutralizing species.

2.1.1 Debye Shielding

The Debye shielding is described as the ability of the plasma to shield out electric potentials that are applied to it. If a charged particle is introduced into a quasineutral plasma, particles with the opposite sign of charge will redistribute to screen the potential of the test charge [Che74a].

If the plasma were cold, the shielding would be perfect; however, with increasing temperature, particles at the edge of the cloud gain enough thermal energy to escape from the electrostatic potential well and the shielding is not complete. Therefore, the Debye length λ_D defines the shielding distance and is given by

$$\lambda_D^2 = \frac{\epsilon_0 k_B T_e}{n_e e^2} \tag{2.1}$$

Of course, for the nonneutral plasma there are no charges of the opposite sign to shield the field of an introduced test particle. Referring to R. C. Davidson [Dav90b] in the nonneutral case, the perturbed potential $\delta\Phi$ associated with introducing the test electron

2.1 Fundamental Properties of Nonneutral Plasmas

is superimposed on the dc space charge potential Φ_r . The total electrostatic potential is given by

$$\Phi = \Phi_r + \delta\Phi \quad (2.2)$$

The Poisson equation for the total electrostatic potential Φ can subsequently be expressed as

$$\frac{1}{r} \frac{\partial \Phi_r}{\partial r} + \frac{\partial^2 \Phi_r}{\partial r^2} + \nabla^2 \delta\Phi = \frac{e}{\epsilon_0} n_{e,max} \cdot \exp\left(\frac{e\delta\Phi}{k_B T_e}\right) + \frac{e\delta(r)}{\epsilon_0} \quad (2.3)$$

where $n_e(r) = n_{e,max} \cdot \exp\left(-\frac{e\Psi(r)}{k_B T_e}\right) \cong n_{e,max}$ is the electron distribution for a nonneutral plasma of finite temperature with the effective potential $\Psi(r) = \Phi_A - \Phi_r$.

For $\frac{e\delta\Phi}{k_B T_e} \ll 1$ the exponential factor can be expanded to

$$\exp(x) = 1 + x + \frac{x^2}{2} + \dots \stackrel{x \ll 1}{\approx} \exp\left(\frac{e\delta\Phi}{k_B T_e}\right) = 1 + \frac{e\delta\Phi}{k_B T_e} \quad (2.4)$$

With $\frac{1}{r} \frac{\partial \Phi_r}{\partial r} + \frac{\partial^2 \Phi_r}{\partial r^2} = \frac{en_e(r)}{\epsilon_0}$ and the Debye length λ_D one obtains the differential equation

$$\nabla^2 \delta\Phi = \frac{1}{\lambda_D^2} \delta\Phi + \frac{e\delta(r)}{\epsilon_0} \quad (2.5)$$

The solution of equation 2.5 is given by

$$\delta\Phi = -\frac{e}{4\pi\epsilon_0 r} \cdot \exp\left(-\frac{r}{\lambda_D}\right) \quad (2.6)$$

which represents the shielded potential surrounding the test electron.

2.1.2 Plasma Frequency

Another example of the collective behavior of a plasma is the plasma frequency, representing the time scale after which the electrons have established a shielded equilibrium, when the plasma is perturbed. The plasma frequency is defined by [Che74b]

$$\omega_{pe} = \sqrt{\frac{n_e e^2}{\epsilon_0 m_e}} \quad (2.7)$$

where n_e is the electron density.

Above this frequency, electrons are unable to respond to a perturbation and the plasma becomes transparent for electromagnetic waves.

Further collective phenomena such as the evolution of plasma instabilities will be discussed in chapter 3.

2. GABOR LENS – BASIC PRINCIPLES

2.1.3 Nonneutral Plasma Definition

In general, there are three conditions that must be satisfied for an ionized gas to be called a plasma [Che74c]:

1. The expansion of the plasma cloud must be much larger than its Debye length.

$$\lambda_D \ll L_{plasma} \quad (2.8)$$

2. A collective behavior requires a certain amount of particles in the Debye sphere

$$N_D = \frac{4}{3} n_e \pi \lambda_D^3.$$

$$N_D \gg 1 \quad (2.9)$$

3. The product of the plasma frequency and the collision times should be larger than one, in order that the electrostatic interaction dominates the gas kinetics.

$$\omega_{pe} t_{ee} > 1 \quad (2.10)$$

The plasma confined in the Gabor space charge lens typically has an electron density of $n_e = 1 \cdot 10^{14} \text{ m}^{-3}$ and an electron temperature of $T_e \approx 100 \text{ eV}$.

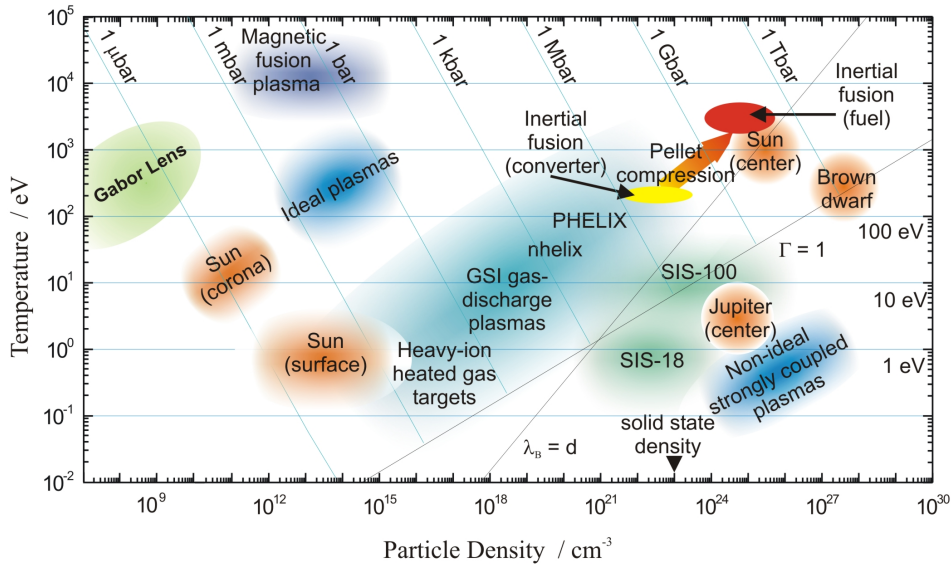


Figure 2.1: Existence diagram of various plasmas [Meu06].

Therefore, the plasma frequency is calculated to $\omega_{pe}=563$ MHz, the Debye length to $\lambda_D=7.4$ mm and the number of electrons in the Debye sphere to $N_D=1.7 \cdot 10^8$. With an expected plasma expansion of $L_{plasma,r}=75$ mm in radial and $L_{plasma,l}=286$ mm in longitudinal direction and mean collision times of $t_{ee}=10$ ms, it fulfills all mentioned conditions.

Figure 2.1 shows the classification of the nonneutral plasma within the existence diagram of various plasmas.

2.2 Nonneutral Plasma Confinement

Inside Gabor space charge lenses, electrons are confined due to the crossed configuration of external magnetic and electric fields. Figure 2.2 shows the typical schematic layout of a Gabor lens used at the Institute for Applied Physics.

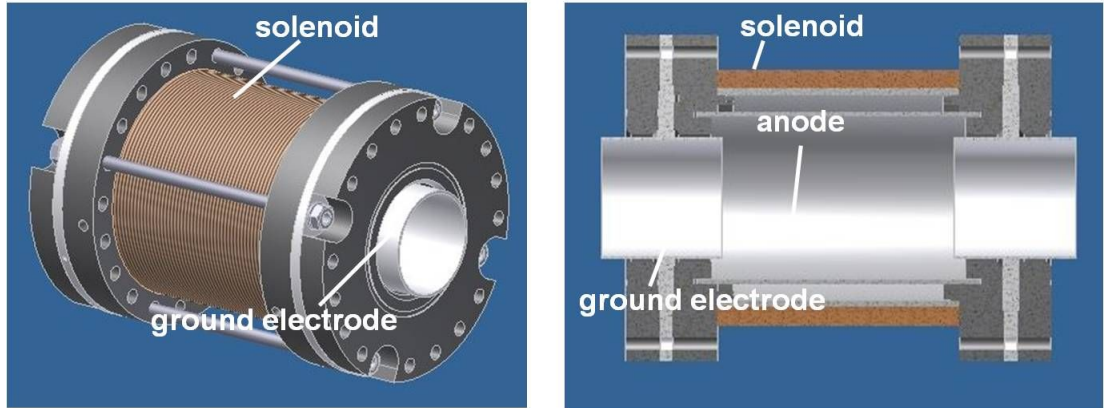


Figure 2.2: Typical layout of a Gabor lens used at IAP.

The potential well created by a cylindric electrode system confines the electrons in longitudinal direction, while the magnetic field of a solenoid or Helmholtz coils prevents the loss of electrons in radial direction. Dependent on the confining fields, a maximum electron density in each direction is deduced.

2.2.1 Longitudinal Confinement

Electrons that are produced within the lens volume are unable to escape in longitudinal direction due to the potential barrier created by the electrode system. The confined

2. GABOR LENS – BASIC PRINCIPLES

electron column reduces the positive potential of the anode and the maximum confinement is reached when the space charge potential of the electrons is equal to the applied anode potential $\Phi_r = \Phi_A$ (see figure 2.3).

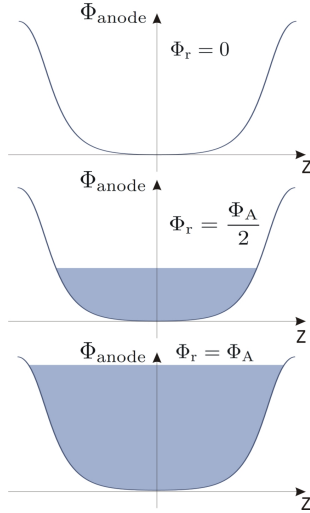


Figure 2.3: Longitudinal electron confinement within the potential well of the electrode system.

Assuming a cold, homogeneously distributed plasma column, the space charge potential can be calculated by

$$\Phi_r(r) = - \int_0^{R_A} E(r) dr = \frac{n_e e R_A^2}{4\epsilon_0} \quad (2.11)$$

with the assumption $\Phi_r = \Phi_A$ one can define the maximum electron density in longitudinal direction by

$$n_{e,l,max} = \frac{4\epsilon_0 \Phi_A}{e R_A^2} \quad (2.12)$$

Referring to [Meu06] loss channels between the anode and the ground electrode lower the maximum radial expansion of the plasma column R_p to the radius of the ground electrode R_G .

For this reason, another definition for the maximum confined electron density might be useful.

Assuming that $\Phi_r < \Phi_A$ one can calculate the potential in case of $r < R_p$ to

$$\Phi_{r,in}(r) = - \int E(r) dr = \frac{n_e e r^2}{4\epsilon_0} + C_1 \quad (2.13)$$

and in case of $r > R_p$ to

$$\Phi_{r,out}(r) = - \int E(r)dr = \frac{n_e e R_p^2}{2\epsilon_0} \ln(r) + C_2 \quad (2.14)$$

Under the condition of $\Phi_r(R_A) = \Phi_A$ the constant C_2 is given by

$$C_2 = \Phi_A - \frac{n_e e R_p^2}{2\epsilon_0} \ln(R_A) \quad (2.15)$$

Replacing C_2 in equation 2.14 results in

$$\Phi_{r,out}(r) = \Phi_A - \frac{n_e e R_p^2}{2\epsilon_0} \ln\left(\frac{R_A}{r}\right) \quad (2.16)$$

With $\Phi_{r,in}(R_p) = \Phi_{r,out}(R_p)$ one can define C_1

$$C_1 = \Phi_A - \frac{n_e e R_p^2}{2\epsilon_0} \ln\left(\frac{R_A}{R_p}\right) - \underbrace{\frac{n_e e R_p^2}{4\epsilon_0}}_{\Phi_r(R_p)} \quad (2.17)$$

By replacing C_1 in equation 2.13 the resulting potential in the inner part obtains the form:

$$\Phi_{r,in}(r) = \Phi_A - \frac{n_e e}{4\epsilon_0} (R_p^2 - r^2) - 2 \cdot \Phi_r(R_p) \ln\left(\frac{R_A}{R_p}\right) \quad (2.18)$$

With $\Phi_{r,in}(R_p) = \Phi_A - 2 \cdot \Phi_r(R_p) \ln\left(\frac{R_A}{R_p}\right)$ the maximum electron density results in

$$n_{e,l,max} = \frac{4\epsilon_0 \Phi_A}{e R_p^2 \left(1 + 2 \ln\left(\frac{R_A}{R_p}\right)\right)} \quad (2.19)$$

Assuming the ground electrode radius as maximum radius of the electron cloud, the deviation of the density calculated by equation 2.12 or equation 2.19 is small if the R_A/R_p -ratio is close to 1.

In the case of the used Gabor lens $R_A/R_p=1.13$ and, therefore, $2 \ln\left(\frac{R_A}{R_p}\right) \approx 0.24$. The correction adds up to a 3% effect.

To further estimate the electron density resulting from the experiment or the numerical simulation in comparison to the theoretically predicted electron density, the confinement efficiency κ_l for the longitudinal confinement is introduced:

$$\kappa_l = \frac{n_{e,l}}{n_{e,l,max}} \quad (2.20)$$

2. GABOR LENS – BASIC PRINCIPLES

2.2.2 Radial Confinement

An axial symmetric magnetic field confines the electrons in radial direction. The embedded plasma column rotates about the axis of symmetry of the lens. Consequently, different forces act on a electron and are represented in figure 2.4. The associated Lorentz force F_L is directed radially inward and balances all of the radially outward forces as the centrifugal force F_C and the electrostatic force F_R .

The following discussion concerning the mathematical description of the transverse electron confinement refers to the argumentation of R. C. Davidson [Dav74].

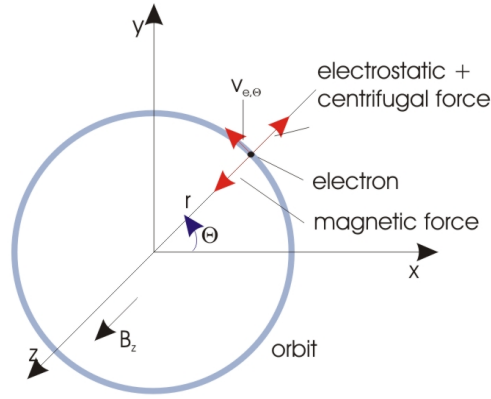


Figure 2.4: Scheme of forces acting on an electron.

The force balance equation is given by

$$-\frac{m_e v_{e,\Theta}^2}{r} = -eE_r - e v_{e,\Theta} B_z \quad (2.21)$$

where $v_{e,\Theta}(r)$ is the azimuthal velocity and $E_r(r)$ the radial electric field.

Assuming a cold electron cloud without any neutralizing ion background, it is possible to calculate the electric space charge field by applying Gauss's law

$$\Phi_E = \oint_S \vec{E} \cdot \vec{n} da = \frac{q}{\epsilon_0} \quad (2.22)$$

and integrating it over $0 < r < R_p$. The electric field is subsequently given by

$$E_r = -\frac{n_e e r}{2\epsilon_0} = -\frac{m_e}{2e} \omega_{pe}^2 r \quad (2.23)$$

where $\omega_{pe} = \sqrt{\frac{n_e e^2}{\epsilon_0 m_e}}$ is the plasma frequency.

Introducing the angular velocity $\omega_e = \frac{v_{e,\theta}}{r}$, equation 2.21 can be expressed as

$$-\omega_e^2 = \frac{\omega_{pe}^2}{2} - \omega_e \Omega_e \quad (2.24)$$

where $\Omega_e = \frac{eB}{m_e}$ is the electron cyclotron frequency.

The solution to equation 2.24 is

$$\omega_e = \omega_e^\pm = \frac{\Omega_e}{2} \left[1 \pm \left(1 - \frac{2\omega_{pe}^2}{\Omega_e^2} \right)^{\frac{1}{2}} \right] \quad (2.25)$$

ω_e^\pm represents the two possible mean rotation velocities of the electron column as a whole and independently of the radius. For low densities, the fast rotational mode ω_e^+ corresponds to all electrons gyrating around the axis of symmetry at the cyclotron frequency, whereas the slow rotational mode ω_e^- corresponds to an ExB rotation of the plasma column. The high density limit is known as the Brillouin flow limit [Bri45], and can also be expressed by the confinement efficiency κ_r :

$$\kappa_r = \frac{2\omega_{pe}^2}{\Omega_e^2} = 1 \quad (2.26)$$

In this case, the two rotational frequencies are equal $\omega_e^+ = \omega_e^- = \Omega_e/2$ and correspond to a rigid rotation of the column with angular velocity $\Omega_e/2$.

Figure 2.5 shows the confinement efficiency as a function of the two rotational frequencies ω_e^+ and ω_e^- and consequently the associated electron motion.

From the Brillouin flow density limit ($2\omega_{pe}^2 = \Omega_e^2$), the maximum electron density now results in [Meu06]

$$n_{e,r,max} = \frac{\epsilon_0 B_z^2}{2m_e} \quad (2.27)$$

In reality, the plasma has a high electron temperature and the interaction of electrons with residual gas is not negligible. Ions are created by electron impact ionization and despite being extracted from the lens volume due to the positive anode potential, they will form a neutralizing background for the nonneutral plasma column. Especially in the case of application as a focusing device, the influence of ions on the confinement is no longer negligible.

Therefore, it is useful to extend the discussed theoretical radial confinement on the

2. GABOR LENS – BASIC PRINCIPLES

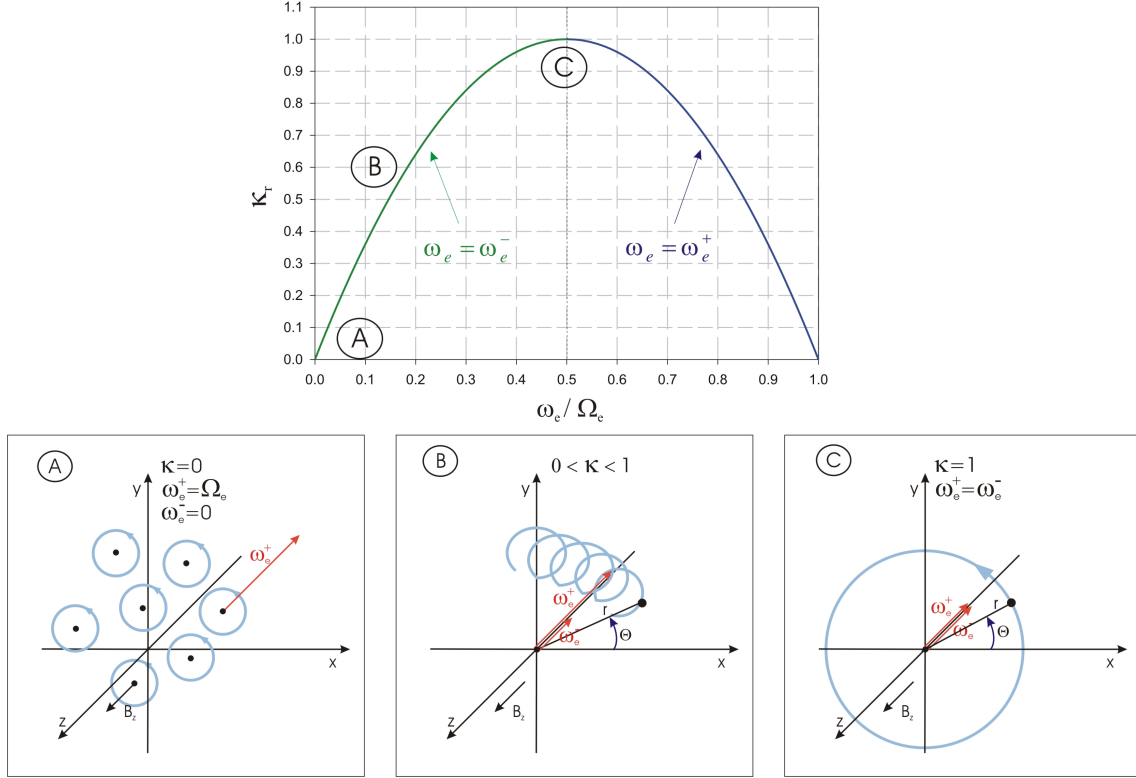


Figure 2.5: Confinement efficiency κ_r as a function of the two rotational frequencies ω_e^+ and ω_e^- (top). Illustration of the associated electron motion for different confinement efficiencies (bottom).

fractional neutralization $f = \text{const.}$ [Dav74].

If only single ionization is assumed, equation 2.25 is modified to

$$\omega_e = \omega_e^\pm = \frac{\Omega_e}{2} \left[1 \pm \left(1 - \frac{2\omega_p^2}{\Omega_e^2} (1-f) \right)^{\frac{1}{2}} \right] \quad (2.28)$$

For complete neutralization ($f=1$), the frequencies result in $\omega_e^+ = \Omega_e$ and $\omega_e^- = 0$. In this case, the magnetic field is solely acting on the electrons and therefore the plasma no longer performs a $\mathbf{E} \times \mathbf{B}$ rotation.

Taking the neutralization factor f into account it is possible to calculate the maximum electron density by

$$n_{e,r} = \frac{\epsilon_0 B_z^2}{2m_e} (1-f) \quad (2.29)$$

In analogy to 2.2.1, another definition of the confinement efficiency for the radial confinement is introduced, in order being able to compare the experimental and numerical results to the theoretically predicted:

$$\kappa_r = \frac{n_{e,r}}{n_{e,r,max}} \quad (2.30)$$

2.2.3 Operation Function

In case of $n_{e,r}=n_{e,1}$, one can define a configuration rule for the magnetic field and the applied potential

$$\Phi_A = \frac{eR_p^2 \left(1 + 2 \ln \left(\frac{R_A}{R_p}\right)\right) B_z^2}{8m_e} (1 - f) \quad (2.31)$$

For the idealized case, assuming $R_A \approx R_p$ and $f=0$, equation 2.31 is simplified to

$$\Phi_A = \frac{eR_A^2 B_z^2}{8m_e} \quad (2.32)$$

Equation 2.31 and 2.32 represent a operation prescription for the Gabor lens. The difference between the idealized case and the operation prescription for the prototype Gabor lens, assuming the presented corrections, is illustrated in figure 2.6. Note that only for demonstration purpose the neutralizing ion background was assumed to $f=0.25$, in the discussed cases in chapter 6 the value is lower.

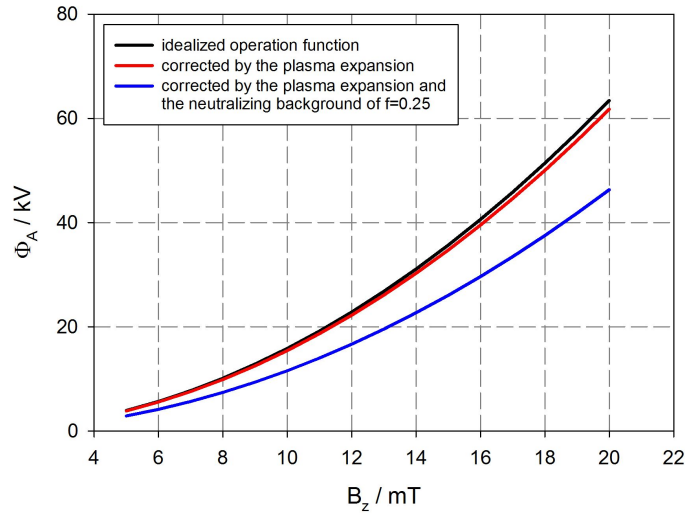


Figure 2.6: Operation function of the prototype Gabor lens for different corrections.

2. GABOR LENS – BASIC PRINCIPLES

Along the operation function a stable confinement of the plasma cloud is assumed and was also experimentally verified by [Meu06]. Figure 2.7 shows the mapping quality of the lens represented by the emittance growth of the passing He^+ -ion beam ($W_b=110 \text{ keV/u}$, $I_b=1.2 \text{ mA}$) as a function of the confining potential and magnetic field calculated by equation 2.32.

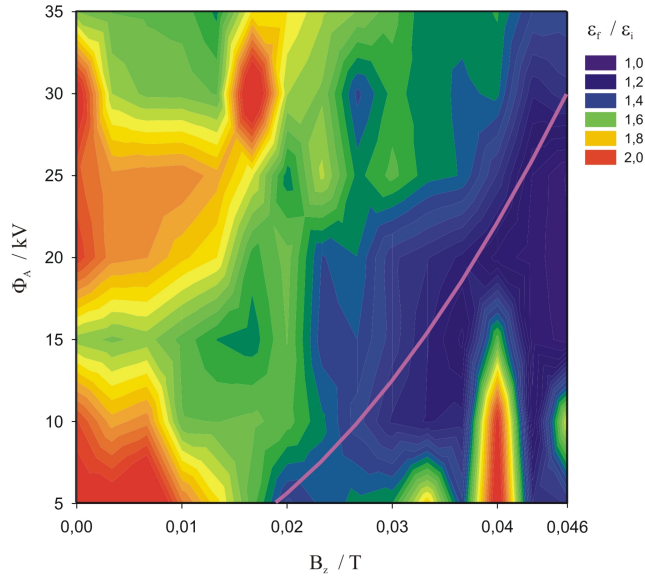


Figure 2.7: Mapping quality of a Gabor lens represented by the emittance growth and as a function of the external fields (obtained from [Meu06]).

The emittance growth along the operation function of the used lens type (pink line) is negligible compared to regions without proper field configuration.

In the following chapters, the field configuration in terms of the operation point will be expressed as the quotient of the longitudinal and the radial confinement strength $\frac{B_z}{B_A}$. The anode potential is replaced by the equivalent magnetic field B_A calculated from the results of equation 2.31 assuming $f=0$. For $\frac{B_z}{B_A} = 1$, the operation point is achieved.

2.3 Thermal Equilibrium and Electron Temperature

The motion of the electrons forming a hot plasma involves a number of stochastic processes and requires a statistical description [Pie10a].

In thermodynamic equilibrium, the particles attain a Maxwell-Boltzmann distribution, which essentially describes how the total energy of the system is distributed to its particles and, of course, varies with the temperature. Therefore, the temperature of a many particle system in thermal equilibrium can be characterized as the energy of the random particle motion averaged by their number density.

In many cases, the lifetimes of plasmas are insufficient to guarantee that a thermal equilibrium has been reached [Hut05a]. Given that the nonneutral plasma is confined by static fields, the lifetimes are very long (hours and even days). Following the argumentation of [OD98] for a pure electron plasma without neutralizing background or neutral atoms, Coulomb interactions between the particles must bring the plasma to a state of thermal equilibrium. In this context, note that the term *thermal equilibrium* should not be confused with the thermal equilibrium of charge state distribution discussed in section 2.3.2.

In case of a real plasma, the total energy and total canonical angular momentum are not conserved exactly. Collisions with neutrals change the plasma energy and angular momentum, and most importantly small field errors and construction errors break the cylindrical symmetry and apply a small torque on the plasma.

In particular, the interaction of electrons with neutrals is not negligible, since the Gabor lens is used in an environment with an assumed high residual gas pressure right behind the ion source.

In this context, the temperature of the nonneutral plasma confined in the Gabor lens is best described by a flow equilibrium that is achieved due to all energy gain and loss processes of the electrons. Between two collisions, the electron gains kinetic energy in the electric field. When the electron collides with an atom, it not only loses energy depending on the kind of collision; moreover, it is also deflected, which means a change in the direction of the momentum vector. Additionally considering particle losses and production, a steady state is reached when the energy loss equals the energy gain of the system [Pie10b]. This simplified assumption is illustrated in figure 2.8.

2. GABOR LENS – BASIC PRINCIPLES

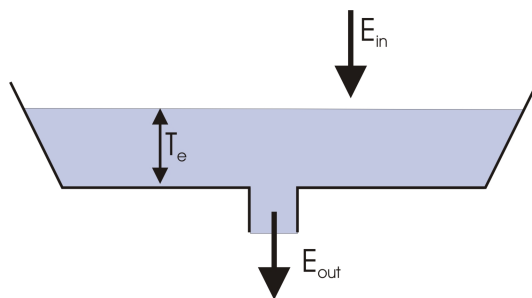


Figure 2.8: Scheme of a flow equilibrium.

In order to develop a non-invasive temperature diagnostics by plasma emission spectroscopy, it is necessary to know the expected population of atomic states in a plasma to predict the radiative behavior, and this is closely related to thermodynamic parameters such as electron temperature and density. Therefore, the relevant interaction processes of the nonneutral plasma, particularly with neutrals but also with charged particles, will be discussed in the following paragraph.

2.3.1 Particle Collisions and Thermalization

In case of the nonneutral plasma, the relevant collisions are electron-electron collisions and those with neutral atoms. All following collision frequencies and production rates are calculated for the beam and plasma parameters discussed in chapters 5 and 6. Even though the interactions of electrons with ions are not dominant, for the sake of completeness the possible interaction processes are also presented.

2.3.1.1 Electron-Atom Collisions

The electron-atom interaction can be divided into **elastic collisions** that particularly change the momentum of the deflected particle and **inelastic collisions** that lead to either excitation or ionization of the atom.

Figure 2.9 illustrates the frequency of **elastic collisions** with helium atoms as a function of the residual gas pressure. For the special cases of hydrogen and helium, the

2.3 Thermal Equilibrium and Electron Temperature

collision frequency simply scales with the pressure p or the number density n_n [Fra09].

$$\nu_{en,e} = 3,07 \cdot 10^{11} \cdot \frac{273}{T} \cdot p \quad [p \text{ in Pa}] \quad (2.33)$$

$$t_{en,e} = \frac{1}{\nu_{en,e}} \quad (2.34)$$

where $t_{en,e}$ is the time between the collisions.

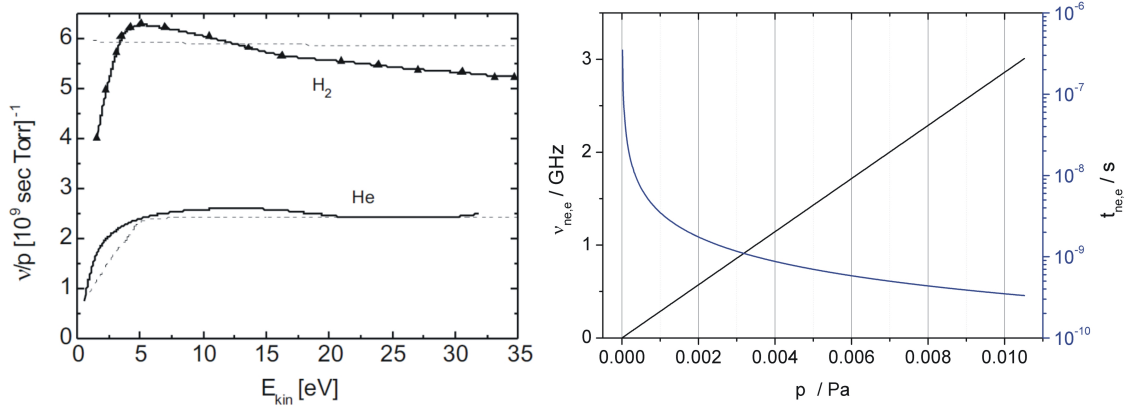


Figure 2.9: Frequency for elastic collisions between electrons and neutrals for hydrogen and helium as a function of the energy [Fra09] (left) and frequency and collision times as a function of the residual gas pressure for He (right).

In the case of **inelastic interactions**, the electron-atom collision frequency and time is given by

$$\nu_{en,i} = n_n \langle \sigma v \rangle = \frac{n_n}{n_e} \int_0^\infty f_e(v) \sigma(v) v d^2v \quad (2.35)$$

$$t_{en,i} = \frac{1}{\nu_{en,i}} \quad (2.36)$$

where $f_e(v)$ is the electron distribution function usually corresponding to a Maxwellian velocity distribution.

For simplicity, the frequencies illustrated in figure 2.10 are estimated by

$$\nu_{en,i} = n_n \sigma_{ion}(E) v \quad (2.37)$$

where $\sigma_{ion}(E)$ is the total ionization cross section for electrons of incident energy E interacting with neutral atoms [KR94] and n_n is the number density of target atoms. Including the number density of projectile particles - in the discussed case, the electron

2. GABOR LENS – BASIC PRINCIPLES

density n_e - the production rate of secondary particles can be defined by

$$\frac{dn}{dt} = n_n n_e \sigma_{ion}(E) v \quad (2.38)$$

Figure 2.10 shows the collision frequency t_{en} and production rate $\frac{dn}{dt}$ of electrons with energy E interacting with helium and argon atoms.

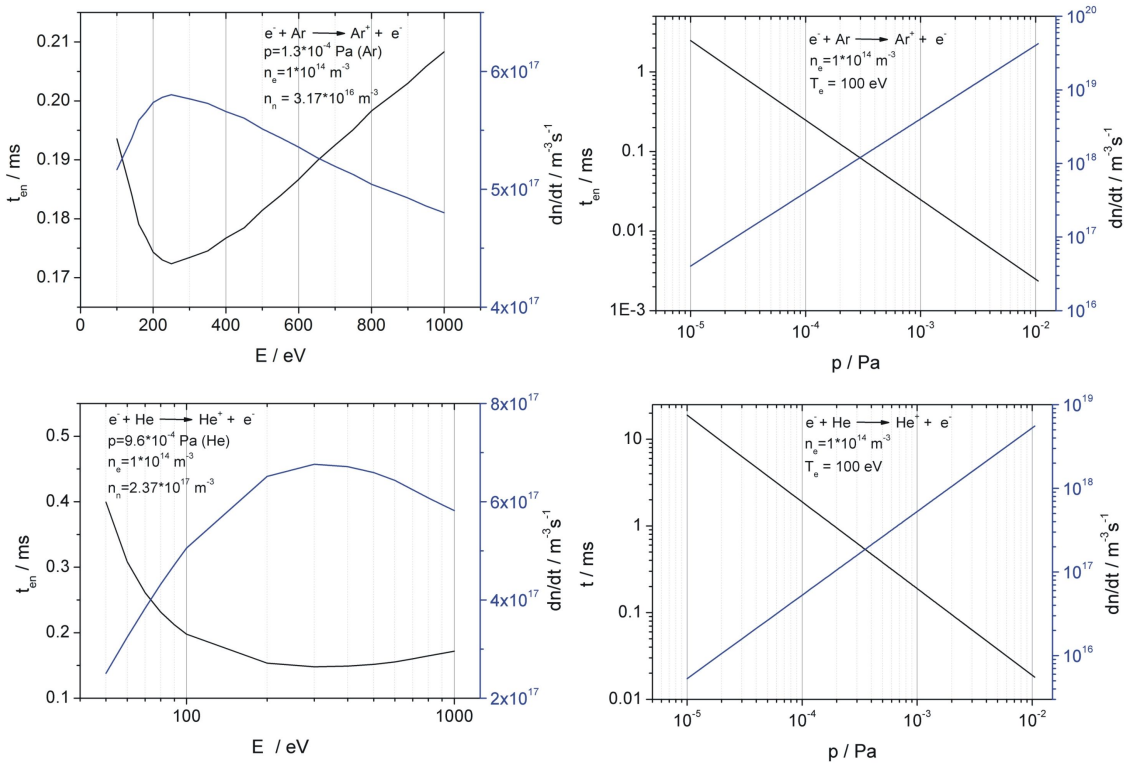


Figure 2.10: Frequency of inelastic collisions between electrons and neutrals for argon and helium as a function of energy (left) and as a function of residual gas pressure (right). The cross section data is obtained from [SSB⁺00] and [fSaT].

2.3.1.2 Electron-Electron Collisions

The self-interaction of electrons is of particularly great importance with respect to the thermalization times of the electron ensemble. The electron-electron collision frequency [GR10a] is given by

$$\nu_{ee} = \frac{2^{1/2} e^4 \ln \Lambda n_e}{12 \pi^{3/2} \epsilon_0^2 m^{1/2} T_e^{3/2}} \quad (2.39)$$

2.3 Thermal Equilibrium and Electron Temperature

where T_e is in units of Joule.

The Coulomb logarithm $\ln \Lambda$ is defined as

$$\ln \Lambda \approx \ln \left(\frac{12\pi}{Z} n_e \lambda_D^3 \right) \approx \ln \left(\frac{12\pi}{Z} n_e \left(\frac{\epsilon_0 T_e}{n_e e^2} \right)^{3/2} \right) \quad (2.40)$$

In case of the nonneutral plasma cloud, the Coulomb logarithm is comparable to the solar corona and amounts to $\ln \Lambda = 21.16$.

Figure 2.11 shows the calculated electron-electron collision frequencies and collision times, respectively, as a function of the electron temperature.

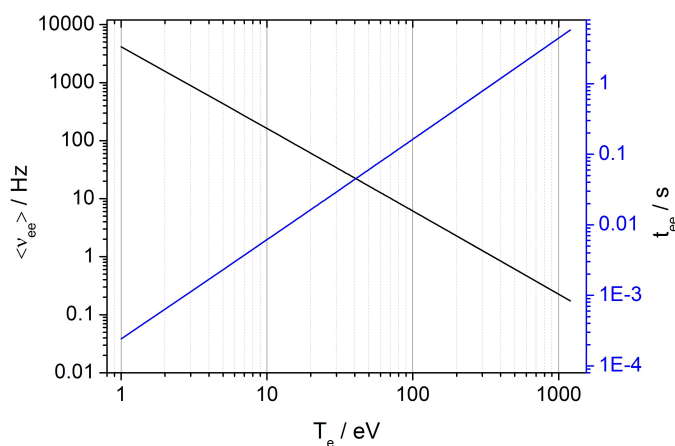


Figure 2.11: Calculated electron-electron collision frequencies and collision times as a function of electron temperature assuming an electron density of $n_e = 1 \cdot 10^{14} \text{ m}^{-3}$.

The relaxation time t_{eq} is defined as the rate at which velocity distributions will alter in certain ways as a result of encounters between charged particles [Spi56]. If test particles with a primary temperature of T_1 are introduced into the electron ensemble of temperature T_2 , the values of T_1 and T_2 approach each other at a rate given by

$$\frac{dT_2}{dt} = \frac{T_1 - T_2}{t_{eq}} \quad (2.41)$$

The time in which the equipartition of energies is established, also termed as thermalization time [Meu06], [Spi56], is

$$t_{eq} = \frac{\epsilon_0^2 (18\pi m_e)^{1/2} (kT_1 + kT_2)^{3/2}}{e^4 \ln \Lambda n_e} \quad (2.42)$$

Electron-electron collisions will lead to a Maxwellian velocity distribution for the electrons in the time scales illustrated in figure 2.12. Of course, this is a function of the

2. GABOR LENS – BASIC PRINCIPLES

primary temperature of the electrons introduced into the nonneutral plasma as well as the plasma density.

Note that the thermalization time t_{eq} represents a maximum limit only as presented in section 2.1.3. In the case of the nonneutral plasma the thermalization time of the electron ensemble follows the plasma frequency $1/\omega_{pe}$ and falls in the range of ns [Meu06].

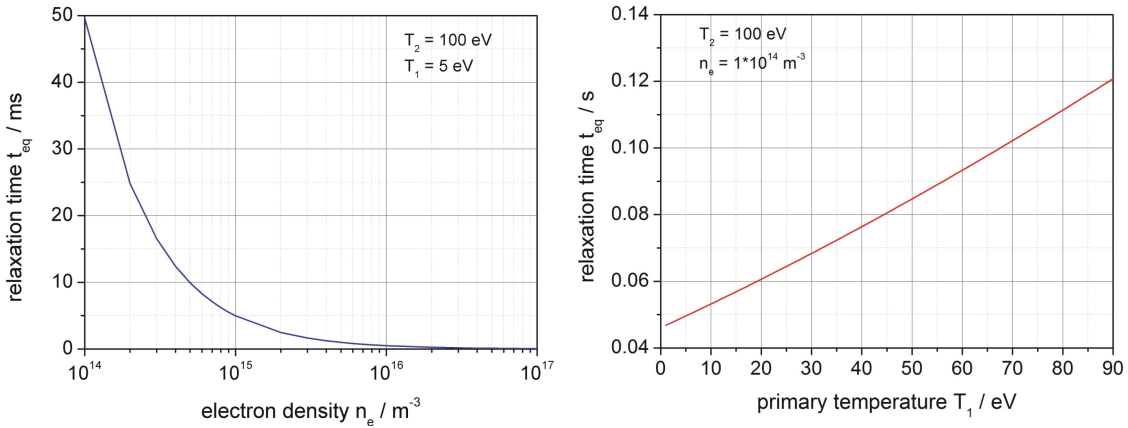


Figure 2.12: Thermalization times due to the electron density (left) and the primary temperature of particles introduced into the electron ensemble (right).

2.3.1.3 Ion-Atom Collisions

It is particularly important to take ion atom collisions into account, due to the Gabor lens used as a focusing device for ion beams. Primary interaction processes between beam ions or produced residual gas ions with neutral atoms are (1) **charge exchange** and (2) **ionization**:

1. $A^+ + B \longrightarrow A + B^+$
2. $A^+ + B \longrightarrow A^+ + B^+ + e^-$

Figure 2.13 shows the **charge exchange** reaction rates and times for helium and argon ions. The presented global reaction rates were calculated for the beam transport measurements discussed in chapter 6, assuming constant ion beam currents of $I_b=3 \text{ mA}$ for helium and $I_b=35 \text{ mA}$ for argon.

In case of the He^+ -beam with a beam energy of $W_b=50.3 \text{ keV}$, an electron capture rate of $1.98 \cdot 10^{16} \text{ m}^{-3}\text{s}^{-1}$ can be expected.

2.3 Thermal Equilibrium and Electron Temperature

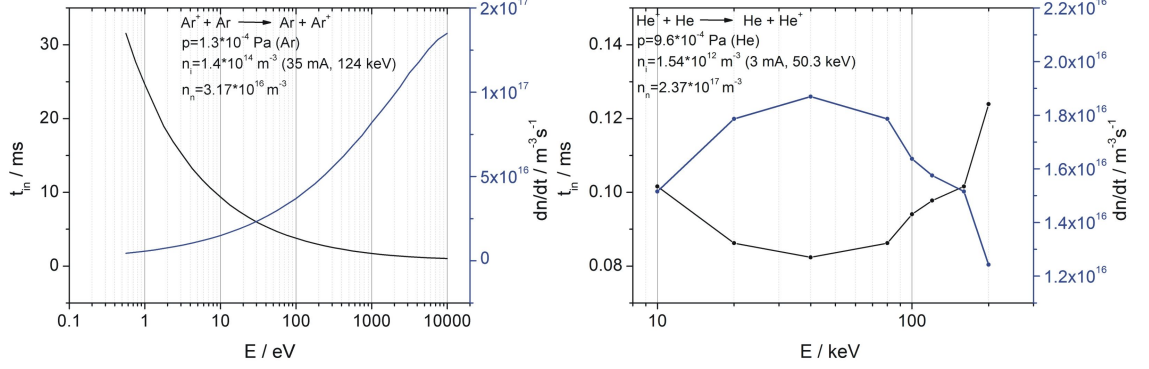


Figure 2.13: Charge exchange reaction times and rates for argon (left) and helium (right) ions. The cross section data is obtained from [Phe91] and [BS58].

Even though the reaction rate for the Ar^+ -beam with an energy of $W_b=124 \text{ keV}$ cannot be determined due to lacking data for higher beam energies than $W_b=10 \text{ keV}$, from the trend of the cross section it is still possible to assume a charge exchange reaction rate of more than $1.5 \cdot 10^{17} \text{ m}^{-3} \text{ s}^{-1}$.

Note that the reaction rates of electrons with residual gas ions produced in the lens volume can also be determined for different values of the anode potential as incident energy of ions with charge q .

Due to the high charge exchange reaction rates, which is the dominant process in this context, the influence on the transmission of the ion beam through the low energy beam transport section holds particular interest. Considering the charge exchange cross sections σ_{ce} , one can estimate the transmission Θ of the ion beam from

$$N_{loss} = N_{ion} \cdot \exp(-\sigma_{ce} n_n \Delta s) \quad (2.43)$$

to

$$\Theta = \frac{N_{loss}}{N_{ion}} = \exp(-\sigma_{ce} n_n \Delta s) \quad (2.44)$$

Of course, this is a very general approach for the entire low energy beam transport section given that the Gabor lens does not have to be served with further gas, as discussed in section 2.4.

Moreover, the **ionization** rates for the ion-atom-collisions are of great importance due to the production of secondary electrons in the lens volume, which might influence the

2. GABOR LENS – BASIC PRINCIPLES

focusing performance as well as the degree of space charge compensation of the ion beam in the low energy beam transport section.

Figure 2.14 shows the ionization cross sections, collision frequency and the reaction rates for the helium and the argon beam, again calculated for beam currents of 3 mA and 35 mA. In case of the Ar^+ -beam, the cross sections only up to $W_b=24$ keV were considered to calculate the presented values due to lacking data for higher beam energies. Still it can be assumed that the production rates are much higher for the Ar^+ -beam than for the He^+ -beam.

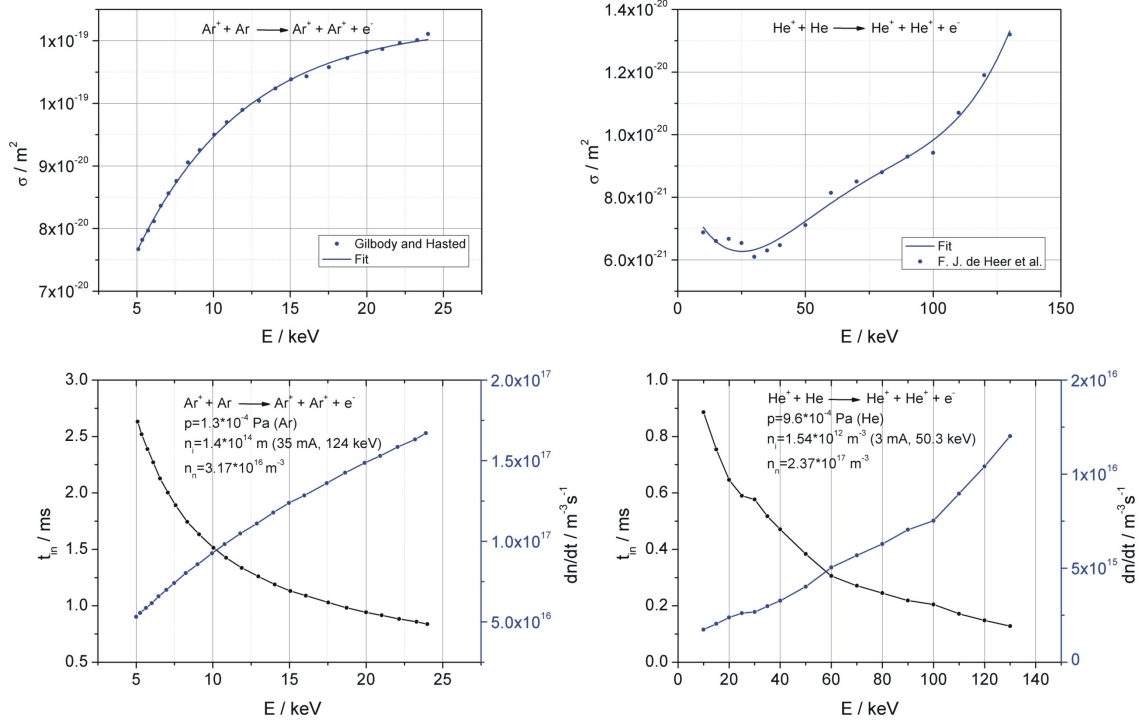


Figure 2.14: Cross sections for ionizing ion-atom collisions, the collision frequency, and reaction rates for Ar^+ on Ar [SHK59] (left) and He^+ on He [dHSM66] (right).

2.3.1.4 Ion-Electron Collisions

Possible ion-electron interaction processes are **radiative recombination** and **electron impact ionization**.

During the process of the **radiative recombination**, an ion recombines with an electron by emitting a photon. The radiative recombination cross section can be calculated

2.3 Thermal Equilibrium and Electron Temperature

by the semi-empirical formula of Kim and Pratt, given by [KP83]:

$$\sigma_{RR} = \frac{8\pi}{3\sqrt{3}} \cdot \alpha(\lambda_e)_r^2 \chi \ln \left(1 + \frac{\chi}{2 \cdot (n_0)_{eff}^2} \right) \quad (2.45)$$

with $\chi = \frac{2 \cdot Z_{eff}^2 \cdot R_y}{E}$, where R_y is the Rydberg energy, $Z_{eff} = \frac{1}{2}(Z + q)$ the effective nuclear charge with nuclear charge Z , α the fine structure constant, q the charge state, $(\lambda_e)_r^2$ the reduced compton wavelength that can be approximated by $(\lambda_e)_r^2 = \frac{137}{r_e} \cong 137 \cdot \frac{e^2}{m_0 c^2} \cong 137 \cdot 2.82 \cdot 10^{-15} \text{ m}$, E the electron energy and $(n_0)_{eff}$ the effective principal quantum number.

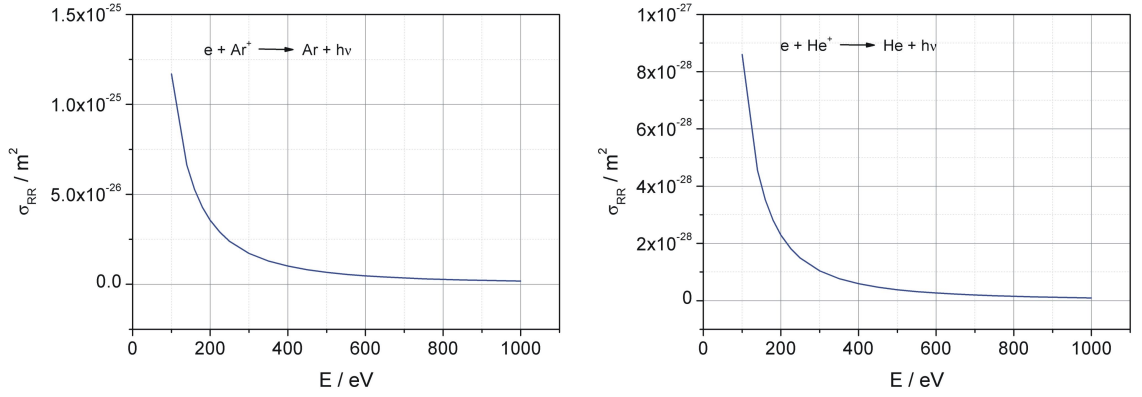


Figure 2.15: Calculated radiative recombination cross sections for Ar^+ (left) and He^+ (right) as a function of the incident electron energy.

Figure 2.15 shows the calculated radiative recombination cross sections for helium and argon ions. The cross sections are very small and the collisions times are estimated to be in the region of 10^4 - 10^6 s for the 12.6 keV/u He^+ -beam as well as the 3.1 keV/u Ar^+ -beam, assuming an incident electron energy of 100 eV and incident angle of 90° . Therefore, this reaction process is negligible for the considered cases.

The **electron-impact ionization** cross section for the reaction $e + \text{Ar}^+ \rightarrow \text{Ar}^{2+} + 2e$ can be calculated by a simple empirical formula [MSF⁺80]:

$$\sigma_{i,i+1} = \frac{1.4 \cdot 10^{-13}}{E_e E_i} \cdot \ln \left(1 + \frac{E_e}{E_i} \right) \quad (2.46)$$

where E_e is the electron energy and E_i the ionization potential of Ar.

Figure 2.16 shows the calculated ionization cross sections for argon and the experimentally determined for helium by [DHT61].

2. GABOR LENS – BASIC PRINCIPLES

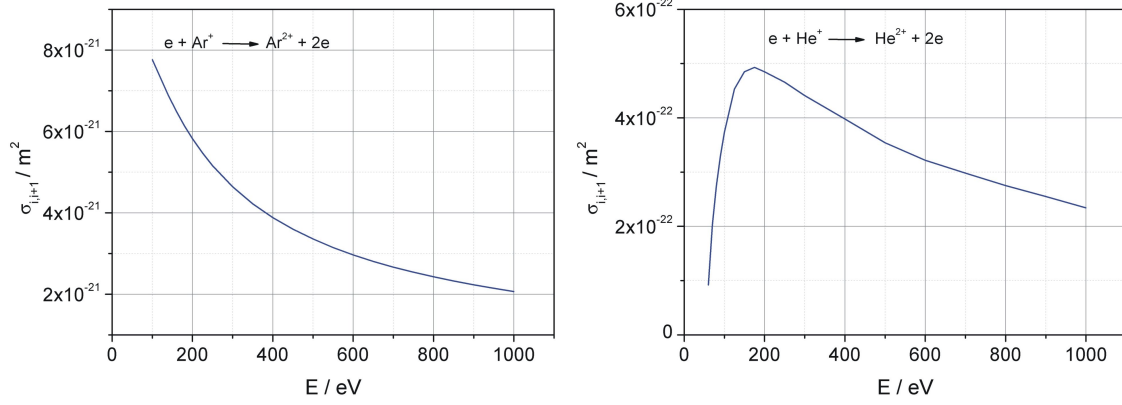


Figure 2.16: Calculated and measured [DHT61] ionization cross sections for Ar^+ (left) and He^+ (right) as a function of the incident electron energy.

For the 12.1 keV/u He^+ -beam, the collision time is clearly above 1.25 ms and for the 3.1 keV/u Ar^+ -beam the collision time is even in the range of s, assuming an incident electron energy of 100 eV and incident angle of 90° .

In summary, it can be stated that the ion-electron interactions play only a minor role in the contemporaneous collision processes.

2.3.2 Equilibrium States

The estimate of dominant particle interaction processes is necessary to evaluate an appropriate equilibrium model that describes the plasma state sufficiently. In the state of complete thermodynamic equilibrium (TE), the rate of every atomic process is exactly balanced by the rate of its inverse process. The most important processes that have to be exactly balanced are:

- | | | |
|------------------------------------|----------------------|------------------------------|
| 1. electron impact excitation | \rightleftharpoons | electron impact deexcitation |
| 2. electron impact ionization | \rightleftharpoons | three-body-recombination |
| 3. absorption and induced emission | \rightleftharpoons | spontaneous emission |
| 4. photo ionization | \rightleftharpoons | radiative recombination |

However, this is usually not attained in laboratory plasmas and thus the description of the plasma by a few thermodynamic variables is no longer possible [Hut05a].

The only practical way of investigating such non-equilibrium plasmas without involving

2.3 Thermal Equilibrium and Electron Temperature

extensive numerical and theoretical calculations is to approximate the plasma state by simplified models [LH68]. In the following, plasma models that describe population kinetics under certain thermodynamic conditions are explained.

2.3.2.1 Local Thermodynamic Equilibrium

In the plasma state of local thermodynamic equilibrium (LTE), all distribution functions with the exception of the radiation energy are determined by Boltzmann statistics and the Saha ionization distribution [CLCR]:

1. The Maxwell Boltzmann velocity distribution:

$$f_M(v) = n 4\pi \left[\frac{m}{2\pi kT} \right]^{\frac{3}{2}} \exp\left(-\frac{mv^2}{2kT}\right) v^2 \quad (2.47)$$

and in terms of energy

$$f_M(W) = n \frac{2}{\sqrt{\pi}} \frac{1}{(kT)^{\frac{3}{2}}} W^{\frac{1}{2}} \exp\left(-\frac{W}{kT}\right) \quad (2.48)$$

2. The Boltzmann formula

$$\frac{n_i}{n} = \frac{g_i}{U(T)} \exp\left(-\frac{E_i}{kT}\right) \quad (2.49)$$

where g_i is the statistical weight of the i^{th} level and $U(T) = \sum_i g_i \exp\left(-\frac{E_i}{kT}\right)$ the partition function.

3. The Saha equation:

$$\frac{n_z n_e}{N_{z-1}} = 2 \frac{U_z(T)}{U_{z-1}(T)} \frac{(2\pi m_0 kT_e)^{\frac{3}{2}}}{h^3} \exp\left(-\frac{\chi_{z-1} - \Delta\chi_{z-1}}{kT}\right) \quad (2.50)$$

In the LTE state, T is equal in all above-listed distribution functions, with the exception of the thermal radiation given by the Planck function also depending on T. Therefore, it is only possible to speak with caution of a plasma temperature, and in the following the temperature in the Boltzmann distributions will be denoted electron temperature T_e .

The LTE state is often found in laboratory plasmas of relatively high density and relatively low temperature when collisional processes are far more important than radiative

2. GABOR LENS – BASIC PRINCIPLES

processes and radiative processes do not affect population distributions.

A validity criterium for the applicability can be given by [Hut05c]

$$n_e \gg 10^{19} \left(\frac{T}{e}\right)^{\frac{1}{2}} \left(\frac{\Delta E}{e}\right)^3 m^{-3} \quad (2.51)$$

where T/e and $\Delta E/e$ are the temperature and energy level difference in eV, respectively. This approximation results from relating collisional transition rates mainly caused by electrons to radiative decay rates.

It is necessary to proof whether the populations of the atomic levels can be described by the Boltzmann distribution, in order that a simple equilibrium model can be applied to describe the plasma state sufficiently. In case of the nonneutral plasma, an electron density of $n_e > 1 \cdot 10^{23} \text{ m}^{-3}$ is required to assume a LTE state. Furthermore, important recombination processes are missing especially involving ion reactions.

2.3.2.2 The Steady-State Coronal Model

In order to explain some features of the spectrum of the solar corona, an atomic model that has been found useful in discussing low-density laboratory plasmas, has been proposed [McW65].

Compared to the detailed balance of the collisional processes with the corresponding inverse processes as described in the LTE model, the excited level populations in the coronal model are determined from a balance between collisional excitations from, and radiative decays to the ground level. Ground level populations of ions are determined from a balance between collisional ionization rates and radiative and dielectronic recombination rates.

Owing to the low electron densities and radiation field, collisional deexcitations and three-body-recombinations are insignificant [CLCR].

Referring to R. W. P. McWhirter in [McW65] the equations that describe the steady-state coronal model are:

1. The Maxwell Boltzmann velocity distribution (see equation 2.47)
2. The ionization and recombination balance

$$n_e n_{(z-1,1)} S_{(z-1,1)} = n_{(z,1)} n_e \alpha_{z,1} \quad (2.52)$$

2.3 Thermal Equilibrium and Electron Temperature

where $S_{(z-1,1)}$ is the collisional ionization coefficient and $\alpha_{z,1}$ the radiative recombination coefficient.

3. The collisional excitation from ground level and the spontaneous decay into ground level

$$n_e n_{(z,1)} K_{(i<k)} = n_{(z,k)} \sum_{i<k} A_{ki} \quad (2.53)$$

With the last equation the line intensity for an optically thin plasma can be assumed as:

$$I_{ki} = \frac{1}{4\pi} \int n_e n_{z,k} K_{(i<k)} \frac{A_{ki}}{\sum_{i<k} A_{ki}} ds \quad (2.54)$$

where the integration is over the depth of the plasma viewed by the detector and $K_{i<k}$ is the excitation coefficient.

In this context, J. Boffard [BLD04] provides a more clear definition of the emitted photon flux for a particular transition $i \rightarrow j$:

$$\Phi_{ij} = \frac{A_{ij}}{\sum_{l<i} A_{il}} n_e n_0 \int_0^\infty \sigma_{(0i)}(E) f(E) \left(\frac{2E}{m_e}\right)^{\frac{1}{2}} dE \quad (2.55)$$

where n_0 is the number density of ground state atoms, n_e is the electron density, $\sigma_{(0i)}(E)$ is the ground state excitation cross section into level i as a function of electron energy E , $f(E)$ is the electron energy distribution function usually considered to be Maxwellian, m_e is the electron mass and A is the spontaneous emission rate.

Since the definition of $\sigma_{(0i)}(E)$ in equation 2.55 is rather vague, it might be advantageous to use optical-emission cross sections that include higher cascading levels [BLD04]:

$$Q_{(ij)}(E) = \frac{A_{ij}}{\sum_{l<i} A_{il}} Q_{(i)}^{App}(E) \quad (2.56)$$

where $Q_{(ij)}(E)$ is the optical-emission cross section for the transition $i \rightarrow j$ and $Q_{(i)}^{App}(E)$ the apparent cross section. Both quantities are discussed in further detail in chapter 5. Subsequently, equation 2.55 can be simplified to

$$\Phi_{ij} = n_e n_0 \int_0^\infty Q_{(ij)}(E) f(E) \left(\frac{2E}{m_e}\right)^{\frac{1}{2}} dE \quad (2.57)$$

As previously discussed, the applicability of the coronal model is limited to a range of low electron densities when collisional processes are insignificant in depopulating the

2. GABOR LENS – BASIC PRINCIPLES

states in comparison to radiative processes [CLCR].

A validity criteria is given by

$$n_e < 5.6 \cdot 10^8 (z+1)^6 T_e^{1/2} \exp\left(\frac{1.162 \cdot 10^3 (z+1)^2}{T_e}\right) \text{ cm}^{-3} \quad (2.58)$$

where T_e is the electron temperature in K and $Z=(z+1)$ the nuclear charge.

This criterion is only valid for hydrogenlike ions with nuclear charge of $Z=1,2,4,8,16$.

Overall, it can be summarized that the knowledge of the electron density indicates the way in which atomic levels are populated and depopulated, and consequently the applicability of the discussed plasma models.

Figure 2.17 provides an overview of the applicability of the plasma models due to electron temperature and density.

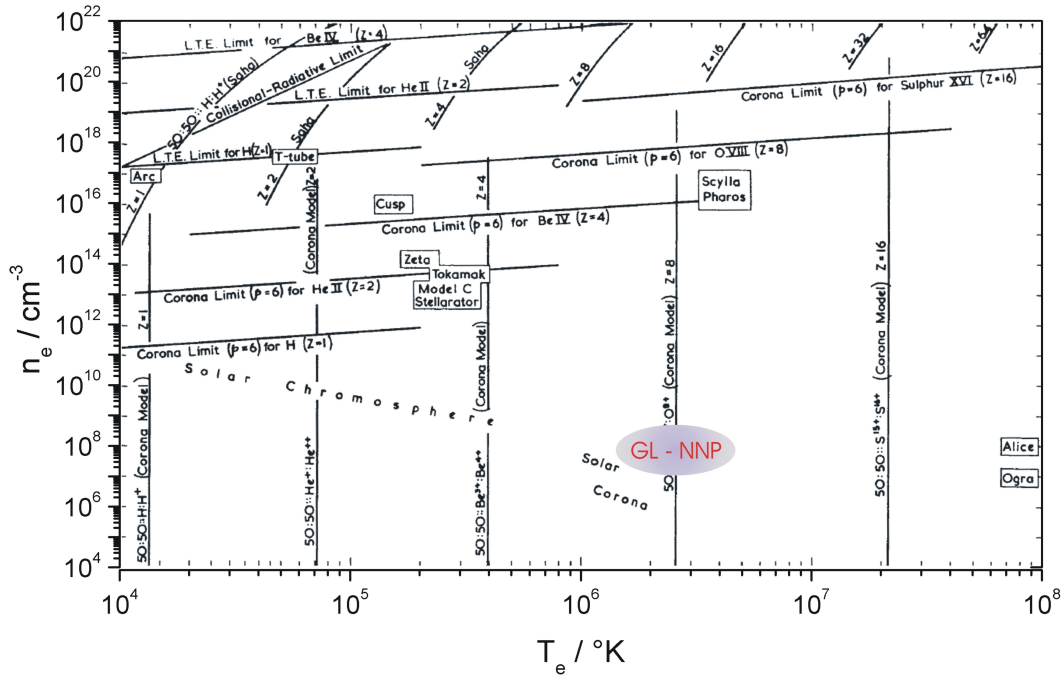


Figure 2.17: Ranges of applicability of the discussed plasma models (obtained from [McW65]).

2.3.2.3 Applicability of the Coronal Model to the Nonneutral Plasma

In the previous description, necessary criteria to justify the applicability of the coronal model to the confined nonneutral plasma were highlighted: the Maxwellian distribution

2.3 Thermal Equilibrium and Electron Temperature

of electrons, the low electron densities, and high temperatures, so only a few atomic processes such as ionization and recombination as well as collisional excitation and spontaneous decay are balanced.

Each requirement and its validity in the case of the nonneutral plasma is discussed in turn as follows.

The mean electron density for the confined nonneutral plasma column is known to be in the range of $\bar{n}_e = 1 \cdot 10^{14} \text{ m}^{-3}$. This could be validated by several experiments and is strongly supported with numerical simulations. The electron temperature is assumed to be in the region of $T_e \approx 100 \text{ eV}$ (see chapter 5).

Due to the thermalization process in terms of the long confinement times, as discussed in section 2.3.1.2, the electrons are assumed to have a Maxwellian distribution.

Furthermore, the electron density is low enough that the main atomic excitation processes are a result of electron-atom collisions while these levels depopulate by spontaneous decay.

However, the electron impact ionization and the recombination of ion electron pairs is not balanced. The ions are extracted from the lens volume due to the positively charged anode. The duration time of the ions is in the order of μs , while the recombination times are in the order of s , so this process is very unlikely.

In the low energy region, the ions also do not contribute to the excitation processes of atoms, although the probability increases with higher ion energies and higher gas pressures i.e. atom number densities. For a better estimate of the contribution of atomic excitation due to ion-atom collisions, it is necessary to consider the corresponding cross sections.

However, at least for the low energy region one can assume that the atomic levels are excited by solely electron collisions, while the contribution of ion-atom and ion-electron interactions to the emitted spectrum of the nonneutral plasma is negligible.

Therefore, for a level populated by only electron-atom interaction, equation 2.57 remains valid given that this very general assumption simply represents the production rate for transitions out of a specified atomic level.

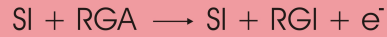
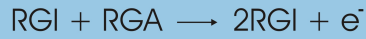
The temperature measurement method and its validity with respect to the population for different atomic levels will be further discussed in chapter 5.

2.4 Electron Production and Losses

2.4.1 Electron Production and Nonneutral Plasma Ignition

In the proposed lens design of D. Gabor [Gab47], electrons were produced by a filament. Owing to a special magnetic cusp configuration, the emitted electrons were able to enter the lens volume.

As discussed in detail in section 2.3.1 for the different types of space charge lenses built at the Institute for Applied Physics (IAP), the assumed main production process of electrons is the residual gas ionization by electrons, residual gas and beam ions:



The different lens designs which are essentially scaled versions of the original design at IAP by J. Pozimski [Poz90], are presented in figure 2.18.

The total length of the original design at IAP is $z=216$ mm and of the three segmented lens is $z=400$ mm while both lenses' aperture is 72 mm. The scaled lens in radial direction was designed in the scope of this thesis and will be discussed in further detail in chapter 4.

Through analogy with quasineutral plasmas, it is possible to describe the ignition of the nonneutral plasma by Paschen's law with the restriction of electrons only produced by residual gas ionization. Note that in the nonneutral case, the term ignition actually means the generation of the electron cloud.

The increase dN in the electron number along a flight path d is given by [Zoh13]

$$\frac{dN}{dd} = N_0\alpha \quad (2.59)$$

resulting in

$$N = N_0 \cdot \exp(\alpha d) \quad (2.60)$$

α is the first Townsend coefficient and defined by

$$\alpha = A \cdot \exp\left(-\frac{Bpd}{U}\right) \quad (2.61)$$

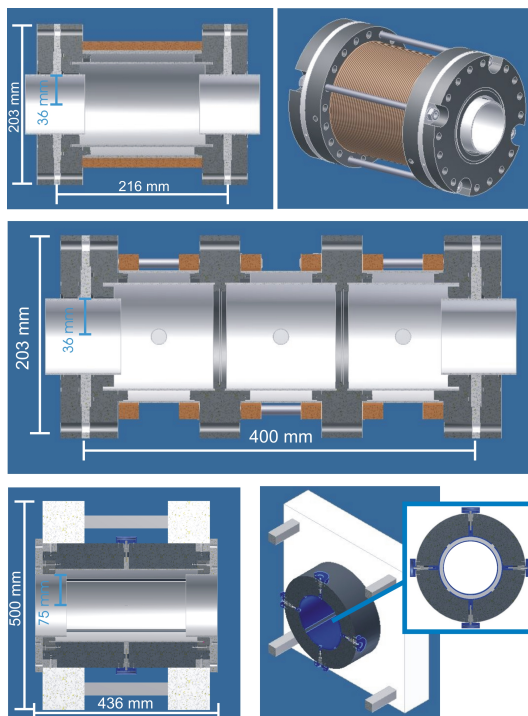


Figure 2.18: Different types of space charge lenses at IAP: original concept (top), scaled in z-direction (middle) and scaled in r-direction (bottom).

A and B are experimentally determined gas constants and for helium as residual gas $A=3 \frac{1}{\text{cm Torr}}$ and $B=34 \frac{\text{V}}{\text{cm Torr}}$ [Tam08]. The electron multiplication per mean free path is represented by α/p and U/pd describes the energy gain of an electron per mean free path.

In this estimate of the Paschen law for the nonneutral plasma, the second Townsend coefficient γ and consequently the production of secondary electrons on metal surfaces is neglected. The criterion for the ignition is

$$\frac{N}{N_0} = \exp(\alpha d) > 1 \quad (2.62)$$

which essentially means that more electrons are produced than lost.

This leads to the equation of the nonneutral plasma ignition:

$$U = \frac{Bpd}{\ln(Apd)} \quad (2.63)$$

The distance d is given by the crossed electric and magnetic fields. The calculated ignition curve of the nonneutral plasma for helium as background gas is illustrated in

2. GABOR LENS – BASIC PRINCIPLES

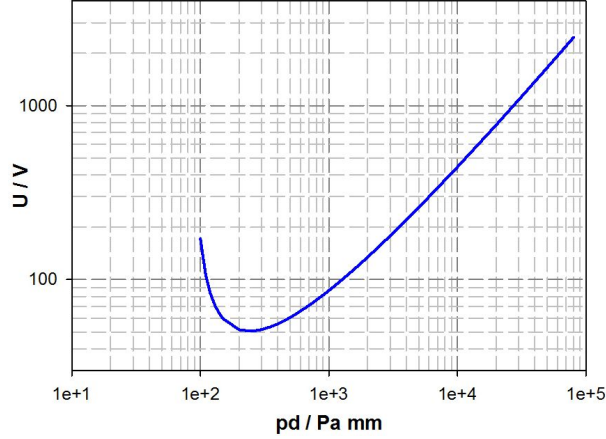


Figure 2.19: Theoretically predicted ignition curve for helium.

figure 2.19. To further investigate the electron production experimentally, the nonneutral plasma ignition curves were measured for different lens types. For one parameter setting of anode potential and magnetic field configured regarding the operation function, the number density of residual gas atoms was increased until the first light signal was detected by the CCD camera.

The ignition curve for the original lens design, the lens type scaled in longitudinal direction and the prototype lens scaled in radial direction is represented in figure 2.20.

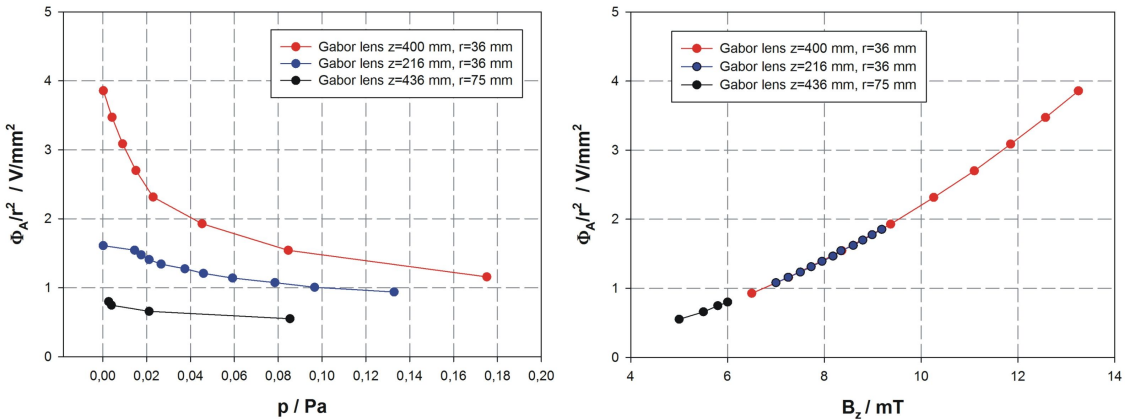


Figure 2.20: Measured ignition curves of the nonneutral plasma confined within different lens types for helium as residual gas as a function of the potential (left). The anode potential was configured according to the lens work function and normalized to the radius in order to compare all lens types (right).

For the shorter lens, a lower ratio of potential and magnetic field is required to ignite the nonneutral plasma than for the three-segmented one. By comparison, the prototype lens built for GSI already shows an ignition of the nonneutral plasma for an anode potential below 1 kV. This tendency is also predicted by the calculated ignition curve.

However, the experimentally observed short filling times (in the order of $> \text{ms}$) for the Gabor lens operated as a stand-alone system cannot be explained by the interaction of electrons and ions with the residual gas alone. Accordingly, it is necessary to consider the impact of particle losses (electrons and ions) on the production rate.

2.4.2 Electron Losses

The confinement of electrons within the Gabor lens is not perfect. Owing to particle collisions, field inhomogeneities and the finite electron temperature, electrons are lost in longitudinal and radial direction.

In longitudinal direction, the electron is confined by the potential well, while it has a degree of freedom along the magnetic field lines. If the kinetic energy of the electron is higher than the potential barrier, it is lost.

Furthermore, the whole electron ensemble has a finite temperature, and therefore electrons at the edge of the plasma cloud have enough thermal energy to escape from the potential well.

The electron **losses in longitudinal direction** are theoretically described by a loss current $I_{\text{loss},l}$ [Meu06]:

$$I_{\text{loss},l} = 2\pi \int_0^{R_A} j_e(r) \cdot r dr \quad (2.64)$$

with the simple approximation for j_e :

$$j_e(r) = en_e(r)v_{\text{th}} \quad (2.65)$$

where $v_{\text{th}} = \sqrt{\frac{kT_e}{m_e}}$ is the thermal velocity of electrons and $n_e(r)$ the flux of electrons represented by the Boltzmann formula:

$$n_e(r) = n_e(r, \Phi_r = 0) \exp\left(-\frac{e\Phi_r}{kT_e}\right) \quad (2.66)$$

2. GABOR LENS – BASIC PRINCIPLES

It is evident from equation 2.66 that the electron loss current exponentially increases with the plasma temperature.

The transport of electrons across the magnetic field lines by particle collisions is assumed to be the major **radial loss process**.

The radial loss current is divided into several current fractions:

$$I_{loss,r} = I_{loss,fill} + I_{loss,diff1} + I_{loss,diff2} + I_{loss,diff3} \quad (2.67)$$

where $I_{loss,fill}$ is the loss current by exceeding the maximum radial electron density limit. The other loss currents are a result of the collisional transport across the magnetic field. $I_{loss,diff1}$ is the diffusion current dependent on density gradients within the plasma. Electrons can escape from the plasma, especially at the edge, and the change in density causes a drift motion in radial direction. $I_{loss,diff2}$ is the loss current described by electron-electron collisions. The electron performs a ExB drift within the crossed fields. Collisions lead to an energy transfer and, of course, to a change in the electron's trajectory to larger radii. The diffusion velocity of this process is given by [Meu06]

$$v_{diff} = \eta_E \omega_e^- r \quad (2.68)$$

where ω_e^- is the angular velocity of the ExB rotation (see section 2.1.2) and η_E the efficiency of the energy exchange during one cycle.

The $I_{loss,diff2}$ may be calculated to

$$I_{loss,diff2} = \frac{Q \cdot v_{diff}}{R_p} \quad (2.69)$$

where $v_{diff} = \frac{E}{B}$ for $\kappa_r \ll 1$ and $v_{diff} = \frac{\Omega_e}{2} R_p$ for $\kappa_r = 1$.

Besides the electron-electron interactions, it is also necessary to take collisions of electrons with neutral atoms into account [DO78]. $I_{loss,diff3}$ represents the loss current caused by electron elastically scattering from ambient neutral atoms.

In this context, it is very important to mention that the electron losses across the magnetic field on the anode also represent a new production channel for low energy secondary electrons. Despite their contribution to the average electron density being assumed to be negligible, the losses close to the anode generate a shielding potential by secondary electrons and, thus influencing the dynamic of the confined electron ensemble [Sch09].

The loss channels and the dependency of particle losses on the external fields were experimentally investigated and will be discussed in the following.

2.4.3 Experimentally Investigated Particle Losses by X-Ray Spectroscopy

Particle losses were experimentally investigated by detection of the emitted x-ray spectrum with a gamma-spectrometer. As reviewed earlier, electron losses may occur in both directions, namely longitudinally as well as radially. However, only the radial losses on the anode or longitudinal losses on the ground electrode may produce the detected Bremsstrahlungs spectrum [Kla13]. The experimental set-up and an example of the measured x-ray emission is shown in figure 2.21.

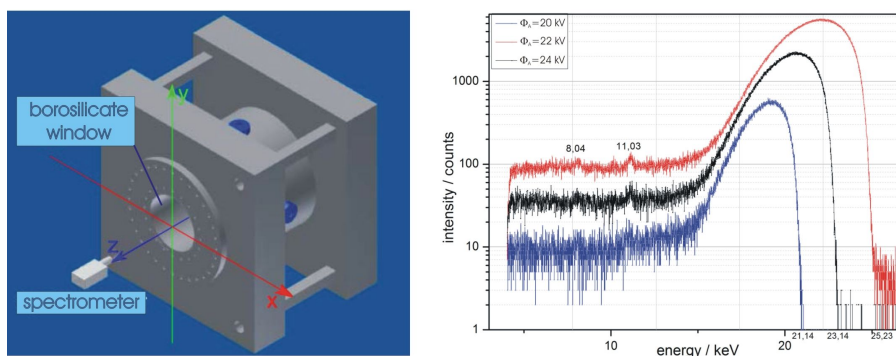


Figure 2.21: Experimental set-up (left) and an example of emitted Bremsstrahlung-spectra for different anode potentials (right) [Kla13].

The performed experiments affirm the anode as the main production region for Bremsstrahlung and also the numerically calculated electric space charge field in combination with the external fields show electron loss channels between anode and ground electrode [Meu06].

Within these loss regions, electrons are accelerated towards the anode with the maximum possible energy given by the applied anode voltage.

The produced x-ray spectrum is detectable starting from a value of the anode voltage of $\Phi_A = 15$ kV and shows a strong dependency on the applied voltage. Furthermore, the dependency of the Bremsstrahlungs spectrum on the confining magnetic field was also investigated.

Figure 2.22 shows the measured gamma count rate as a function of the anode potential Φ_A (for $B_z = 11.9$ mT, $p = 1.7 \cdot 10^{-5}$ Pa) and the magnetic field on axis B_z (for $\Phi_A = 22$ kV, $p = 5.1 \cdot 10^{-5}$ Pa). The detected intensity I_x was divided by the residual gas pressure p

2. GABOR LENS – BASIC PRINCIPLES

and the ion current I to minimize the influence of a variation in the plasma state during the measurement.

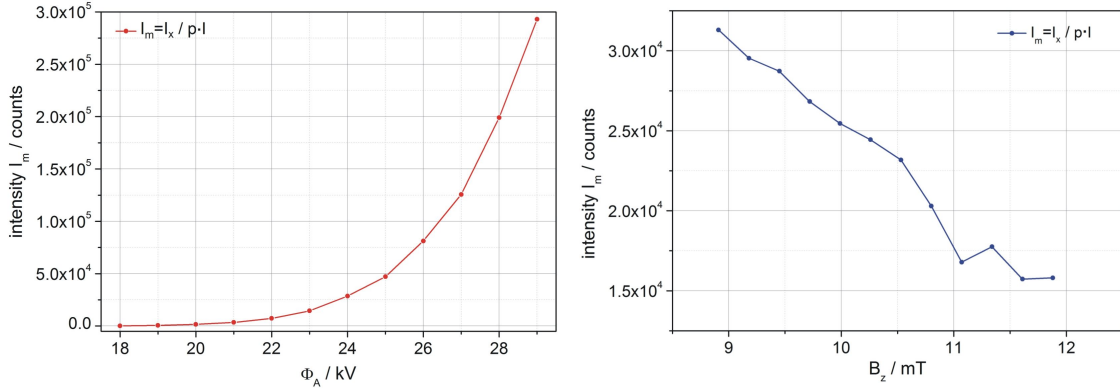


Figure 2.22: Measured x-ray emission as a function of the anode potential Φ_A (left) and the magnetic field B_z (right). The detected intensity I_x was divided by the residual gas pressure p and the ion current I to minimize the influence of a variation in the plasma state during the measurement (based on data from [Kla13]).

With increasing anode potential, the intensity of the x-ray emission increases exponentially, while the increase of the magnetic field shows a reduction of the detected count rate. These facts prompt the conclusion that the transport of electrons across the magnetic field scales with $\approx B_z^{-2}$.

Referring to [GR10b], the classical thermal diffusivity is given by

$$D_{\perp} \approx \nu r_c^2 \quad (2.70)$$

where $r_c = \frac{\sqrt{kT/m}}{eB/mc}$.

ν stands for the particle collision and may be replaced in case of the nonneutral plasma, either by the electron-electron ν_{ee} or the electron-neutral collision frequency ν_{en} .

However, it is necessary to further investigate the transport process in the case of electrons confined by the Gabor lens theoretically.

2.5 Numerical Simulation of the Nonneutral Plasma State

Two simulation codes - one treating the plasma as a macroscopic fluid, while the other applying a kinetic description - were used to investigate the equilibrium and stability properties of the nonneutral plasma [MDS13].

2.5.1 GABOR-M

For the simulation of the equilibrium plasma state, the code GABOR-M developed by [Meu06] and [Poz97] was used.

GABOR-M is a 2D hydrodynamics code, where the loss current is used as a free parameter. By recursive insertion of electrons and calculation of the force balance equation, the lens volume is filled step-by-step. The result is an equilibrium density distribution based on the given parameters such as anode potential Φ_A , magnetic field B_z and the longitudinal loss current $I_{\text{loss},l}$.

Figure 2.23 shows a flow chart of the simulation procedure.

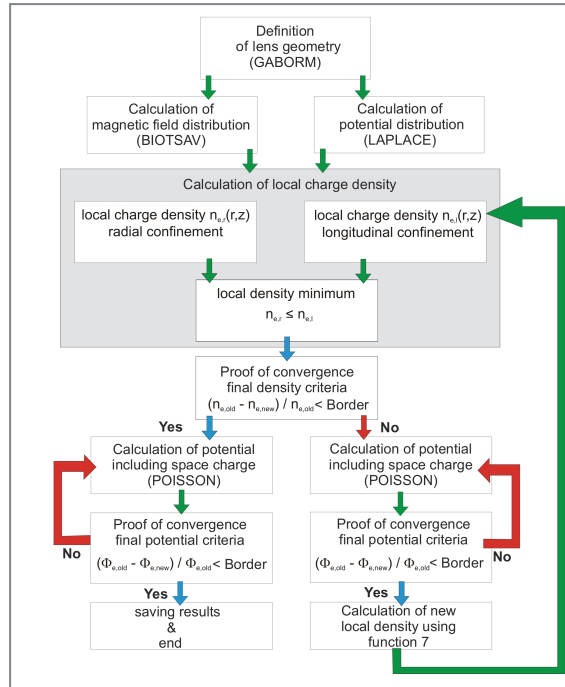


Figure 2.23: Schematic overview of the iterative calculation procedure of the code GABOR-M [Meu06].

2. GABOR LENS – BASIC PRINCIPLES

With regard to the comparability of the simulation and measurements, one needs to mention that the code GABOR-M neglects radial loss processes and the influence of collisions.

2.5.2 GAB_LENS

GAB_LENS is a 3D Particle-in-Cell code developed by [Dro] using a constant number of macroparticles.

As a starting condition, the electrons are homogeneously distributed over the entire lens volume. The particle motion inside the lens is followed by a symplectic middle-step algorithm and every lost particle is immediately re-generated inside the lens, with random position and random momentum direction. Consequently, the number of particles is conserved, yet overall the energy is not. The macrocanonical state is approaching the most probable equilibrium state [MDS13].

Figure 2.24 shows an example of the simulated evolution of a Diocotron mode using GAB_LENS.

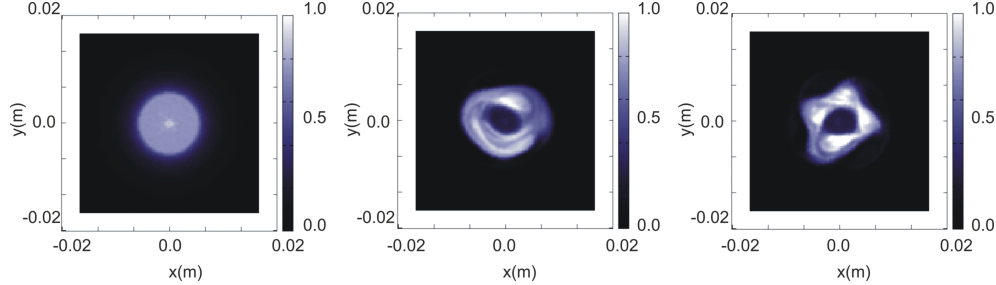


Figure 2.24: Comparison of transverse equilibrium density distributions for different conditions. Colour code: normalized density [MDS13].

The occurrence and description of nonneutral plasma instabilities will be further discussed in chapter 3.

2.6 Theory of Ion Beam Transport

Since the Gabor lens is used as a focusing device in the low energy beam transport section of an accelerator facility, the important concepts of the theory of ion beam transport are first introduced, before the focusing principle is described.

2.6.1 Emittance

A beam is an ensemble of charged particles that are accelerated and guided within electromagnetic fields. Rather than describing the beam motion by calculating single particle trajectories, the time evolution of particles in the phase space is described by the six-dimensional density distribution function [Bro04]

$$f = f(x, y, z, p_x, p_y, p_z, t) \quad (2.71)$$

If the particle interaction is negligible Liouville's theorem states that under the influence of conservative forces, the particle density in phase space remains constant. This may be written by [Lio38]:

$$\frac{df}{dt} = 0 \quad (2.72)$$

In terms of particle dynamics, the division of equation into the subspaces x - p_x , y - p_y und z - p_z is of great interest [Wie09]. Instead of transverse momentum components, the spatial deviations x' and y' are commonly used and defined by:

$$x' = \frac{dx}{dz} = \frac{v_x}{v_z} = \frac{p_x}{p_z} = \tan \theta, \quad y' = \frac{dy}{dz} = \frac{v_y}{v_z} = \frac{p_y}{p_z} = \tan \theta \quad (2.73)$$

Assuming the paraxial approximation ($p_x \ll p_z$), the spatial deviation is represented by the divergence angle $\tan \theta \approx \theta$.

In the transverse subspaces x - x' and y - y' , the particle ensemble occupies the area $A_x = \int \int dx dx' = \pi \epsilon_x$ and $A_y = \int \int dy dy' = \pi \epsilon_y$, respectively. The occupied area enclosed by an ellipse is called the **emittance**, and is defined by

$$\epsilon = \frac{A}{\pi} \quad (2.74)$$

Liouville's theorem allows the description (distribution and location) of the beam along the transport line only by knowledge of the emittance, without having to calculate the trajectory of the individual particle [Wie07a].

2. GABOR LENS – BASIC PRINCIPLES

In accelerator physics, different definitions for the emittance are used. In order to compare emittances at different beam energies, it is necessary to normalize the emittance with the common relativistic parameters β and γ [Bro04]. Moreover, it is often also reasonable to state a fractional emittance to reduce the influence of a beam halo or the measured background produced by neutral atoms.

A useful definition for the emittance that also considers the charge density distribution besides the occupied area within the sub phase space is the rms-emittance. The second moments of the distribution are used to define the rms-emittance for the two dimensional subspace [Sac71]:

$$\epsilon_{rms} = \sqrt{\langle x^2 \rangle \langle x'^2 \rangle - \langle xx' \rangle^2} \quad (2.75)$$

Even though the emittance is a conserved quantity with respect to Liouville's theorem, the rms-emittance might change due to a change in the distribution of the particle beam.

In the presented results of the beam transport measurements and simulations, the normalized rms-emittance is claimed, given by

$$\epsilon_{rms,n} = \beta_z \cdot \gamma_z \cdot \epsilon_{rms} \quad (2.76)$$

2.6.2 Kurtosis

The kurtosis measures the peakedness of a distribution and is defined as the ratio of the fourth moments and the squared second moments of the spatial beam profile [Lot11].

$$V_y = \frac{\langle y^4 \rangle}{\langle y^2 \rangle^2} \quad (2.77)$$

For this reason, the determination of the kurtosis allows a classification of the spatial beam distribution: A kurtosis of $V=2$ represents a homogeneous KV distribution, while $V=2.25$ corresponds to a Waterbag distribution. A Gaussian distribution is given for a value of $V=3$.

Figure 2.25 represents the different projections of the KV and the Gaussian distribution and their spatial profile. It can generally be stated that for a beam with a kurtosis of $V>2$, the density is larger for smaller radii, while for $V<2$ the density is larger for greater radii. In the latter case, the beam shows a hollow distribution.

It's important to note that the evolution of the kurtosis V leads to a change in the rms-emittance.

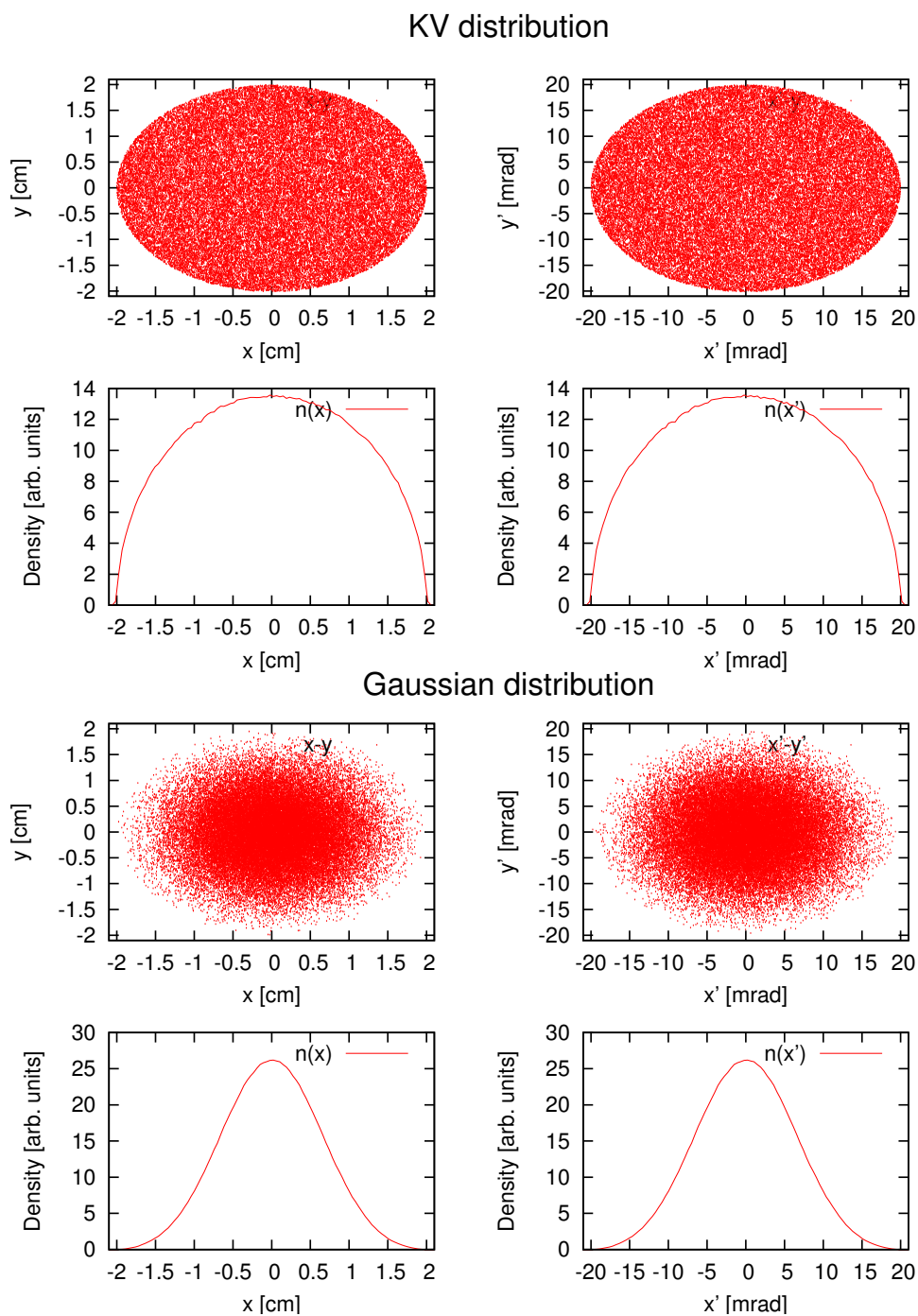


Figure 2.25: Projections of the KV and Gaussian distribution and their spatial profile.

2. GABOR LENS – BASIC PRINCIPLES

2.6.3 Brightness

Prior to discussing the influence of space charge forces on the ion beams, another quantity that also represents the quality of the beam shall be introduced. The **brightness** is defined as

$$B = \frac{I_b}{\epsilon_x \epsilon_y \pi^2} \quad (2.78)$$

The brightness describes the mean current density in the 4-dimensional phase space (x, x', y, y') for a given particle energy [Zha99] and is also related to the luminosity L of a particle accelerator:

$$L = \dot{N}_p \frac{N_T}{A} \quad (2.79)$$

where \dot{N}_p the number of projectiles per unit time and N_T/A the number of target particles per unit area [Hin08].

2.6.4 Perveance

Besides the emittance, the **perveance** reflects an important property for the description of the ion beam and its transport [Gab08]. While the emittance describes the size of the beam in phase space, the perveance defines the space charge of the ion beam.

Under the influence of its own space charge forces, namely the electric space charge, the former parallel beam of homogeneous density distribution expands in x and y . The perveance is defined by

$$K = \frac{1}{4\pi\epsilon_0} \sqrt{\frac{m}{2qe}} \frac{I_b}{U_a^{3/2}} \quad (2.80)$$

where I_b represents the ion beam current, q the charge state and U_a the accelerating voltage.

This essentially means that the value of the perveance represents the strength of acting space charge forces.

2.6 Theory of Ion Beam Transport

Project	Ion Species	$I_{b,max}$ [mA]	U_a [kV]	β	K
HOSTI	He ⁺	3	50.3	0.0052	0.0004
HOSTI	Ar ⁺	35	124	0.0026	0.0033
HOSTI	Ar ⁺	25	88	0.0022	0.004
HSI	U ⁴⁺	15	130.9	0.0022	0.0016
HSI upgrade	U ⁴⁺	30	130.9	0.0022	0.0032
FRANZ (current status)	He ⁺	2	14	0.0027	0.0016
FRANZ (planned)	p	200	120	0.016	0.0031

Table 2.1: Comparison of the beam parameters for different projects.

Table 5.1 shows the most important beam parameters for different projects, particularly the calculated perveance for the beam transport measurements discussed in chapter 6 (see also figure 2.26).

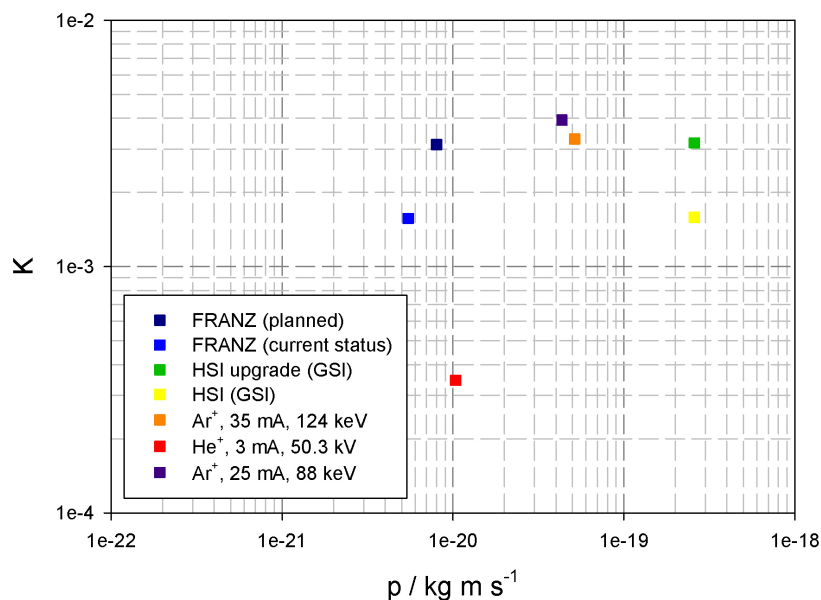


Figure 2.26: Illustration of the perveance as a function of the momentum for different projects.

2. GABOR LENS – BASIC PRINCIPLES

2.6.5 Envelope Equation

The motion of an ion beam is predominantly influenced by the emittance, the perveance, and the ion optics. The perveance causes an expansion of the beam in transverse direction and a focusing device is necessary to match the beam into a given aperture.

A non-relativistic beam with a uniform density (KV distribution) transported by a uniform focusing channel is described by the paraxial equations for the envelopes a and b [And95]:

$$a'' + k_x a - \frac{2K}{(a+b)} - \frac{\epsilon_x^2}{a^3} = 0 \quad (2.81)$$

$$b'' + k_y b - \frac{2K}{(a+b)} - \frac{\epsilon_x^2}{b^3} = 0 \quad (2.82)$$

where k_x, k_y represents the external focusing force and ϵ_x, ϵ_y the emittance.

Equations 2.81 and 2.82 were first derived by Kapchinskiy and Vladimirskiy [KV59] and are known as the KV envelope equations. Lapostolle and Sacherer discovered that these equations are valid for all density distributions with elliptical symmetry and not only for uniform density beams [Wan08]. In such a case, the envelope functions are twice the rms envelope radii $a=2 \cdot \sqrt{\langle x^2 \rangle}=2X$ and $b=2 \cdot \sqrt{\langle y^2 \rangle}=2Y$, respectively, while the emittances are equal to four times the rms-emittance $\epsilon_x = 4 \cdot \epsilon_{x,rms}$ and $\epsilon_y = 4 \cdot \epsilon_{y,rms}$, respectively, so one can derive the rms envelope equation [Lee04].

The ratio D of emittance ϵ_x, ϵ_y and the perveance K defines whether the beam dynamics is dominated by the space charge forces or by the emittance of the beam [Gro00].

For a round beam ($a=b$), one can determine D from equation 2.81:

$$D = \frac{K \cdot a^2}{\epsilon_x^2} = \frac{K \cdot X^2}{4\epsilon_{x,rms}^2} \quad (2.83)$$

If $D \gg 1$, the beam is space charge dominated, whereas it is emittance dominated if $D \ll 1$.

The results of the beam transport experiments for an emittance dominated 50.3 keV, He⁺-beam with $D=0.16$ and for a space charge dominated 124 keV, Ar⁺-beam with $D=7.34$ will be discussed in chapter 6.

2.7 Focusing Principle of the Gabor Lens

If the electron density is homogeneously distributed in an cylindrical region of length l and radius r of the lens, one can assume a radial focusing force $F_r=qE_r$ on a positively

2.7 Focusing Principle of the Gabor Lens

charged ion beam passing through the electron column (see figure 2.27).

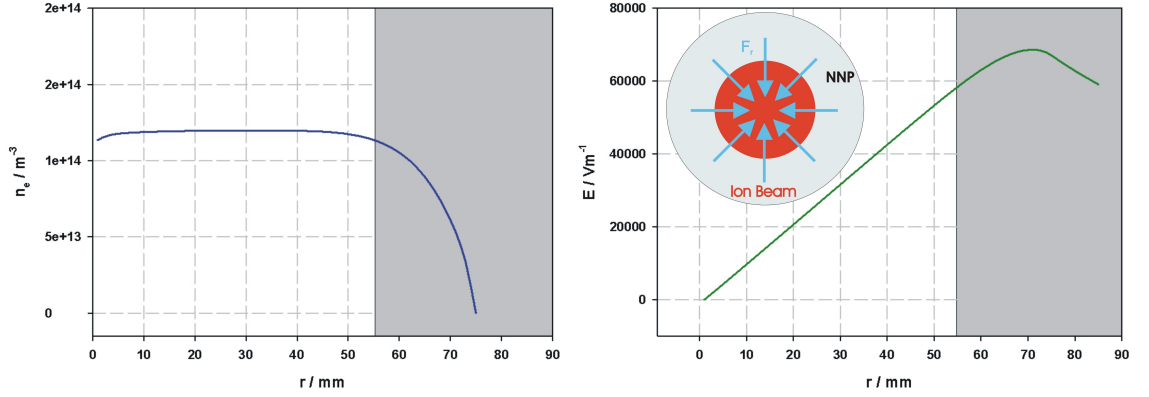


Figure 2.27: Example of the electric space charge field in the case of an homogeneously distributed electron cloud and the resulting forces on the ion beam. The nonlinearity in the electric field is a result of the Debye drop off at the edge of the plasma cloud.

The electric field of the confined electron cloud is calculated by applying Gauss's theorem and results in

$$E_r = -\frac{n_e e}{2\epsilon_0} r \quad (2.84)$$

The trajectory of an ion can be described by the following equation of motion [Rei89]:

$$m_i \ddot{r} = q E_r \quad (2.85)$$

To eliminate the time dependency at constant beam velocity $v_{z,i} = \frac{dz}{dt}$, it is possible to use

$$\ddot{r} = r'' \dot{z}^2 + r' \ddot{z} \quad (2.86)$$

while $r' \ddot{z}$ is neglected since the ions are not accelerated.

Inserting equation 2.84 and equation 2.86 into equation 2.85 results in the equation of motion for an ion that passes the electric space charge field of the electron column [Rei89]

$$r'' + q \frac{n_e e}{2v_{z,i}^2 m_i \epsilon_0} r = 0 \quad (2.87)$$

$$r'' + k_G^2 r = 0 \quad (2.88)$$

2. GABOR LENS – BASIC PRINCIPLES

According to equation 2.87, the Gabor lens focusing constant can be expressed by

$$k_G^2 = \frac{qen_e}{2m_i v_i^2 \epsilon_0} \quad (2.89)$$

By using the thin-lens-approximation ($kl \ll \pi/2$) one can define the focal length $f^{-1} = k_G^2 l$ [Wie07b] of the Gabor lens as:

$$\frac{1}{f_G} = \frac{r'}{r} = \frac{qen_e l}{2m_i v_i^2 \epsilon_0} = \frac{en_e l}{4\epsilon_0 U_a} \quad (2.90)$$

In more practical units, the focal length f_G is given by

$$\frac{1}{f_G} = \frac{Zl}{AW_B} \frac{en_e}{4\epsilon_0} = \frac{Zl}{AW_B} \cdot n_e \cdot 4,52 \cdot 10^{-9} \text{ Vm} \quad (2.91)$$

where W_B is the ion energy in eV/u, Z is the ion charge, A the atomic weight, l the length of the space charge lens, and n_e the confined electron density.

2.8 Numerical Simulation of the Beam Transport

In the presented numerical results GABOR-M was used to calculate the equilibrium plasma state for a given parameter setting of the lens, while the code LINTRA was used to track a particle distribution through the transport section, including the lens. LINTRA is a multi particle transport code that represents the beam by typically 10,000 to 30,000 particles.

One advantage of LINTRA over other codes is the implementation of a compensation degree and therefore the possible modification of the space charge forces [Poz97], [Meu01]. The radial density distribution of electrons within the beam potential is initially determined and therefore the beam potential. In a next step, the space charge forces are calculated by solving the Poisson's equation. From the space charge forces, the new particle distribution follows under consideration of the external fields.

However, the influence of produced secondary particles is neglected in the code.

3

Nonneutral Plasma Instabilities

3.1	Experimental Observation of Nonneutral Plasma Instabilities	49
3.2	Diocotron Instability	51

3.1 Experimental Observation of Nonneutral Plasma Instabilities

In a nonneutral plasma, a wide range of plasma waves and related instabilities are observed. In case of an unstable electron cloud, the resulting space charge field is strongly nonlinear and causes an emittance growth of an ion beam when the lens is used as a focusing device. For this reason, the investigation of instabilities depending on the electron confinement and the related plasma parameters holds significant interest in terms of providing a stable focusing performance of the lens.

In this context, the plasma state as a function of the confining fields was investigated by analyzing the intensity profile of the plasma emission and the extracted residual gas current. Given that the light density distribution is correlated to the electron density distribution (see chapter 5), an asymmetry of the plasma cloud indicates an unstable plasma state, and even more so if a temporal variation of the extracted residual gas ions is also observed.

Figure 3.1 demonstrates how the plasma state evolves in relation to the operation function of the lens.

3. NONNEUTRAL PLASMA INSTABILITIES

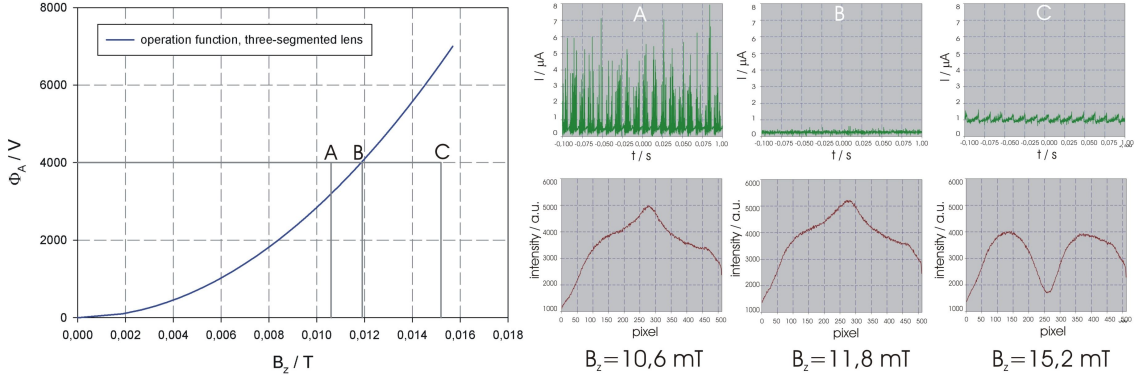


Figure 3.1: Operation function of the three-segmented lens (left). Measured residual gas ion current and light density profile as a function of the magnetic field (right). The anode potential and the residual gas pressure were kept constant at $\Phi_A=4\text{ kV}$ and $p=6\cdot 10^{-2}\text{ Pa}$ (He) [Sch09].

While the anode potential and the residual gas pressure were kept constant at $\Phi_A=4\text{ kV}$ and $p=6\cdot 10^{-2}\text{ Pa}$ (He), the magnetic field was varied. In case A, the light density shows an almost homogeneous distribution with the exception of the peak at the center. By calculating the intensity profile of the almost circular plasma emission, particularly the central part is overestimated and even more due to the spatial integration by the optical exposure. However, the ion current shows a strong fluctuation over time.

In case C, a hollow profile of the light density distribution and a variation of the detected residual gas ion current with constant frequency is observed. At the operation point (case B), the plasma state is temporally constant and the light density distribution shows the expected profile.

In other words, two different kinds of instabilities could be experimentally identified. While the instability represented by case A has not yet been classified, it is assumingly connected to an inhomogeneity of the electron density distribution in longitudinal direction.

The occurring hollow profile in case C is associated with the theoretically well-described diocotron instability.

3.2 Diocotron Instability

The diocotron instability was theoretically first described by MacFarlane [MH50]. It corresponds to a shear in the flow velocity of the cylindrically confined nonneutral plasma column and is observed at strong magnetic fields. In case of quasineutral plasmas, this process is described as Kelvin-Helmholtz instability.

At strong magnetic confining fields, the gyration radius of the electrons becomes smaller and the column is more compressed. Accordingly, the confinement condition given by the anode potential is locally exceeded and thus electrons can escape from this region. The occurring hollow profile provides the basis for the evolution of diocotron surface modes [Dro13].

Referring to [KTY01] and [Kna66] in case of a perturbation on one of the originated sheet surfaces, charges are produced, yielding an $E \times B$ flow in the plasma due to the perturbed electric field. As a result of the described mechanisms, the opposite surface is also perturbed and the motion of this surface causes a reciprocal perturbation. If the coupling of the waves now yields a positive feedback, the diocotron instability occurs. Figure 3.2 illustrates the physical mechanisms that prompt the diocotron surface mode.

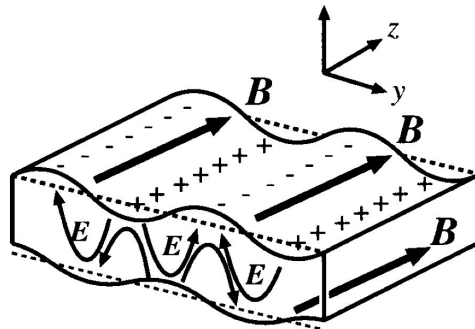


Figure 3.2: Illustration of the physical mechanisms that lead to the evolution of diocotron surface modes (obtained from [KTY01]).

Furthermore, the shape of the electron density profile has a strong influence on the stability of the diocotron mode.

As presented in chapter 2, in the idealized case the motion of the electron column within a magnetic field under the influence of space charge forces is described as a rigid rotation if the electron density is uniform along the radius. However, if the electron density is

3. NONNEUTRAL PLASMA INSTABILITIES

nonuniform, the description of the electron motion becomes more complicated since there is a shear in the angular velocity (see figure 3.3).

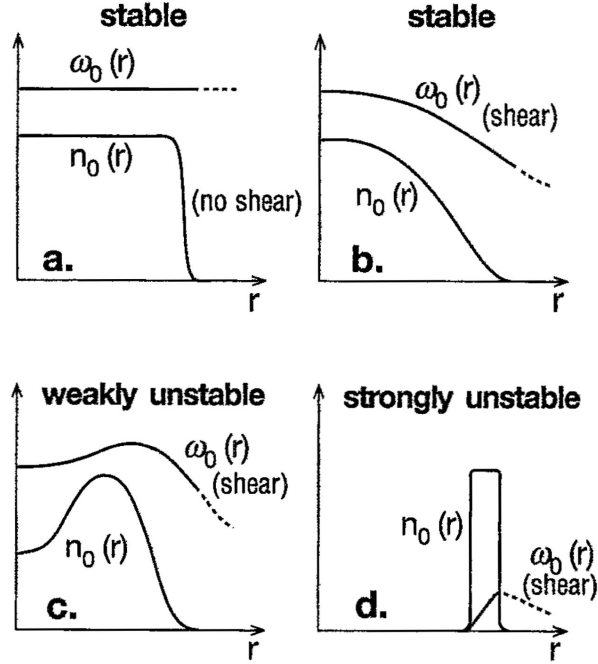


Figure 3.3: Density profiles and corresponding angular velocity profiles for different scenarios (obtained from [Gou95]).

Depending on the thickness and position of the electron layer within the confining trap, a mathematical description of the occurring diocotron wave modes was derived by Ronald C. Davidson [Dav01].

The following discussion is narrowed down to the important results of the theoretical studies.

Figure 3.4 illustrates the density profile of the electron layer (hollow distribution) within the conduction walls of the cylindrical trap.

The density profile has the properties of

$$n_e^0(r) = \begin{cases} 0, & r < r_b^- \\ n_e = \text{const.}, & r_b^- \leq r < r_b^+ \\ 0, & r_b^+ \leq r < b \end{cases} \quad (3.1)$$

In order to investigate the linear stability properties of the electron layer corresponding to the equilibrium density profile $n_e^0(r)$, it is necessary to solve the eigenvalue equation

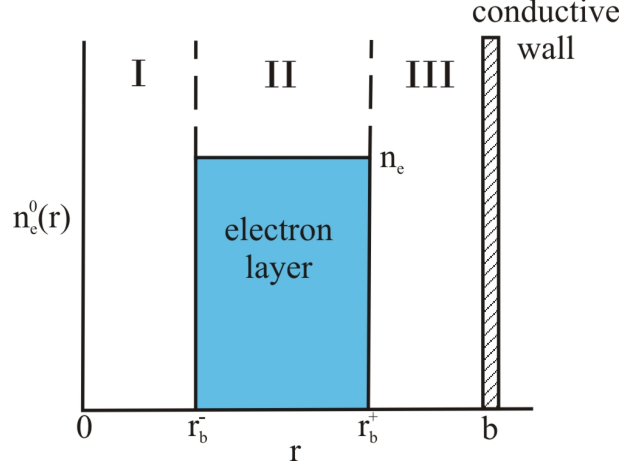


Figure 3.4: Electron density profile assumed for the calculation of the stability-instability diagram.

derived from the Poisson's equation

$$\left(\frac{1}{r} \frac{\partial}{\partial r} r \frac{1}{r^2} \frac{\partial^2}{\partial \theta^2} \right) \phi(r, \theta, t) = \frac{en_e(r, \theta, t)}{\epsilon_0}$$

$$\frac{1}{r} \frac{\partial}{\partial r} r \frac{\partial}{\partial r} \delta\Phi^l(r) - \frac{l^2}{r^2} \delta\Phi^l(r) = -\frac{l}{\Omega_e r} \frac{\delta\Phi^l(r)}{[\omega - l\omega_{re}^-]} \frac{\partial}{\partial r} \omega_{pe}^2(r) \quad (3.2)$$

where ω is the the complex eigenfrequency, $\omega_{pe}(r)$ the plasma frequency, $\omega_{re}^-(r) = \omega_D \left[1 - \left(\frac{r_b^-}{r} \right)^2 \right]$ for $r_b^- < r < r_b^+$ the angular velocity in the electron layer and $\omega_D = \frac{\omega_{pe}^2(r)}{2\Omega_e}$ the diocotron frequency.

This equation is simplified for $r \neq r_b^-$ and $r \neq r_b^+$ to

$$\frac{1}{r} \frac{\partial}{\partial r} r \frac{\partial}{\partial r} \delta\Phi^l(r) - \frac{l^2}{r^2} \delta\Phi^l(r) = 0 \quad (3.3)$$

By solving equation 3.3 separately in three different regions (I, II, III) according to figure 3.4, after arithmetic operations the following quadratic equation is obtained:

$$\left(\frac{\omega}{\omega_D} \right)^2 - b_l \left(\frac{\omega}{\omega_D} \right) + c_l = 0 \quad (3.4)$$

whereas $b_l = -l \left[1 - \left(\frac{r_b^-}{r_b^+} \right)^2 \right] + 2 - \left[\left(\frac{r_b^+}{b} \right)^{2l} + \left(\frac{r_b^-}{b} \right)^{2l} \right]$ and $c_l = \left(\frac{r_b^-}{r_b^+} \right)^{2l} \left[1 - \left(\frac{r_b^+}{b} \right)^{2l} \right]^2$ result from several algebraic manipulations [Gla12].

The solution of the dispersion relation (equation 3.4) is given by

$$\omega = \frac{1}{2} \omega_D \left[b_l \pm (b_l^2 - 4c_l)^{1/2} \right] \quad (3.5)$$

3. NONNEUTRAL PLASMA INSTABILITIES

From this equation, important properties of the diocotron modes l depending on the geometrical factors $\frac{r_b^+}{b}$ and $\frac{r_b^-}{b}$ can be derived [Gla12]. Figure 3.5 illustrates the stability limits of the instability and its manifestation. Note that only the region above the 45° line has a solution, given that $r_b^+ > r_b^-$.

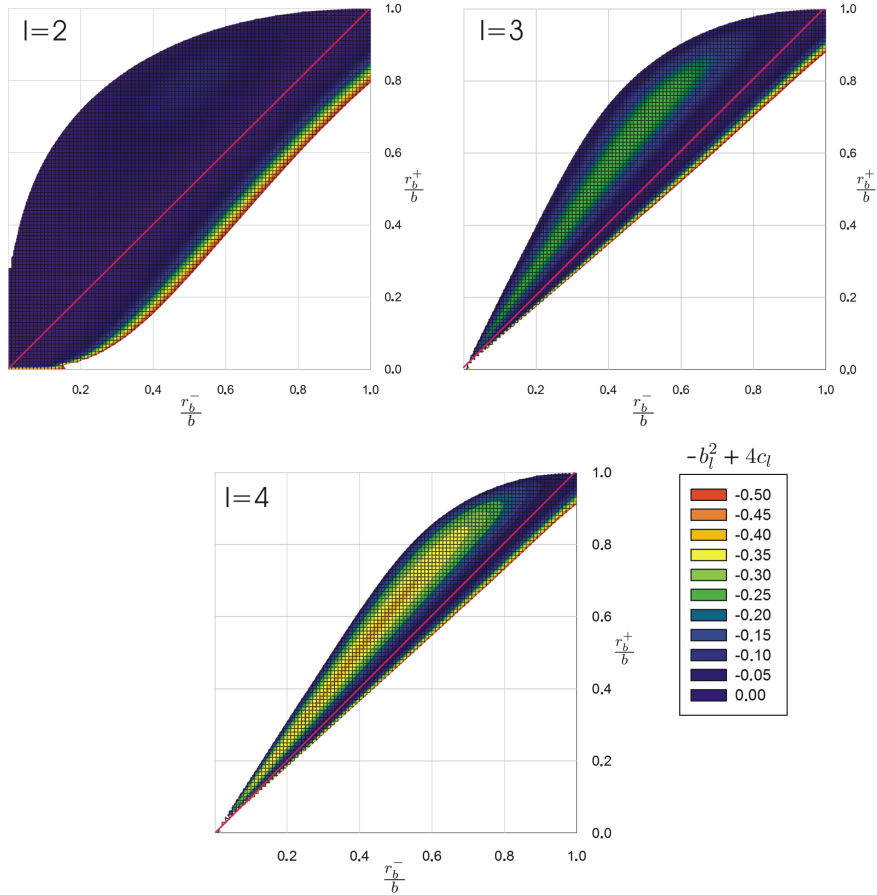


Figure 3.5: Stability-instability diagram showing the stability limits of the diocotron modes l [Gla12].

The stability-instability diagram may subsequently be used to characterize the instability observed in the experiment by analyzing the layer thickness and its distance from the center and the conductive wall, respectively (see section 5.4).

Besides the comprehensible reason for the development of the hollow profile due to a strong magnetic field, the residual gas pressure also influences the dynamics of the system. Figure 3.6 shows the occurrence of a hollow profile corresponding to an in-

creased residual gas pressure but for similar Gabor lens settings.

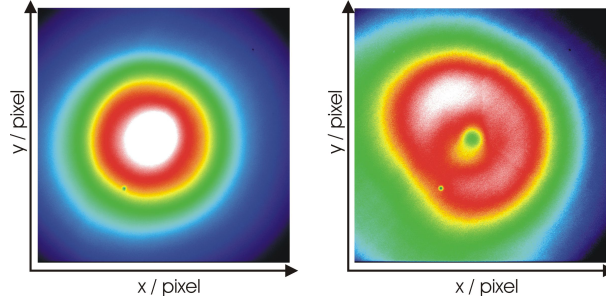


Figure 3.6: Picture of a light density distribution for different pressures of helium and similar field strengths, $\Phi_A=6.5$ kV, $B_z=12.1$ mT, $p=7.8\cdot 10^{-3}$ Pa (left) and $\Phi_A=6.5$ kV, $B_z=12.9$ mT, $p=4.8\cdot 10^{-2}$ Pa (right) [Sch11].

A possible explanation is the change in the confinement condition as a result of an increased neutralizing ion background f that might correspond to the previously discussed reason for the occurrence of a hollow profile.

However, another interesting aspect of the diocotron instability is the balancing process of transverse and longitudinal mean kinetic energies in time. Figure 3.7 shows the transverse and longitudinal electron energies of an electron cloud confined by a Gabor lens (original design) calculated for $B_z=13.2$ mT and $\Phi_A=1850$ V as a function of time.

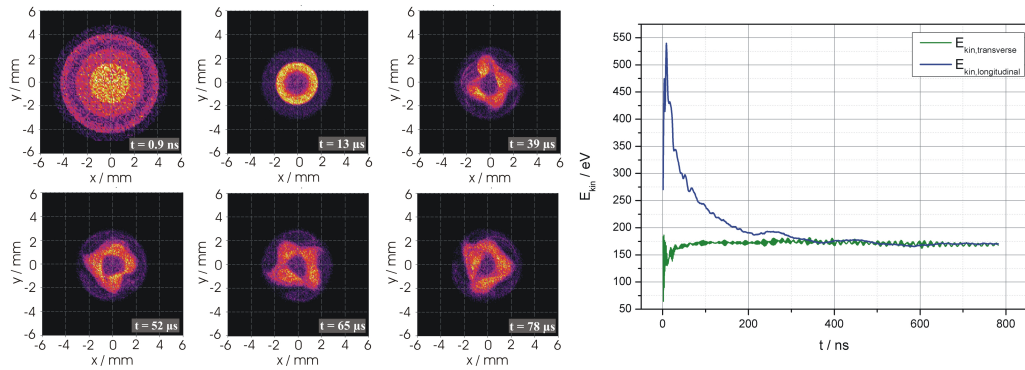


Figure 3.7: Evolution of the diocotron mode and the related integrated density profile (left) as well as the mean kinetic energy in both planes (right) as a function of time.

While the electron density is homogeneously distributed at the very beginning of the simulation, the kinetic energies in both planes show the largest deviation. After a certain time, the energies become more balanced, although the integrated density profile

3. NONNEUTRAL PLASMA INSTABILITIES

shows a vortex of the electron layer. Therefore, another possible explanation for the appearance of the hollow profile in case of the high residual gas pressure could be as follows:

The electrons within the lens volume oscillate longitudinally through the positive potential well created by the anode. In case of an interaction process with a residual gas atom, they lose part of their kinetic energy. With increasing residual gas pressures, this effect may also lead to an unbalanced distribution of kinetic energy in both planes causing the formation of the described instability.

In this context, the importances of the energy balance within the system becomes evident and the physical mechanisms that lead to an equilibrium state have to be investigated in further detail. In particular, the experimental determination of the electron density and temperature represents a helpful tool in this context.

4

Design of the Prototype Gabor Lens for GSI

4.1 Gabor Lens Requirements and Design of the Electrode System	57
4.1.1 The R_A/R_p Ratio	58
4.1.2 The R_A/L_A Ratio	58
4.2 The Magnetic System	60
4.2.1 Beam Transport Simulations	62
4.2.2 Reasons for an Emittance Growth	63
4.3 Technical Specifications	66

4.1 Gabor Lens Requirements and Design of the Electrode System

The imposed requirements for the design of the Gabor lens involved transporting an $^{238}\text{U}^{4+}$ beam with an energy of 2.2 keV/u at a beam radius of up to 50 mm. In particular, the necessity for a linear electric space charge field E_r within the beam region to avoid emittance growth reflected a major challenge in designing the electrode system.

4. DESIGN OF THE PROTOTYPE GABOR LENS FOR GSI

4.1.1 The R_A/R_p Ratio

As discussed earlier, the maximum expansion of the confined plasma cloud R_p is given by the radius of the ground electrode R_G . Owing to the field configuration in the region between anode and ground electrode, the confinement of electrons is not allowed. Given that the electrons still have one degree of freedom in longitudinal direction along the magnetic field lines, this region represents a loss channel. Therefore, the ratio of anode-to-ground radius R_A/R_p limits the maximum confinement efficiency κ_1 in longitudinal direction and consequently the focusing strength of the Gabor lens.

Figure 4.1 shows the radial space charge potential of the confined electron cloud as a function of the R_A/R_p ratio. The increase of the ground radius connected to an increased maximum expansion of the plasma cloud leads to a higher filling degree of the lens volume, assuming a constant maximum electron density of $n_e = 3,45 \cdot 10^{15} \text{m}^{-3}$. The red line indicates a complete depression of the anode potential by the electron cloud, which is represented by a confinement efficiency of $\kappa_1=1$.

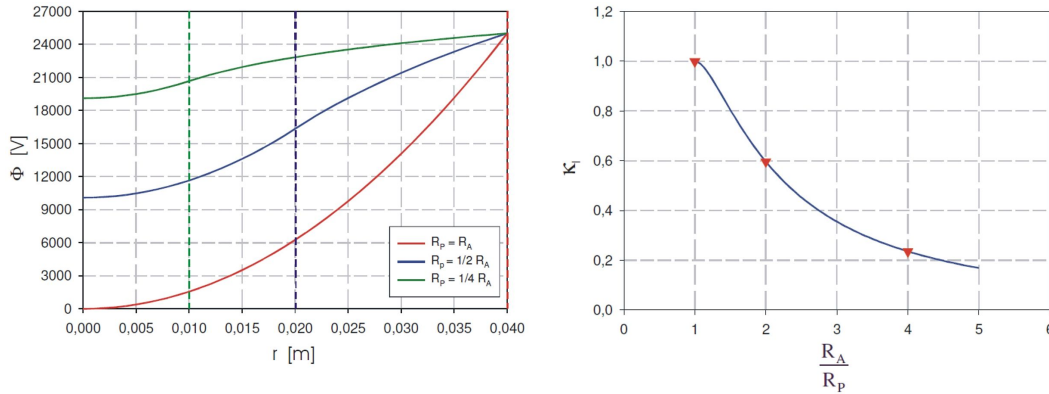


Figure 4.1: Radial space charge potential of the confined plasma cloud as a function of the R_A/R_p ratio (left) and the influence of the R_A/R_p ratio on the longitudinal confinement efficiency (right), (obtained from [Meu06]).

To optimize the confinement while preventing a high voltage sparkover, a ratio of $R_A/R_p=1.13$ was chosen for the prototype lens.

4.1.2 The R_A/L_A Ratio

According to the requirements of transporting ion beams with radii up to 50 mm, it was necessary to double the size of the prototype lens' aperture compared to former designs.

4.1 Gabor Lens Requirements and Design of the Electrode System

Therefore, the anode length L_A also had to be chosen depending on the anode radius to prevent a significant decrease in the axis potential of the lens. Figure 4.2 shows the on axis potential as a function of the R_A/L_A ratio compared to the confinement efficiency κ_1 in longitudinal direction.

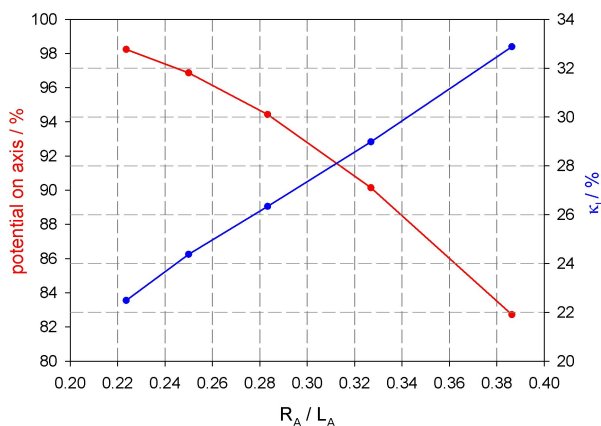


Figure 4.2: Simulated potential decrease on axis and confinement efficiency κ_1 as a function of the R_A/L_A ratio for $B_z=8.3$ mT and $\Phi_A=10$ kV.

It can be noted that the potential increases with higher R_A/L_A values, while the confinement efficiency decreases.

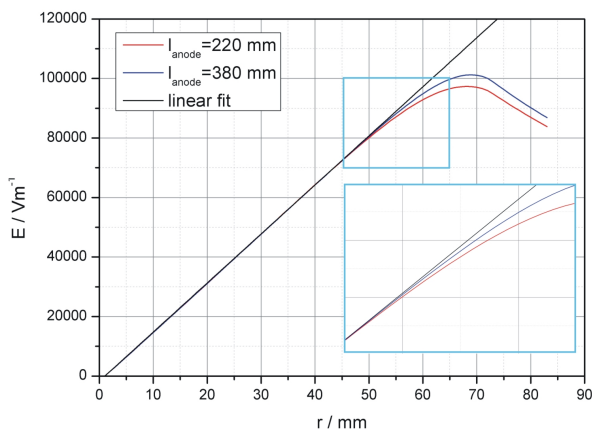


Figure 4.3: Linearity of the calculated electric space charge field as an example for different anode lengths ($B_z=8.3$ mT, $\Phi_A=10$ kV).

In order to decide the design concerning the length of the electrode system, it is also necessary to consider the shape of the electric space charge field, given that the length

4. DESIGN OF THE PROTOTYPE GABOR LENS FOR GSI

of the anode compared to its radius influences the shape of the potential and thus the distribution of electrons within this potential well. Figure 4.3 shows the radial electric space charge field for widely differing anode lengths. In case of the longer anode ($L_A=380$ mm), the linearity of the electric field as a function of the radius is much more pronounced than in the case of the shorter anode ($L_A=220$ mm). In light of possible aberrations of the beam due to non-linearities in the electric focusing field, a ratio of $R_A/L_A=0.25$ was chosen with simultaneous consideration of compensating the decrease in the confinement efficiency by higher field strengths.

4.2 The Magnetic System

Towards the purpose of technical flexibility, for the magnetic system it was made use of a pair of Helmholtz coils. With respect to the primary considerations concerning the design of the electrode system, the length of the Helmholtz coils had to be adapted.

Figure 4.4 shows the calculated B_z -component of the magnetic field for different gap widths of the coils using CST EM Studio. The coil gap is defined as the distance between the center of each coil.

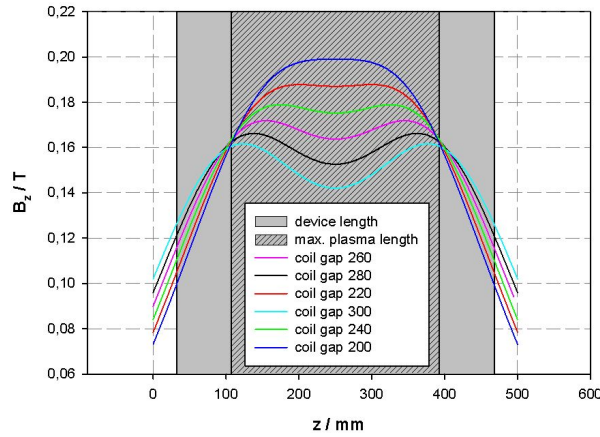


Figure 4.4: Axial magnetic field B_z as a function of the gap width of the coils.

The homogeneity of the magnetic field decreases due to the reduced overlap of the fields. At a gap width of 300 mm, the length of the magnetic system matches the electrode system. Although the drop in the magnetic field on axis only amounts to 12%, it was necessary to investigate the influence of the inhomogeneity on the electron confinement and distribution.

Therefore, in another simulation the charge density distribution calculated for a field configuration using a perfect homogeneous magnetic field was compared to the configuration using the magnetic coil system with a gap width of 300 mm.

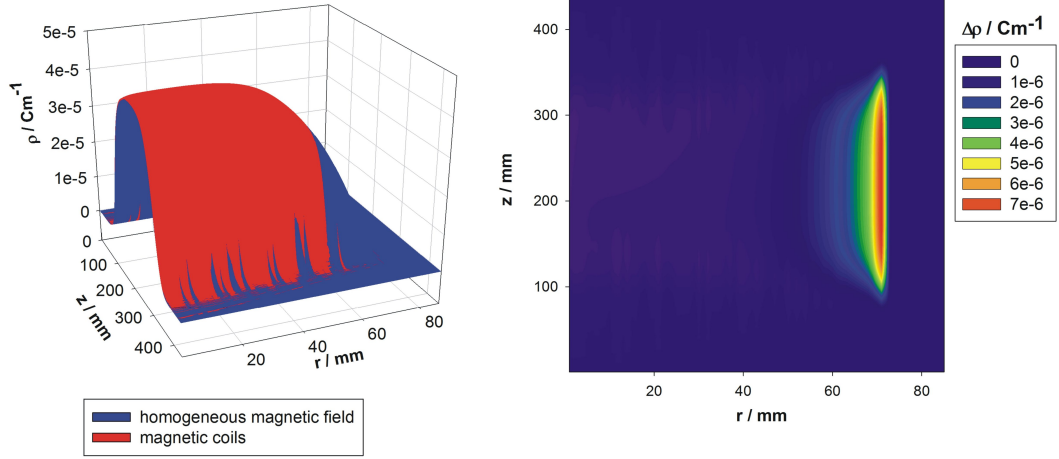


Figure 4.5: Influence of field homogeneity on the charge density distribution (left) and difference in the charge density for different magnetic fields (right).

Figure 4.5 shows the calculated charge density distribution in case of a homogeneous field and the magnetic coils for $\Phi_A=30$ kV, $B_z=13$ mT.

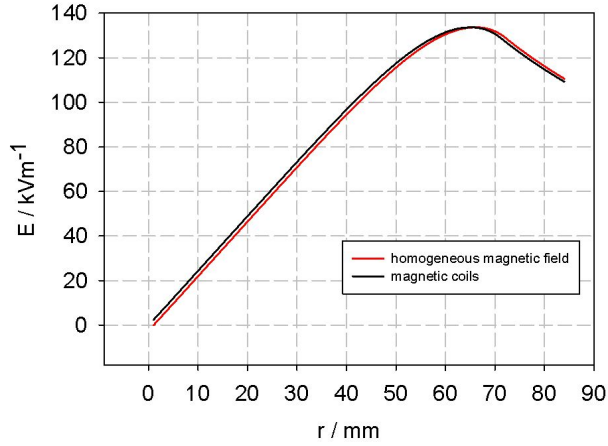


Figure 4.6: Comparison of electric space charge fields calculated for different magnetic fields.

The difference of the charge density indicates a deviation in the confinement, especially at a larger radius of the electron cloud.

4. DESIGN OF THE PROTOTYPE GABOR LENS FOR GSI

In light of the design parameters, this deviation only affects beams with radii larger than 50 mm and, thus still fulfilling the requirements. Moreover, the comparison of the electric space charge fields only shows fine distinctions (see figure 4.6).

Furthermore, beam transport simulations were performed to examine these results, as discussed in the following section.

4.2.1 Beam Transport Simulations

The beam transport of $^{238}\text{U}^{4+}$ with an energy of 2.2 keV/u was simulated using the code LINTRA (see section 2.8) to further investigate the influence of the confinement efficiency of the Gabor lens on beam emittance. For these calculations, a homogeneous phase space distribution at the entrance of the beam line and a space charge compensation of 100% within the whole transport section was assumed. Figure 4.7 shows the beam envelope along the transport section, which consists of an initial drift section with different lengths, the space charge lens and a second drift of 650 mm.

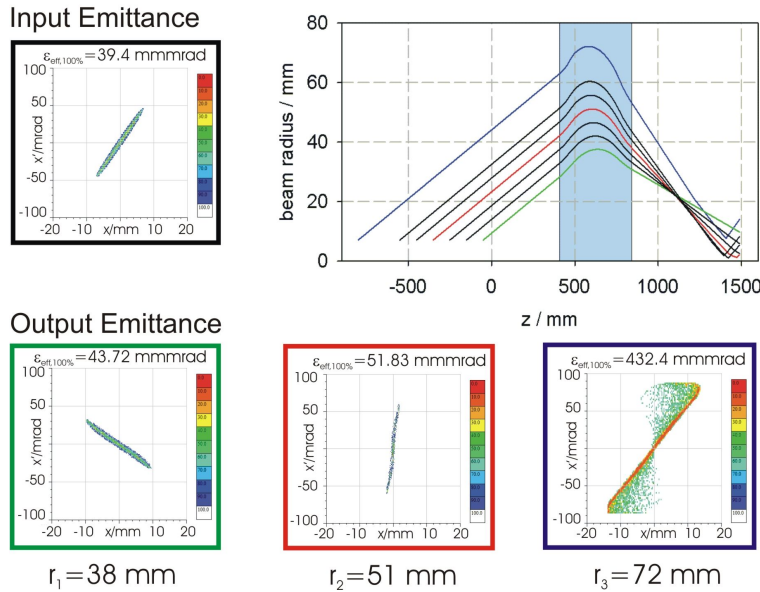


Figure 4.7: Beam envelope along the transport section, input emittance and output emittance for selected beam radii.

Moreover, the output emittance at the end of the second drift for different beam radii at the center of the space charge lens ($r_{1,\text{beam}}=38 \text{ mm}$, $r_{2,\text{beam}}=51 \text{ mm}$, $r_{3,\text{beam}}=72 \text{ mm}$)

is also presented [Sch10]. Figure 4.8 shows the emittance growth as a function of the beam radius at the center of the space charge lens for the selected cases (see color code).

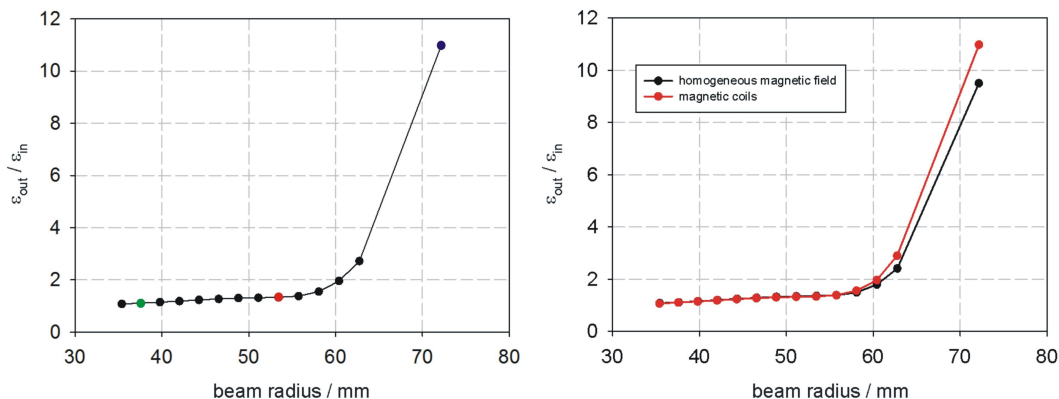


Figure 4.8: Emittance growth as a function of the beam radius (left) and comparison of the focusing quality for different magnetic fields (right).

Comparing these results of beam transport simulations to simulations performed assuming an electron cloud confined by a homogeneous magnetic field, differences in the performance of the lens only appear for larger beam radii.

4.2.2 Reasons for an Emittance Growth

The transport of an ion beam by a focusing device would ideally be free of aberrations. However, as previously implied, there are several effects that lead to an emittance growth of the beam.

To generally investigate possible reasons for an emittance growth of an ion beam focused by the Gabor lens, further beam transport simulations were performed using the code LINTRA.

A homogeneous beam distribution of 50 keV He⁺-ions was tracked through a first drift section of the length $l_1=210$ mm, followed by the Gabor lens for different settings of the realistic fields and another drift section of $l_2=50$ mm.

If the electrons are homogeneously distributed in order that the created space charge field is linear in radial direction, the performance of the Gabor lens is assumed as illustrated in figure 4.9.

In reality, the beam distribution is usually not found to be homogeneous or monoenergetic and plasma instabilities of the nonneutral plasma are observed for unmatched

4. DESIGN OF THE PROTOTYPE GABOR LENS FOR GSI

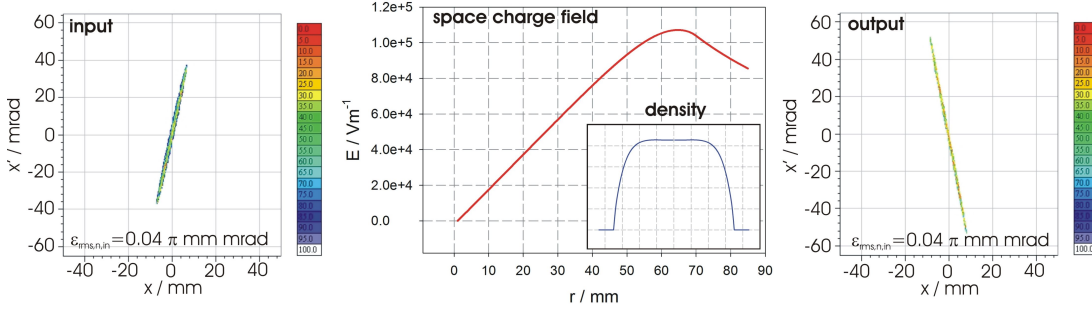


Figure 4.9: Homogeneous input distribution of a 50 keV He^+ -beam (left), self-electric field of the electrons calculated for Gabor lens parameters of $\Phi_A=20$ kV and $B_z=10$ mT using the code GABOR-M (middle), and resulting emittance after the described transport section (right).

configuration of the confining fields. The influence of the effects on the phase space distribution of the beam is subsequently described.

4.2.2.1 Chromatic Aberrations

Regarding equation 2.91, one very clear reason for the emittance growth of an ion beam passing through the confined electron cloud is the energy spread of the beam itself, which causes chromatic aberrations [Rei08]. The focal length of the Gabor lens is energy dependent and therefore sensitive to variations in beam energy.

In order to demonstrate the influence of chromatic aberrations, the phase space distribution for a 50 keV He^+ -beam with a large energy spread of ± 1 keV after passing the lens was calculated and is illustrated in figure 4.10.

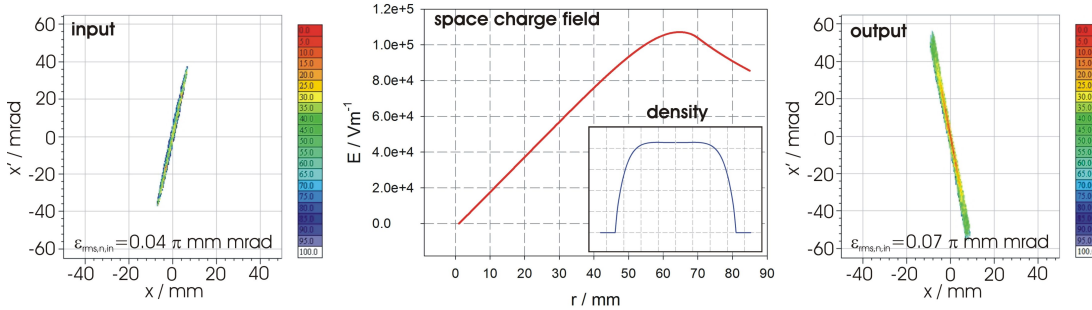


Figure 4.10: Homogeneous input distribution of a 50 keV He^+ -beam with an energy spread of ± 1 keV (left), self-electric field of the electrons calculated for Gabor lens parameters of $\Phi_A=20$ kV and $B_z=10$ mT (middle), and resulting emittance (right).

Note that usually the energy spread of the beam is lower in the application field of the Gabor lens.

4.2.2.2 Spherical Aberrations

The homogeneity of the electron density distribution is a necessary requirement for the focusing quality of the Gabor space charge lens. If the radius of the ion beam is larger than the electron cloud, the nonlinear part of the electric space charge field resulting from the Debye drop off of the plasma cloud lowers the focusing strength and causes aberrations [Rei08] (see figure 4.11).

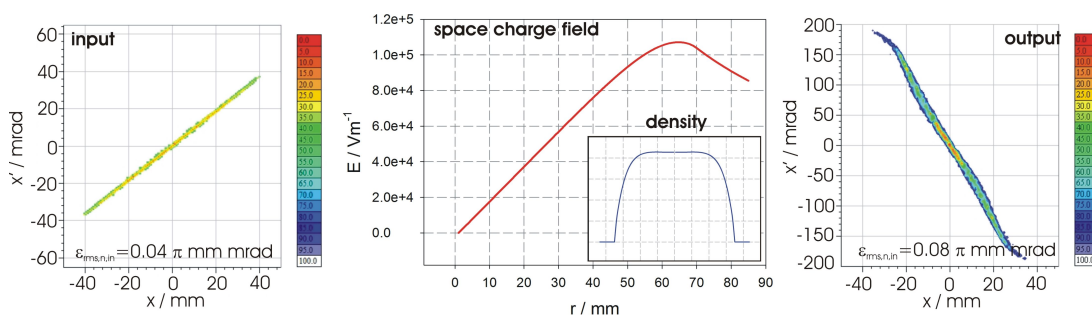


Figure 4.11: Homogeneous input distribution of a 50 keV He^+ -beam (left), self-electric field of the electrons calculated for Gabor lens parameters of $\Phi_A=20$ kV and $B_z=10$ mT (middle), and resulting emittance (right).

In the presented case, the beam radius in the center of the lens was $r_b=57.7$ mm, thus more than twice as high than previously discussed cases ($r_b=22.6$ mm).

4.2.2.3 Plasma Instabilities

In particular, plasma instabilities (see chapter 3) cause an emittance growth of the ion beam.

The occurrence of a hollow profile of the electron cloud could be experimentally verified, representing the initial situation for the evolution of the theoretically well-described diocotron instability. As a result of the hollow electron distribution, the electric space charge field is only linear over a short radial distance (see figure 4.12).

4. DESIGN OF THE PROTOTYPE GABOR LENS FOR GSI

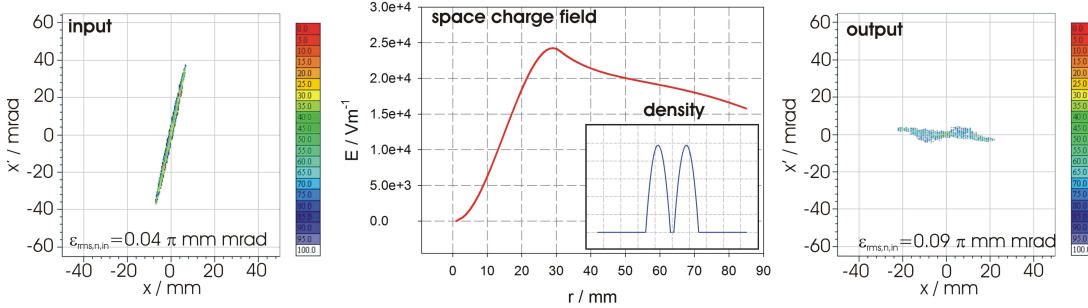


Figure 4.12: Homogeneous input distribution of a 50 keV He^+ -beam (left), self-electric field of the electrons calculated for Gabor lens parameters of $\Phi_A=20$ kV and $B_z=6.3$ mT (middle), and resulting emittance (right).

4.3 Technical Specifications

With respect to the previously discussed design criteria, a prototype Gabor lens was constructed and built. Figure 4.13 shows the technical drawing and pictures of the final design.

The total length of the prototype is 436 mm with an aperture of 150 mm. The maximum magnetic field strength is $B_{z,\text{max}}=160$ mT and the electrode system including the insulator is constructed for a maximum potential of $\Phi_A=50$ kV. Thus far, the applied maximum voltage has not exceeded $\Phi_A=30$ kV.

The potential created by the electrode system for $\Phi_A=30$ kV and the comparison of the measured and simulated magnetic field for an exciting current of $I_B=5$ A are presented in figure 4.14.

The ground electrodes were provided with threads in order to allow the adjustment of the plasma column's expansion by varying the ground length. The insulator is made of *Vinidur*, a robust material with a dielectric strength of 15 kV/mm. A cover made of stainless steel with an *Vinidur* inlay (see [Kla13]) and also a high voltage feed through was constructed to render this device scoop-proof.

For further investigations, the anode was quartered to study possible steering effects of the beam: by applying a slightly different potential to one quarter, it is assumed that the center of the plasma column is moved off axis, thereby steering the beam. Indeed, the possible steering effect could not be studied within the scope of this thesis.

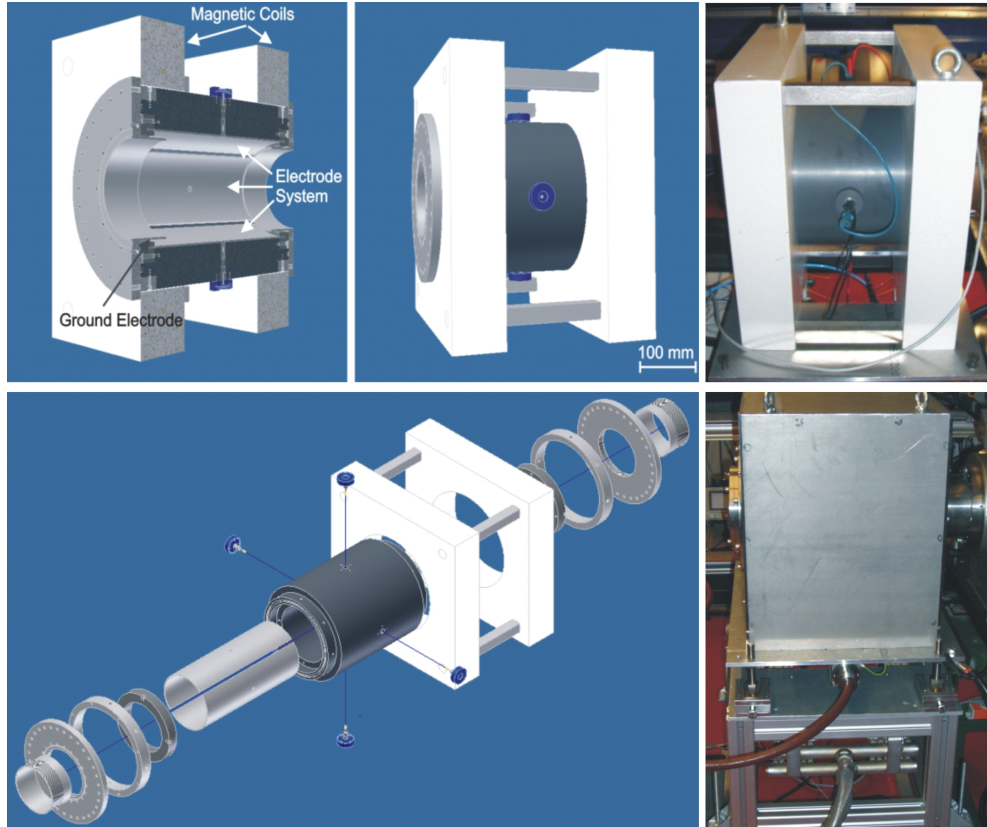


Figure 4.13: Technical drawing and pictures of the prototype Gabor lens for GSI.

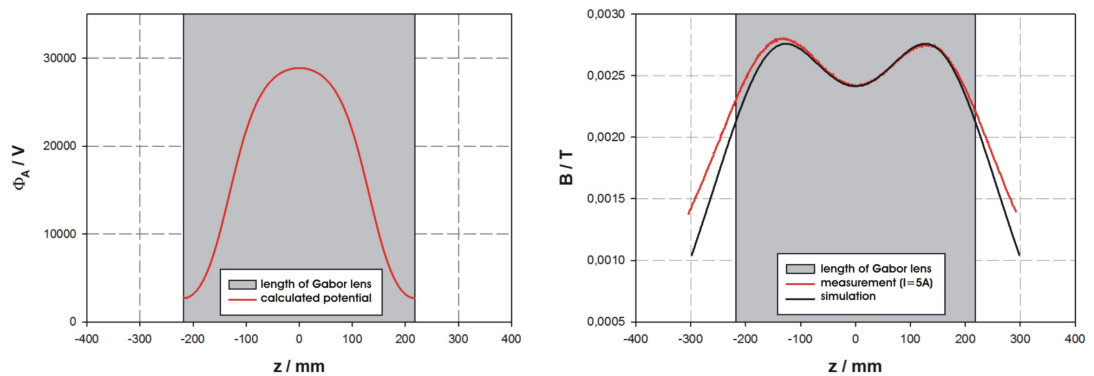


Figure 4.14: Calculated potential on axis for $\Phi_A = 30$ kV (left) and comparison of measured and simulated magnetic field (right).

4. DESIGN OF THE PROTOTYPE GABOR LENS FOR GSI

5

Nonneutral Plasma Diagnostics

5.1	Experimental Set-Up	70
5.1.1	CCD Cameras	71
5.1.2	Momentum Spectrometer	72
5.1.3	Pepperpot Emittance Scanner	72
5.2	Residual Gas Ion Current	73
5.2.1	Current Profile and Time Structure	73
5.2.2	Electron Density Measurement	74
5.2.3	Phase Space Distribution	78
5.3	Plasma Emission	80
5.3.1	Symmetry	80
5.4	Time-Resolved Optical Diagnostics	84
5.5	Electron Temperature Measurement	88
5.5.1	The Term Scheme of the Helium Atom	88
5.5.2	Line-Ratio Technique	89
5.5.3	The Optical-Emission Cross Sections	94
5.5.4	Basic Principles	95
5.5.5	The Optical Method	96
5.5.6	Experimental Set-Up	97
5.5.7	Results of the Optical-Emission Cross Section Measurement	113
5.5.8	Determination of the Nonneutral Plasma Temperature	117

5. NONNEUTRAL PLASMA DIAGNOSTICS

5.1 Experimental Set-Up

Diagnostics techniques are important to extract information about the plasma properties and its state from the confined electron column. A major challenge involves the development of non-invasive, optical techniques, given that conventional optical diagnostics for the nonneutral plasma are effectively non-existent.

In order to determine the plasma properties without influencing and distracting the system, two quantities are observed, namely the extracted residual gas ion current and the photons emitted from the plasma. Figure 5.1 shows the experimental set-up for the plasma diagnostics performed at IAP in parallel to the beam transport measurements at GSI discussed in chapter 6.

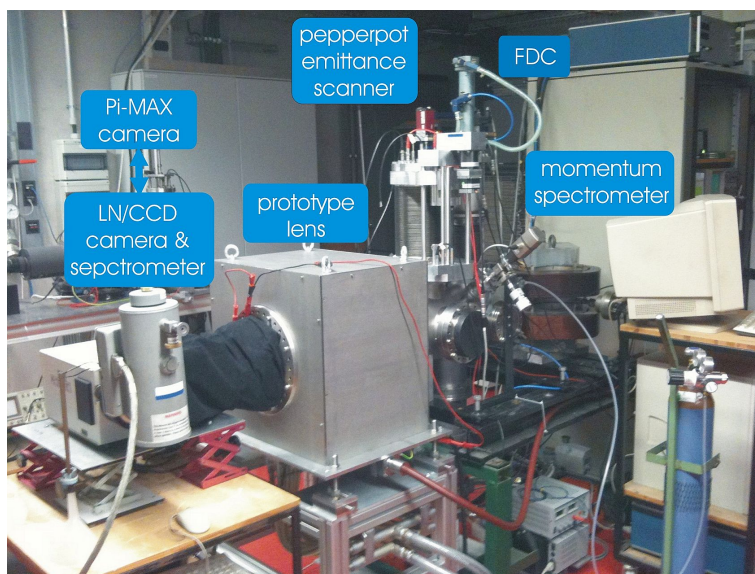


Figure 5.1: Experimental set-up for the diagnostics of the nonneutral plasma confined by the Gabor lens.

The plasma emission is detected by two different CCD cameras. One camera is equipped with a monochromator to analyze the emitted spectrum, while the other uses an intensifier that enables time-resolved diagnostics of the light distribution. The ion current is detected by either a Faraday cup (FDC), a pepperpot emittance scanner or a momentum spectrometer to analyze the time structure, the phase space distribution or to measure the electron density.

The main diagnostic elements will be discussed in the following.

5.1.1 CCD Cameras

For the optical diagnostics, two cameras are provided: the liquid nitrogen cooled CCD camera (LN/CCD) including a spectrometer and the fast PI-MAX:1K camera from Princeton Instruments, equipped with an intensifier.

The intensifier of the PI-MAX:1K CCD camera using a P43 phosphor screen enables very short exposure times, down to ≥ 2 ns. For this reason, the camera is well-suited for the time-resolved diagnostic of the nonneutral plasma state. The measured gain curve as a function of the software gain of the camera is shown in figure 5.2.

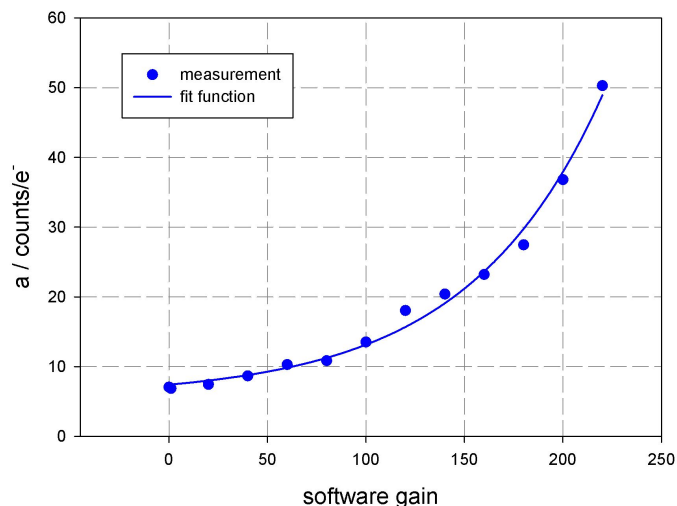


Figure 5.2: Measured gain curve of the intensifier as a function of the software gain [Gla12].

The camera gain is the conversion between the number of photoelectrons recorded by the CCD and the number of digital units (*counts*) contained in the image. By increasing the software gain, the detected light signal grows exponentially.

The knowledge of the gain enables the evaluation of the camera performance for a given setting in order to determine the read out noise contained in the detected image.

The chip of the LN/CCD camera (also from Princeton Instruments) is cooled down to a temperature of -120°C to reduce dark current and therefore noise in the measured intensity signal. The camera has a very high quantum efficiency in the visible region of 80% (see figure 5.3, VIS A/R coating) and is well-suited to the detection of very low signals, which require long exposure times. The LN/CCD camera is equipped with a Czerny-Turner-monochromator that splits the emitted light into its wavelengths using

5. NONNEUTRAL PLASMA DIAGNOSTICS

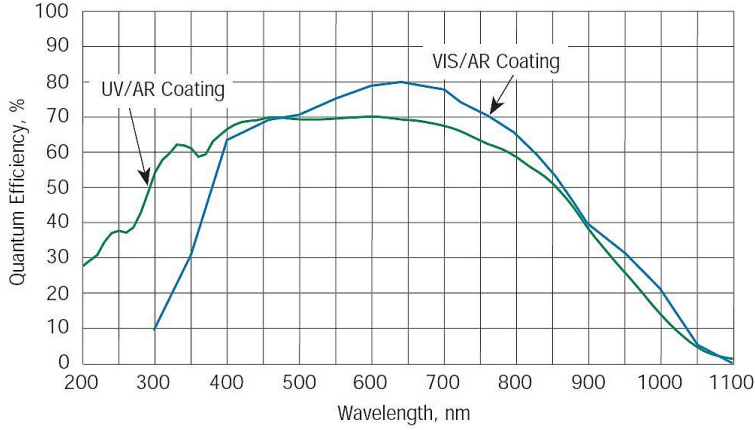


Figure 5.3: Quantum efficiency of the detector (VIS A/R coating) [LNC97].

three different grids (100 g/mm, 300 g/mm and 1800 g/mm) [Sch09].

For the emission spectroscopy, it was necessary to calibrate the optical system concerning the wavelength and the absolute intensity. The calibration procedure will be described in detail in section 5.5.6.4.

5.1.2 Momentum Spectrometer

It is possible to measure the velocity of a particle of known mass by its deflection in a homogeneous magnetic field. When the particle enters the magnet in perpendicular direction, it is forced on circular orbit with radius r if the value of the Lorentz force F_L is equal to the centrifugal force F_c :

$$qB = \frac{mv}{r} \quad (5.1)$$

The used momentum spectrometer consists of a dipole with a vacuum chamber of fixed deflection radius r . Therefore, the variable parameter is the magnetic field that is increased during the measurement.

For an ion of known species and charge state, the measured spectrum corresponds to the count rate as a function the ion energy calculated from the velocity.

5.1.3 Pepperpot Emittance Scanner

A pepperpot emittance scanner is used to measure the phase space distribution of the residual gas ions, in a procedure similar to the slit-grid emittance measurement

described in chapter 6: by introducing a pepperpot mask into the beam, it is split into several beamlets, which drift a given distance to a phosphorus screen. The incident particles cause a scintillation of the screen that is viewed by a CCD camera (see figure 5.4) [Pfi10].

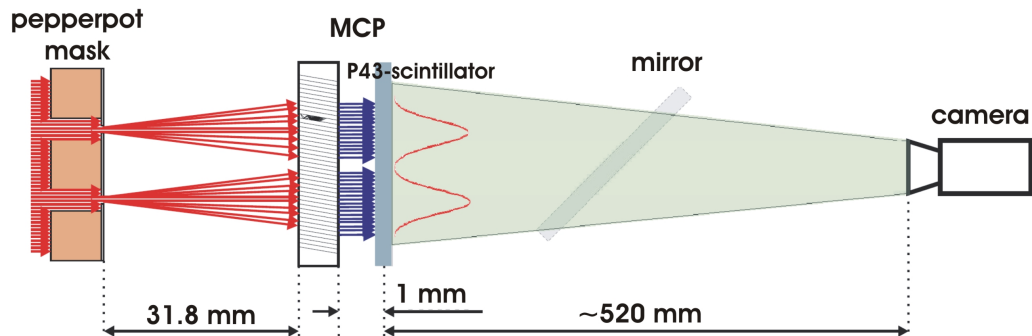


Figure 5.4: Measurement scheme of the pepperpot emittance scanner (obtained from [Pfi10]).

The used emittance scanner has a P43 phosphorus screen as scintillator with a quick fall time that in principle enables a time-resolved emittance measurement in the region of μs .

The pepperpot emittance scanner offers the advantage over other methods that emittances in both directions x and y are determined within one shot. For this reason, it is also a quick method to measure the phase space distribution of a beam.

5.2 Residual Gas Ion Current

As previously discussed in chapter 2, ions are mainly produced by electron impact ionization. Owing to the positive anode potential, these residual gas ions are extracted from the lens volume and are detected by different devices to analyze the time structure, the energy and their distribution in phase space.

5.2.1 Current Profile and Time Structure

The value and particularly the time structure of the ion current is measured by a Faraday cup (FDC). An oscilloscope connected to the FDC directly displays the ion current due

5. NONNEUTRAL PLASMA DIAGNOSTICS

to a preceding resistance of $10\text{ k}\Omega$.

Figure 5.5 provides an example of the ion current as a function of the lens parameters.

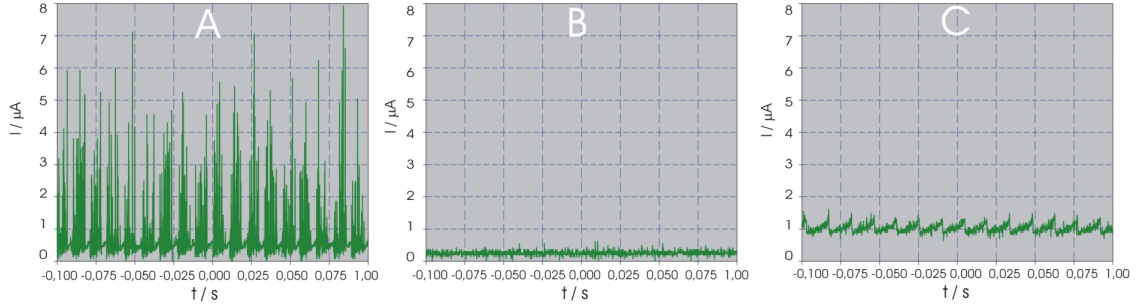


Figure 5.5: Example of different current signals detected by the Faraday cup.

In case A ($\Phi_A=4\text{ kV}$, $B_z=10.6\text{ mT}$, $p=6 \cdot 10^{-2}\text{ Pa}$, He), the ion current is strongly fluctuating, as well as in case C ($\Phi_A=4\text{ kV}$, $B_z=15.2\text{ mT}$, $p=6 \cdot 10^{-2}\text{ Pa}$, He), but with the difference that the current also shows a periodic time structure. The ion current is directly related to the electron plasma state. Using the ion current as a trigger signal for the optical diagnostic, it is possible to investigate the evolution of an instability (see chapter 3). Case B ($\Phi_A=4\text{ kV}$, $B_z=11.8\text{ mT}$, $p=6 \cdot 10^{-2}\text{ Pa}$, He) indicates that the plasma is temporally constant and for this reason also situated in thermalized state since the equalization of energies is a matter of time.

Note that the ion current yields important information about the plasma state in connection with the other diagnostic elements such as the optical diagnostics, which will be introduced in section 5.3.1.

5.2.2 Electron Density Measurement

It is possible to determine the confined electron density from the residual gas ion energy detected by a momentum spectrometer. The basic idea behind this diagnostic method is that the ions gain their energy in the potential well of the anode, which is reduced by confined electrons. If the ions have a lower energy $q\Phi_i$ compared to what they should have gained from the anode potential Φ_A , it is possible to calculate the density using equation

$$n_{e,w/o\text{beam}} = \frac{4\epsilon_0\Phi_r}{eR_p^2 \left(1 + 2 \ln \left(\frac{R_A}{R_p}\right)\right)} \quad (5.2)$$

whereas $\Phi_r = \Phi_A - \Phi_i$.

A scheme of the electron density measurement is presented in figure 5.6.

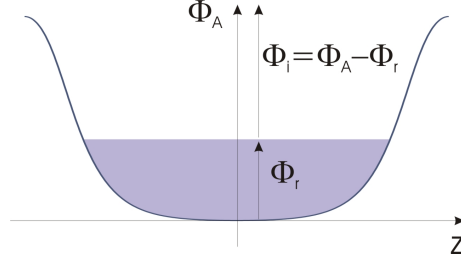


Figure 5.6: Scheme of the density measurement.

The transport of the residual gas ions through the experimental set-up illustrated in figure 5.1 was investigated in order to evaluate the presented measurement technique. Ions are generated for a parameter setting of $B_z = 8.1 \text{ mT}$, $\Phi_A = 8 \text{ kV}$ and $p = 7.8 \cdot 10^{-5} \text{ Pa}$ (Ar), assuming a homogeneous residual gas distribution at room temperature, and are tracked through the lens volume using the code GABOR-M.

Figure 5.7 shows the trajectories of the Ar^+ -ions calculated from the start position in the middle of the lens to the entrance of the spectrometer.

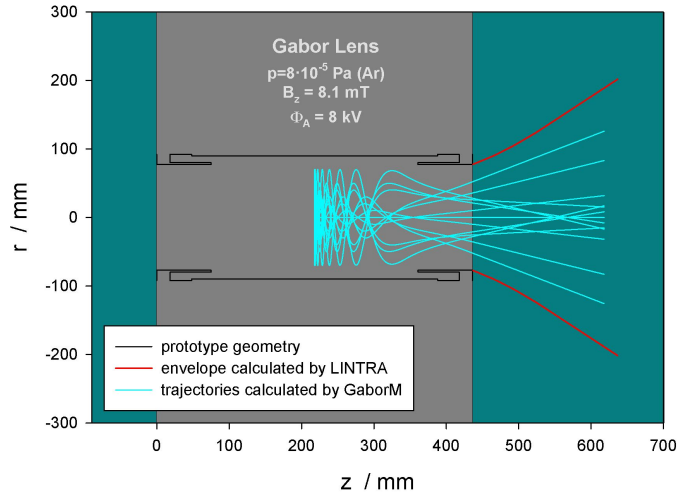


Figure 5.7: Calculated trajectories for the Ar^+ -ions produced in the lens volume.

First, they oscillate within the space charge potential of the electron cloud before being extracted with a large divergence angle. Consequently, the transmission through the diagnostic box is only around 0.93% and both the emittance and the energy spectrum

5. NONNEUTRAL PLASMA DIAGNOSTICS

are cropped (see figure 5.8).

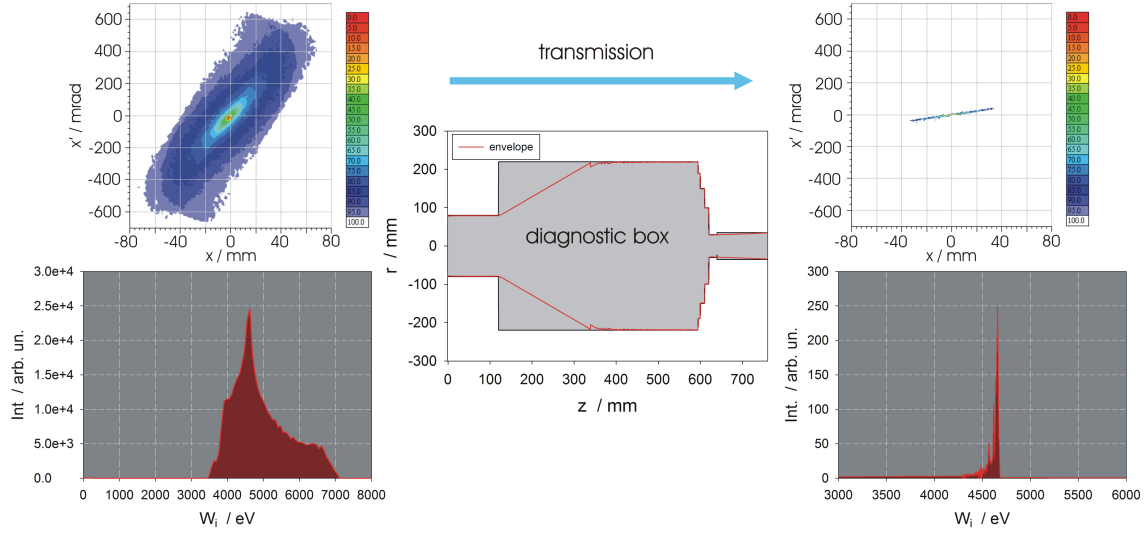


Figure 5.8: Transmission of the residual gas ions through the diagnostic box.

Although the energy spectrum is cropped, the maximum of the peak remains at the same energy value. Thus, the energy value of the peak with the highest count rate is used for the density calculation, independently of the residual gas.

Figure 5.9 illustrates the calculated energy spectrum in comparison to the measured one.

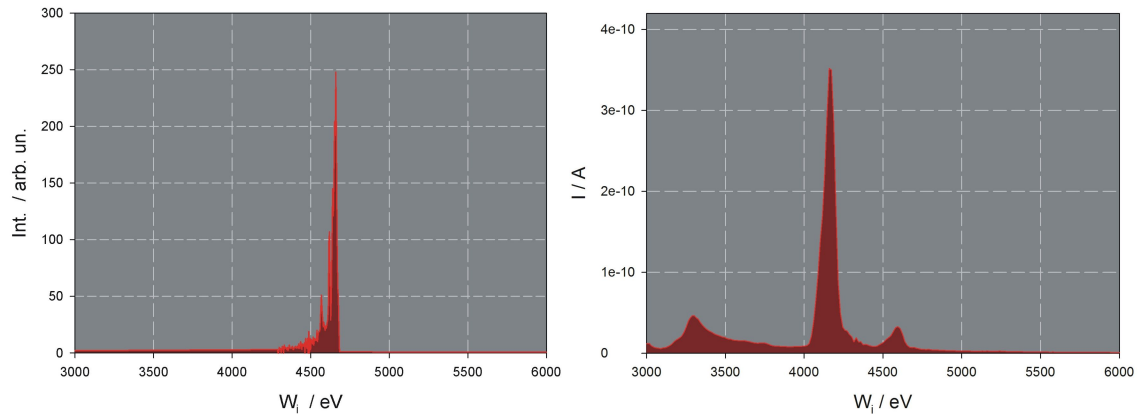


Figure 5.9: Comparison between calculated (left) and measured energy spectrum (right) of extracted Ar^+ -ions.

The deviation between the calculated and the measured mean electron density is around

24% in the case of argon as residual gas, while the agreement in case of helium is much better, namely around 10% (see chapter 6).

As an example, typical energy spectra of He⁺ and Ar⁺-ions for lens parameters close to the operation point are illustrated in figure 5.10.

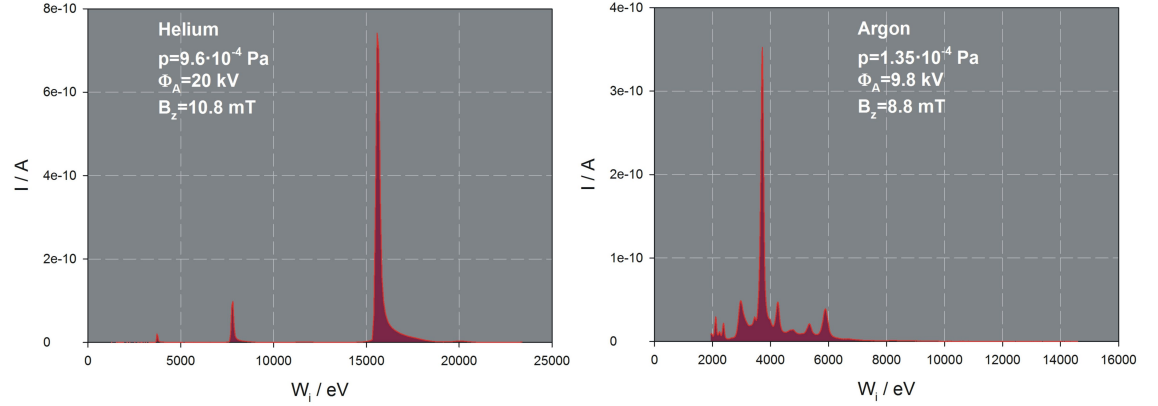


Figure 5.10: Typical energy spectra of He⁺-ions (left) and Ar⁺-ions (right) extracted from the lens volume close to the operation point of the lens.

In this context, another method for determining the density shall be discussed. Referring to equation 2.90 introduced in chapter 2, the focusing strength of the Gabor lens is only dependent on the variables electron density n_e and acceleration voltage U_a of the ion beam. Assuming a round beam, one can define the focal length as

$$\frac{1}{f_G} = \frac{\Delta y'}{y} = \frac{en_e l}{4\epsilon_0 U_a}$$

For this reason, the transverse momentum of the ion beam affected by the plasma column gives also an indirect evidence for the mean electron density confined in the Gabor lens. From the change in the divergence angle of a beam of known radius, the mean electron density is calculated by

$$n_e = \frac{4\epsilon_0 U_a}{e \cdot l} \frac{\Delta y'}{y} \quad (5.3)$$

The change in the divergence angle $\Delta y'$ from the drifted beam y'_1 to the focused beam y'_2 is determined by the twiss parameters of the emittance ellipse and is illustrated in figure 5.11.

The angle φ between the y axis and the major axis of the ellipse is given by

$$\varphi = \frac{\arctan\left(\frac{2\alpha}{\gamma - \beta}\right)}{2} \quad (5.4)$$

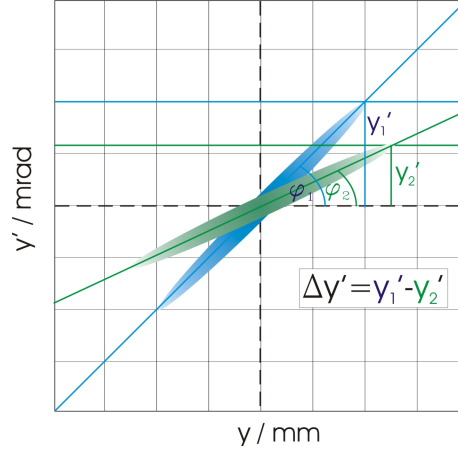


Figure 5.11: Scheme of density measurement by the change in the measured phase space distribution of a beam passing the nonneutral plasma cloud.

Subsequently, the divergence angle can be calculated by

$$y' = \tan(\varphi) \cdot y \quad (5.5)$$

Of course, this method fails at an angle of $\varphi = 90^\circ$, yet represents a quite good systematic in any other case.

5.2.3 Phase Space Distribution

The measurement of the distribution of extracted residual gas ions by an emittance scanner enables the determination of changes in the plasma state as well as the production region. For this reason, an emittance measurement using a slit-grid emittance scanner was performed for the prototype lens in comparison to the previously discussed numerical simulations. The result is illustrated in figure 5.12 and to compare with the uncropped phase space distribution in figure 5.8.

The calculated and the measured phase space distribution particularly differ in the angle, possible due to the neglected fringe field of the magnetic system in the numerical simulation. Other possible explanations include occurring ionization or charge exchange processes due to the interaction of the ions with the residual gas atoms.

Furthermore, it is possible to measure the time variant phase space distribution by a fast diagnostic system such as a pepperpot emittance scanner.

A detailed time-resolved investigation of the change in the emittance as function of the

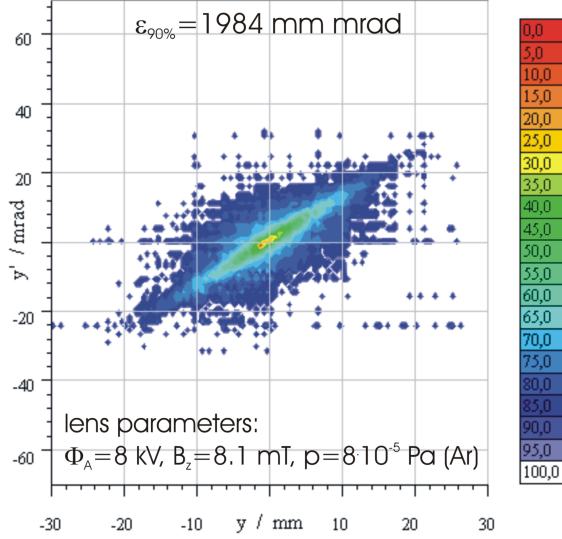


Figure 5.12: Example of slit-grid emittance measurement of residual gas ions extracted from the prototype lens for a parameter setup of $\Phi_A=8$ kV, $B_z=8.1$ mT, $p=8 \cdot 10^{-5}$ Pa (Ar).

lens parameters and the residual gas pressure was not possible within the scope of this thesis. Accordingly, a general proof-of-principle for the applicability of the emittance measurement for the analysis of the plasma cloud was performed.

As an example, the measured emittance of the residual gas ions by the pepperpot emittance scanner is shown in figure 5.13

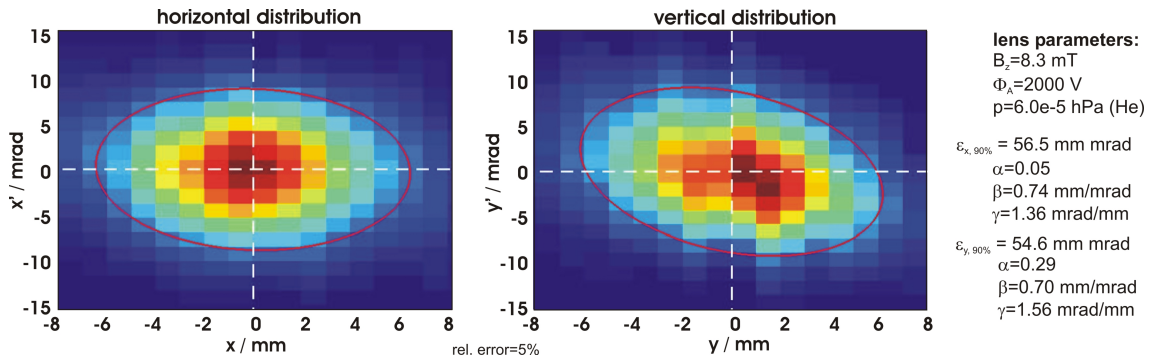


Figure 5.13: Example of pepperpot emittance measurement of residual gas ions extracted from a Gabor lens (original design at IAP) for a parameter setup of $\Phi_A=2$ kV, $B_z=8.3$ mT, $p=6 \cdot 10^{-3}$ Pa (He).

5.3 Plasma Emission

Radiative transitions in an atom are a result of excitation processes produced by an incident particle. As discussed in chapter 2, in case of the nonneutral plasma, the residual gas atoms are mainly excited by electron impact. For this reason, the intensity, which is detected by one of the introduced CCD cameras, is directly correlated to the density of the confined electron plasma and is illustrated in figure 5.14 as a function of the Gabor lens parameters.

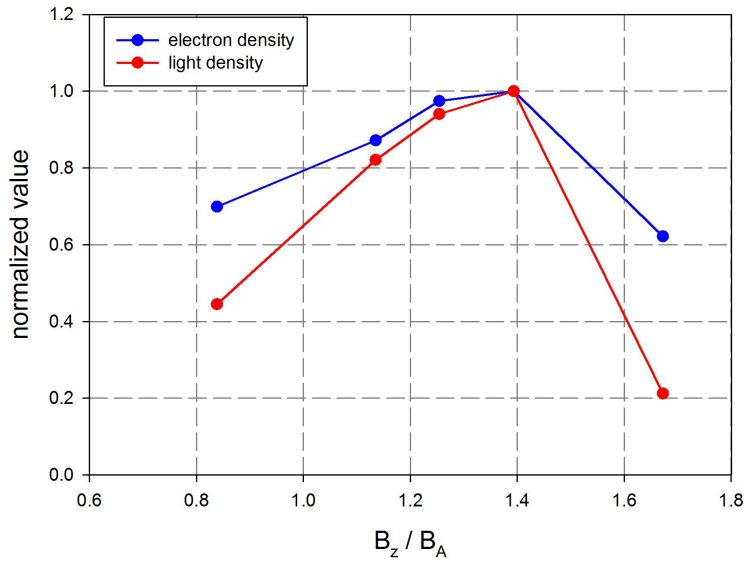


Figure 5.14: Correlation of electron density and measured intensity for $\Phi_A=9.8$ kV and $p=1.36 \cdot 10^{-4}$ Pa (Ar).

In connection to this, the light density distribution also represents the distribution of electron within in the lens volume very well, even though the central part of the plasma cloud is slightly overestimated compared to numerical simulations, which is a result of the spatial integration by the optical measurement. Nevertheless, the plasma emission yields information about the plasma state.

Its detailed analysis will be discussed subsequently.

5.3.1 Symmetry

Given that the light density distribution corresponds to the electron density distribution, it can be used for the analysis of the nonneutral plasma state.

The diocotron instability, represented by a hollow distribution of electrons, as well as other instabilities that lead to a change in the transverse electron density, can be characterized by the determination of the symmetry of the detected light density distribution. There are two methods of analysis: in one case, the rotational symmetry of the plasma cloud is determined, while in the other case, the symmetry is evaluated by a statistical description of the given light density distribution.

For the evaluation of the symmetry, it is necessary to find the center of the measured light density distribution in a first step. The center of mass, where the weighted relative position of the distributed pixels sums to zero, is typically used:

$$\sum_{i=1}^n m_i(x_i - X) = 0 \quad (5.6)$$

where m_i is the pixel value, x_i the single pixel x-coordinate and X the center-of-mass in x. The same is valid for the y-coordinate.

However, especially in case of distributions that are deformed and strongly differ from the usual round shape of the plasma cloud, it is sometimes more practical to find the maximum intensity in the picture.

If the center is found, the picture is normalized (i.e. 0 is the minimum while 1 is the maximum) and the rotational symmetry is determined by the algorithm

$$S_{rot} = \sum_{i=1}^N \left(\sum_{i=1}^{\frac{N}{2}} \int_0^R I(r, \frac{2\pi \cdot i}{N}) dr - \sum_{i=\frac{N}{2}+1}^N \int_0^R I(r, \frac{2\pi \cdot i}{N}) dr \right) \quad (5.7)$$

In other words, the normalized intensity value for each pixel in the picture is summed from the center of the distribution to the edge of the picture for each angle from 0° to 179° and subtracted from the integrated intensity of each angle from 180° to 359° . The result for every run is added up and finally represents the rotational symmetry S_{rot} [Rei]. In the case of a perfect circle, the rotational symmetry $S_{rot}=0$. Note that it becomes necessary to crop the picture according to the minimum length from the center of the plasma to the edge of the photograph, if the electron cloud is not exactly centered.

Figure 5.15 illustrates the analyzing procedure using MATLAB for a nearly perfect circle.

5. NONNEUTRAL PLASMA DIAGNOSTICS

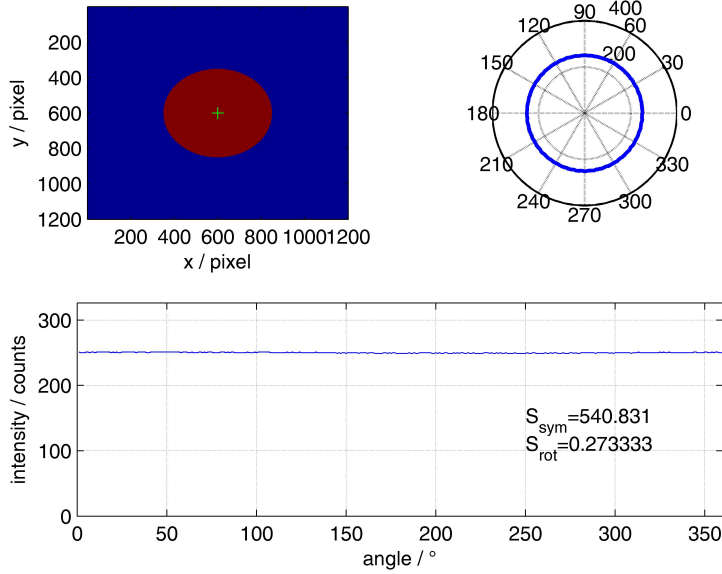


Figure 5.15: Example of the described procedure to determine the symmetry of the detected light density distribution for a nearly perfect circle.

For the determination of the symmetry factor S_{sym} , the mean intensity μ_I is weighted with its standard deviation σ_I after integrating the intensity for each angle from 0° to 359° [Sch11]:

$$S_{sym} = \frac{\mu_I}{\sigma_I^2} \quad (5.8)$$

$$\mu_I = \frac{1}{N} \sum_{i=1}^N \int_0^R I\left(r, \frac{2\pi \cdot i}{N}\right) dr$$

$$\sigma_I^2 = \frac{1}{N} \sum_{i=1}^N \left(\int_0^R I\left(r, \frac{2\pi \cdot i}{N}\right) dr - \mu_I \right)^2$$

Besides demonstrating the analyzing method for a perfect circle, the results for different types of distributions are presented in figure 5.16. Despite no concrete value of the symmetry factor S_{sym} that characterizes the degree of symmetry, its advantage over the rotational symmetry S_{rot} is that the magnitude of the intensity is considered.

The symmetry factor S_{sym} indicates a hollow distribution of the detected light density within the measurement series in case of a constant density. For this reason, both values are presented in the following to evaluate the symmetry of the plasma cloud.

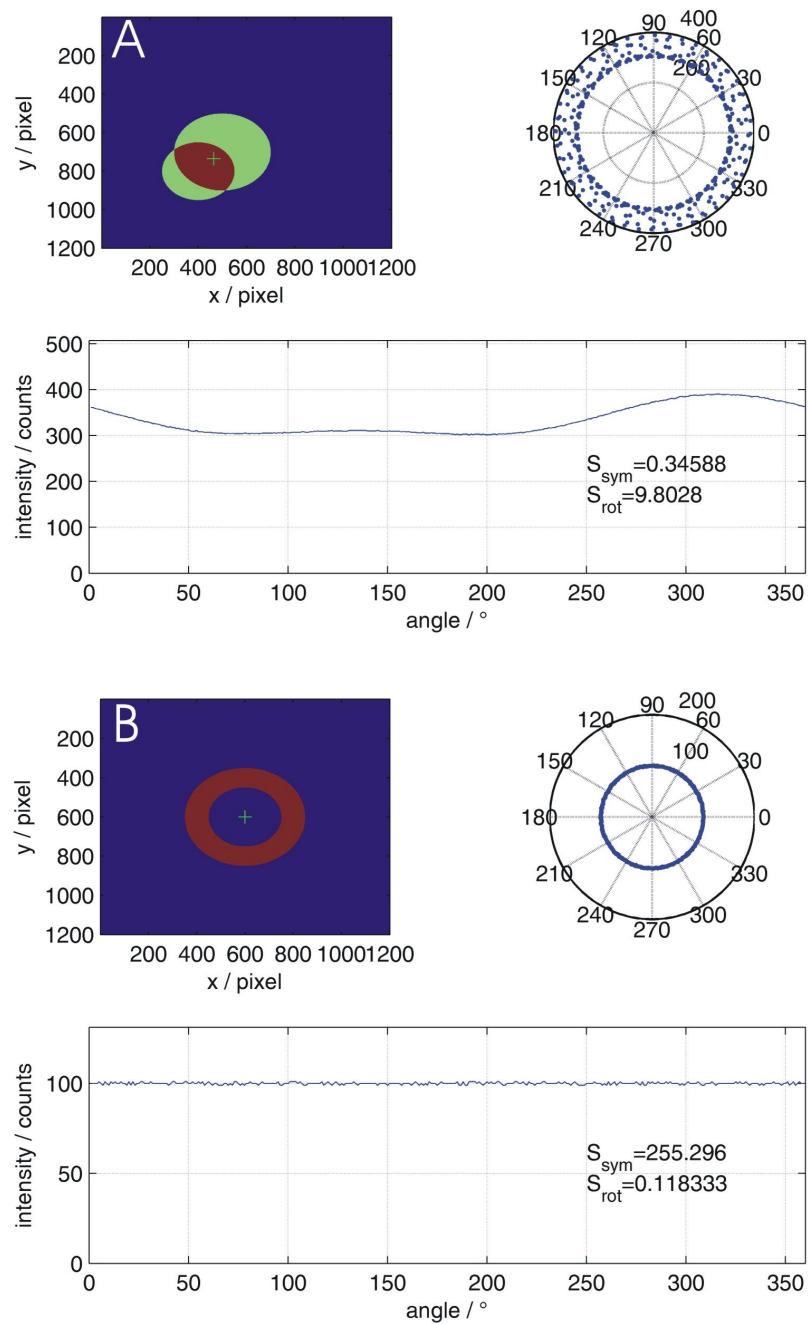


Figure 5.16: Example of the described procedure to determine the symmetry of the detected light density for a asymmetric (A) and hollow distribution (B).

5.4 Time-Resolved Optical Diagnostics

The time-resolved measurement is a very good example for the application of the presented quantities as a part of the plasma diagnostics.

The appearance of a plasma instability can be proved by measuring the ion current, the intensity magnitude and the light density distribution.

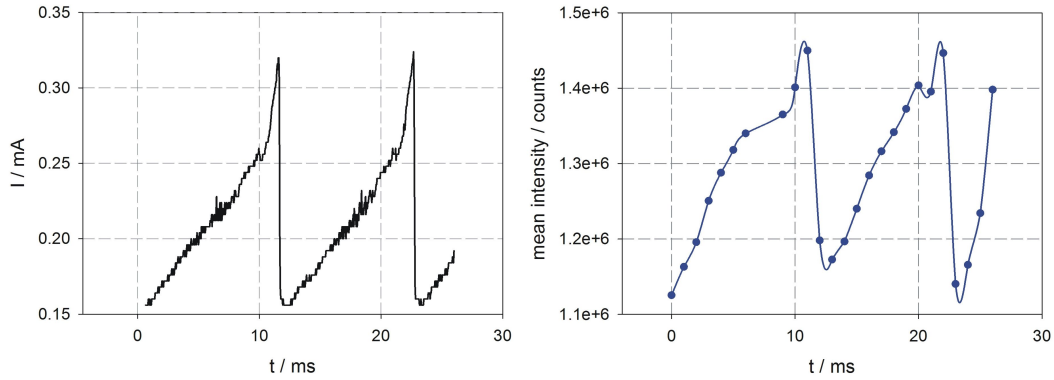


Figure 5.17: Residual gas ion current (left) and measured intensity signal (right) of an temporal unstable plasma mode.

To investigate the time dependent evolution of the instability, it is possible to use the ion current as a trigger signal for the optical exposure. Figure 5.17 represents the observed ion current and intensity variation when the plasma becomes unstable. It is necessary to accumulate the measured light signal on the CCD chip for many periods of the ion current in order to achieve a sufficient signal strength.

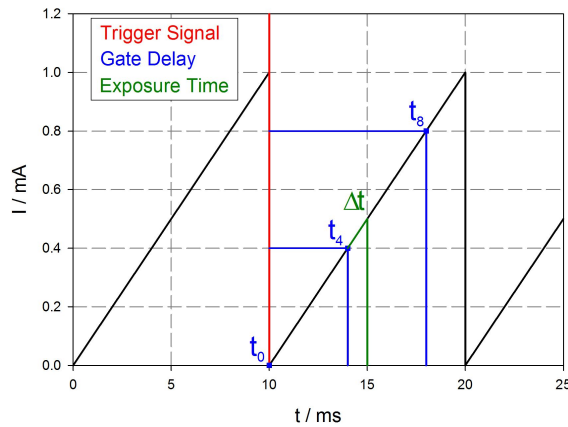


Figure 5.18: Measurement scheme for the time-resolved optical diagnostic.

5.4 Time-Resolved Optical Diagnostics

Accordingly, a stable ion current frequency is needed to measure the signal of the time-dependent instability always at the same temporal position. Figure 5.18 describes the measurement scheme for the time-resolved optical diagnostic. The oscilloscope transmits a TTL pulse to the CCD camera at the falling edge of the current signal. When receiving the signal, the camera releases an exposure with a given exposure time. The signal is accumulated on the CCD chip before being processed by the camera software. To measure along the increasing ion current, it is necessary to set a time delay (gate delay) between the TTL pulse received by the camera and the point in time of interest. Figure 5.19 shows an example of the measured unstable plasma confined by the three-segmented lens with parameters of $\Phi_A=3.4$ kV, $B_z=12$ mT, and $p=7.9 \cdot 10^{-2}$ Pa using the described time-resolved diagnostic method.

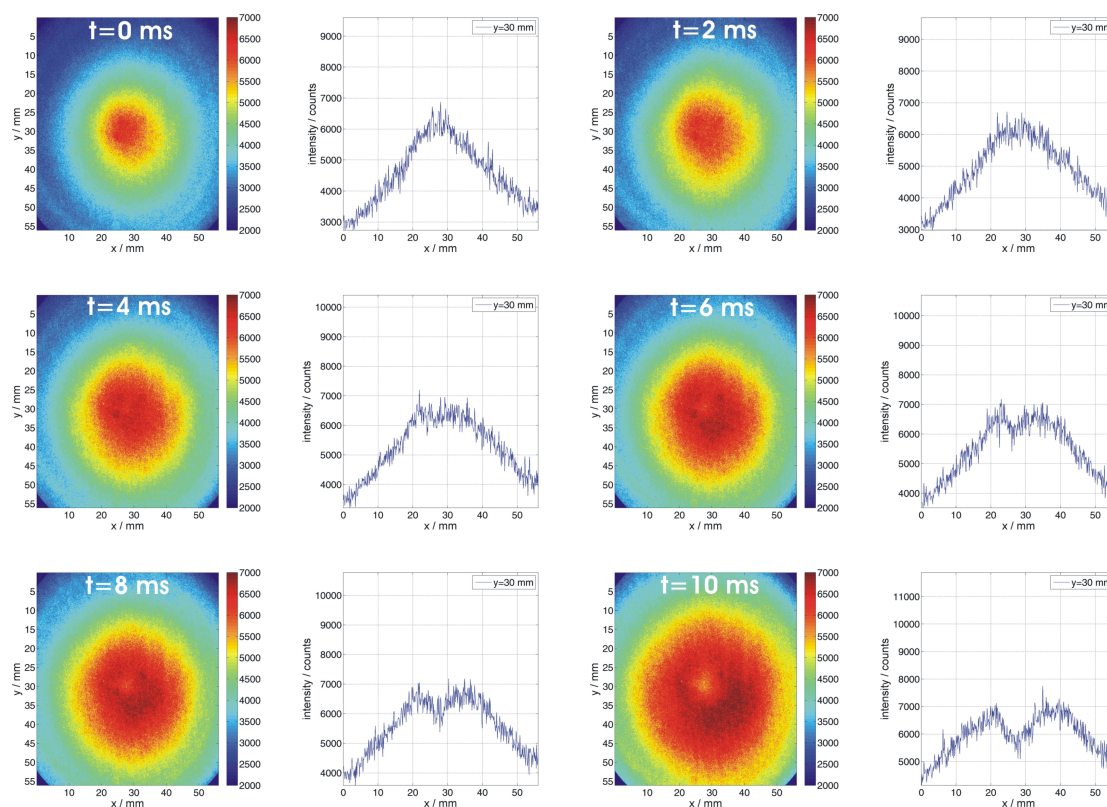


Figure 5.19: Measured light density distribution and its central profile in time steps of 2 ms (based on data from [Gla12] for the three-segmented lens).

The exposure time and gate delay amounts to $t=1$ ms, while the signal is accumulated

5. NONNEUTRAL PLASMA DIAGNOSTICS

on the CCD chip for 500 exposures. The light density evolves from a previously homogeneous to a hollow distribution within 10 ms. This process repeats every 10 to 11 ms and can be described as pulsing of the plasma cloud. It should be mentioned that the ion current and the intensity (see figure 5.17) varies during this time, but never drops to zero. Therefore, it does not represent a destructive mode of a plasma instability.

This behavior of the electron cloud can also be determined by the symmetry analysis discussed in the previous section. Figure 5.20 shows the rotational symmetry S_{rot} as well as the symmetry factor S_{sym} for the presented measurement.

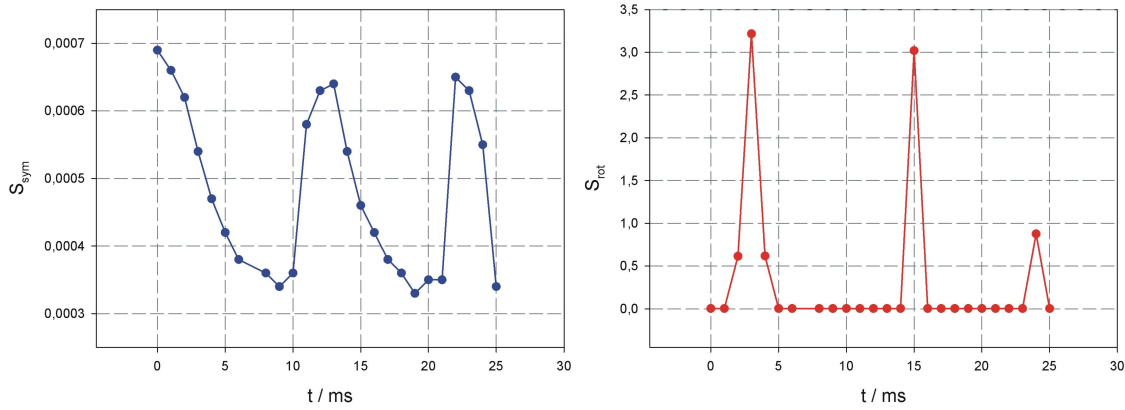


Figure 5.20: Symmetry factor (left) and rotational symmetry (right) as a function of time.

The symmetry factor S_{sym} indicates an increasing asymmetry of the plasma cloud in time, while the rotational symmetry S_{rot} shows a rapid rise on the half of the falling edge when the hole in the distribution first visually appears. Note that for the analysis, the center of the light density distribution was given by the center-of-mass.

According to section 3.2, the hollow profile is associated with the diocotron instability. The properties of the diocotron modes l are strongly dependent on the geometrical factors $\frac{r_b^+}{b}$ and $\frac{r_b^-}{b}$, which essentially means the electron layer thickness and distance from the center or the conductive wall. By measuring the inner r_b^- and outer radius r_b^+ of the detected hollow distribution in comparison to the expansion of the anode b , it is possible to characterize the instability referring to the stability-instability diagram illustrated in figure 5.21.

5.4 Time-Resolved Optical Diagnostics

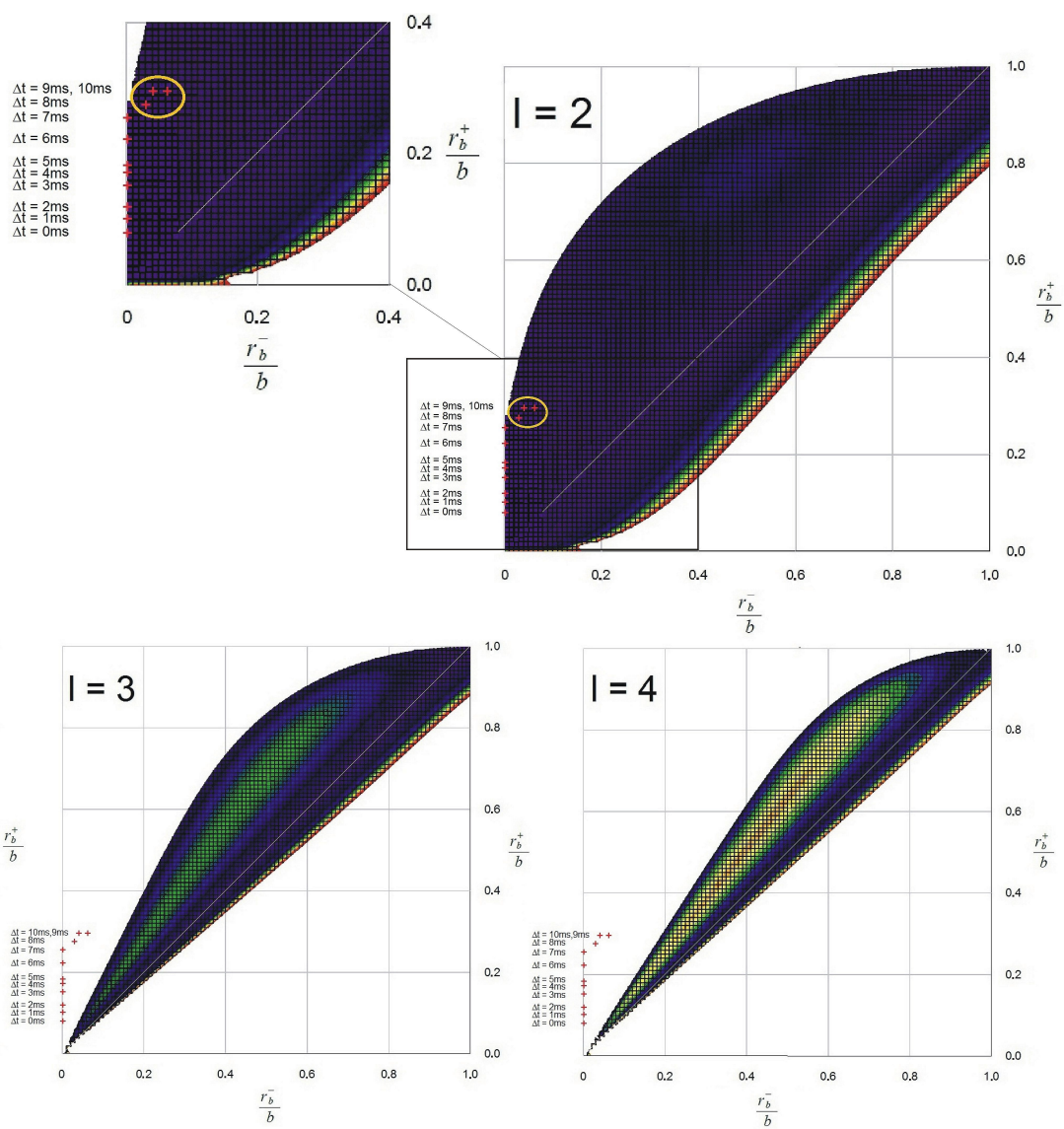


Figure 5.21: Characterization of the observed instability by the geometrical expansion of the detected hollow profile [Gla12].

5.5 Electron Temperature Measurement

In plasma physics, the spectroscopy represents a common non-invasive method to determine the plasma parameters, given that radiating atoms provide an insight into plasma processes and allow a real time observation [Fan06].

It is possible to determine the electron temperature from the measurement of the electron atom interactions. In case of the nonneutral plasma, the plasma emission is described by the coronal model introduced in chapter 2 (see equation 5.11). In coronal equilibrium, the atomic excitation is given solely by electron impact and deexcitation solely by photon decay.

For an appropriate description of the plasma, one would have to use a radiative-collisional-model. However, if two transitions from levels populated and decaying in the described way, one can use the line-ratio technique described by J. Boffard [BLD04]. Therefore, the different processes that lead to the population of a specific atomic level must be well understood.

5.5.1 The Term Scheme of the Helium Atom

Prior to introducing the line-ratio technique for the electron temperature measurement, the term scheme of the helium atom shall be discussed. Owing to its simplicity, it was mainly used as residual gas for spectroscopic investigations.

The ground state of the helium atom is the singlet state. According to the Pauli principle the electrons only differ in their spin projection quantum number but not in their spatial quantum numbers.

In singlet state the following applies for the total spin [Dem09]:

$$\mathbf{S} = \mathbf{s}_1 + \mathbf{s}_2 = \mathbf{0} \quad (5.9)$$

While the ground state can only be realized as singlet state, the excited states ($n \geq 2$) appear as singlet as well as triplet state.

In the case of an excited helium atom, the triplet state can be divided into three fine structure components with the quantum number J of the total angular momentum \mathbf{J} due to the spin-orbit coupling. The size and the energetic order of the deviation is dependent on the type and strength of the coupling between angular momentum and spin. The terms of the helium atom can be described by the *spectroscopic notation* to

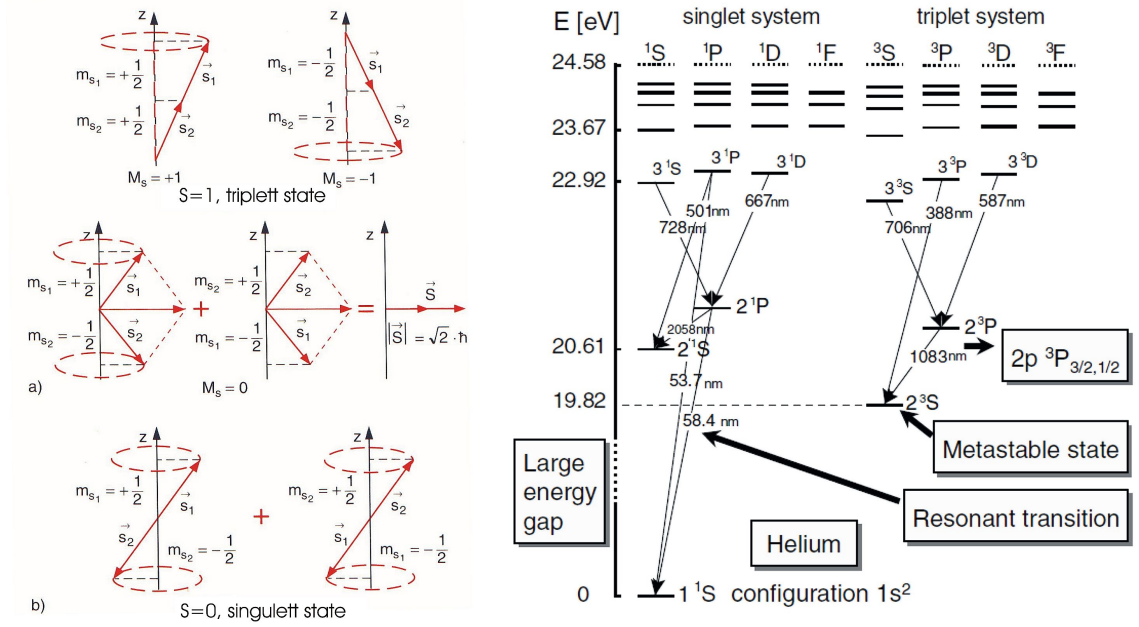


Figure 5.22: Vector model of the three triplet states and of the singlett state (left), (obtained from [Dem09]). Grotrian diagram of the helium with some important transitions and levels (right), (obtained from [Fan06]).

denote the splitting of configurations according to the L, S and J values of the electrons:

$$n^{2S+1}L \tag{5.10}$$

while n is the energy level and $2S+1$ the multiplicity of the atomic state. The value of the orbital angular momentum L is given using capital letters. Thus, S represents a state where $L=0$, P means $L=1$, and so on [Ten11].

5.5.2 Line-Ratio Technique

Radiative transitions in an atom are a result of an excitation process mainly produced by the interaction between the atom and either an incident electron or photon [Hut05c]. The **Radiative processes** between bound and free-bound states of importance are generally:

1. An electron excited in an upper atomic level that decays spontaneously within the life time τ of the state into a lower level with the emission of a photon (spontaneous emission).

5. NONNEUTRAL PLASMA DIAGNOSTICS

2. The electron in the lower level absorbs a photon by a transition to an upper level (excitation).
3. The presence of radiation induces the decay of an electron excited in an upper atomic level to a lower one (stimulated decay).
4. An incident photon ejects one or more electrons from an atom (photoionization).
5. An incident electron is captured by an ion emitting a photon (radiative recombination).

The probabilities of these radiative transitions are given by the Einstein coefficients.

The **collisional processes** induced by electron collisions are:

1. An incident electron excites a bound electron in an upper atomic level (electron impact excitation).
2. An incident electron deexcites an electron in an upper atomic level into a lower level with the emission of a photon (impact deexcitation).
3. An incident electron ejects an electron from an atom (impact ionization).
4. Two electrons interacting near an ion resulting in a recombination of one electron onto the ion, with the third particle carrying away the resulting energy (three-body recombination) [Pla].
5. An atom captures an electron into an upper energy level while using the electron's energy loss to excite another electron into an upper atomic level (dielectronic recombination).
6. An atom emits an electron from an excited atomic level (autoionization).

Especially the radiative processes occur in a plasma state of LTE while the nonneutral plasma is assumed to be in a coronal equilibrium. Therefore, the photon flux is a result of the first collisional process, i.e. the electron impact excitation and the first radiative process, i.e. the spontaneous decay. According to the coronal model (see section 2.3.2.2), the photon flux of a line transition is described by

$$\Phi_{ij} = n_e n_0 \int_0^\infty Q_{(ij)}(E) f(E) \left(\frac{2E}{m_e} \right)^{\frac{1}{2}} dE \quad (5.11)$$

5.5 Electron Temperature Measurement

with an assumed electron energy distribution function $f(E)$ characterized by a Maxwellian distribution

$$f(E, T_e) = \frac{2\sqrt{E}}{\sqrt{\pi} (kT_e)^{3/2}} \exp\left(-\frac{E}{kT_e}\right) \quad (5.12)$$

allows the measurement of the electron temperature if the electron density is known. For simplicity, it is common practice to use the line ratio of two emission lines, which is only dependent on the electron temperature and no longer on the electron density [BLD04]:

$$\frac{\Phi_{ij}^{Obs}}{\Phi_{ab}^{Obs}} = \frac{\int_{E_1}^{\infty} Q_{ij} \exp[-E/kT_e] E dE}{\int_{E_2}^{\infty} Q_{ab} \exp[-E/kT_e] E dE} \quad (5.13)$$

E_1 and E_2 are the energy thresholds for the regarded line transitions. The electron temperature is measured using two emission lines from different excited states.

However, not every line transition is suitable for the electron temperature measurement, necessitating a careful examination of the emission lines. A list of possible helium line transitions is presented in table 5.1. Referring to R. F. Boivin et al. [BLB⁺07], transitions ending at the ground state 1^1S and at metastable levels 2^1S and 2^3S will not be considered since the plasma is not optically thin with respect to these transitions and the resulting intensities are strongly affected by re-absorption. Moreover, it is said to be advisable to avoid $D \rightarrow P$ transitions because their energy transfer cross sections are large and also inversely proportional to the energy difference between the levels. Furthermore, the line ratio of the selected transitions should be as dependent as possible on the temperature, as well as being as least dependent as possible on the electron density. However, the $D \rightarrow P$ transitions are strongly dependent on the electron density and therefore inappropriate for a temperature determination.

In order to proof the applicability of the presented line-ratio technique within the scope of this thesis, the measurement of optical-emission cross sections was performed and will be discussed in the following paragraph. Besides the determination of optical-emission cross sections, the measurements allowed a comparison between the emission spectra produced by the incident electron beam on the gas target and the nonneutral plasma emission.

Figure 5.23 illustrates the emission spectra of helium excited by an electron beam

5. NONNEUTRAL PLASMA DIAGNOSTICS

transition	wavelength [nm]	applicability	energy threshold E [eV]
$6^1\text{S} \rightarrow 2^1\text{P}$	417.0	yes	24.20
$5^1\text{S} \rightarrow 2^1\text{P}$	443.8	yes	24.01
$4^1\text{S} \rightarrow 2^1\text{P}$	504.8	yes	23.67
$3^1\text{S} \rightarrow 2^1\text{P}$	728.1	yes	22.91
$5^3\text{S} \rightarrow 2^3\text{P}$	412.0	yes	23.97
$4^3\text{S} \rightarrow 2^3\text{P}$	471.3	yes	23.59
$3^3\text{S} \rightarrow 2^3\text{P}$	706.5	yes	22.71
$6^3\text{D} \rightarrow 2^3\text{P}$	382.0	no	24.21
$5^3\text{D} \rightarrow 2^3\text{P}$	402.6	no	24.04
$4^3\text{D} \rightarrow 2^3\text{P}$	447.1	no	22.73
$6^1\text{D} \rightarrow 2^1\text{P}$	414.4	no	24.21
$5^1\text{D} \rightarrow 2^1\text{P}$	438.7	no	24.04
$4^1\text{D} \rightarrow 2^1\text{P}$	492.2	no	22.73
$3^1\text{D} \rightarrow 2^1\text{P}$	667.8	no	23.07
$4^1\text{P} \rightarrow 2^1\text{S}$	396.5	no, metastable	23.74
$3^1\text{P} \rightarrow 2^1\text{S}$	501.6	no, metastable	23.08

Table 5.1: Helium line transitions and their applicability to the temperature determination by the presented line-ratio technique.

($W_b=82$ eV, $I_b=4.6$ μA , $\Delta t=1200$ s) and by the confined electron cloud within the Gabor lens ($\Phi_A=4$ kV, $B_z=4$ mT, $\Delta t=10$ s).

In the case of the spectrum produced by the incident electron beam, one can assume that the levels are populated by electron impact and radiative decay solely. The comparison of the emission spectra shows a good agreement of the intensity and accordingly the level population, only for specific transition of the singulett system like $5^1\text{S} \rightarrow 2^1\text{P}$ (443.8 nm), $4^1\text{S} \rightarrow 2^1\text{P}$ (504.8 nm) and $3^1\text{S} \rightarrow 2^1\text{P}$ (728.1 nm). The popular yellow line of helium (587.5 nm), which was first observed in the spectrum of the sun during the solar eclipse of 1868 [Lan00], is completely underrepresented by the emission spectrum produced by the beam.

In existing publications that considered the application of electron impact excitation cross section from ground state combined with the branching ratios, the line ratio of transitions in the same spectral region and with similar branching ratios were chosen for

5.5 Electron Temperature Measurement

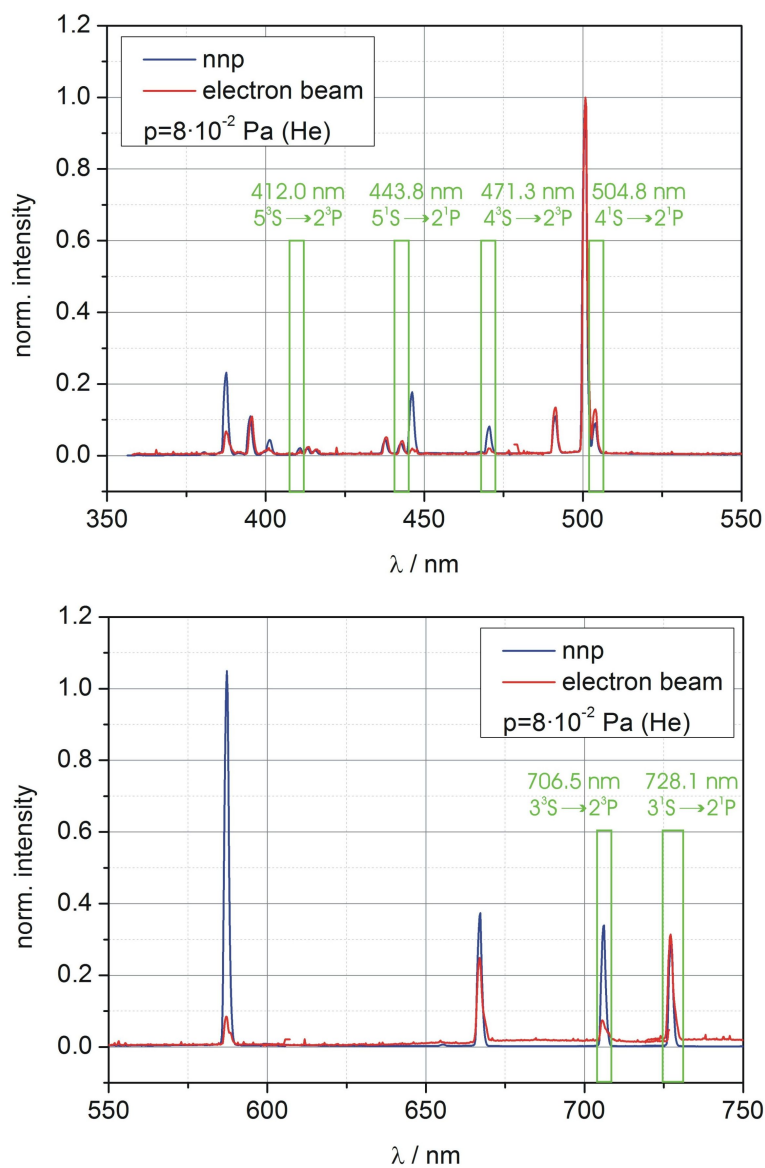


Figure 5.23: Comparison of emission spectra of helium excited by an electron beam ($W_b=82$ eV, $I_b=4.6$ μ A, $\Delta t=1200$ s) and by the confined electron cloud within the Gabor lens ($\Phi_A=4$ kV, $B_z=4$ mT, $\Delta t=10$ s).

the sake of simplicity (see [BLB⁺07],[Chr99]). Since the optical-emission cross section Q_{ij} includes the branching ratio

$$Q_{ij}(E) = \frac{A_{ij}}{\sum_{l<i} A_{il}} Q_i^{app}(E) \quad (5.14)$$

5. NONNEUTRAL PLASMA DIAGNOSTICS

one may overcome this limitation and compare any suitable line transitions.

The comparison of emission spectra in figure 5.23 provides a clear evidence for the choice of appropriate emission lines, i.e. those that are populated in the same way as in the emission spectrum excited by the incident beam. Given that the intensity of the transition 443.8 nm is quite low, the transitions 728.1 nm and 504.8 nm were chosen for the electron temperature measurement.

5.5.3 The Optical-Emission Cross Sections

In physics, a wide range of measured cross sections are used for different applications. However, the knowledge of excitation cross sections are of particular interest for the description and modeling of laboratory and astrophysical plasmas.

The excitation cross sections are subdivided into the direct electron-impact excitation, the apparent and the optical-emission cross section. Therefore, one can speak of many different types of cross sections that can lead to some confusion with respect to their right distinction and application especially in plasma diagnostics [BLD04].

During the past 100 years, many authors have described the excitation of helium due to electron collision. In this context, it is important to highlight the work of J. H. Lees [Lee32] in 1932 and R. M. St. John et al. [JML64] in 1964, who presented a complete measurement of absolute excitation functions for all transitions of helium as a function of the electron energy. In 1980, B. Van Zyl et al. [ZDCH80] performed a benchmarking of electron excitation cross section for particular atomic transitions and incident electron energies.

Despite the great number of publications in this field, uncertainties remained concerning the kind of cross section presented. Furthermore, the database of cross sections for electron energies above 200 eV was insufficient and the influence of the target gas pressure in terms of radiation trapping on the results remained unclear.

An additional experiment has been prepared to further investigate atomic excitation processes as a result of electron collisions and to expand the database of optical-emission cross sections particularly for higher electron beam energies. Optical-emission cross sections for all visible transitions of the helium atom were measured and applied to the determination of the electron temperature of the confined nonneutral plasma using the presented line-ratio technique.

The measurement of the helium excitation by an incident electron beam, followed by

the detection of the nonneutral plasma emission by the same optical system, allowed the direct comparison of the different excitation processes despite possible calibration errors.

In this section, the optical method is introduced and the experimental set-up to measure excitation cross sections is described. Furthermore, the results of the cross section measurements and the related nonneutral plasma diagnostic are subsequently presented.

5.5.4 Basic Principles

The excitation of an atom or ion from the ground state into an upper level by a collision with an electron is described by the direct electron-impact excitation cross section, while the optical-emission cross section represents the decay of the excited state for a given transition [FLAM94a]. The direct cross section Q_i^d can be expressed by

$$Q_i^d = \sum_j Q_{ij} - \sum_k Q_{ki} \quad (5.15)$$

where the optical-emission cross section is defined as

$$Q_{ij} = \frac{\Phi_{ij}(E)}{n_0 \cdot (I(E)/e)} \quad (5.16)$$

Φ_{ij} is the measured photon emission rate per unit beam length, $I(E)$ the measured electron current and n_0 the target gas density.

The apparent cross section is the sum of the optical-emission cross sections over all possible decay channels from the excited state:

$$Q_i^{app} = \sum_j Q_{ij} \quad (5.17)$$

Furthermore, the apparent cross section also includes a contribution from electron-impact excitation into higher levels, in addition to the cascade contribution given by depopulation of the excited state by photon decay:

$$Q_i^{app} = Q_i^d + \sum_k Q_{ki} \quad (5.18)$$

Figure 5.24 represents the different atomic excitation and deexcitation process related to the different kinds of cross sections. Emphasis was placed on the measurement of the optical-emission cross section using the optical method.

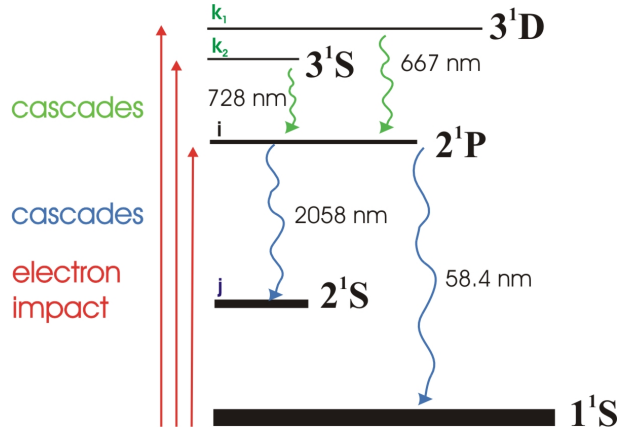


Figure 5.24: Population of atomic levels by electron impact and the cascade contribution from upper levels.

5.5.5 The Optical Method

Referring to A. R. Filippelli et al. [FLAM94b], there are two different ways to measure excitation cross sections: Through the *energy loss method*, it is possible to measure the angular distribution of scatter electrons passing a gas target that have lost energy corresponding to an internal excitation of the target atom. The *optical method* relates the intensity of the decay radiation to the cross section for production of the excited state by the collision process.

Within the scope of this thesis, the optical method was used to determine the optical-emission cross sections. Figure 5.25 represents a scheme of the cross section measurement.

A mono-energetic electron beam passes a target gas (helium in the discussed case) and the resulting radiation due to the depopulation of excited atomic states is detected.

To apply the optical method, three basic assumptions must be valid [FLAM94b]:

1. The atoms are excited by the incident electron beam solely. This can be verified by demonstrating that the intensity is proportional to the target gas number density (accordingly the target gas pressure) and to the beam current.
2. The emitting region shall only be slightly larger than the electron beam to ensure that the relation between the emitting atoms and colliding electrons remains constant within the observation region.

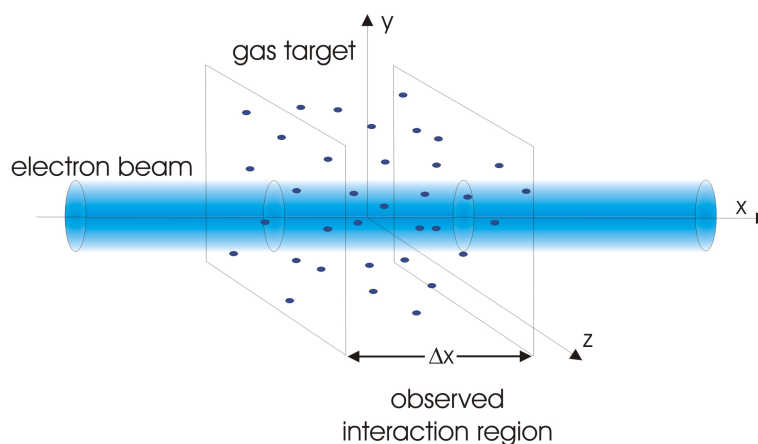


Figure 5.25: Scheme of the optical-emission cross section measurement.

3. The gas pressure has to be low enough that radiation trapping has a negligible effect on the intensities and their spatial distribution.

Since the ratio of photons, electrons and residual gas atoms is required to determine the optical-emission cross section, the intensity measurement must undergo particularly careful examination.

The measurement techniques and related problems in the determination of the correct number of emitted particles will be discussed in the following paragraphs.

5.5.6 Experimental Set-Up

The experimental set-up for the cross section measurement consists of a volume type source to generate and extract the electron beam and a solenoid to match the beam into the interaction region, which comprises a gas filled vacuum vessel, a Faraday cup (FDC) to measure the electron current, a borosilicate window for the optical investigation and an energy detector to evaluate the electron energy and its distribution function. Figure 5.26 shows a scheme and photograph of the cross section experiment.

5.5.6.1 Electron Source and Beam Current Measurement

To generate the electron beam, the plasma chamber of the volume type source (see 5.27) is filled with helium as residual gas at a pressure of typically $p=7.2$ Pa.

Electrons that are produced by an heated filament are accelerated towards the positively charged wall of the plasma chamber. In order to reach an effective ionization of

5. NONNEUTRAL PLASMA DIAGNOSTICS

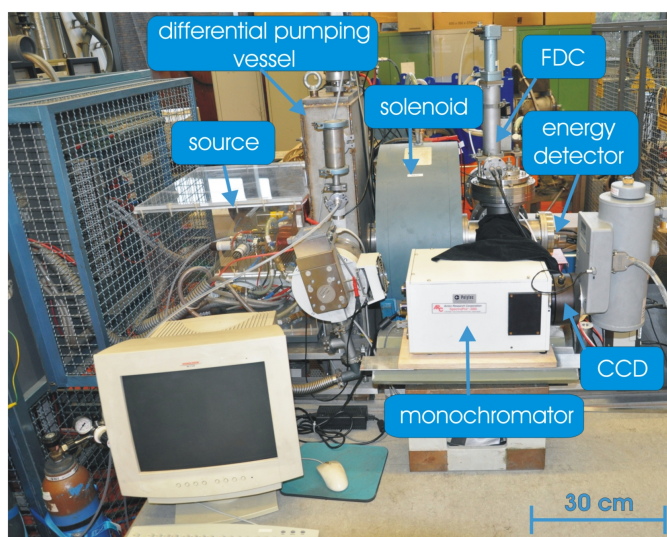
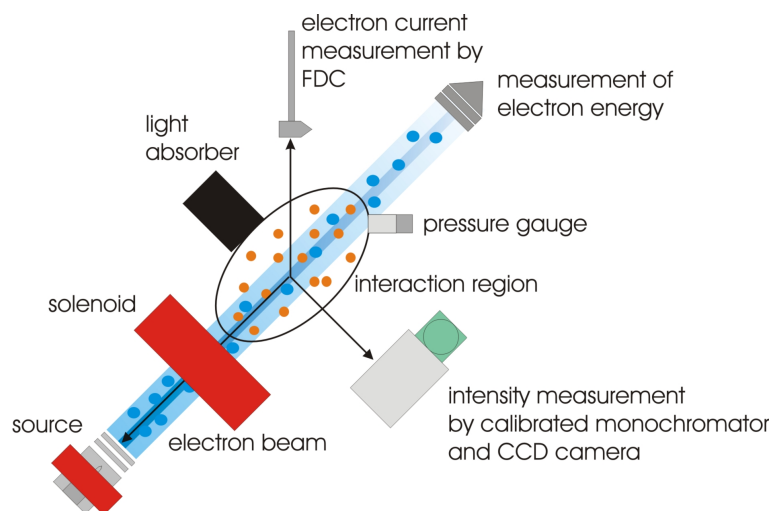


Figure 5.26: Scheme (top) and photograph (bottom) of the cross section experiment.

the gas, the trajectories of the electrons are extended by the magnetic field of a solenoid surrounding the plasma chamber. The illustrated filter and bending magnet was not used in this case. Subsequently, the generated plasma electrons are accelerated within the potential between the extraction and the ground electrode while the screening is kept at potential slightly lower (20 V) than the extraction potential. Maximum electron energies of around 1830 eV and currents in the range of 5 to 500 μA were achieved.

The beam current and consequently the number density of incident electrons was measured directly in the observed interaction region by a movable Faraday cup with an

5.5 Electron Temperature Measurement

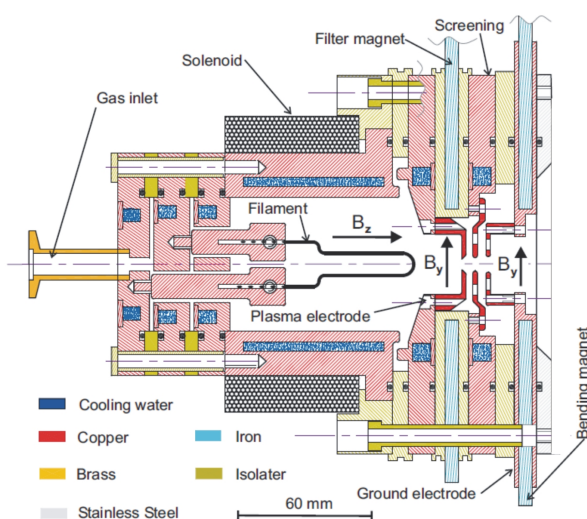


Figure 5.27: Scheme of the volume type source used to generate the electron beam [Gab08].

aperture of 3 cm and a maximum depth of 3.3 cm (see figure 5.28).

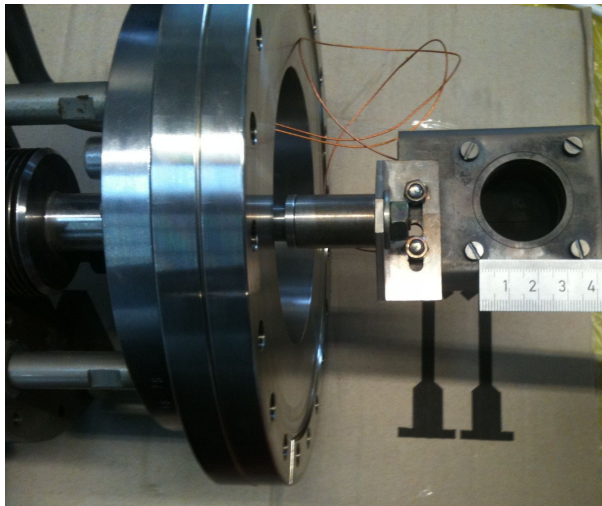


Figure 5.28: Picture of the movable Faraday cup in order to detect the electron beam current in the interaction region.

The electron current was also measured by the repelling electrode at the entrance of the Faraday cup considering scattered and back scattered electrons. Both the FDC and the repelling electrode were connected to a pico amperemeter (Keithley No. 6485) in order to precisely measure the current. For this reason, the current used in the determination

5. NONNEUTRAL PLASMA DIAGNOSTICS

of the optical-emission cross is given by the total current:

$$I_{tot} = I_{FDC} + I_{rep} \quad (5.19)$$

5.5.6.2 Electron Energy

The energy of the electron beam does not necessarily correspond to an externally applied voltage. According to [FLAM94c], contact potential differences between dissimilar metal conjunctions and dielectric films from pump oil contamination on the source elements that become charged under electron impact cause a shift in the beam energy. Therefore, an independent determination of the electron beam energy is useful.

The energy shift can be defined by the voltage difference at threshold for an optical transition of the gas target [FLAM94c]. These transitions are found to be in the region of around 20 eV to 23 eV for helium. Owing to the low electron currents in this particular energy region, it was not possible to record a sufficient intensity signal and consequently another measurement method was used.

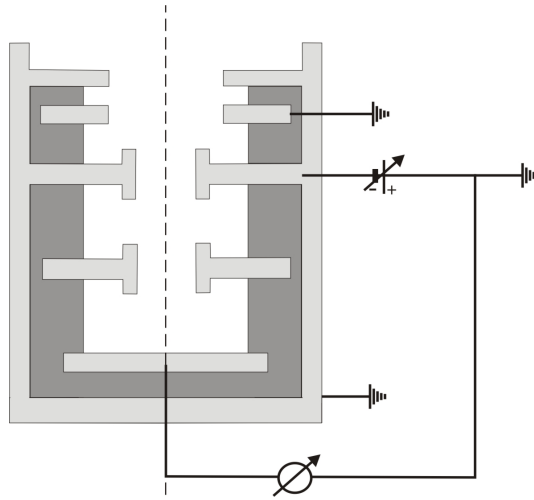


Figure 5.29: Scheme of the used energy detector to determine the electron energy distribution.

The energy distribution of the extracted electron beam was measured with an energy detector installed at the end of the beam line immediately after the observed interaction region. The energy detector consists of two cylindrical electrodes and a collector (see figure 5.29). While the first electrode is kept on ground potential, a negative voltage is applied to the second electrode to retard electrons (retarding field method). The

5.5 Electron Temperature Measurement

electron current is measured by the collector. By increasing the negative voltage of the filter electrode, the measured electron current drops down to zero if the applied potential is higher than the electron energy. The measured current is the sum of all particles with an energy above the limiting energy. From the derivation dI/dU , it is possible to calculate the energy distribution of the beam [Sch86]. Figure 5.30 illustrates the detection scheme and analysis of the electron energy distribution on the basis of a measured example.

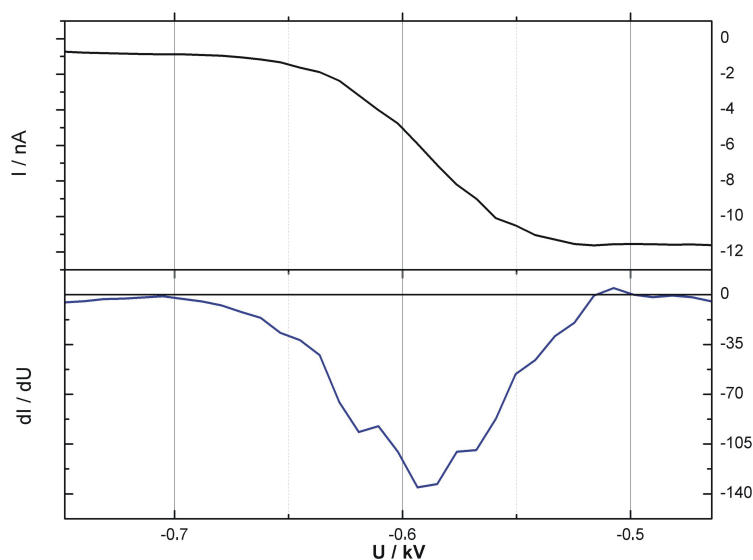


Figure 5.30: Measured electron current (top) and derivative of the current (bottom) as a function of the stopping potential.

In order to determine the mean electron energy, a from the software Origin 8.5 predefined Gaussian function

$$y = y_0 + \frac{A}{w\sqrt{\pi/2}} e^{-\frac{2(x-x_c)^2}{w^2}} \quad (5.20)$$

was fitted to the measured data points. x_c represents the center of the peak and hence the mean electron energy.

Simulations for a monoenergetic electron beam concerning the precision of the detector and the evaluation of measurement technique predict a deviation of 21% from the expected value. In figure 5.31, the comparison of the expected energy value, the measurement and the simulation as a function of the extraction voltage is presented.

However, the measurements could not confirm this result and show a much better agreement with the expected energy value of the beam for high beam energies. Unfortunately,

5. NONNEUTRAL PLASMA DIAGNOSTICS

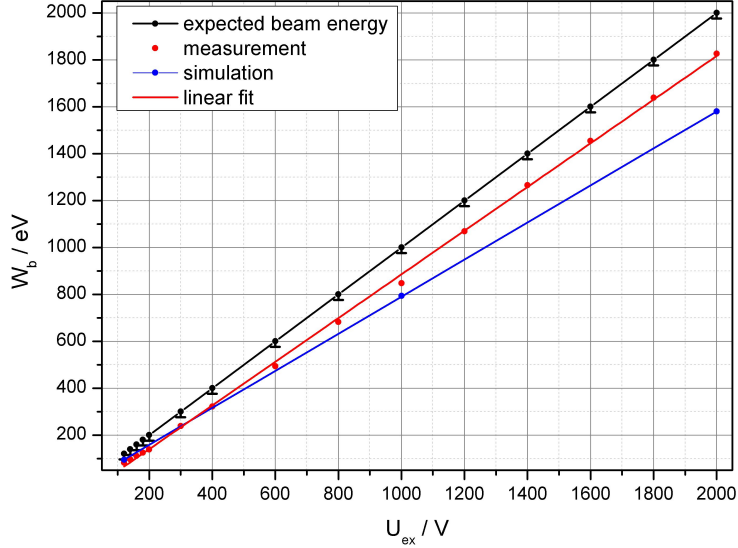


Figure 5.31: Comparison of the expected beam energy, the measurement and the simulation as a function of the extraction voltage.

the greatest uncertainty occurs in the low energy region that might result from a larger beam radius compared to the radius of the beam at higher electron energies. In [Sch86], it was demonstrated that a collimated beam improves the agreement with the predicted energy value.

Furthermore, the simulation predicts a widening of the electron energy distribution by the detector. Figure 5.32 shows the current of a monoenergetic electron beam as a function of the applied stopping potential and the resulting electron energy distribution analyzed by the previously explained method. The former monoenergetic beam with an energy of $W_b=120$ eV shows a widening of around 4 eV (3.33%), caused by the detector. For beam energies of $W_b=1000$ eV and $W_b=2000$ eV, the spread to be taken into account is in the same order of magnitude, namely 2.5% and 3.5%.

Nevertheless, the energy value obtained from the conventional retarding field method was used in the presented results. For sure a detailed analysis of the experimental method also in terms of the beam dynamics within the spectrometer remains to be done.

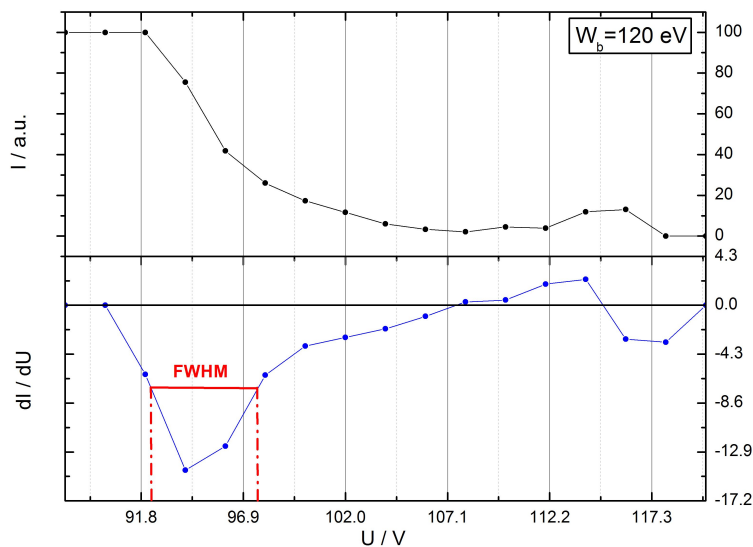


Figure 5.32: Simulated spread of the electron energy distribution caused by the detector.

5.5.6.3 Vacuum Chamber and Target Gas Density

A vacuum chamber with multiple ports for the Faraday cup, the light absorber, the pressure gauge, the borosilicate window for the photon flux measurement, and the energy detector was used. Good vacuum conditions are required to ensure that the background gas density has been reduced to a negligible level. Through a combined pumping system comprising a rotary vane and a turbomolecular pump, a final residual gas pressure of $p=2 \cdot 10^{-5}$ Pa in the vacuum chamber was reached.

Since the electron source was operated at a relatively high residual gas pressure of $p=7.2$ Pa, a differentially pumped vacuum vessel between source and solenoid was installed, allowing the adjustment of the pressure in the different sections almost independently. As a gas inlet for the high purity helium (He 5.0), a fine control valve was used and the pressure was controlled by a Pfeiffer Compact Full Range Gauge, type PKR251. The target gas was introduced to the vacuum chamber in the so-called *flowing mode operation* [FLAM94d]. There are usually two valves (one is partially closed) installed to provide a continuous flow into the vacuum chamber and out of the chamber. However, only one valve for the introduction of gas was used in the discussed experiment, assuming a constant pumping rate of the turbomolecular pump. To achieve a uniform gas density, the target gas was introduced at a location above the pump.

5. NONNEUTRAL PLASMA DIAGNOSTICS

Besides the helium pressure, the ambient temperature T_a was also recorded during the measurement, in order to calculate the correct number density n_0 using the ideal gas law

$$n_0 = \frac{N}{V} = \frac{p}{k_B T_a} \quad (5.21)$$

Note that the read pressure value has to be corrected for helium as residual gas according to figure 5.33.

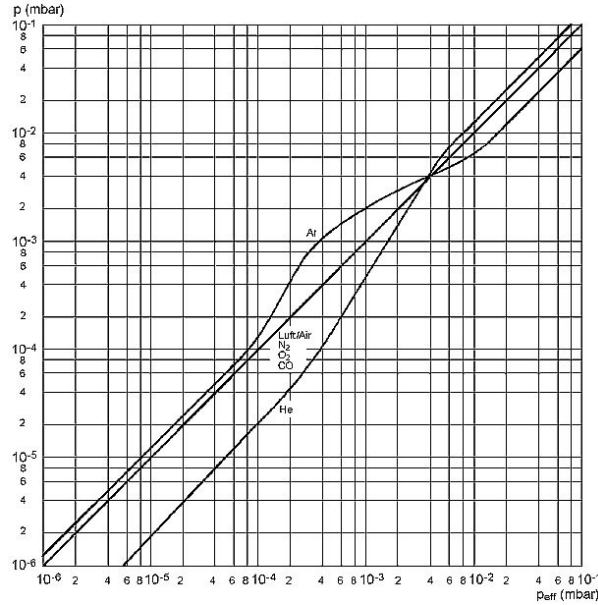


Figure 5.33: Conversion from displayed pressure to effective pressure by the Pfeiffer Compact Full Range Gauge type PKR251 (obtained from [Vaca]).

Only below a pressure of $p=10^{-3} \text{ Pa}=10^{-5} \text{ mbar}$ the residual gas pressure scales linear regarding the displayed value.

As previously mentioned in section 5.5.5, the target gas pressure must be kept below a certain threshold to avoid the influence of radiation trapping on the cross section measurement. Typically required target gas densities n_0 must be kept below 10^{20} m^{-3} , which was fulfilled for all presented experimental data with an average density of $n_0 = 2 \cdot 10^{19} \text{ m}^{-3}$ ($p=8 \cdot 10^{-2} \text{ Pa}$) at room temperature.

5.5.6.4 Photon Flux

The determination of the photon flux was the most challenging part of the measurement. In order to detect the absolute photon flux for specific transitions of helium, a calibration

5.5 Electron Temperature Measurement

of the optical system was performed.

Wavelength Calibration The wavelength calibration is a matter of the pixel number to wavelength assignment. This relation can be expressed by a first-order polynomial [Sch09]:

$$\lambda(n) = k_0 + n \cdot k_1 \quad (5.22)$$

In order to calibrate the system, a helium-neon laser that emits light of the wavelength 638.8 nm was used. The calibration procedure was subsequently performed by an internal software (WinSpec32 from Roper Scientific) of the camera.

The errors in calibration result in $\Delta\lambda_{100}=4.8$ nm for the grid 100 g/mm, $\Delta\lambda_{300}=2.5$ nm for the grid 300 g/mm and $\Delta\lambda_{1800}=0.3$ nm for the grid 1800 g/mm.

Absolute Intensity Calibration For the temperature measurement, the line-ratio technique requires at least a relative intensity calibration to compare levels with a large energetic gap. For the optical-emission cross section measurement, it was necessary to perform an absolute intensity calibration to obtain the total number of emitted photons for a given line transition.

The main objective of the calibration is the determination of the relation between the signal developed by the CCD sensor and the photon flux arriving at the detector. It is a common practice to use a radiance source such as a tungsten ribbon lamp that is employed in the visible and near infrared for calibration [FLAM94e]. The radiance of this lamp type is given by Planck's law, which is only dependent on the temperature T:

$$L(\lambda, T) = \epsilon(\lambda, T_t) \cdot \frac{2hc^2}{\lambda^5} \frac{1}{e^{\left(\frac{hc}{\lambda kT}\right)} - 1} \quad (5.23)$$

For the determination of the tungsten's temperature, a pyrometer (*Pyropto* from Hartmann & Braun) calibrated on a black body is used [Glu]. For this reason, it was not possible to detect the true temperature T_t but rather the black body temperature T_{BB} . The relation between true temperature and black temperature is given by

$$\frac{1}{T_t} = \frac{1}{T_{BB}} + \frac{\lambda k}{hc} \ln \epsilon(\lambda, T_t) \quad (5.24)$$

where ϵ is the emissivity.

Furthermore, the pyrometer is equipped with a red filter to measure the temperature

5. NONNEUTRAL PLASMA DIAGNOSTICS

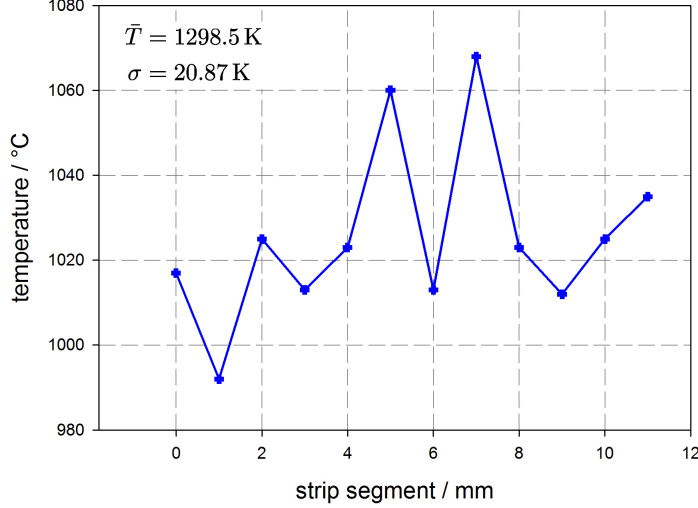


Figure 5.34: Measured temperature along the tungsten strip.

only at the given wavelength of $\lambda=650$ nm. However, the temperature may vary along the tungsten strip and was therefore determined at different positions (see figure 5.34). The error in the temperature measurement for different points along the tungsten strip is estimated by

$$\Delta T_{BB} = \sqrt{\left(\frac{\sigma}{\sqrt{(n)}}\right)^2 + \Delta N^2} = \sqrt{\left(\frac{20.87 \text{ K}}{\sqrt{(12)}}\right)^2 + (3 \text{ K})^2} \quad (5.25)$$

where n is the number of data points along the strip, σ the standard deviation of the measurement and ΔN the read-off accuracy. For the true temperature, the error is

$$\Delta T_t = \left| \frac{\partial T}{\partial T_{BB}} \right| \Delta T_{BB} = \left[\frac{1}{T_{BB}} + \frac{\lambda k}{hc} \ln \epsilon(\lambda, T_t) \right]^{-2} \frac{1}{T_{BB}^2} \cdot \Delta T_{BB} = 7.4 \text{ K} \quad (5.26)$$

The determined mean temperature along the strip was used to calculate the true temperature T_t from equation 5.24 to 1362.62 K with an assumed emissivity of $\epsilon=0.45$ at $\lambda=650$ nm.

Subsequently, the radiance for the true temperature of $T_t=1362.62$ K in the visible region can be calculated using Planck's law. Figure 5.35 represents the expected photon flux arriving at the CCD sensor.

The error in the radiance L shown in figure 5.35 is calculated to

$$\Delta L = \left| \frac{\partial L}{\partial T_t} \right| \Delta T_t \quad (5.27)$$

5.5 Electron Temperature Measurement

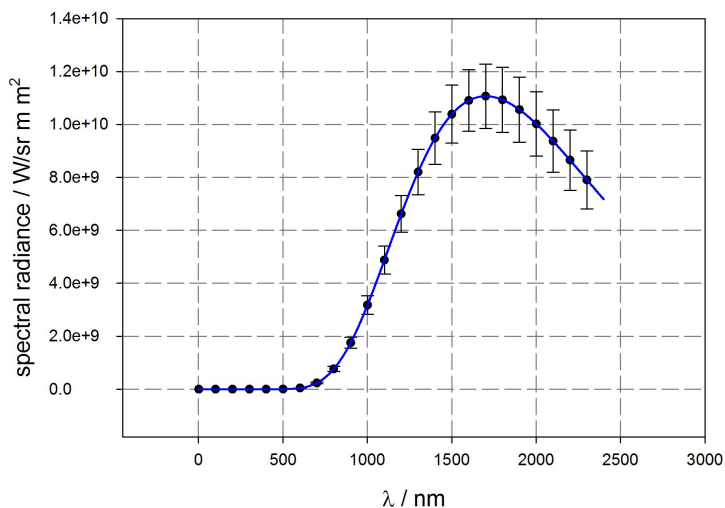


Figure 5.35: Spectral radiance L emitted by the tungsten strip lamp. The error bars result from an uncertainty in the temperature determination along the tungsten strip.

with

$$\frac{\partial L}{\partial T_t} = -\frac{2\pi h^2 c^3}{\lambda^6 k T_t^2} \cdot \epsilon(\lambda, T_t) \cdot \exp\left(-\frac{hc}{\lambda k T_t}\right) + \frac{2\pi h c^2}{\lambda^5} \cdot \exp\left(-\frac{hc}{\lambda k T_t}\right) \cdot \frac{\partial \epsilon(\lambda, T_t)}{\partial T_t} \quad (5.28)$$

The signal from the tungsten strip lamp developed by the CCD sensor for an exposure time of 10 s is shown in figure 5.36.

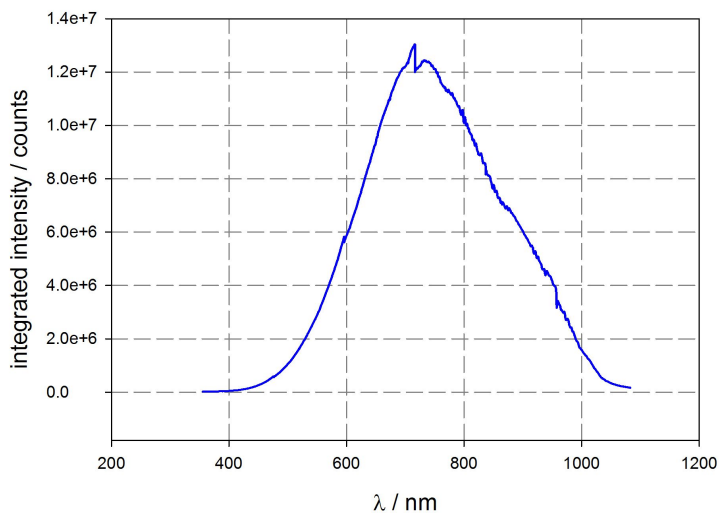


Figure 5.36: Signal of the tungsten strip lamp developed by the CCD sensor using the grid 300 g/mm of the monochromator.

5. NONNEUTRAL PLASMA DIAGNOSTICS

In particular for higher wavelengths the light signal is underestimated by the CCD sensor. From the determined Planck curve and the measured spectrum by the CCD sensor, it is possible to calculate a calibration factor K for each transition.

Since the spectral lines show a finite energy uncertainty, the integrated line intensity is used to determine the total number of emitted photons. Therefore, the calibration factor K for each transition had to be calculated according to following procedure:

The theoretically predicted Planck curve $L(\lambda, T)$ was integrated over the wavelength region (from λ_1 to λ_2) for the transition of interest:

$$L(\lambda_{ij,theo}) = \int_{\lambda_1}^{\lambda_2} L(\lambda, T) d\lambda \quad (5.29)$$

The unit is J/sm²sr.

The spectral radiance $L(\lambda_{ij,theo})$ is converted into the photon flux Φ by [Mil08]

$$\Phi = L(\lambda_{ij,theo}) \cdot \Omega \cdot A \quad (5.30)$$

whereas Ω is the solid angle and A the projected area. The photon flux has the unit J/s.

The solid angle Ω is determined by the entrance slit of the monochromator and the distance from the tungsten strip lamp, which also corresponds to the observed interaction region within the cross section measurement and can be calculated using the analytical expression derived by A. van Oosterom and J. Strackee [OS83]

$$\Omega = 4 \arctan \frac{w_x \cdot w_y}{2h \cdot \sqrt{4h^2 + w_x^2 + w_y^2}} \quad (5.31)$$

In the discussed case, $h=33.5$ cm represents the distance from the tungsten strip lamp to the slit, while $w_x=210 \mu\text{m}$ and $w_y=1.2$ cm represents the slit width and height. Figure 5.37 illustrates the spanned solid angle and the projected area on the CCD chip. The theoretical number of emitted photons n_{ph} results from dividing the photon flux Φ by the photon energy $E = h \cdot c/\lambda$ and multiplying it by the exposure time t of the calibration measurement

$$n_{ph} = \frac{\Phi \cdot t \cdot \lambda}{h \cdot c} \quad (5.32)$$

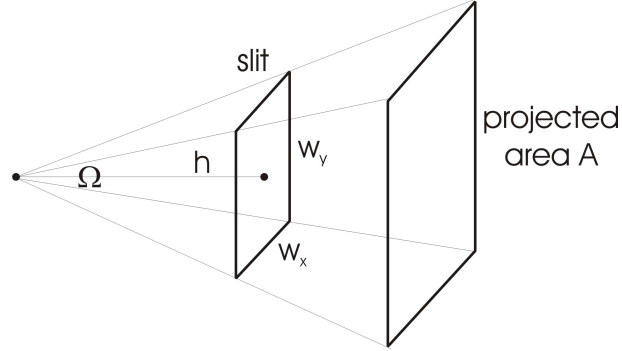


Figure 5.37: Illustration of the spanned solid angle and the projected area on the CCD chip.

The calibration factor K is now given by the ratio of the emitted photons n_{ph} and the actually measured count rate I_{ij}^{cal} that was also integrated over the wavelength region for the transition of interest.

$$K = \frac{n_{ph}}{I_{ij}^{cal}} \quad (5.33)$$

Besides the measured and integrated count rate I_{ij}^{exp} for a specific transition within an exposure time t , the observed beam length Δx and the transmission T_{ij} of the borosilicate window were also taken into account to further achieve a photon flux of a measured transition within the cross section experiment.

Considering the previously discussed calibration procedure, the optical-emission cross section can be calculated by

$$Q_{ij} = \frac{e \cdot K \cdot I_{ij}^{exp}}{In_0 \Delta x \cdot t \cdot T_{ij}} \quad (5.34)$$

The transmission of the borosilicate window for the visible region is specified by Pfeiffer Vacuum [Vacb] and illustrated in figure 5.38. The effective length of the beam from which radiation is collected, Δx , is calculated by

$$\Delta x = \frac{w_x}{M} \quad (5.35)$$

whereas w_x is the physical width of the entrance slit and M its magnification by the optical system [FLAM94f].

5. NONNEUTRAL PLASMA DIAGNOSTICS

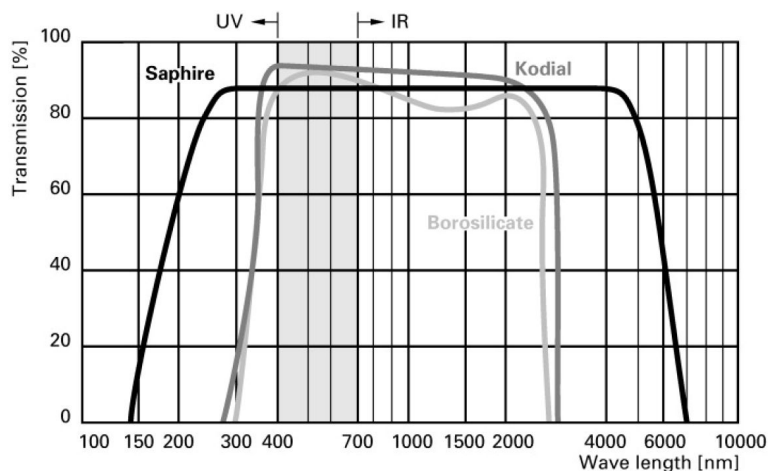


Figure 5.38: Transmission curve of the used borosilicate window as a function of the wavelength (obtained from [Vacb]).

The magnification M represents the ratio of physical width w_x of the slit and the measured width w_{CCD} of the slit by the CCD camera. Figure 5.39 shows a picture of the slit and its profile, from which the projected width of $w_{\text{CCD}}=445.36 \mu\text{m}$ was determined ($512 \text{ pixel} \approx 1.2 \text{ cm}$). The resulting magnification of the optical measurements for the presented results is $M=2.12$.

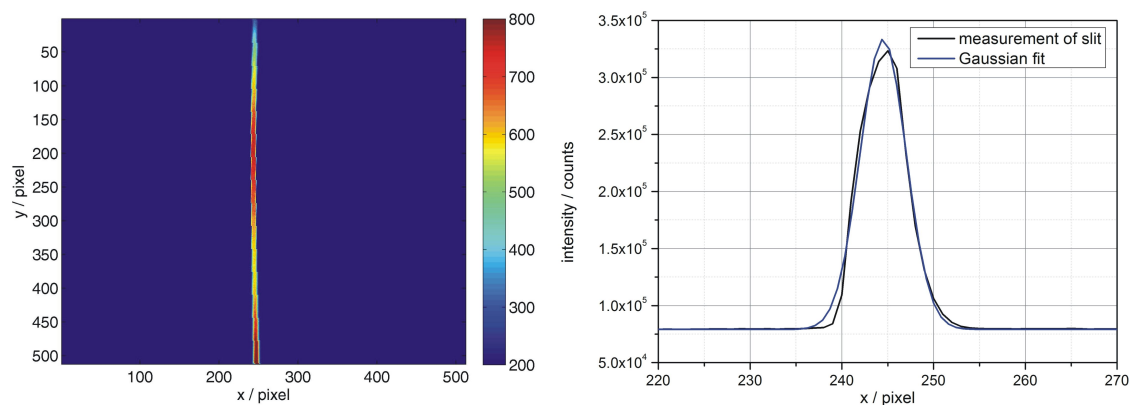


Figure 5.39: Measurement of the magnification of the optical system in order to determine the effective length Δx of the beam from which radiation is collected.

Given the low electron currents and target gas densities, the exposure times were increased up to 20 minutes per spectral slice for the grid 300 g/mm to achieve a sufficient signal-to-noise ratio. Furthermore, the exposures had to be corrected from the back-

5.5 Electron Temperature Measurement

ground emission of the tungsten filament of the electron source. The heated tungsten produced a background emission according to Planck's law, contaminating the optical measurements.

For every electron energy, four exposures at different central wavelength were needed to cover the whole visible spectrum. In order to limit the total time of the experiment to 30 hours, a background picture was not taken for every measurement point. Therefore, it was necessary to ensure that the background did not change during the experiment. Figure 5.40 shows the average intensity for every spectral region as a function of time.

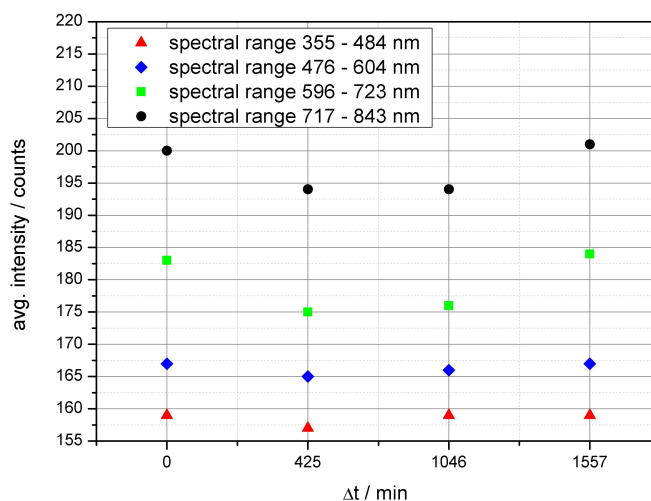


Figure 5.40: Background measurement for different spectral regions as a function of time.

It becomes apparent that there are only minor changes in intensity and hence it is reasonable to state that the background remained constant during the measurement.

Other requirements for the application of the optical method are the proportionality of the intensity to the beam current and the target gas pressure.

Figure 5.41 shows the results of the previously performed experiments to verify that the atoms are solely excited by the incident electron beam and clearly show the required proportionality for the transitions used in the temperature measurement. However, there are also some emission lines, e.g. 501 nm and 396 nm that deviate from the proportionality and show a pressure dependency (see figure 5.42). The pressure dependency is associated with the resonant absorption of emissions from resonance levels and is generally assumed to have a negligible influence on the emissions from non-resonant levels [BLD04].

5. NONNEUTRAL PLASMA DIAGNOSTICS

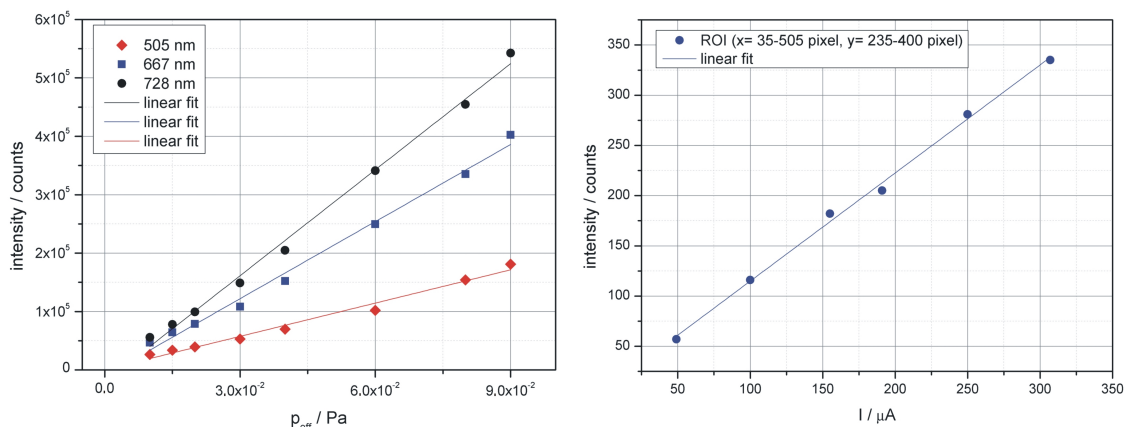


Figure 5.41: Proportionality of the intensity to the beam current and the target gas pressure.

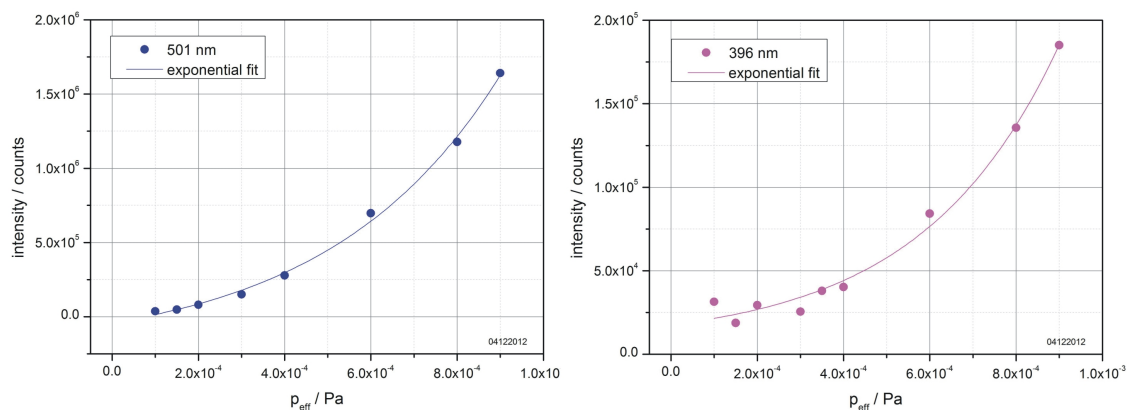


Figure 5.42: Examples of the measured pressure dependence of emission lines for selected levels of He.

The final requirement, namely that the detected part of the beam is only slightly larger than the emitting region, could not strictly be fulfilled. Figure 5.43 shows some examples of the measured beam profile as a function of its energy and for different settings of the solenoid.

The beam could not be aligned precisely during the measurement series and it is clearly evident that the beam shows a variation in its diameter, as well as the y-position of the exposure. In order to keep the region of interest (ROI) for all measurements constant, the total CCD array was analyzed for the intensity determination.

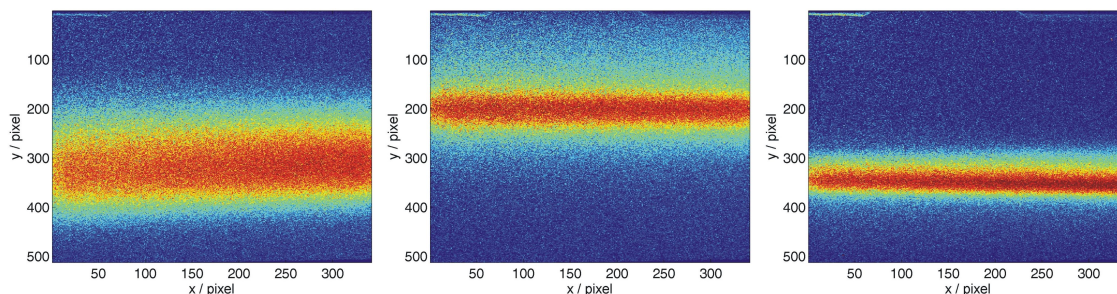


Figure 5.43: Example of the change in beam size and position for different energies ($W_{b,1}=125$ eV, $W_{b,2}=238$ eV and $W_{b,3}=1069$ eV) and settings of the magnetic field ($B_{z,1}=0.7$ mT, $B_{z,2}=1$ mT and $B_{z,3}=2$ mT) of the solenoid.

5.5.7 Results of the Optical-Emission Cross Section Measurement

The optical-emission cross sections for 9 transitions in the He-atom were measured with the experimental set-up shown in figure 5.26. The data was obtained at a pressure of $p=8 \cdot 10^{-2}$ Pa, in order that the target gas density was high enough to detect a sufficient intensity signal for exposure times of 20 minutes for every spectral range, yet low enough that pressure effects are negligible for almost all transitions in He (see figures 5.41 and 5.42). The electron current detected by a Faraday cup directly in the photographed interaction region varied from $4 \mu\text{A}$ at the lowest energy to around $530 \mu\text{A}$ for the highest energy. Figure 5.44 shows the results of the optical-emission cross section measurements for all transitions in He with sufficient intensity signal.

Given the main objective of the further performed optical-emission cross section measurement of obtaining data especially in the high energy region, the experimental resolution for the low energy region is too small to draw a conclusive comparison between the presented results and previously published work. Nevertheless, a deviation in the shape of the transitions into resonance levels (501 nm and 396 nm) in the energy region between 82 and 140 eV can be observed by comparing Graph A,C,D, or E to B in figure 5.44.

For a general evaluation of the obtained data, the benchmark cross sections measured by B. Van Zyl et al. [ZDCH80] were used. Based on the high accuracy of their experiment, it is possible to use these cross sections to calibrate the optical detection system of the cross section apparatus.

It is evident that the presented results only approximately agree with those of B. Van

5. NONNEUTRAL PLASMA DIAGNOSTICS

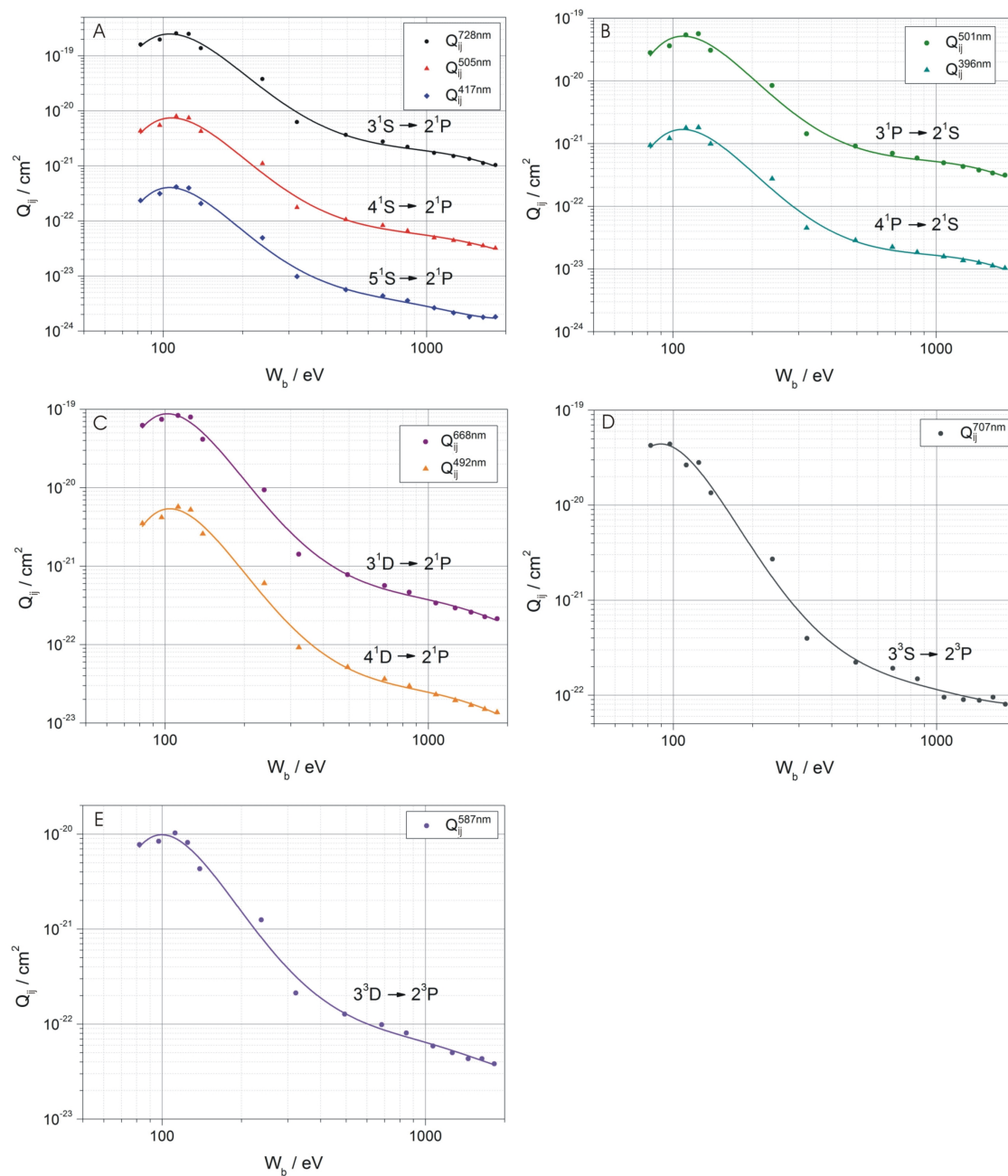


Figure 5.44: Families of optical-emission cross sections for (A) singlet S, (B) singlet P, (C) singlet D, (D) triplet S and (E) triplet D.

Zyl et al (see figure 5.45). At an electron energy of 100 eV the measured cross section value for the transition $3^1S \rightarrow 2^1P$ (728 nm) is $Q_{ij,exp}^{728nm} = 2.03 \cdot 10^{-19} \text{ cm}^2$, while the

5.5 Electron Temperature Measurement

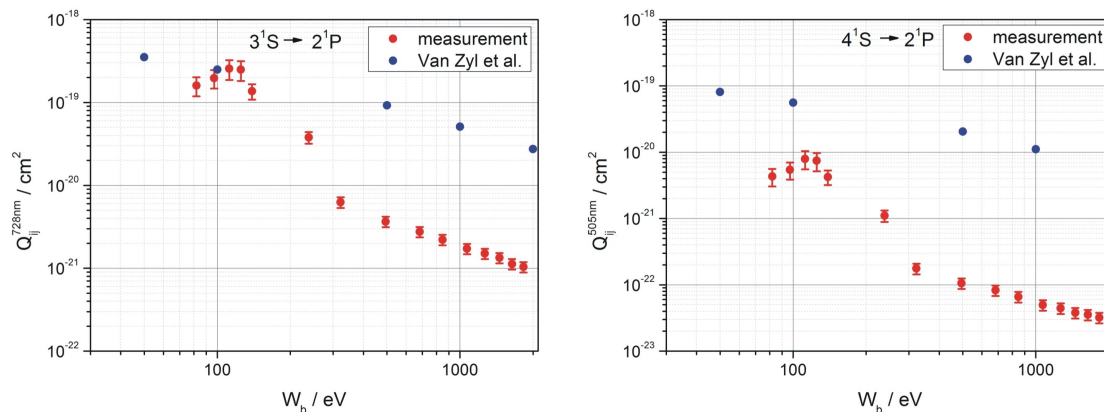


Figure 5.45: Comparison of measured optical-emission cross sections to benchmark cross sections by [ZDCH80].

stated value of B. Van Zyl et al. is $Q_{ij}^{728nm} = 2.44 \cdot 10^{-19} \text{ cm}^2$. The difference between these results amounts to 16.8%, which is quite good considering the deviating experimental methods.

However, at an electron energy of around 1830 eV the agreement is only 4% (while the difference is 96%), comparing $Q_{ij,exp}^{728nm} = 1.07 \cdot 10^{-21} \text{ cm}^2$ to $Q_{ij}^{728nm} = 2.75 \cdot 10^{-20} \text{ cm}^2$. Especially at the high energy region, the results of the optical-emission cross sections show a great variance.

Furthermore, the results also show an increased deviation in the lower spectral region: for the transition $4^1S \rightarrow 2^1P$ (505 nm), the cross section value at 100 eV is $Q_{ij,exp}^{505nm} = 5.44 \cdot 10^{-21} \text{ cm}^2$ in relation to $Q_{ij}^{505nm} = 5.6 \cdot 10^{-20} \text{ cm}^2$ presented by Van Zyl et al., with the difference amounting to 90.3%. For an electron beam energy of about 1830 eV, the deviation even increases to 99.4%, comparing $Q_{ij,exp}^{505nm} = 3.21 \cdot 10^{-23} \text{ cm}^2$ to $Q_{ij}^{505nm} = 5.83 \cdot 10^{-21} \text{ cm}^2$.

The variance at different spectral regions particularly indicates a major uncertainty in the intensity calibration.

5.5.7.1 Sources of Error

Despite great care being taken during the measurement, the tungsten strip lamp used was not a calibrated standard source. In this respect, it becomes difficult to estimate the error in the intensity measurement. The error in intensity calculated from the variation of the emission temperature of the tungsten strip lamp reaches $\Delta I_{505nm}^{exp} / I_{505nm}^{exp} = 16.8\%$

5. NONNEUTRAL PLASMA DIAGNOSTICS

for 505 nm and $\Delta I_{728\text{nm}}^{\text{exp}}/I_{728\text{nm}}^{\text{exp}}=13.1\%$ for 728 nm. The relative error in the target gas number density remains constant for all presented results at $\Delta n/n = 1.2\%$ and the absolute error in the current measurement amounts to $\Delta I = \pm 0.5 \mu\text{A}$. For a beam energy of 100 eV, the relative error in the cross section measurement for the transition $3^1\text{S} \rightarrow 2^1\text{P}$ is $\Delta Q_{728\text{nm}}^{\text{opt}}/Q_{728\text{nm}}^{\text{opt}} = 25.1\%$ and for the transition $4^1\text{S} \rightarrow 2^1\text{P}$ is $\Delta Q_{505\text{nm}}^{\text{opt}}/Q_{505\text{nm}}^{\text{opt}} = 28.9\%$.

In the context of the measurement accuracy, it was observed that the width of the electron energy distribution varies as a function of the beam energy, thus representing another source of error. Figure 5.46 shows the measured FWHM at different beam energies in absolute and relative units.

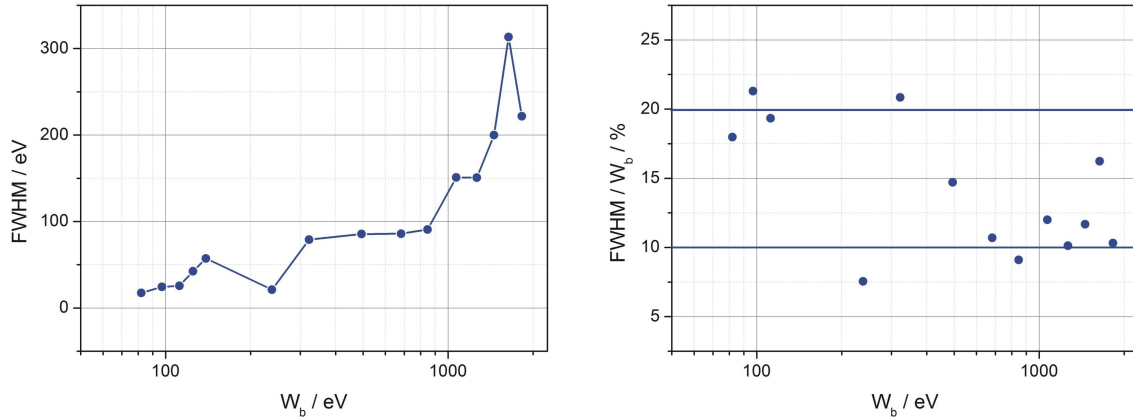


Figure 5.46: Measured spread of the electron energy distribution (FWHM) as a function of the beam energy in absolute (left) and relative units (right).

The FWHM amounts to 15-20%, although it is important to note that the detector already imprints a spread in the beam energy of 3.5%.

Even though the optical-emission cross sections contain uncertainties, they were used for the electron temperature determination for a straightforward verification of the experimental method. Because the measurement errors remain the same in both experiments, it is still possible to study the fundamental properties of both systems. Furthermore, the uncertainty in the absolute intensity value becomes negligible since intensity ratios are used.

5.5.8 Determination of the Nonneutral Plasma Temperature

To proof the line-ratio technique for the application to the nonneutral plasma in order to determine the electron temperature, the calibrated optical system was installed at the entrance of the prototype Gabor lens, right before the ground electrode and the plasma emission was frontally photographed through a borosilicate window (see figure 5.1). Given that the height of the entrance slit of the monochromator is 1.2 cm, only the core of the plasma cloud was detected.

In order to simplify the experiment, the same residual gas pressure of $p=8 \cdot 10^{-2}$ Pa (He) used during the optical-emission cross section measurement was chosen. The exposure time could be limited to 20 s per spectral range due to the high emission rate.

Figure 5.47 shows the results of the electron temperature measurement from the intensity ratio of the emission lines 728 nm and 505 nm.

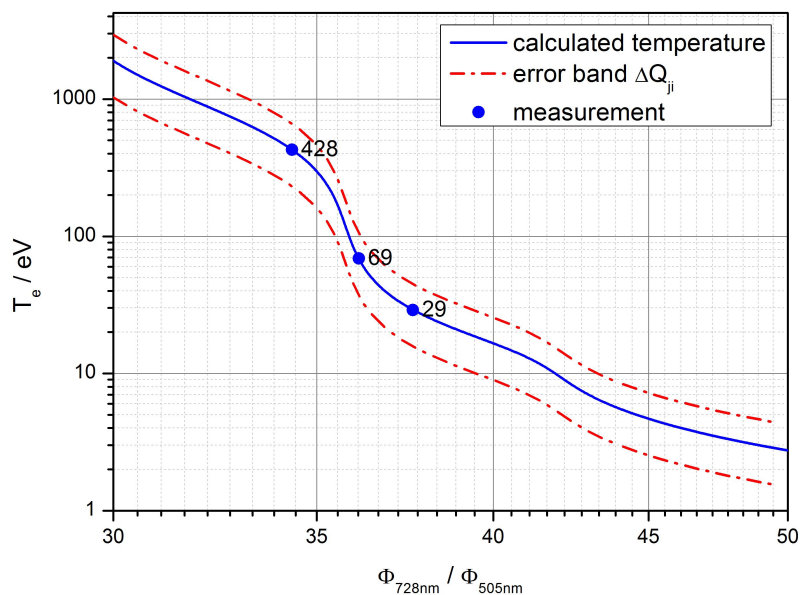


Figure 5.47: Electron temperature measurement by the line ratio-technique for emission lines 728 nm and 505 nm at a residual gas pressure of $p=8 \cdot 10^{-2}$ Pa (He).

Two of the three lens parameters were close to the operation function in order to ensure a homogeneous electron energy distribution in both planes, while one parameter setup was chosen to deviate from the operation function. The temperature 428 eV was measured for lens parameter settings far from the operation point for an anode poten-

5. NONNEUTRAL PLASMA DIAGNOSTICS

tial of $\Phi_A=3500$ V and a magnetic field of $B_z=4$ mT, while the temperature of 69 eV at $\Phi_A=2500$ V and $B_z=4.5$ mT, and the temperature of 29 eV at $\Phi_A=2000$ V and $B_z=4$ mT was measured for lens parameters close to the operation function.

The error band results from the error in the optical-emission cross section and represents an maximum error estimate. Furthermore, the maximum error in the intensity ratio amounts to almost 30%. However, it can be assumed that the errors in intensity underlie statistics and might at least partly compensate each other. Therefore, a sufficient number of measurements is required to estimate a realistic value.

Besides the electron temperature, the electron density was also determined for the claimed Gabor lens settings. Figure 5.48 shows the electron temperature and density as a function of the anode potential.

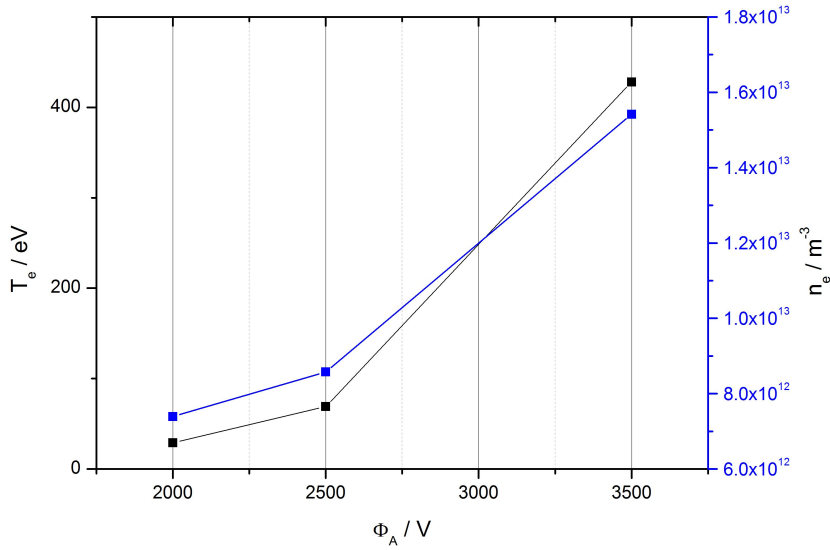


Figure 5.48: Measured electron temperature and density as a function of the anode potential.

Both values show the same tendency to grow with increasing anode potential, which is also represented by the theory (see section 2.4.2). By determining the most important nonneutral plasma parameters, it is possible to validate the numerical simulations that always suffered from the uncertainty in the electron production and losses. From the knowledge of electron density and temperature, one can estimate the order of magnitude of related parameters and further specify the dynamics of such a system in more detail.

5.5 Electron Temperature Measurement

Figure 5.49 shows the results of the plasma state simulations for the previously presented lens parameter settings using the code GABOR-M.

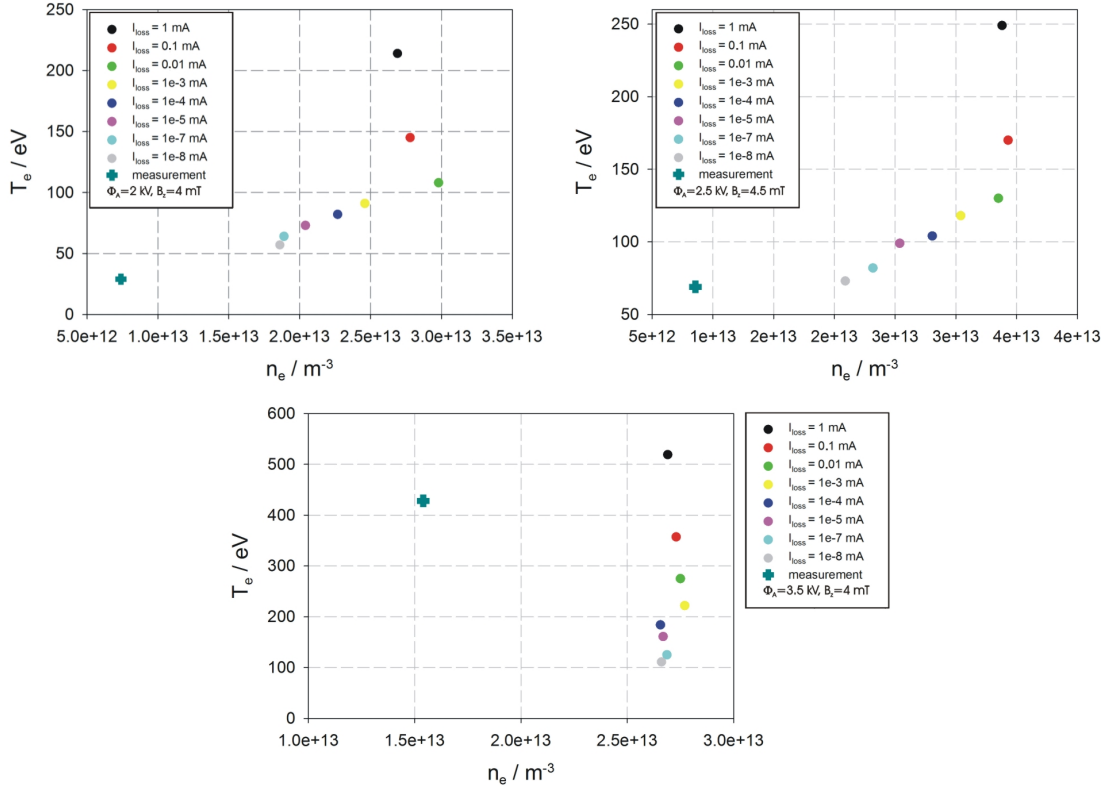


Figure 5.49: Simulation of the plasma state for different Gabor lens settings using the code GABOR-M.

In order to investigate the evolution of the equilibrium state with respect to electron density and temperature, the electron loss current was varied. For lens parameter settings close to the operation function, an approximation of the numerical to the experimental results for very low electron loss currents of 10 nA with a remaining offset in density are attained. Far away from the operation point, the results of the simulation and the experiment strongly differ.

The discussed measurements represent a proof-of-principle for the application of the line-ratio technique to the nonneutral plasma. Therefore, the method certainly has to be further investigated, especially concerning the measurement error and the pressure dependence. However, at present this demonstrates the first evidence of a tempera-

5. NONNEUTRAL PLASMA DIAGNOSTICS

ture determination applied to a nonneutral plasma by optical diagnostics. Despite the aforementioned measurement uncertainties, the line-ratio technique looks very promising and could open up a new possibility for the non-invasive temperature diagnostic of a nonneutral plasma.

6

Beam Transport Measurements at GSI

6.1	Experimental Set-Up	121
6.1.1	Multicusp Ion Source (MUCIS)	123
6.1.2	Slit-Grid Emittance Scanner	124
6.2	High-Voltage Conditioning and Commissioning of the Gabor Lens	125
6.3	Results of the Beam Transport Measurements and the Comparative Performed Nonneutral Plasma Diagnostics	128
6.3.1	Beam Transport Simulation	128
6.3.2	Emittance Dominated Beam Transport	129
6.3.3	Technical Issues	136
6.3.4	Space Charge Dominated Beam Transport	138
6.3.5	Summary	146

6.1 Experimental Set-Up

As a part of the planned FAIR project at GSI, the requirements of the existing High Current Injector (HSI) concerning brightness and intensity, especially of the delivered $^{238}\text{U}^{4+}$ -beam, will be more challenging [AHS10]. In particular, the transport of intense, i.e. space charge dominated, beams is a major challenge for the low energy beam transport section.

6. BEAM TRANSPORT MEASUREMENTS AT GSI

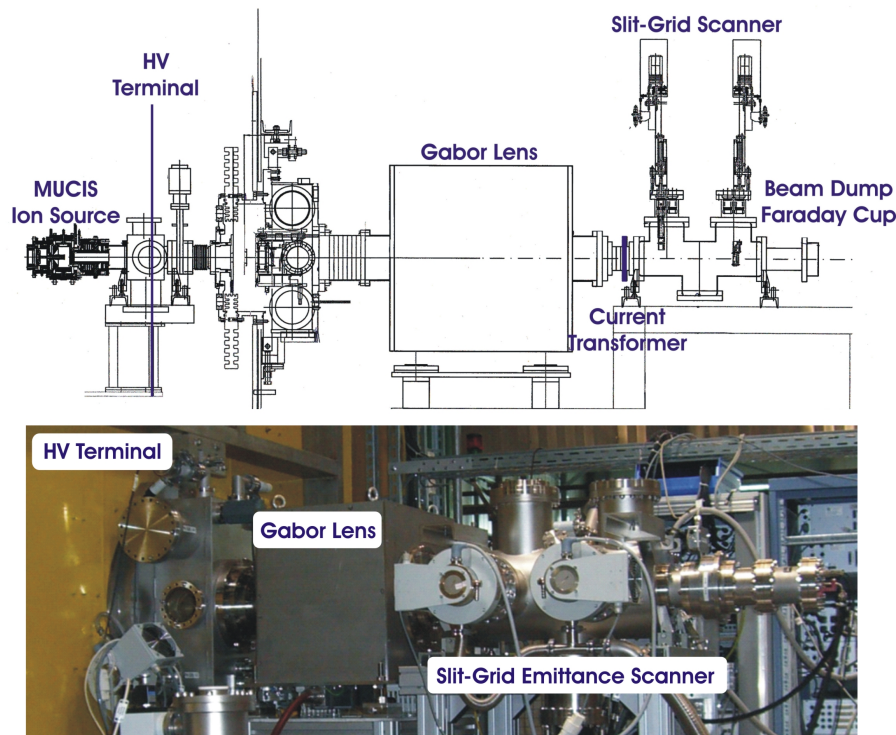


Figure 6.1: Scheme of the HOSTI beamline (not to scale, obtained from [HA]) and photograph of the experimental set-up.

The advantage of a Gabor lens compared to conventional focusing devices, i.e. quadrupol magnets, solenoids and electrostatic einzel lenses, is the controlled confinement of electrons within the beam potential. For this reason, the prototype lens was tested at the High Current Test Injector (HOSTI) at GSI to investigate the beam transport of an ion beam regarding beam radius, energy, pulsed beam operation and to acquire experience in a real accelerator environment.

The HOSTI is an exact copy of the terminal north, operative HSI, which is running at GSI [AHS10]. The scheme of the HOSTI beamline is shown in figure 6.1. The ion beam is provided by a MUCIS ion source with a 13 hole triode extraction system. The source was operated in 1 Hz mode with 1.25 ms pulse length. The extracted beam is subsequently accelerated up to its maximum energy by the installed post-acceleration system. The emittance of the ion beam was measured behind the Gabor lens with a slit-grid emittance scanner. Several other diagnostic tools are installed to measure the ion beam current along the beam line: a Faraday cup right after the extraction system

of the ion source, a current transformer right behind the Gabor lens, a small Faraday cup between slit and grid inside the vacuum chamber of the emittance scanner and, finally, a beam dump. Note that in the discussion of beam transport measurements, the claimed current is measured by the current transformer right behind the lens. The functional principle of the main components is described in the following sections.

6.1.1 Multicusp Ion Source (MUCIS)

The Multicusp ion source belongs to the filament driven ion sources with non-axial filament configuration and is presented in figure 6.2. Electrons are generated by ther-

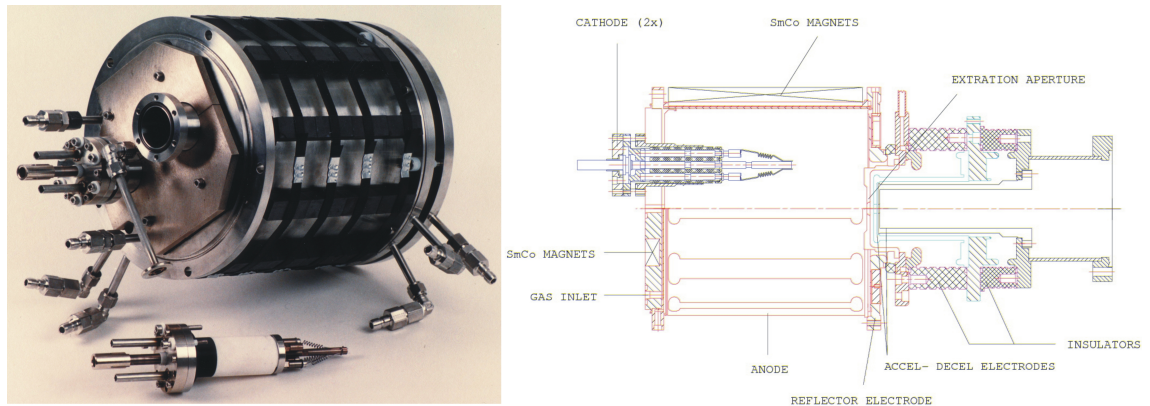


Figure 6.2: Photograph and scheme of the MUCIS ion source [HA].

moionic emission from up to 6 spiral tantalum filaments placed symmetrically relatively to the beam axis and accelerated towards the anode. On their way, they are able to produce more charge carriers by impact ionization.

The way of the electron within the plasma generator is extended by the multi-cusp field of the 60 SmCo permanent magnets (1.8 Tesla), forcing the particles on circular orbits. The beam is extracted by a triode system comprising a plasma, screening and ground electrode with 13 holes of 3 mm in diameter [AHS10]. The emission area is 0.92 cm^2 and the allowed extraction voltage up to 33 kV.

The MUCIS can essentially be used to generate all types of gaseous ions from light to heavy gases such as H_2 , D_2 , He, CH_4 , Ne, N_2 , Ar, Kr, and Xe. However, in the presented work, emphasis was placed on transport studies of He^+ and Ar^+ -beams.

6.1.2 Slit-Grid Emittance Scanner

The phase space distribution of the transported ion beam is measured by a slit-grid emittance scanner with one plane.

The measurement principle is as follows: a slit with the size of 80 mm x 0.1 mm is step-wise driven through the ion beam to mask the beam and only transmit one beamlet with a given spatial coordinate.

After a drift distance of 291 mm, the expanded beamlet hits the wires of the grid located behind the slit and produces a current signal that is detected. For every spatial coordinate, i.e. slit position, an intensity distribution as a function of the angle between beam axis, slit and grid is measured. This results in a phase space distribution from which the emittance is calculated [Pfi10].

Figure 6.3 shows a scheme of the emittance measurement by the slit-grid scanner. The

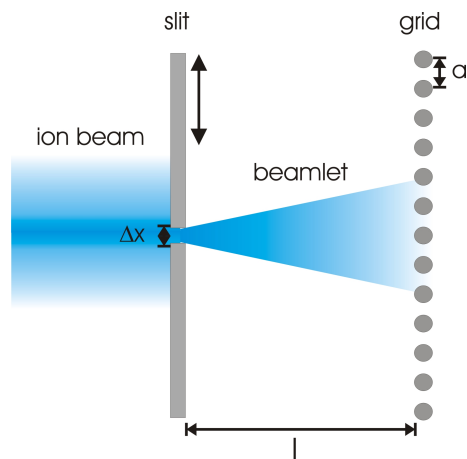


Figure 6.3: Scheme of emittance measurement.

error in the emittance measurement is described by

$$\Delta\epsilon = \Delta x \cdot \Delta x' \quad (6.1)$$

whereas Δx is the height of the slit.

The resolution of the emittance scanner due to the angle is particularly a function of the distance between the wires a , the distance l between slit and grid, as well as the number of used wires n [Sar94]:

$$\Delta x' = \frac{a}{(n+1) \cdot l} \quad (6.2)$$

6.2 High-Voltage Conditioning and Commissioning of the Gabor Lens

In the following results of the emittance measurement ($n=1$ and $n=3$), the resolution in angle is 1.4 mrad resp. 0.7 mrad. This corresponds to a measuring error in the emittance of $\Delta\epsilon_y=0.14$ mm mrad resp. $\Delta\epsilon_y=0.07$ mm mrad.

Owing to the pulsed beam operation, the emittance measurement was triggered. Due to operating conditions, the time frame of the measurement was $500 \mu\text{s}$ within the beam pulse, starting after $750 \mu\text{s}$ (see figure 6.4).

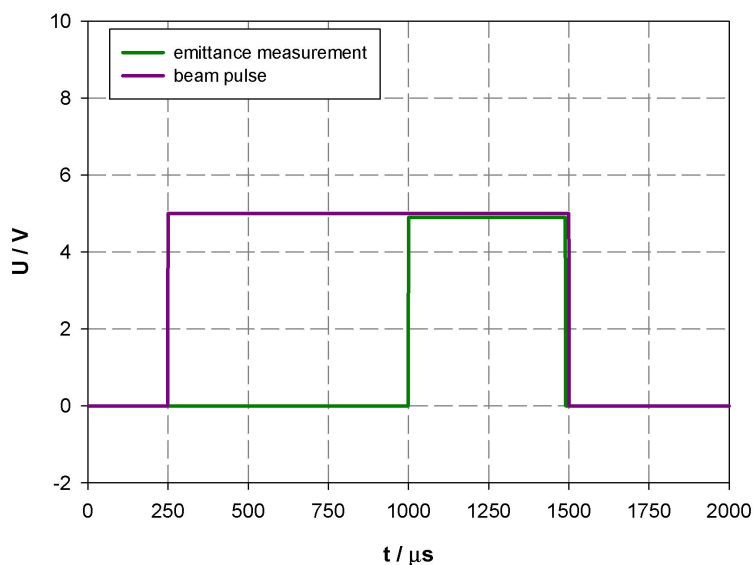


Figure 6.4: Time frame of emittance measurement within the beam pulse.

6.2 High-Voltage Conditioning and Commissioning of the Gabor Lens

Before the lens is put into operation, high-voltage conditioning is necessary to remove contaminations such as dust and moisture, as well as other imperfections, especially when the device is exposed to a new environment.

It is necessary to overcome the binding energy between particle and material, in order to remove the particles from the electrode surface. The binding energy depends on the type of binding (chemical or physical), the particle itself and the material of the surface [Kla13].

In the case of the Gabor lens, the loss electrons (as discussed in chapter 2) have enough

6. BEAM TRANSPORT MEASUREMENTS AT GSI

energy to overcome the binding energy between particle and surface. Therefore, the applied conditioning procedure for the Gabor lens is comparable to the usual high-voltage conditioning, whereby the voltage is increased until it sparks, but with the difference that the projectiles are provided by the already confined plasma cloud itself. This conditioning process can also be described as electron scrubbing [Mar80].

An example of the high-voltage conditioning procedure for the prototype Gabor lens is represented in figure 6.5. Referring to [Kla13], the increase in the current of the voltage

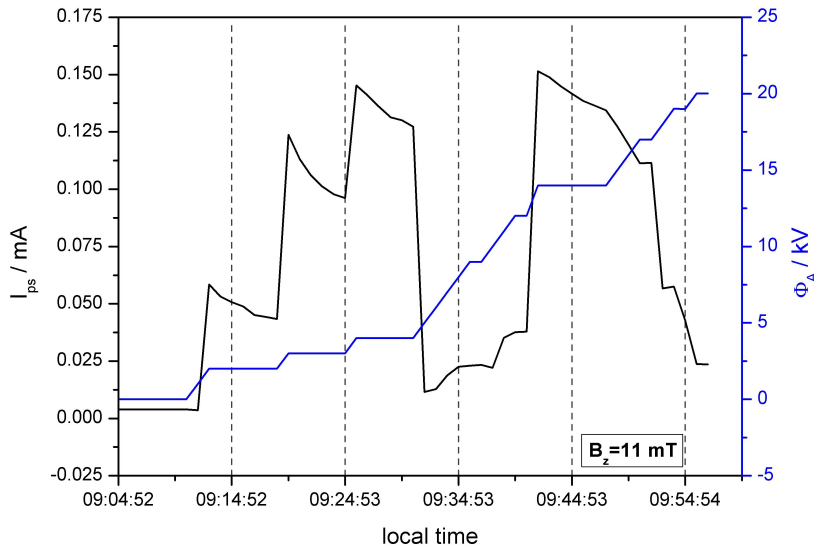


Figure 6.5: Example of the high-voltage conditioning procedure for the prototype Gabor lens. I_{ps} represents the displayed current of the power supply.

power supply can be explained by a growth of the production process in the plasma: in case of the Gabor lens, one can expect that CO is leaking from the electrodes and the Vinidur insulator by electron bombardment. The degassing of deposits leads to a higher electron production rate and consequently an increase in the current of the high voltage power supply. Another conclusive argument for an increased production rate is the correlation of the power supply current with the measured residual gas ion current emitted from the lens volume (see figure 6.6). After the increase of the current, it is necessary to wait for the system to relax prior to the voltage being further increased. Figure 6.7 shows how the final pressure and the maximum applied voltage developed during the conditioning phase and before the lens was transported to GSI. A maximum potential of $\Phi_A=30$ kV and a final pressure of $p=1.6 \cdot 10^{-5}$ Pa was reached. It is important

6.2 High-Voltage Conditioning and Commissioning of the Gabor Lens

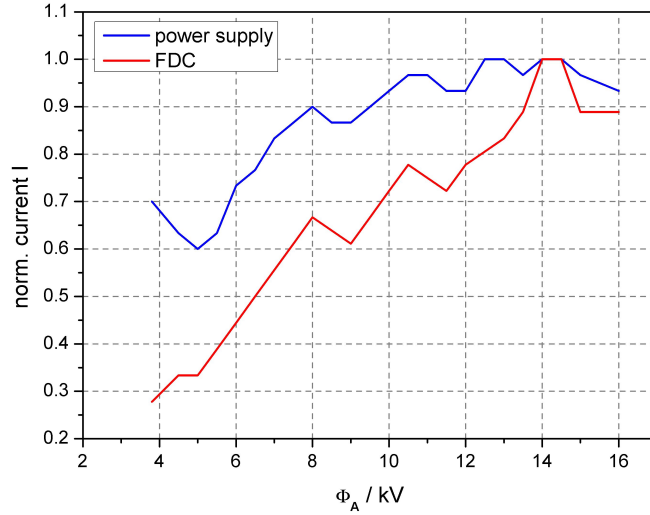


Figure 6.6: Correlation of the normalized power supply current and extracted residual gas ion current as a function of the anode potential for $B_z = 8.1 \text{ mT}$, $p=4.1 \cdot 10^{-5} \text{ Pa}$ (based on data from [Kla13]).

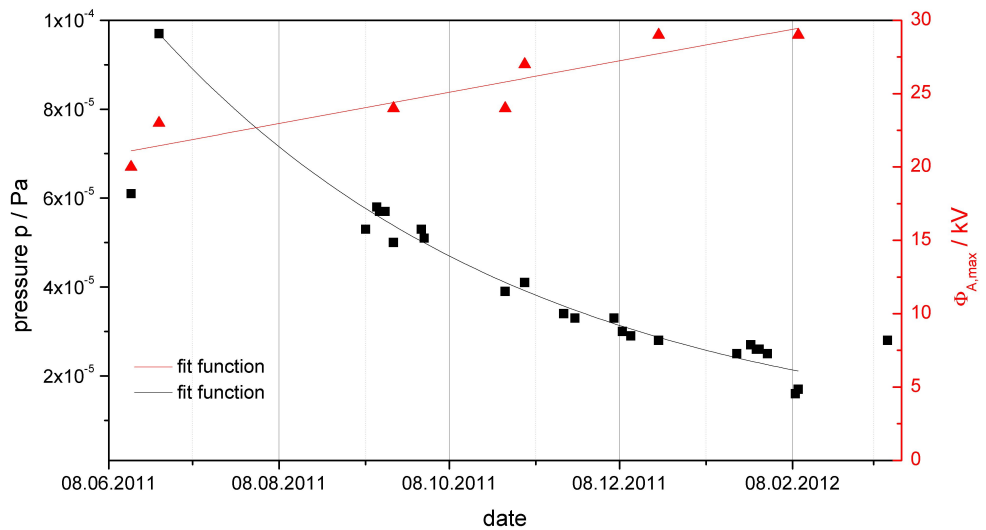


Figure 6.7: Development of final pressure and maximum applied voltage $\Phi_{A,max}$ during the conditioning phase (based on data from [Kla13]).

to note that this represents the long term investigation of the Gabor lens conditioning. If the lens is already conditioned and the vacuum system is vented, it only takes around 30-50 minutes until the lens is ready again for operation (see figure 6.5).

6.3 Results of the Beam Transport Measurements and the Comparative Performed Nonneutral Plasma Diagnostics

The results of the beam transport measurements in comparison with the performed plasma diagnostics for the same lens parameters will be discussed in the following. The main idea behind these studies is to investigate the beam-plasma interaction by comparing the measured plasma parameters such as electron density and its distribution influenced by the beam with the parameters of the unaffected plasma cloud.

The experiments were divided into two parts: emittance dominated and space charge dominated beam transport experiments. In a first step, the transport of a 3 mA, 50.3 keV He⁺-beam as a function of the Gabor lens parameters was investigated.

Nonlinear forces that affect the beam and lead to an emittance growth are produced, e.g. by nonlinear focusing forces or an inhomogeneous density distribution of the beam particles. In the discussed case, the perveance and therefore the influence of the beam space charge on the transport is negligible, and thus one can essentially study the performance of the Gabor lens as a focusing optic.

In a second step, experiments using a 35 mA, 124 keV Ar⁺-beam were performed. By increasing the beam current, does not only the perveance increase by a factor of 8.2 but also the ion number density gradually reaches the order of magnitude of the electron density confined by the Gabor lens. As a result of the increased production of secondary electrons by the beam (see chapter 2), the focusing strength of the lens might be affected.

Therefore, the high current measurements represented a necessary step towards investigating the influence of the discussed processes on the focusing performance of the lens and the general evaluation of the quality of the ion beam transport by the prototype Gabor lens.

6.3.1 Beam Transport Simulation

Beam transport simulations using the code LINTRA (see section 2.8) were performed in parallel to the experiments. In order to obtain an input distribution for the transport calculations, the drifted beam measured by the slit-grid emittance scanner 260 mm behind the exit of the lens, was traced back to the start position of 210 mm before

6.3 Results of the Beam Transport Measurements and the Comparative Performed Nonneutral Plasma Diagnostics

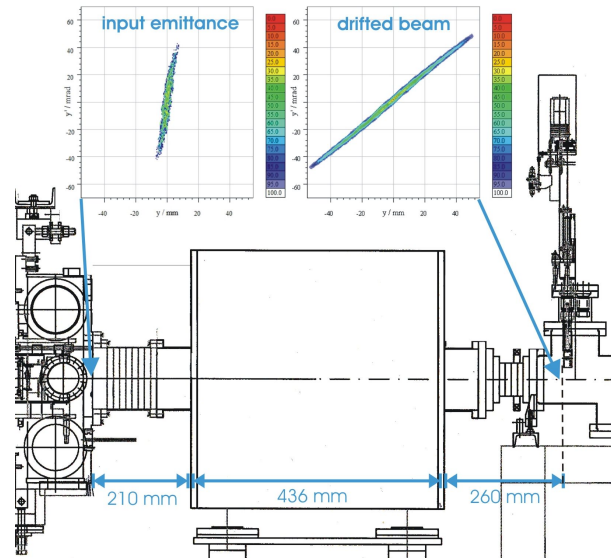


Figure 6.8: Simulations were performed for the illustrated part of the transport section, starting at the exit of the vacuum chamber right behind the post-acceleration gap and ending at the slit of the slit-grid emittance scanner.

the lens' entrance. Figure 6.8 illustrates the scheme of the transport section. In the following, all discussed emittance figures represent the phase space distribution at the end of the transport line and thus the slit position of the slit-grid emittance scanner.

6.3.2 Emittance Dominated Beam Transport

In the presented results, the transport of a 3 mA, 50.3 keV He^+ -beam as a function of the Gabor lens parameters was investigated and compared to the numerical results of the beam transport simulation. However, assuming the realistic confining fields used in the experiment, the calculated phase space distribution did not represent the measured very well due to overestimation of the electron density.

The simulated emittance was matched to the measured phase space distribution by varying the magnetic field, and in connection to this, the electron density. Even though the simulation could not represent the real plasma state for a given parameter set of the lens, the motivation in this context was to investigate the influence of the electron density distribution on the ion beam.

6. BEAM TRANSPORT MEASUREMENTS AT GSI

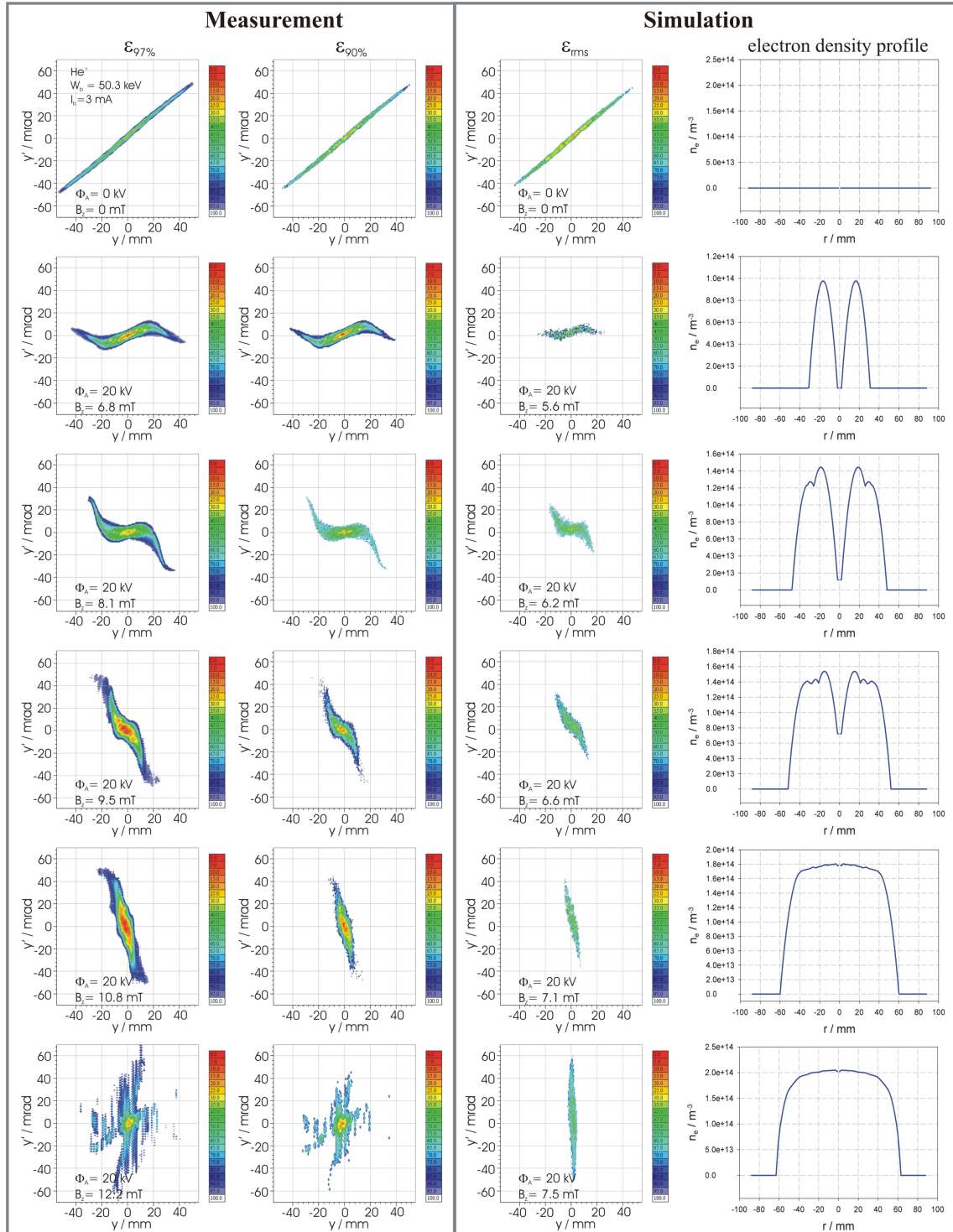


Figure 6.9: Results of the beam transport measurements for a 12.6 keV/u He^+ -beam in comparison with numerical simulations.

6.3 Results of the Beam Transport Measurements and the Comparative Performed Nonneutral Plasma Diagnostics

Just as in the simulation, the magnetic field was also varied in the experiment in order to achieve a rapid rise in density and evaluate the focusing performance depending on the operation point for the given potential of $\Phi_A=20$ kV. The residual gas pressure in the beam line was kept constant at $p=9.6 \cdot 10^{-4}$ Pa. Figure 6.9 shows the result of the beam transport measurements compared to the numerical simulation.

For each measurement point, the values of the 100%-emittance $\epsilon_{100\%}$, the 97%-emittance $\epsilon_{97\%}$ adjusted by the background and the normalized rms-emittance $\epsilon_{\text{rms,n,e}}$ as well as the calculated $\epsilon_{\text{rms,n,s}}$ are listed in table 6.1. Indeed, the beam radius is underesti-

B_z [mT]	$\epsilon_{100\%}$ [mm mrad]	$\epsilon_{97\%}$ [mm mrad]	$\epsilon_{\text{rms,n,e}}$ [π mm mrad]	$\epsilon_{\text{rms,n,s}}$ [π mm mrad]
0	3568	122	0.166	0.155
6.8	4912	290	0.374	0.185
8.1	5340	351	0.453	0.237
9.5	5635	246	0.318	0.172
10.8	5906	249	0.321	0.158
12.2	5291	730	0.940	0.157

Table 6.1: Change in the measured emittance due to a variation in the magnetic confining field of the Gabor lens.

mated by the numerical simulation, still the shape of the phase space distribution is in good agreement with the measurement. By comparing measurement and simulation, the strong dependency of the beam emittance on the confined electron density distribution is evident. With increasing magnetic field, the former hollow electron density distribution becomes more homogeneous and the phase space distribution also shows less aberrations.

Figure 6.10 shows the intensity profiles for the y and y' plane of the measured phase space distribution. With growing focusing strength, the intensity profile becomes more peaked.

However, at a magnetic field strength of $B_z=12.2$ mT, the plasma cloud seems to be unstable, as is also represented in the normalized rms-emittance of the measurement.

The measured and calculated normalized rms-emittances as well as the kurtosis as a function of the confining fields are presented in figure 6.11. The operation point is marked with a green line and was calculated by equation 2.31 for $f=0$. Still, from the beam current a low neutralization factor of $f=0.02$ could be assumed.

In case of the unstable plasma state, the working point has already been overcome.

6. BEAM TRANSPORT MEASUREMENTS AT GSI

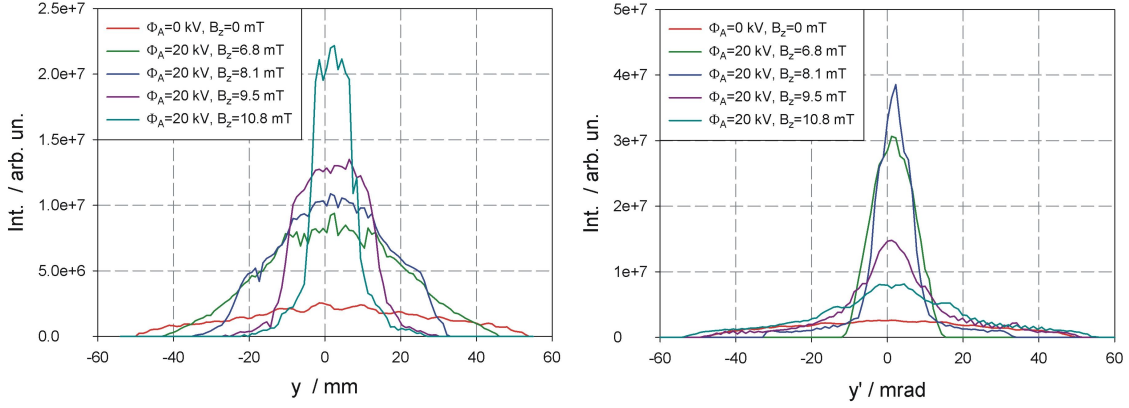


Figure 6.10: Intensity profiles for the y (left) and y' (right) plane as a function of the magnetic confining field.

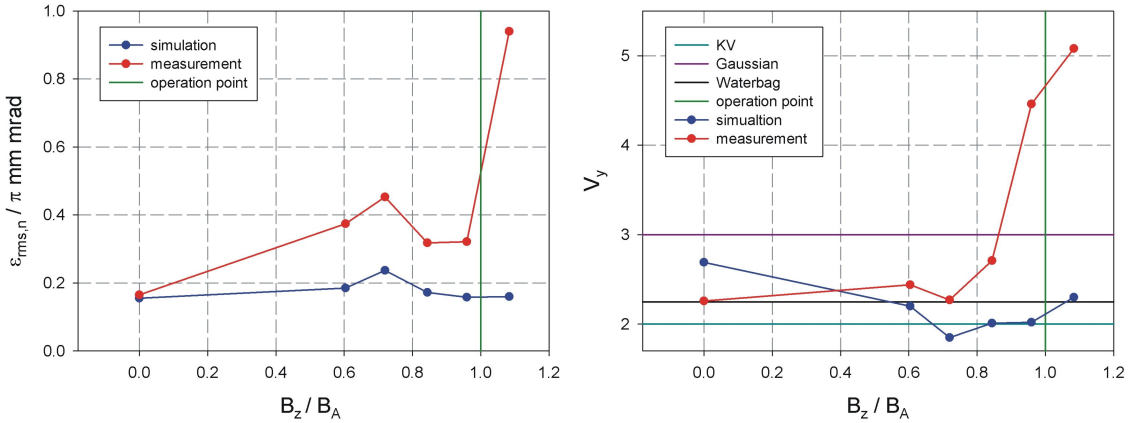


Figure 6.11: Measured and calculated normalized rms-emittances (left) and kurtosis (right) as a function of the confining fields.

Indeed, a similar behavior has been observed in previously performed diagnostic experiments (see section 3.1). Far from the operation point, instabilities arise and a temporally unstable plasma state also effects the ion beam.

Prior to discussing the results of the nonneutral plasma diagnostics, the outcomes of the emittance dominated beam transport measurements related to the quality of the ion optics shall be summarized as follows: an approximately focused beam is achieved for lens parameters of $\Phi_A=20$ kV and $B_z=10.8$ mT. The emittance growth close to the operation point of the lens is less than a factor of 2 and the beam evolves from a Waterbag to a strongly peaked distribution.

6.3 Results of the Beam Transport Measurements and the Comparative Performed Nonneutral Plasma Diagnostics

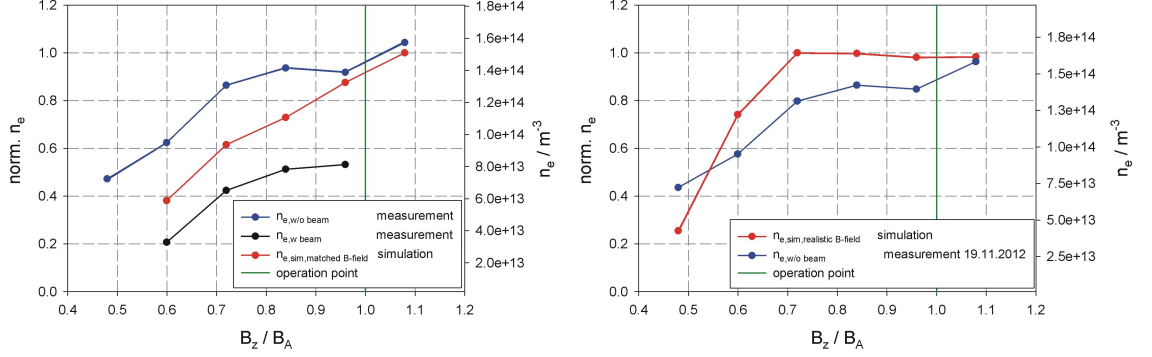


Figure 6.12: Mean electron density determined by different diagnostic techniques, $n_{e,w \text{ beam}}$ and $n_{e,w/o \text{ beam}}$, in comparison to the simulation $n_{e,sim,matched \text{ B-field}}$ (left). Measured density $n_{e,w/o \text{ beam}}$ compared to the density calculation of the plasma state with the realistic magnetic field configuration $n_{e,sim,realistic \text{ B-field}}$ (right).

The phase space distribution measured in the beam transport experiments indicates the shape of the electron density distribution at the moment when the beam passed through the lens volume. Besides the information of the electron density distribution, the electron density $n_{e,w \text{ beam}}$ of the confined plasma cloud was determined from the change in the divergence angle of the beam (see section 5.2.2). Both results represent a very useful information in order to investigate a possible beam-plasma interaction and consequently were compared to the nonneutral plasma diagnostics for the same parameter setup of the lens ($\Phi_A=20 \text{ kV}$, $p=9.6 \cdot 10^{-4} \text{ Pa}$) performed at IAP.

Figure 6.12 shows the mean electron density determined by different diagnostic techniques $n_{e,w \text{ beam}}$ and $n_{e,w/o \text{ beam}}$ in comparison to the simulation $n_{e,sim,matched \text{ B-field}}$. The results differ from the simulated density by around 20%. However, the measured density $n_{e,w/o \text{ beam}}$ compared to the density calculation of the plasma state with the realistic field configuration $n_{e,sim,realistic \text{ B-field}}$ show a better agreement in magnitude as well as the trend of the curve.

In order to determine the cause for these differing results, the measured light density distribution for the given lens parameters was examined and compared to the numerical simulations.

As already discussed in chapter 5 it is possible to estimate the electron density distribution from the detected plasma emission. Although the on-axis intensity might be

6. BEAM TRANSPORT MEASUREMENTS AT GSI

slightly overestimated as a result of the spatial integration by the optical measurement, from the evolution of the light density profile a change in the plasma state can be deduced.

Figure 6.13 shows the detected light density for the same lens parameters that were set during the beam transport measurements, compared to the density calculation of the plasma state with the realistic field configuration. Note that the density profile is not spatially integrated in contrary to the intensity profile.

For the magnetic field of $B_z = 5.4 \text{ mT}$ and $B_z = 6.8 \text{ mT}$, one can observe a light spot on the window presumably produced by massive particle losses. The simulation predicts a hollow density distribution of the electrons for this lens parameter setup. Despite the light density distribution being almost entirely covered, the luminous effect indicates that the electron losses on the axis are caused by a hollow distribution, which is the initial situation for the evolution of the diocotron instability discussed in chapter 3. The remaining profiles do not show any special characteristics and seem to represent a homogeneous plasma distribution. The evaluation of the symmetry S_{sym} and rotational symmetry factors S_{rot} emphasizes the increasing symmetry of the plasma cloud towards the operation point of the lens and is also confirmed by the simulation (see figure 6.14). Overall, it appears that the results of the beam transport as well as the plasma diagnostic measurements are both very-well represented by the numerical simulation: certainly, in case of the beam transport experiment, it is necessary to reduce the growth in electron density by a change in the lens parameters assumed for the numerical simulation to achieve a good representation of the measurement. The nonneutral plasma diagnostics measurements correspond to the numerically predicted behavior of the plasma cloud and only a small deviation in the different densities is observed. Evidently, the numerical simulation better describes the occurring physical processes in the case of the unaffected plasma state i.e. when the lens is used as stand-alone system.

Figure 6.15 shows the comparison of the expected and actual electron density for the beam transport experiments, which only differ in the extent of the electron density. This result implies that the beam is influencing the nonneutral plasma and that for this reason the actual electron density during the beam transport measurements is reduced.

At present, it would be premature to discuss the appearance of beam-driven plasma instabilities, even though they have to be taken into account.

6.3 Results of the Beam Transport Measurements and the Comparative Performed Nonneutral Plasma Diagnostics

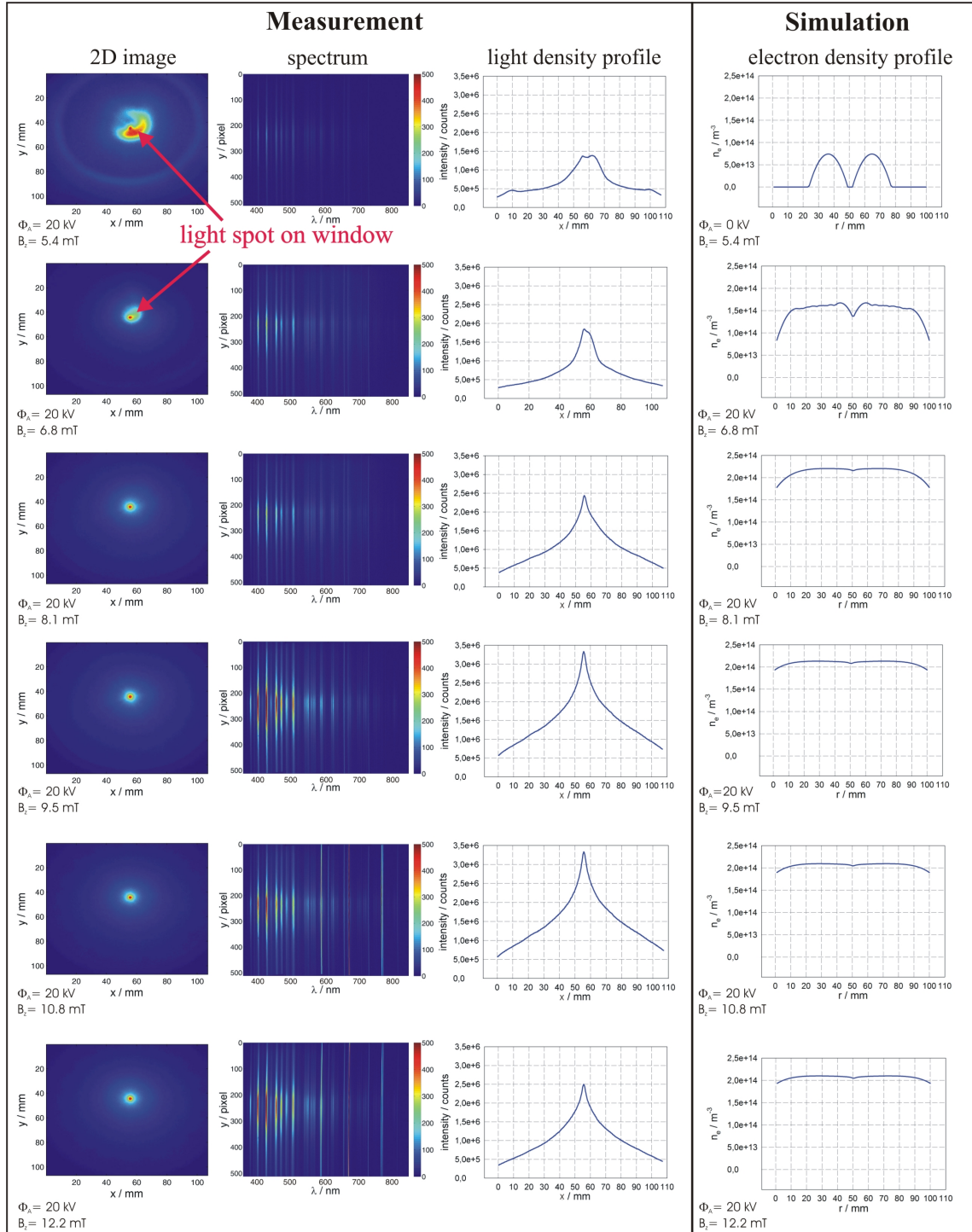


Figure 6.13: Comparison of measured light density distribution and the simulated electron density distribution as well as the emitted spectrum for helium as a function of the lens parameters. The asymmetry of the light density distribution is the result of a light spot on the borosilicate window produced by particle losses.

6. BEAM TRANSPORT MEASUREMENTS AT GSI

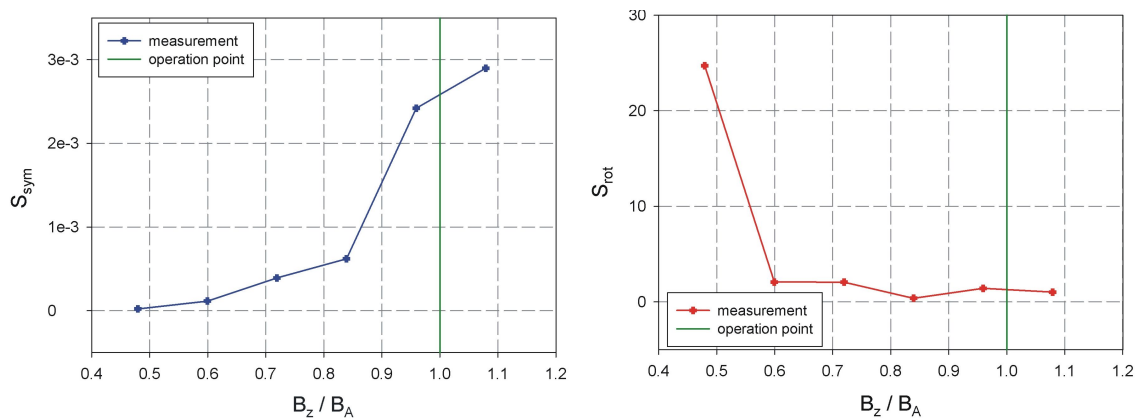


Figure 6.14: Symmetry factor (left) and rotational symmetry (right) of the light density distribution as a function of the lens parameters.

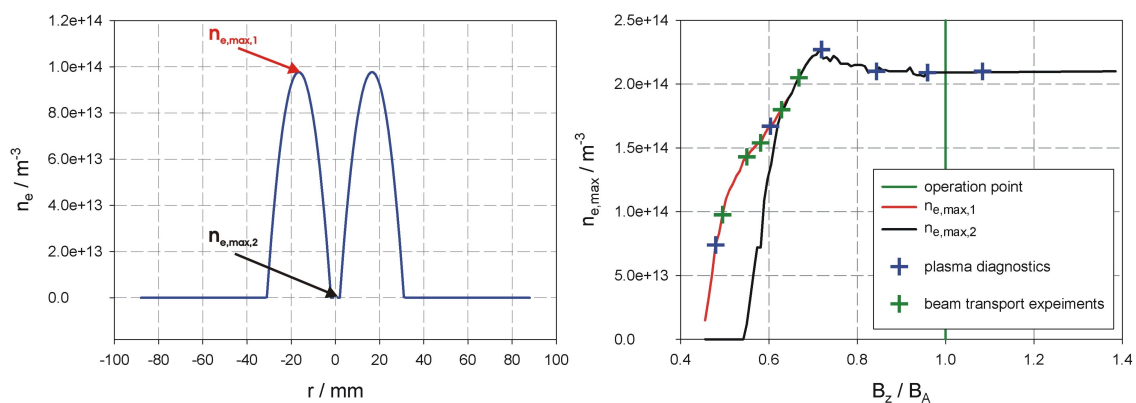


Figure 6.15: Comparison of the expected (plasma diagnostics) and the actual electron density for the beam transport experiments.

However, it is necessary to investigate the influence of plasma-beam interactions on the beam transport in more detail.

6.3.3 Technical Issues

As previously mentioned, it was important to gain practical experience by testing the constructed prototype lens in an real accelerator environment. During the measurement campaign, an increased incidence of high-voltage breakdowns caused by spark-overs was observed. For this reason, the beam line was vented to inspect the insulator of the Gabor lens. Figure 6.16 shows a picture of the insulator between anode and ground electrode, indicating metallic spots on the insulator and also a metallic splint that lowered the

6.3 Results of the Beam Transport Measurements and the Comparative Performed Nonneutral Plasma Diagnostics

distance between anode and ground electrode.

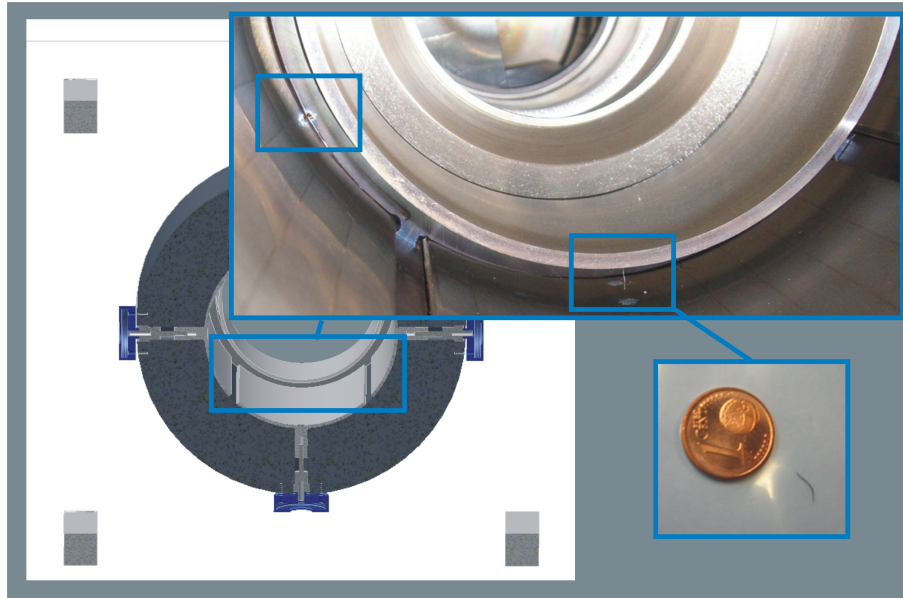


Figure 6.16: Technical assessment of Gabor lens during the measurement campaign.

Besides the evident damages, the insulator also showed a change in color at some positions. The reason for the spots and appearance of the splint could be impurities that entered the device during the transport or the installation and that oriented within the fields during the operation. The general material fatigue is presumably caused by the impinging ion beam.

After the removal of the metallic splint, an iris of $d=50$ mm was installed to protect the insulator from further damage and prevent sparking before the lens was put into operation again. The measurements discussed in the following were all performed with the installed iris at the entrance of the prototype lens.

In this context, one technical improvement to the lens design could be a circular orifices introduced on the anode close to the ground electrode. Indeed, this has already been investigated in former lens designs. The advantage of this optimization is the protection of the insulator, while the electric field is simultaneously flattened.

6.3.4 Space Charge Dominated Beam Transport

The analysis of the space charge dominated beam transport measurements were treated analogously to the presented emittance dominated measurements. In parallel, the important plasma parameters for the same lens settings as used during the beam transport measurements at GSI were determined in diagnostic experiments and compared to numerical simulations of the plasma state.

In case of a high current ion beam, not only the space charge forces become more dominant, but also the production of secondary electrons increases by the interaction processes discussed in chapter 2 as well as beam losses. For example the electron production rate of a 25 mA, 88 keV Ar⁺-beam (number of ions $n_i=1.23 \cdot 10^{14} \text{ m}^{-3}$) on Ar atoms (with number density of $n_n=3.2 \cdot 10^{16} \text{ m}^{-3}$ for a residual gas pressure of $p=1.3 \cdot 10^{-4} \text{ Pa}$) results to $2.8 \cdot 10^{17} \text{ m}^{-3}\text{s}^{-1}$ using again the ionization cross section for $W_B=24 \text{ keV}$ due to lacking data for higher beam energies. Therefore, the number of electrons produced within the lens volume $V=5 \cdot 10^{-3} \text{ m}^3$ per beam pulse amounts to $2 \cdot 10^{11}$ compared to the number of electrons already confined within the lens volume of $5 \cdot 10^{11}$. This means that almost half of the electrons which are already confined in the lens are additionally produced by beam ions. Of course, for this estimate competing effects like recombination processes but also production processes by beam losses are neglected.

To further investigate the influence of the beam current on the focusing quality of the Gabor lens with respect to these effects, beam transport measurements for the same lens parameters but with different ion beam currents were performed.

Figure 6.17 illustrates the phase space distribution of a 2.2 keV/u Ar⁺-beam measured behind the lens for different ion beam currents. During the measurement, the lens parameters as well as the residual gas pressure were kept constant at $\Phi_A=9.5 \text{ kV}$, $B_z=9.7 \text{ mT}$ and $p=1.3 \cdot 10^{-4} \text{ Pa}$ and only the ion beam current was increased. With increasing beam current, the angle in the measured phase space distribution behind the lens also increases, indicating a change in the confined electron density and therefore in the focusing strength of the lens.

It is necessary to highlight that these measurements represent a qualitative evidence only because the ion source parameters such as the filament current, extraction and post-acceleration voltage changed during the measurement, even though the influence on the focusing performance seems to be negligible.

6.3 Results of the Beam Transport Measurements and the Comparative Performed Nonneutral Plasma Diagnostics

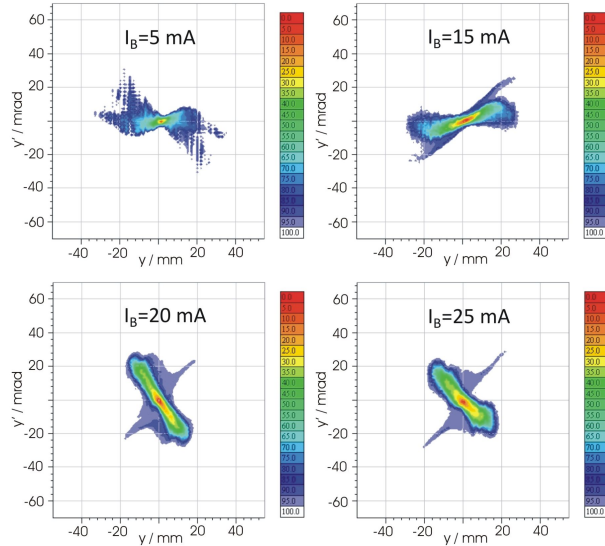


Figure 6.17: Influence of the ion current on the focusing performance of the Gabor lens. During the measurement the lens parameters and the residual gas pressure were kept constant at $\Phi_A=9.5$ kV, $B_z=9.7$ mT and $p=1.3\cdot 10^{-4}$ Pa.

Besides the increased electron production, another possible explanation for the observed change in the focusing strength is the reduction of the electron loss channels due to the positive potential of the ion beam. The beam potential creates a barrier at the entrance and exit of the lens and may be represented by the superposition of the beam, the space charge and the anode potential illustrated in figure 6.18.

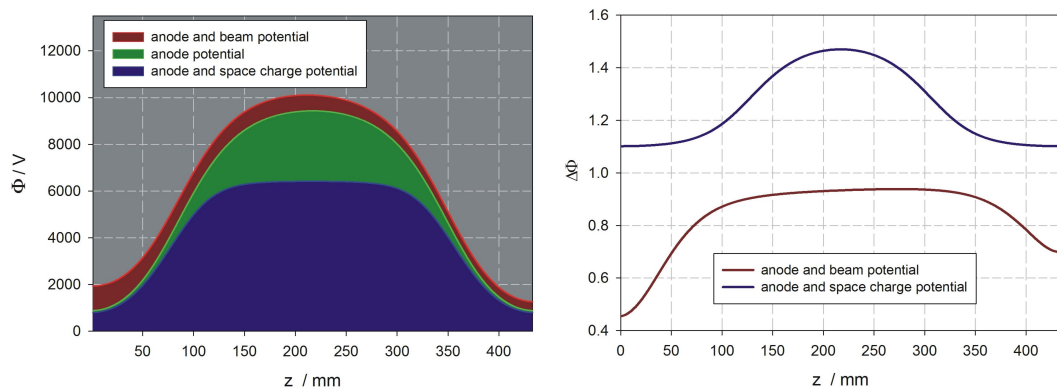


Figure 6.18: Superposition of the anode potential, the space charge potential of the electron cloud and the uncompensated beam potential for an 3.1 keV/u, 35 mA Ar^+ -beam in longitudinal direction.

6. BEAM TRANSPORT MEASUREMENTS AT GSI

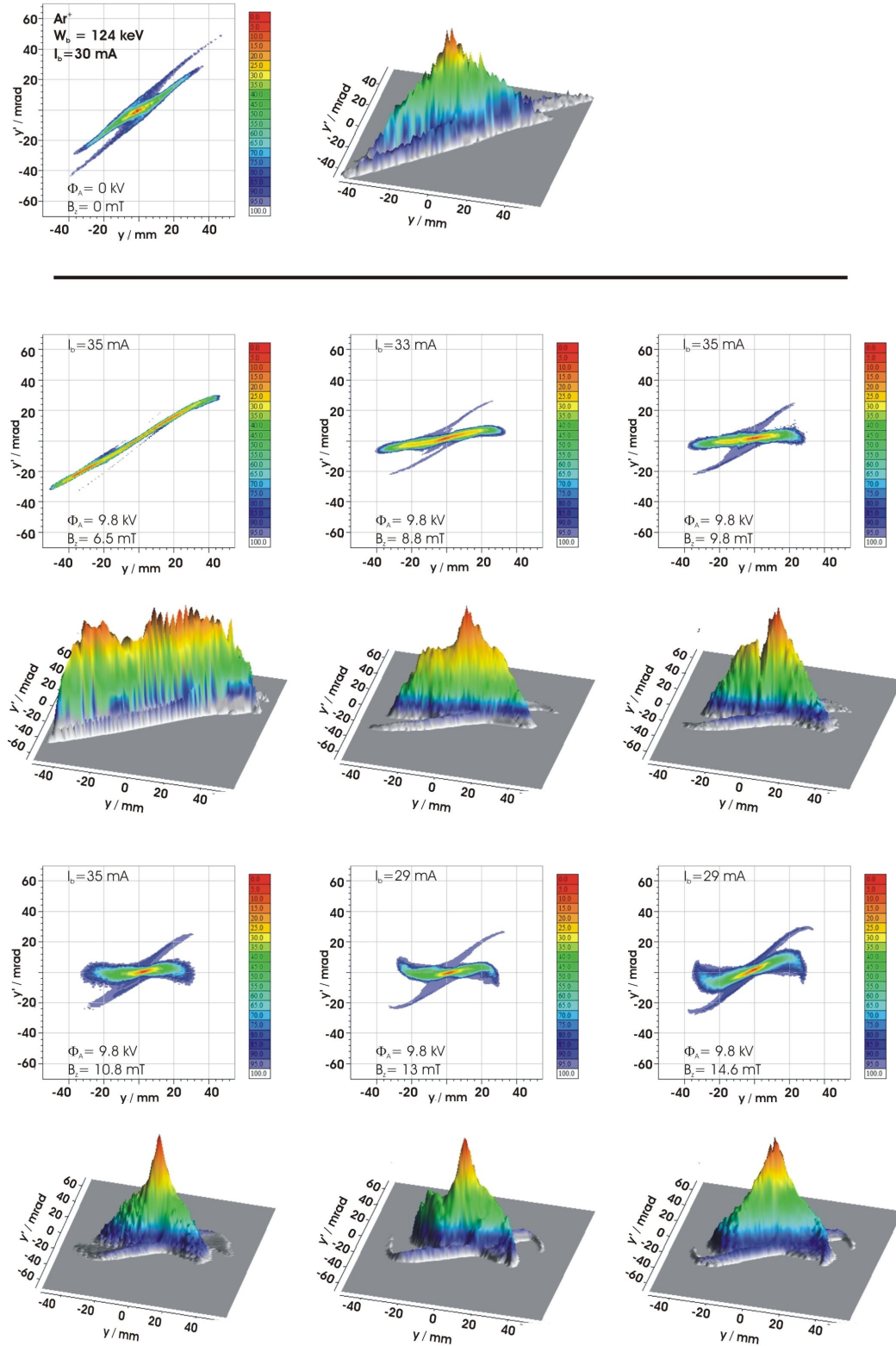


Figure 6.19: Measured emittances and intensity profiles of a 3.1 keV/u Ar^+ -beam as a function of the lens parameters.

6.3 Results of the Beam Transport Measurements and the Comparative Performed Nonneutral Plasma Diagnostics

Unfortunately, the discussed effects are not included in the transport program and for this reason the simulation provides no reasonable results. Therefore, solely the results of the beam transport experiments will be presented and subsequently compared with the results of the performed plasma diagnostic experiments. Figure 6.19 illustrates the measured phase space distributions for a 3.1 keV/u Ar⁺-beam as a function of the lens parameters. The important emittance parameters for the different lens settings are listed in table 6.2.

B_z [mT]	$\epsilon_{100\%}$ [mm mrad]	$\epsilon_{98\%}$ [mm mrad]	$\epsilon_{\text{rms,n,e}}$ [π mm mrad]
0	1861	270	0.170
6.5	1034	324	0.209
8.8	1721	329	0.211
9.7	2034	332	0.214
10.8	2075	377	0.236
13	2395	367	0.236
14.6	2462	381	0.243

Table 6.2: Change in the measured emittance due to the magnetic field of the Gabor lens.

With increasing magnetic field, the focusing strength of the lens also increases. For a magnetic field of $B_z=14.6$ mT, aberrations occur as a result of plasma instabilities and the focusing effect decreases.

By analyzing the beam profiles (see figure 6.20) it can be noted that the beam is de-compensated for the first lens parameter of $\Phi_A=9.8$ kV and $B_z=6.5$ mT but the beam profile becomes more homogeneous throughout the measurement. Figure 6.21 shows the kurtosis and the normalized rms-emittance of the beam as a function of the lens parameters. Again, the operation point is represented by the green line and was calculated using equation 2.31 for $f=0$. Note that in the case of the argon beam, the assumed neutralization factor is much higher ($f=0.16$) compared to the helium beam ($f=0.02$). However, the confining potential is also locally increased due to the superposition of the beam and the anode potential. For this reason, both effects would have to be taken into account for the estimate of the neutralization and therefore the calculation of the operation point.

While the normalized emittance slightly increases, based on the trend of the kurtosis,

6. BEAM TRANSPORT MEASUREMENTS AT GSI

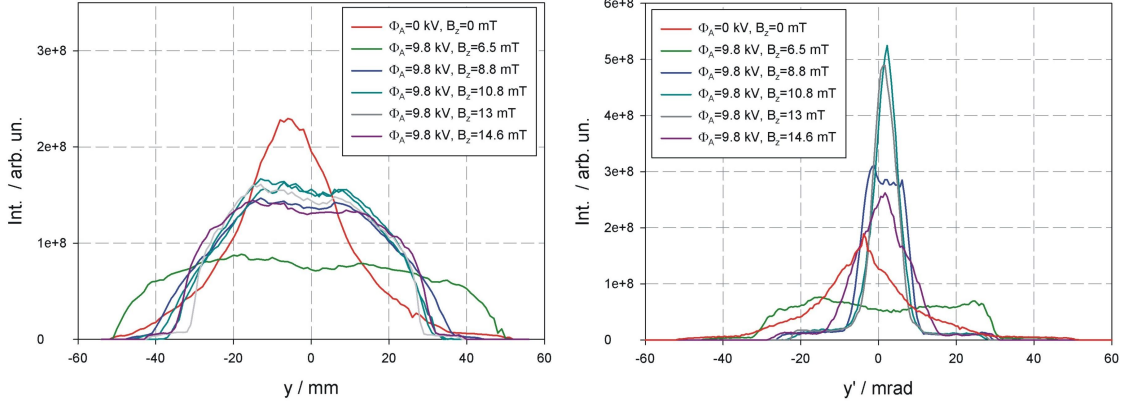


Figure 6.20: Intensity profiles for y (left) and y' (right) for the different settings of the prototype lens.

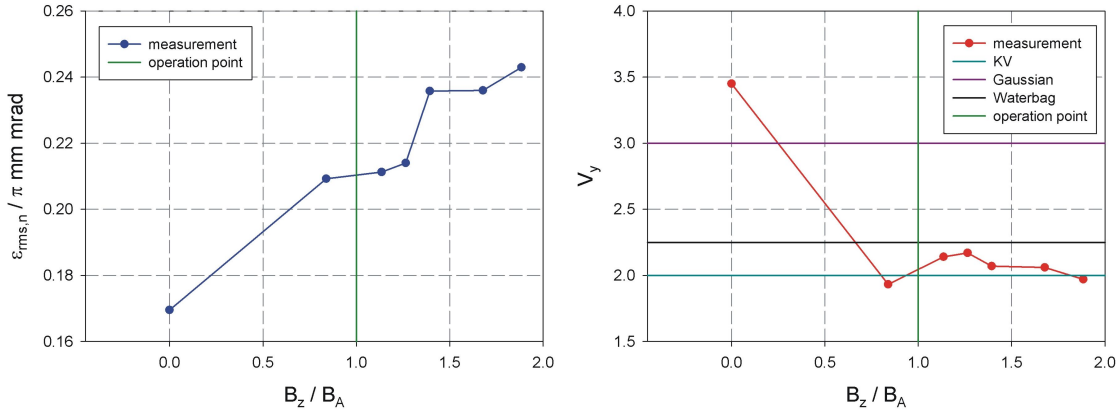


Figure 6.21: Normalized rms-emittance (left) and kurtosis (right) of the Ar^+ -beam as a function of the lens parameters.

the beam profile shape transitions from a former Gaussian into a Waterbag distribution with the beam thus becoming more homogeneous.

At this point, it can be summarized that the transport of a space charge dominated beam by a Gabor lens appears to be very promising. A parallel beam is achieved for lens parameters of $\Phi_A=9.8$ kV and $B_z=10.8$ mT and the normalized rms-emittance only increases by a factor of 1.38.

In analogy to the beam transport measurements, the studies of the nonneutral plasma diagnostics will be discussed in the following.

Figure 6.22 shows the results of the nonneutral plasma diagnostic experiments as a function of the lens parameter setup that was already used during the beam transport

6.3 Results of the Beam Transport Measurements and the Comparative Performed Nonneutral Plasma Diagnostics

measurements ($\Phi_A=9.8$ kV, $p=1.36\cdot 10^{-4}$ Pa). The expected density distribution is wider compared to the helium measurements and seems to represent the results of the beam transport measurements, i.e. the equalization of the beam distribution throughout the variation in the magnetic field.

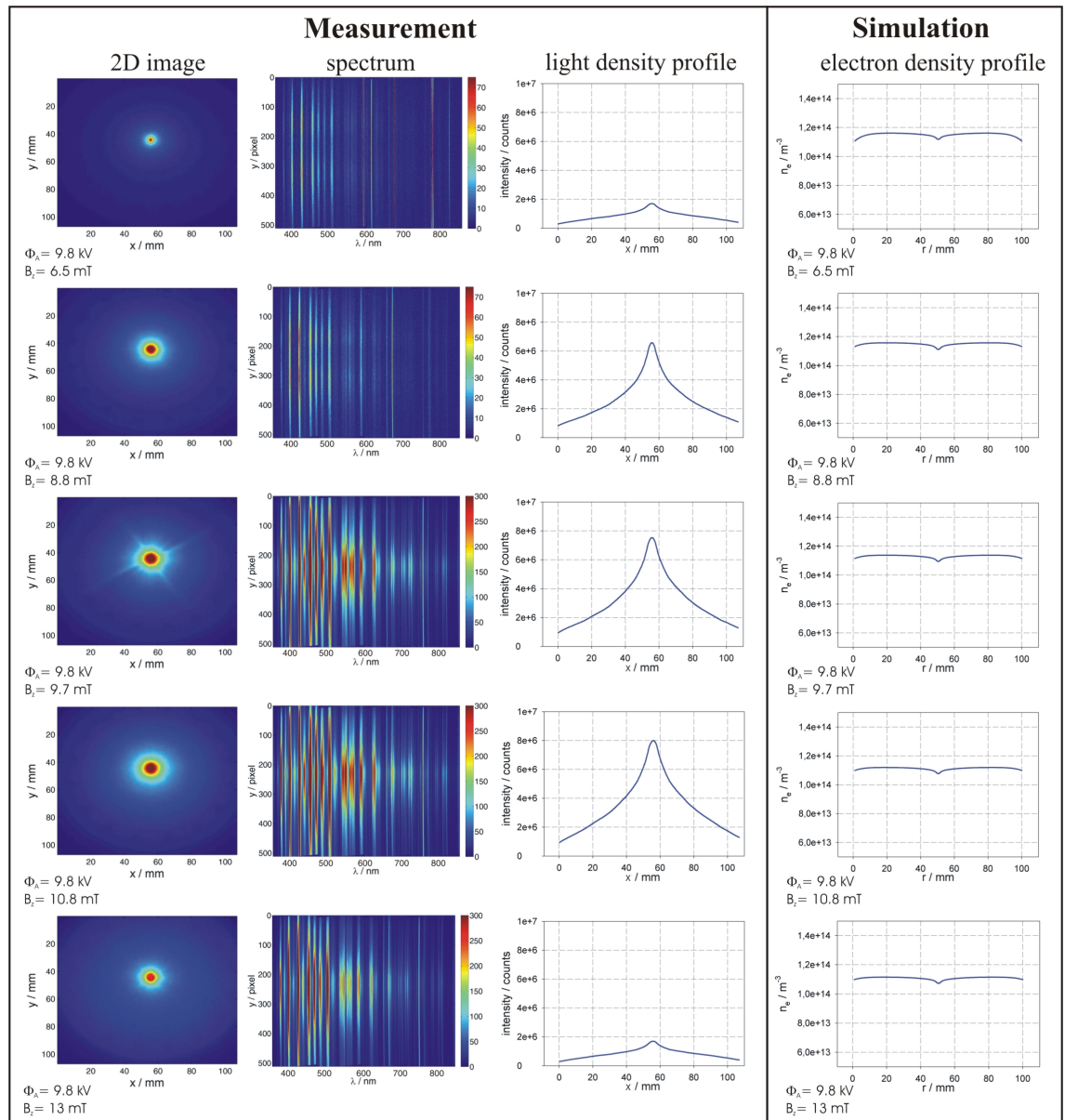


Figure 6.22: Comparison of measured light density distribution and the simulated electron density distribution as well as the emitted spectrum for argon as a function of the lens parameters.

6. BEAM TRANSPORT MEASUREMENTS AT GSI

By contrast, the calculated mean density hardly changes, while in both experiments the density is still growing with increasing magnetic field (see figure 6.23).

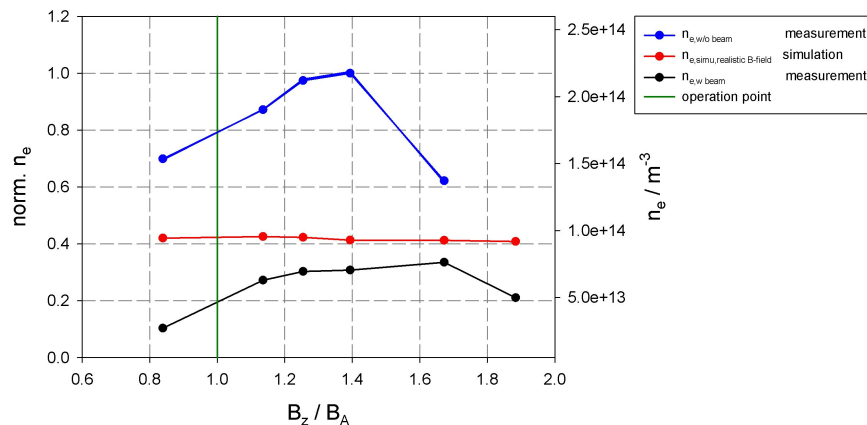


Figure 6.23: Comparison of measured and calculated electron density as a function of the lens parameters.

The densities derived from the experiments differ in extent but show a similar trend. The analysis of the rotational symmetry represents the results beam transport measurements concerning the electron density distribution quite well, although it is not as conclusive as in the helium measurements (see figure 6.24).

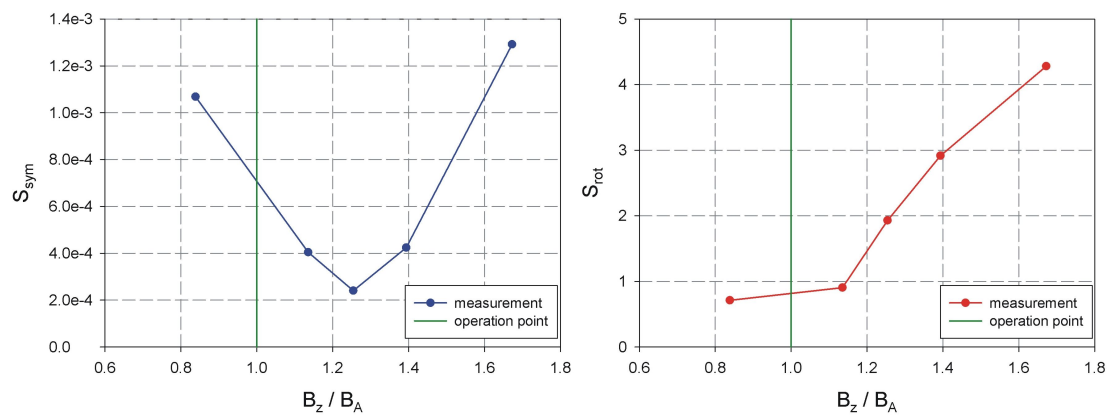


Figure 6.24: Symmetry (left) and rotational symmetry (right) for the discussed measurements series.

The rotational symmetry increases, i.e. becomes more unbalanced after crossing the operation point, while the symmetry factor shows a maximum at the beginning and the end of the measurement series.

6.3 Results of the Beam Transport Measurements and the Comparative Performed Nonneutral Plasma Diagnostics

Finally, the results of both experiments concerning the electron density are compared and presented in figure 6.25.

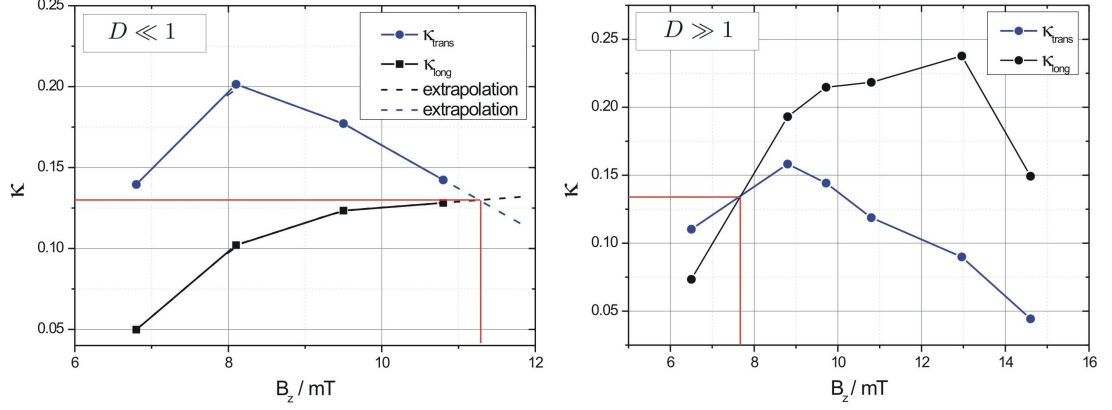


Figure 6.25: Confinement efficiencies as a function of the magnetic field for the emittance dominated beam transport measurements (left) and for the space charge dominated beam transport experiments (right).

The confinement efficiency of the lens in case of the space charge dominated beam transport is higher than for the emittance dominated beam transport. However, the confinement efficiency at the operation point (red line) of the lens is the same in both experiments i.e. independently of the ion species, the beam current and the residual gas in the beam line.

Overall, the confinement efficiency is lower than determined in previous experiments [Meu06], [Sch09]. But at the same time the aperture of the prototype lens and in connection to this the emission area was drastically increased.

From comparing the confinement efficiency for different experiments it results that the emission area was increased by a factor of 14 while the confinement efficiency only decreased by a factor of 2 (see table 6.3).

Confinement Efficiency $\kappa = \kappa_l = \kappa_r$	Emission Area / m^2	Reference
≈ 0.29	$1.26 \cdot 10^{-3}$	[Meu06]
≈ 0.14	$17.67 \cdot 10^{-3}$	this work

Table 6.3: Comparison of confinement efficiency and emission area for different experiments.

6. BEAM TRANSPORT MEASUREMENTS AT GSI

6.3.5 Summary

The analysis of the emittance dominated beam transport measurements demonstrated the strong influence of the shape and, of course, the magnitude of the electron density distribution on the ion beam. In this context, the setting of lens regarding the operation function is of great importance towards optimizing the beam transport and ensuring the stability of the confined electron cloud. First indirect evidence of the influence of the beam on the confined electron cloud was observed. Furthermore, it is necessary to investigate the effect of beam driven instabilities in detail.

Table 6.4 gives an overview over the parameters of the emittance dominated beam transport.

Lens Parameters				Beam Parameters			
Φ_A	B_z	n_e	f	W_B	I_B	Ion Species	$\frac{\epsilon_{rms,n,out}}{\epsilon_{rms,n,in}}$
20 kV	10.8 mT	$8 \cdot 10^{13} \text{ m}^{-3}$	0.5 m	50.3 keV	3 mA	He ⁺	1.93

Table 6.4: Parameters for the emittance dominated beam transport measurements.

Due to the missing beam transport simulations, the results of space charge dominated measurements in comparison to the plasma diagnostic experiments are not as obvious as in the previously performed emittance dominated transport experiments. Nonetheless, the quality of the transport in case of the increased beam current looks very promising. A parallel Ar⁺-beam of 3.1 keV/u was achieved for a lens parameter setup of $\Phi_A=9.8$ kV and $B_z=10.8$ mT by an increase in emittance of only a factor of 1.38.

An overview of the lens and beam parameters for the space charge dominated beam transport is shown in table 6.5.

Lens Parameters				Beam Parameters			
Φ_A	B_z	n_e	f	W_B	I_B	Ion Species	$\frac{\epsilon_{rms,n,out}}{\epsilon_{rms,n,in}}$
9.8 kV	10.8 mT	$7.5 \cdot 10^{13} \text{ m}^{-3}$	1.3 m	124 keV	35 mA	Ar ⁺	1.38

Table 6.5: Parameters for the space charge dominated beam transport measurements.

7

Summary and Conclusion

In the scope of this thesis, a prototype lens for the application at the GSI High Current Injector was designed, constructed and tested with beam. Due to the expected large beam radii, one major issue was the generation and homogeneous confinement of an electron column with comparable radial expansion in order to provide a linear electric space charge field for focusing the beam. Nonlinearities occur due to plasma instabilities or the Debye drop off at the edge of the plasma cloud. Given that plasma instabilities lead to aberrations and limit the focusing performance, the dependence of the plasma state on the external parameters was studied by analyzing of the emitted residual gas atoms and of the plasma emission.

To accomplish this, an experiment with different diagnostic devices was set up. A Faraday cup, momentum spectrometer and pepperpot emittance scanner were used for the analysis of the emitted residual gas ions, while an optical system consisting of a CCD camera and monochromator was used to detect the plasma emission. The time-resolved diagnostics of an temporal unstable plasma state was provided by a CCD camera equipped with an intensifier. The time structure of the measured ion current was used as a trigger signal for the optical exposure.

In order to classify the actual plasma state, the symmetry of the light density distribution, which is directly correlated to the electron density distribution, was examined using two different criteria, namely the rotational symmetry and symmetry factor. It was found that both parameters represent the plasma state very well with respect to its transverse distribution.

Using the described diagnostics, it was possible to study the time-dependent evolution

7. SUMMARY AND CONCLUSION

of a nonneutral plasma instability, as well as characterizing its mode.

The electron density was deduced from the residual gas ion energies measured by the momentum spectrometer. The basic idea of this measurement is that the ions gain their energy from the potential well created by the electrode system, which has already been reduced by confined electrons. A careful examination of this method was performed by the experiment and numerical simulation.

A line-ratio technique, which brings the detected photon flux of two spectral lines into relation, was used to determine the electron temperature by optical spectroscopy. In order to derive the photon flux of a spectral line in coronal equilibrium, the knowledge of the optical-emission cross section for this transition was required.

Unfortunately, the database of optical-emission cross sections especially in the region of electron energies above 200 eV, was insufficient or limited to a small part of the optical spectrum. Therefore, another experiment was set up to measure the optical-emission cross section. In the context of the work, the optical-emission cross section for the most important transitions in helium were determined within the energy region of 80-1830 eV.

Furthermore, the experiment provided the opportunity to study the interaction processes of electrons with the residual gas atoms in more detail, as well as comparing it to the plasma emission. It was observed that the emission spectra differ for some spectral lines. However, some transitions were also identified that result from the same excitation process. These lines were finally used for the temperature determination of the nonneutral plasma. The results for the plasma parameters were compared to the numerical simulation and showed a good agreement for parameter settings of the lens close to the operation point.

As they play an important part for the equilibrium state of the plasma, the electron production and loss mechanisms were investigated theoretically and experimentally. The loss current was derived from the x-ray emission, while the production process was investigated by the plasma ignition as a function of the external parameters

After a systematic analysis of the nonneutral plasma properties, the lens was transported to GSI and installed at the High Current Test Injector at GSI. The performed beam transport measurements were divided into two parts: emittance dominated (He^+ , $I_b=3\text{ mA}$, $W_b=50\text{ keV}$) and space charge dominated beam transport (Ar^+ , $I_b=35\text{ mA}$, $W_b=124\text{ keV}$) experiments.

In both cases, the magnetic field of the prototype lens was varied while the anode potential was kept constant. Accordingly, the confined electron density could be increased rapidly, simultaneously the dependence of the focusing performance on the operation point of the lens could be investigated. The actual electron density was determined from the focal length.

The results of the performed beam transport experiment were compared to the plasma diagnostics and the numerics. In the case of the emittance dominated beam transport it was shown that the affected and unaffected plasma state differ especially in the electron density for the same parameter settings. As a result of these detailed studies first evidence for a possible beam-plasma interaction was found.

For the emittance dominated as well as the space charge dominated beam transport experiments, a good focusing performance close to the assumed operation point of the lens was demonstrated. Far from this operation point, occurrences of instabilities were observed.

The results of the space charge dominated beam transport in particular appear very promising. A parallel Ar^+ -beam of 3.1 keV/u was achieved for a lens parameter set-up of $\Phi_A=9.8$ kV and $B_z=10.8$ mT by an increase in the normalized rms-emittance of only a factor of 1.38.

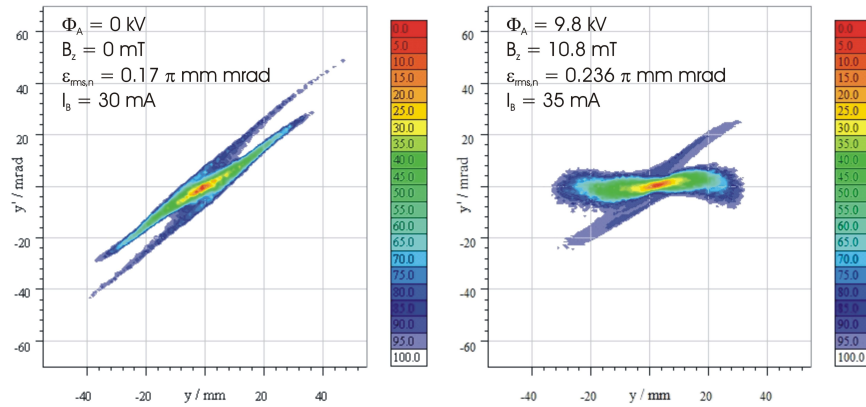


Figure 7.1: Measured phase space distribution of the drifted Ar^+ -beam (left) and the transported beam by the Gabor lens (right). Both emittances were measured at the same position behind the lens.

In the scope of presented work, the prototype lens has successfully been tested at the

7. SUMMARY AND CONCLUSION

GSI High Current Test Injector, especially for the transport of intense space charge dominated beams. Furthermore, the temperature determination of the nonneutral plasma in the regime of a coronal equilibrium by optical spectroscopy was demonstrated for the first time.

In this connection, the influence of a changed electron production and loss rate on the focusing strength as well as the plasma state holds significant interest. In a regime of increased residual gas pressure where interaction processes with neutrals play a major role, the loss- and production rates define the equilibrium state of the system and should further be investigated in order to improve the performance of the whole transport channel.

References

- [AHS10] A. Adonin, R. Hollinger, and P. Spädtke. Measurements of Transverse Ion Beam Emittance Generated by High Current Ion Sources at the GSI Test Injector Facility HOSTI. *Review of Scientific Instruments*, 81(2):02B707, 2010. 2, 121, 122, 123
- [And95] O. A. Anderson. Solution of K-V Envelope Equations. <http://www.osti.gov/bridge/servlets/purl/97297-5IuGq7/webviewable/>, 1995. Accelerator and Fusion Research Division, Lawrence Berkeley Laboratory, University of California, Report Number LBL-36502, C95-05-01. 46
- [BLB⁺07] R. F. Boivin, S. D. Loch, C. P. Ballance, D. Branscomb, and M. S. Pindzola. Line Ratio Diagnostics in Helium and Helium Seeded Argon Plasmas. *Plasma Sources Science and Technology*, 16(3):470, 2007. 91, 93
- [BLD04] J. B. Boffard, C. C. Lin, and C. A. Jr. DeJoseph. Application of Excitation Cross Sections to Optical Plasma Diagnostics. *Journal of Physics D: Applied Physics*, 37(12):R143, 2004. 29, 88, 91, 94, 111
- [Bri45] L. Brillouin. A Theorem of Larmor and Its Importance for Electrons in Magnetic Fields. *Phys. Rev.*, 67:260–266, Apr 1945. 13
- [Bro04] I. G. Brown. *The Physics and Technology of Ion Sources*, pages 65–67. Wiley, 2004. 41, 42
- [BS58] C. F. Barnett and P. M. Stier. Charge Exchange Cross Sections for Helium Ions in Gases. *Phys. Rev.*, 109:385–390, Jan 1958. 23, 164
- [Che74a] F. F. Chen. *Introduction to Plasma Physics*, pages 8–9. Plenum Press, 1974. 6

REFERENCES

- [Che74b] F. F. Chen. *Introduction to Plasma Physics*, page 73. Plenum Press, 1974. 7
- [Che74c] F. F. Chen. *Introduction to Plasma Physics*, page 11. Plenum Press, 1974. 8
- [Chr99] A. Christmann. *Untersuchungen der Zusammensetzung energetischer Helium-Atomstrahlen und deren Anwendung zur Plasmadiagnostik*. PhD thesis, Ruhr-Universität Bochum, 1999. 93
- [CLCR] H. K. Chung, R. W. Lee, M. H. Chen, and Y. Ralchenko. The How to for FLYCHK @ Nist. http://nlte.nist.gov/FLY/Doc/Manual_FLYCHK_Nov08.pdf. Manual, 2008. 27, 28, 30
- [Dav74] R. C. Davidson. *Theory of Nonneutral Plasmas*, pages 4–10. Number Bd. 805323465 in *Frontiers in Physics*, no. 43. Benjamin Press, 1974. 12, 14
- [Dav90a] R. C. Davidson. *Physics of Nonneutral Plasmas*, page 1. Imperial College Press, 1990. 6
- [Dav90b] R. C. Davidson. *Physics of Nonneutral Plasmas*, pages 59–61. Imperial College Press, 1990. 6
- [Dav01] R. C. Davidson. *Physics Of Nonneutral Plasmas*, pages 295–306. Allied Publishers, 2001. 52
- [Dem09] W. Demtröder. *Experimentalphysik 3 - Atome, Moleküle und Festkörper*, pages 184–186. Number Bd. 3 in *Springer-Lehrbuch*. Springer, 2009. 88, 89, 168
- [dHSM66] F. J. de Heer, J. Schutten, and H. Moustafa. Ionization and Electron Capture for Helium Ions Incident on Noble and Diatomic Gases between 10 and 150 keV. *Physica*, 32(10):1793–1807, 1966. 24, 164
- [DHT61] K. T. Dolder, M. F. A. Harrison, and P. C. Thonemann. A Measurement of the Ionization Cross-Section of Helium Ions by Electron Impact. *Proceedings of the Royal Society of London. Series A, Mathematical and Physical Sciences*, 264(1318):367–378, 1961. 25, 26, 164

-
- [DO78] M. H. Douglas and T. M. O’Neil. Transport of a Nonneutral Electron Plasma due to Electron Collisions with Neutral Atoms. *Physics of Fluids*, 21(6):920–925, 1978. 36
- [Dro] M. Droba. GAB_LENS - private communication. v, 40
- [Dro13] M. Droba. High-Current Beam Transport Simulations Including Gabor Lenses in Varying Non-Neutral Plasma States. In *Proceedings of the International Particle Accelerator Conference IPAC’13*, number TUPWO008, Shanghai, China, 2013. 51
- [Fan06] U. Fantz. Basics of Plasma Spectroscopy. *Plasma Sources Science and Technology*, 15(4):S137, 2006. 3, 88, 89, 168
- [FLAM94a] A. R. Filippelli, C. C. Lin, L. W. Anderson, and J. W. McConkey. Principles and Methods for Measurement of Electron Impact Excitation Cross Sections for Atoms and Molecules by Optical Techniques. volume 33 of *Advances In Atomic, Molecular, and Optical Physics*, pages 6–8. Academic Press, 1994. 95
- [FLAM94b] A. R. Filippelli, C. C. Lin, L. W. Anderson, and J. W. McConkey. Principles and Methods for Measurement of Electron Impact Excitation Cross Sections for Atoms and Molecules by Optical Techniques. volume 33 of *Advances In Atomic, Molecular, and Optical Physics*, page 3. Academic Press, 1994. 96
- [FLAM94c] A. R. Filippelli, C. C. Lin, L. W. Anderson, and J. W. McConkey. Principles and Methods for Measurement of Electron Impact Excitation Cross Sections for Atoms and Molecules by Optical Techniques. volume 33 of *Advances In Atomic, Molecular, and Optical Physics*, pages 28–29. Academic Press, 1994. 100
- [FLAM94d] A. R. Filippelli, C. C. Lin, L. W. Anderson, and J. W. McConkey. Principles and Methods for Measurement of Electron Impact Excitation Cross Sections for Atoms and Molecules by Optical Techniques. volume 33 of *Advances In Atomic, Molecular, and Optical Physics*, pages 16–17. Academic Press, 1994. 103

REFERENCES

- [FLAM94e] A. R. Filippelli, C. C. Lin, L. W. Anderson, and J. W. McConkey. Principles and Methods for Measurement of Electron Impact Excitation Cross Sections for Atoms and Molecules by Optical Techniques. volume 33 of *Advances In Atomic, Molecular, and Optical Physics*, pages 31–32. Academic Press, 1994. 105
- [FLAM94f] A. R. Filippelli, C. C. Lin, L. W. Anderson, and J. W. McConkey. Principles and Methods for Measurement of Electron Impact Excitation Cross Sections for Atoms and Molecules by Optical Techniques. volume 33 of *Advances In Atomic, Molecular, and Optical Physics*, page 22. Academic Press, 1994. 109
- [Fra09] G. Franz. *Low Pressure Plasmas and Microstructuring Technology*, pages 5–37. Springer Publishing Company, Incorporated, 1st edition, 2009. 19, 164
- [fSaT] National Institute for Standard an Technology. Electron-Impact Cross Sections for Ionization and Excitation. http://physics.nist.gov/PhysRefData/Ionization/atom_index.html. Database. 20, 164
- [Gab47] D. Gabor. A Space-Charge Lens for the Focusing of Ion Beams. *Nature*, 160:89–90, 1947. i, 1, 32
- [Gab08] C. Gabor. *Untersuchungen zur zerstörungsfreien Emittanzmessung an einem negativen Wasserstoffionenstrahl*. PhD thesis, Goethe-Universität Frankfurt, 2008. 44, 99, 168
- [Gla12] B. Glaeser. *Zeitaufgelöste Diagnose eines nichtneutralen Plasmas in einer Gabor-Plasma-Linse*. Bachelor thesis, Goethe-Universität Frankfurt, 2012. 53, 54, 71, 85, 87, 165, 167, 168
- [Glu] Bestimmung der Austrittsarbeit von Wolfram aus der Richardson-Gleichung. http://iaprfq.physik.uni-frankfurt.de/PDF/Versuche_files/Gluemission.pdf. Experiment Instruction. 105
- [Gon13] A. Goncharov. Invited Review Article: The Electrostatic Plasma Lens. *Review of Scientific Instruments*, 84(2):02110–1, 2013. 1

-
- [Gou95] R. W. Gould. Dynamics of Non-Neutral Plasmas. *Physics of Plasmas*, 2(6):2151–2163, 1995. 52, 165
- [GR10a] R. J. Goldstone and P. H. Rutherford. *Introduction to Plasma Physics*, page 172. Plasma Physics Series. Taylor & Francis, 2010. 20
- [GR10b] R. J. Goldstone and P. H. Rutherford. *Introduction to Plasma Physics*, page 191. Plasma Physics Series. Taylor & Francis, 2010. 38
- [Gro00] P. Groß. *Untersuchungen zum Emittanzwachstum intensiver Ionenstrahlen bei teilweiser Kompensation der Raumladung*. PhD thesis, Goethe-Universität Frankfurt, 2000. 46
- [HA] R. Hollinger and A. Adonin. Private communication. 122, 123, 170
- [Hin08] F. Hinterberger. *Physik Der Teilchenbeschleuniger und Ionenoptik*, pages 64–65. Springer London, Limited, 2008. 44
- [Hut05a] I. H. Hutchinson. *Principles of Plasma Diagnostics*, page 221. Cambridge University Press, 2005. 3, 17, 26
- [Hut05b] I. H. Hutchinson. *Principles of Plasma Diagnostics*, pages 225–226. Cambridge University Press, 2005. 3
- [Hut05c] I. H. Hutchinson. *Principles of Plasma Diagnostics*, pages 223–225. Cambridge University Press, 2005. 28, 89
- [JML64] R. M. St. John, F. L. Miller, and C. C. Lin. Absolute Electron Excitation Cross Sections of Helium. *Phys. Rev.*, 134:A888–A897, May 1964. 94
- [Kla13] S. Klaproth. *Indirekte Messung von Teilchenverlusten in einer Gabor-Linse*. Bachelor thesis, Goethe-Universität Frankfurt, 2013. 37, 38, 66, 125, 126, 127, 164, 165, 170
- [Kna66] W. Knauer. Diocotron Instability in Plasmas and Gas Discharges. *Journal of Applied Physics*, 37(2):602–611, 1966. 51
- [KP83] Y. S. Kim and R. H. Pratt. Direct Radiative Recombination of Electrons with Atomic Ions Cross Sections and Rate Coefficients. *Phys. Rev. A*, 27:2913–2924, jun 1983. 25

REFERENCES

- [KR94] Y.-K. Kim and M. E. Rudd. Binary-Encounter-Dipole Model for Electron-Impact Ionization. *Phys. Rev. A*, 50:3954–3967, Nov 1994. 19
- [KTY01] S. Kondoh, T. Tatsuno, and Z. Yoshida. Stabilization Effect of Magnetic Shear on the Diocotron Instability. *Physics of Plasmas*, 8(6):2635–2640, 2001. 51, 165
- [KV59] I. Kapchinsky and V. Vladimírsky. Limitations of Proton Beam Current in a Strong Focusing Linear Accelerator Associated with Beam Space Charge. In *Proceedings of the 2nd International Conference On High-Energy Accelerators HEACC'59*, pages 274–288, CERN, Switzerland, 1959. 46
- [Lan00] K. R. Lang. *The Sun from Space*, page 23. Number Bd. 1 in Astronomy and Astrophysics Library. Springer-Verlag GmbH, 2000. 92
- [Lee32] J. H. Lees. The Excitation Function of Helium. *Proceedings of the Royal Society of London. Series A, Containing Papers of a Mathematical and Physical Character*, 137(831):173–186, 1932. 94
- [Lee04] S. Y. Lee. *Accelerator Physics*, page 70. World Scientific Publishing Company, Incorporated, 2004. 46
- [LH68] W. Lochte-Holtgreven. *Plasma diagnostics*, pages 42–51. North-Holland Publishing Company Amsterdam, 1968. 27
- [Lio38] J. Liouville. Note sur la théorie de la variation des constantes arbitraires. *Journal de Mathématiques*, 3(1):349, 1838. 41
- [LNC97] The Leader in Spectroscopic Detection, April 1997. Manual. 72, 167
- [Lot11] M. Lotz. *Fokussier- und Abbildungseigenschaften von Solenoiden*. Bachelor thesis, Goethe-Universität Frankfurt, 2011. 42
- [Mar80] K. Marton. *Vacuum Physics and Technology*, pages 447–448. Methods in Experimental Physics. Elsevier Science, 1980. 126
- [McW65] R. W. P. McWhirter. *Plasma Diagnostic Techniques*, pages 201–261. Pure and Applied Physics. Academic Press, 1965. 28, 30, 164

-
- [MDS13] O. Meusel, M. Droba, and K. Schulte. Experimental Studies of Stable Confined Electron Clouds Using Gabor Lenses. In *Proceeding of the Joint INFN-CERN-EuCARD-AccNet Workshop on Electron-Cloud Effects*, pages 157–160, Isola d’Elba, Italy, 2013. CERN. v, 39, 40, 163, 165
- [Meu01] O. Meusel. *Untersuchungen zum Transport niederenergetischer und hochperveanter Strahlen schwerer Ionen mit einer Doppel-Gabor-Plasmalinse*. Master thesis, Goethe-Universität Frankfurt, 2001. 48
- [Meu06] O. Meusel. *Fokussierung und Transport von Ionenstrahlen mit Raumladungslinsen*. PhD thesis, Goethe-Universität Frankfurt, 2006. ii, iv, 2, 8, 10, 13, 16, 21, 22, 35, 36, 37, 39, 58, 145, 163, 165, 166
- [MH50] G. G. MacFarlane and H. G. Hay. Wave Propagation in a Slipping Stream of Electrons: Small Amplitude Theory. *Proceedings of the Physical Society. Section B*, 63(6):409, 1950. 51
- [Mil08] S. Miller. A low Cost Setup for Performing an Absolute Photon Calibration, 2008. Technical Report, University of Arizona. 108
- [Mob73] R. M. Mobley. Gabor Lens - Experimental Results at Brookhaven. <http://www.osti.gov/bridge/servlets/purl/6512779-MMGkyv/6512779.pdf>, 1973. Technical Report, Brookhaven National Laboratory. 2
- [MSF⁺80] A. Muller, E. Salzborn, R. Frodl, R. Becker, H. Klein, and H. Winter. Absolute Ionisation Cross Sections for Electrons Incident on O⁺, Ne⁺, Xe⁺ and Arⁱ⁺ (i=1,...,5) Ions. *Journal of Physics B: Atomic and Molecular Physics*, 13(9):1877, 1980. 25
- [OD98] T. M. O’Neil and Daniel H. E. Dubin. Thermal Equilibria and Thermodynamics of Trapped Plasmas with a Single Sign of Charge. *Physics of Plasmas*, 5(6):2163–2193, 1998. 17
- [OS83] A. Van Oosterom and J. Strackee. The Solid Angle of a Plane Triangle. *Biomedical Engineering, IEEE Transactions on*, BME-30(2):125–126, 1983. 108

REFERENCES

- [Pfi10] J. Pfister. *Entwicklung und Anwendung schneller Strahldiagnose für Ionenstrahlen*. PhD thesis, Goethe-Universität Frankfurt, 2010. 73, 124, 167
- [Phe91] A. V. Phelps. Cross Sections and Swarm Coefficients for Nitrogen Ions and Neutrals in N₂ and Argon Ions and Neutrals in Ar for Energies from 0.1 eV to 10 keV. *Journal of Physical and Chemical Reference Data*, 20(3):557–573, 1991. 23, 164
- [Pie10a] A. Piel. *Plasma Physics - An Introduction to Laboratory, Space, and Fusion Plasmas*, page 73. Springer Verlag, 2010. 17
- [Pie10b] A. Piel. *Plasma Physics - An Introduction to Laboratory, Space, and Fusion Plasmas*, pages 94–95. Springer Verlag, 2010. 17
- [Pla] Plasma Dictionary Web. <http://plasmadictionary.llnl.gov/>. Three-Body Recombination. 90
- [PMSY90] J. A. Palkovic, F. E. Mills, C. Schmidt, and D. E. Young. Gabor Lens Focusing of a Proton Beam. *Review of Scientific Instruments*, 61(1):550–552, 1990. ii, 2
- [Poz90] J. Pozimski. *Messungen an einer Gabor-Plasma-Linse*. Master thesis, Goethe-Universität Frankfurt, 1990. 32
- [Poz97] J. Pozimski. *Untersuchungen zum Transport raumladungskompensierter niederenergetischer und intensiver Ionenstrahlen mit einer Gabor Plasma-Linse*. PhD thesis, Goethe-Universität Frankfurt, 1997. iv, 39, 48
- [Rat01] U. Ratzinger. Commissioning of the New GSI High Current Linac and HIF Related RF Linac Aspects. *Nuclear Instruments and Methods in Physics Research Section A: Accelerators, Spectrometers, Detectors and Associated Equipment*, 464:636–645, 2001. 2
- [Rei] H. Reichau. Private communication. 81
- [Rei89] M. Reiser. Comparison of Gabor Lens, Gas Focusing, and Electrostatic Quadrupole Focusing for Low-Energy Ion Beams. In *Proceedings of the*

-
- 1989 *IEEE Particle Accelerator Conference PAC'89*, pages 1744–1747, Chicago, USA, 1989. ii, 47
- [Rei08] M. Reiser. *Theory and Design of Charged Particle Beams*. Wiley Series in Beam Physics and Accelerator Technology. Wiley, 2008. 64, 65
- [Ros07] G. Rosner. Future Facility: FAIR at GSI. *Nuclear Physics B - Proceedings Supplements*, 167(0):77–81, 2007. ii, 2
- [Sac71] F. J. Sacherer. RMS Envelope Equations with Space Charge. In *4th IEEE Particle Accelerator Conference PAC'71*, pages 1105–1107, Chicago, USA, 1971. 42
- [Sar94] M. Sarstedt. *Untersuchungen zu Strahlformierung und Transport intensiver Ionenstrahlen und ihrer Injektion in einen RFQ-Beschleuniger*. PhD thesis, Goethe-Universität Frankfurt, 1994. 124
- [Sch86] A. Schönlein. *Emittanzwachstum und Raumladungskompensation beim Transport intensiver Ionenstrahlen*, pages 68–74. GSI-Report: Gesellschaft für Schwerionenforschung. GSI, 1986. 101, 102
- [Sch09] K. Schulte. *Untersuchung von Messmethoden zur Parameterbestimmung eines Nichtneutralen Plasmas*. Master thesis, Goethe-Universität Frankfurt, 2009. 36, 50, 72, 105, 145, 165
- [Sch10] K. Schulte. Space Charge Lens for Focusing Heavy Ion Beams. In *Proceedings of the Linear Accelerator Conference LINAC'10*, pages 298–300, 2010. 63
- [Sch11] K. Schulte. Studies on Electron Cloud Dynamics for an Optimized Space Charge Lens Design. In *Proceedings of the International Particle Accelerator Conference IPAC'11*, pages 3493–3495, 2011. 55, 82, 165
- [SF06] P. Spiller and G. Franchetti. The FAIR Accelerator Project at GSI. *Nuclear Instruments and Methods in Physics Research Section A: Accelerators, Spectrometers, Detectors and Associated Equipment*, 561(2):305–309, 2006. ii, 2

REFERENCES

- [SHK59] Th. J. M. Sluyters, E. De Haas, and J. Kistemaker. Charge Exchange, Ionization and Electron Loss Cross-Sections in the Energy Range 5 to 24 keV. *Physica*, 25:1376–1388, 1959. 24, 164
- [Spi56] L. Spitzer. *Physics of Fully Ionized Gases*, pages 76–81. Interscience Tracts on Physics and Astronomy, vol. 3. Interscience Publishers, 1956. 21
- [SSB⁺00] A. A. Sorokin, L. A. Shmaenok, S. V. Bobashev, B. Möbus, M. Richter, and G. Ulm. Measurements of Electron-Impact Ionization Cross Sections of Argon, Krypton, and Xenon by Comparison with Photoionization. *Phys. Rev. A*, 61:022723, Jan 2000. 20, 164
- [Tam08] A. S. Tampe. *Aufbau und Inbetriebnahme einer Funkenkammer*. Bachelor thesis, Goethe-Universität Frankfurt, 2008. 33
- [Ten11] J. Tennyson. *Astronomical Spectroscopy: An Introduction to the Atomic and Molecular Physics of Astronomical Spectra*, page 62. World Scientific Publishing Company Incorporated, 2011. 89
- [Vaca] Pfeiffer Vacuum. Compact Full Range Gauge PKR251. Manual. 104, 169
- [Vacb] Pfeiffer Vacuum. Product Data Sheet. <http://www.pfeiffer-vacuum.de/productPdfs/PF410011-T.de.pdf>. 109, 110, 169
- [Wan08] T. P. Wangler. *RF Linear Accelerators*, page 298. Physics Textbook. Wiley, 2008. 46
- [Wie07a] H. Wiedemann. *Particle Accelerator Physics*, pages 155–159. SpringerLink: Springer e-Books. Springer London, Limited, 2007. 41
- [Wie07b] H. Wiedemann. *Particle Accelerator Physics*, pages 122–123. SpringerLink: Springer e-Books. Springer London, Limited, 2007. 48
- [Wie09] C. Wiesner. *Schnelles Choppersystem für hochintensive Protonenstrahlen*. Master thesis, Goethe-Universität Frankfurt, 2009. 41
- [ZDCH80] B. Van Zyl, G. H. Dunn, G. Chamberlain, and D. W. O. Heddle. Benchmark Cross Sections for Electron-Impact Excitation of n^1s Levels of He. *Phys. Rev. A*, 22:1916–1929, Nov 1980. 94, 113, 115, 169

REFERENCES

- [Zha99] H. Zhang. *Ion Sources*, pages 60–61. Springer Science Press, 1999. 44
- [Zoh13] H. Zohm. Plasmaphysik - Vorlesungsskript. <http://www.aug.ipp.mpg.de/E2/Mitarbeiter/Zohm/scripts/Plasmaphysik1.pdf>, WS 2012/13. 32

REFERENCES

List of Figures

1	Exemplarische Darstellung der berechneten zeitlichen Entwicklung der Diocotronmoden (von links nach rechts). Der Farbcode kennzeichnet die über z integrierte und normierte Elektronendichte [MDS13].	v
2	Schematische Darstellung der Gabor-Linse im Schnitt (links), in der Vollansicht (Mitte) und ein Foto der Prototyplinse (rechts).	vi
3	Messung der Elektronentemperatur für verschiedene Einstellungen der Gabor-Linse. Die Temperaturen von 29 eV und 69 eV wurden nahe des Arbeitspunktes der Linse bestimmt, während bei 428 eV die Linsenparameter stark vom Arbeitsbereich der Linse abweichen.	viii
4	Gemessene Phasenraumverteilung des gedrifteten Ar^+ -Strahls (links) und des durch die Gabor-Linse transportierten Strahles (rechts). Beide Emittanzen wurden an derselben Stelle hinter der Linse aufgenommen.	x
2.1	Existence diagram of various plasmas [Meu06].	8
2.2	Typical layout of a Gabor lens used at IAP.	9
2.3	Longitudinal electron confinement within the potential well of the electrode system.	10
2.4	Scheme of forces acting on an electron.	12
2.5	Confinement efficiency κ_r as a function of the two rotational frequencies ω_e^+ and ω_e^- (top). Illustration of the associated electron motion for different confinement efficiencies (bottom).	14
2.6	Operation function of the prototype Gabor lens for different corrections.	15
2.7	Mapping quality of a Gabor lens represented by the emittance growth and as a function of the external fields (obtained from [Meu06]).	16
2.8	Scheme of a flow equilibrium.	18

LIST OF FIGURES

2.9	Frequency for elastic collisions between electrons and neutrals for hydrogen and helium as a function of the energy [Fra09] and frequency and collision times as a function of the residual gas pressure for He.	19
2.10	Frequency of inelastic collisions between electrons and neutrals for argon and helium as a function of energy (left) and as a function of residual gas pressure (right). The cross section data is obtained from [SSB ⁺ 00] and [fSaT].	20
2.11	Calculated electron-electron collision frequencies and collision times as a function of electron temperature assuming an electron density of $n_e = 1 \cdot 10^{14} \text{ m}^{-3}$	21
2.12	Thermalization times due to the electron density (left) and the primary temperature of particles introduced into the electron ensemble (right).	22
2.13	Charge exchange reaction times and rates for argon (left) and helium (right) ions. The cross section data is obtained from [Phe91] and [BS58].	23
2.14	Cross sections for ionizing ion-atom collisions, the collision frequency, and reaction rates for Ar^+ on Ar [SHK59] (left) and He^+ on He [dHSM66] (right).	24
2.15	Calculated radiative recombination cross sections for Ar^+ (left) and He^+ (right) as a function of the incident electron energy.	25
2.16	Calculated and measured [DHT61] ionization cross sections for Ar^+ and He^+ as a function of the incident electron energy.	26
2.17	Ranges of applicability of the discussed plasma models (obtained from [McW65]).	30
2.18	Different types of space charge lenses at IAP: original concept (top), scaled in z-direction (middle) and scaled in r-direction (bottom).	33
2.19	Theoretically predicted ignition curve for helium.	34
2.20	Measured ignition curves of the nonneutral plasma confined within different lens types for helium as residual gas as a function of the potential (left). The anode potential was configured according to the lens work function and normalized to the radius in order to compare all lens types (right).	34
2.21	Experimental set-up (left) and an example of emitted Bremsstrahlung-spectra for different anode potentials (right) [Kla13].	37

LIST OF FIGURES

2.22 Measured x-ray emission as a function of the anode potential Φ_A (left) and the magnetic field B_z (right). The detected intensity I_x was divided by the residual gas pressure p and the ion current I to minimize the influence of a variation in the plasma state during the measurement (based on data from [Kla13]).	38
2.23 Schematic overview of the iterative calculation procedure of the code GABOR-M [Meu06].	39
2.24 Comparison of transverse equilibrium density distributions for different conditions. Colour code: normalized density [MDS13].	40
2.25 Projections of the KV and Gaussian distribution and their spatial profile.	43
2.26 Illustration of the perveance as a function of the momentum for different projects.	45
2.27 Example of the electric space charge field in the case of an homogeneously distributed electron cloud and the resulting forces on the ion beam. The nonlinearity in the electric field is a result of the Debye drop off at the edge of the plasma cloud.	47
3.1 Operation function of the three-segmented lens (left). Measured residual gas ion current and light density profile as a function of the magnetic field (right). The anode potential and the residual gas pressure were kept constant at $\Phi_A=4\text{ kV}$ and $p=6\cdot 10^{-2}\text{ Pa}$ (He) [Sch09].	50
3.2 Illustration of the physical mechanisms that lead to the evolution of diocotron surface modes (obtained from [KTY01]).	51
3.3 Density profiles and corresponding angular velocity profiles for different scenarios (obtained from [Gou95]).	52
3.4 Electron density profile for the calculation of the stability-instability diagram.	53
3.5 Stability-instability diagram showing the stability limits of the diocotron modes l [Gla12].	54
3.6 Picture of a light density distribution for different pressures of helium and similar field strengths, $\Phi_A=6.5\text{ kV}$, $B_z=12.1\text{ mT}$, $p=7.8\cdot 10^{-3}\text{ Pa}$ (left) and $\Phi_A=6.5\text{ kV}$, $B_z=12.9\text{ mT}$, $p=4.8\cdot 10^{-2}\text{ Pa}$ (right) [Sch11].	55

LIST OF FIGURES

3.7	Evolution of the diocotron mode and the related integrated density profile (left) as well as the mean kinetic energy in both planes (right) as a function of time.	55
4.1	Radial space charge potential of the confined plasma cloud as a function of the R_A/R_p ratio (left) and the influence of the R_A/R_p ratio on the longitudinal confinement efficiency (right), (obtained from [Meu06]). . .	58
4.2	Simulated potential decrease on axis and confinement efficiency κ_1 as a function of the R_A/L_A ratio for $B_z=8.3$ mT and $\Phi_A=10$ kV.	59
4.3	Linearity of the calculated electric space charge field as an example for different anode lengths ($B_z=8.3$ mT, $\Phi_A=10$ kV).	59
4.4	Axial magnetic field B_z as a function of the gap width of the coils. . . .	60
4.5	Influence of field homogeneity on the charge density distribution (left) and difference in the charge density for different magnetic fields (right). . . .	61
4.6	Comparison of electric space charge fields calculated for different magnetic fields.	61
4.7	Beam envelope along the transport section, input emittance and output emittance for selected beam radii.	62
4.8	Emittance growth as a function of the beam radius (left) and comparison of the focusing quality for different magnetic fields (right).	63
4.9	Homogeneous input distribution of a 50 keV He^+ -beam (left), self-electric field of the electrons calculated for Gabor lens parameters of $\Phi_A=20$ kV and $B_z=10$ mT using the code GABOR-M (middle), and resulting emittance after the described transport section (right).	64
4.10	Homogeneous input distribution of a 50 keV He^+ -beam with an energy spread of ± 1 keV (left), self-electric field of the electrons calculated for Gabor lens parameters of $\Phi_A=20$ kV and $B_z=10$ mT (middle), and resulting emittance (right).	64
4.11	Homogeneous input distribution of a 50 keV He^+ -beam (left), self-electric field of the electrons calculated for Gabor lens parameters of $\Phi_A=20$ kV and $B_z=10$ mT (middle), and resulting emittance (right).	65

LIST OF FIGURES

4.12	Homogeneous input distribution of a 50 keV He ⁺ -beam (left), self-electric field of the electrons calculated for Gabor lens parameters of $\Phi_A=20$ kV and $B_z=6.3$ mT (middle), and resulting emittance (right).	66
4.13	Technical drawing and pictures of the prototype Gabor lens for GSI. . .	67
4.14	Calculated potential on axis for $\Phi_A=30$ kV (left) and comparison of measured and simulated magnetic field (right).	67
5.1	Experimental set-up for the diagnostics of the nonneutral plasma confined by the Gabor lens.	70
5.2	Measured gain curve of the intensifier as a function of the software gain [Gla12].	71
5.3	Quantuum efficiency of the detector (VIS A/R coating) [LNC97].	72
5.4	Measurement scheme of the pepperpot emittance scanner (obtained from [Pfi10]).	73
5.5	Example of different current signals detected by the Faraday cup.	74
5.6	Scheme of the density measurement.	75
5.7	Calculated trajectories for the Ar ⁺ -ions produced in the lens volume. . .	75
5.8	Transmission of the residual gas ions through the diagnostic box.	76
5.9	Comparison between calculated (left) and measured energy spectrum (right) of extracted Ar ⁺ -ions.	76
5.10	Typical energy spectra of He ⁺ -ions (left) and Ar ⁺ -ions (right) extracted from the lens volume close to the operation point of the lens.	77
5.11	Scheme of density measurement by the change in the measured phase space distribution of a beam passing the nonneutral plasma cloud.	78
5.12	Example of slit-grid emittance measurement of residual gas ions extracted from the prototype lens for a parameter setup of $\Phi_A=8$ kV, $B_z=8.1$ mT, $p=8 \cdot 10^{-5}$ Pa (Ar).	79
5.13	Example of pepperpot emittance measurement of residual gas ions extracted from a Gabor lens (orginal design at IAP) for a parameter setup of $\Phi_A=2$ kV, $B_z=8.3$ mT, $p=6 \cdot 10^{-3}$ Pa (He).	79
5.14	Correlation of electron density and measured intensity for $\Phi_A=9.8$ kV and $p=1.36 \cdot 10^{-4}$ Pa (Ar).	80

LIST OF FIGURES

5.15	Example of the described procedure to determine the symmetry of the detected light density distribution for a nearly perfect circle.	82
5.16	Example of the described procedure to determine the symmetry of the detected light density for a asymmetric (A) and hollow distribution (B).	83
5.17	Residual gas ion current (left) and measured intensity signal (right) of an temporal unstable plasma mode.	84
5.18	Measurement scheme for the time-resolved optical diagnostic.	84
5.19	Measured light density distribution and its central profile in time steps of 2 ms (based on data from [Gla12] for the three-segmented lens).	85
5.20	Symmerty factor (left) and rotational symmetry (right) as a function of time.	86
5.21	Characterization of the observed instability by the geometrical expansion of the detected hollow profile [Gla12].	87
5.22	Vector model of the three triplett states and of the singulett state (left), (obtained from [Dem09]). Grotrian diagram of the helium with some important transitions and levels (right), (obtained from [Fan06]).	89
5.23	Comparison of emission spectra of helium excited by an electron beam ($W_b=82$ eV, $I_b=4.6 \mu A$, $\Delta t=1200$ s) and by the confined electron cloud within the Gabor lens ($\Phi_A=4$ kV, $B_z=4$ mT, $\Delta t=10$ s).	93
5.24	Population of atomic levels by electron impact and the cascade contribution from upper levels.	96
5.25	Scheme of the optical-emission cross section measurement.	97
5.26	Scheme (top) and photograph (bottom) of the cross section experiment.	98
5.27	Scheme of the volume type source used to generate the electron beam [Gab08].	99
5.28	Picture of the movable Faraday cup in order to detect the electron beam current in the interaction region.	99
5.29	Scheme of the used energy detector to determine the electron energy distribution.	100
5.30	Measured electron current (top) and derivative of the current (bottom) as a function of the stopping potential.	101
5.31	Comparison of the expected beam energy, the measurement and the simulation as a function of the extraction voltage.	102

LIST OF FIGURES

5.32	Spread of the electron energy distribution caused by the detector.	103
5.33	Conversion from displayed pressure to effective pressure by the Pfeiffer Compact Full Range Gauge type PKR251 (obtained from [Vaca]).	104
5.34	Measured temperature along the tungsten strip.	106
5.35	Spectral radiance L emitted by the tungsten strip lamp. The error bars result from an uncertainty in the temperature determination along the tungsten strip.	107
5.36	Signal of the tungsten strip lamp developed by the CCD sensor using the grid 300 g/mm of the monochromator.	107
5.37	Illustration of the spanned solid angle and the projected area on the CCD chip.	109
5.38	Transmission curve of the used borosilicate window as a function of the wavelength (obtained from [Vacb]).	110
5.39	Measurement of the magnification of the optical system in order to de- termine the effective length of the beam.	110
5.40	Background measurement as a function of time.	111
5.41	Proportionality of the intensity to the beam current and the target gas pressure.	112
5.42	Examples of the measured pressure dependence of emission lines for se- lected levels of He.	112
5.43	Example of the change in beam size and position for different energies ($W_{b,1}=125$ eV, $W_{b,2}=238$ eV and $W_{b,3}=1069$ eV) and settings of the mag- netic field ($B_{z,1}=0.7$ mT, $B_{z,2}=1$ mT and $B_{z,3}=2$ mT) of the solenoid. . .	113
5.44	Families of optical-emission cross sections for (A) singlet S, (B) singlet P, (C) singlet D, (D) triplet S and (E) triplet D.	114
5.45	Comparison of measured optical-emission cross sections to benchmark cross sections by [ZDCH80].	115
5.46	Measured spread of the electron energy distribution (FWHM) as a func- tion of the beam energy in absolute (left) and relative units (right). . . .	116
5.47	Electron temperature measurement by the line ratio-technique for emis- sion lines 728 nm and 505 nm at a residual gas pressure of $p=8 \cdot 10^{-2}$ Pa (He).	117

LIST OF FIGURES

5.48	Measured electron temperature and density as a function of the anode potential.	118
5.49	Simulation of the plasma state for different Gabor lens settings using the code GABOR-M.	119
6.1	Scheme of the HOSTI beamline (not to scale, obtained from [HA]) and photograph of the experimental set-up.	122
6.2	Photograph and scheme of the MUCIS ion source [HA].	123
6.3	Scheme of emittance measurement.	124
6.4	Time frame of emittance measurement within the beam pulse.	125
6.5	Example of the high-voltage conditioning procedure for the prototype Gabor lens. I_{ps} represents the displayed current of the power supply. . .	126
6.6	Correlation of the normalized power supply current and extracted residual gas ion current as a function of the anode potential for $B_z = 8.1$ mT, $p=4.1 \cdot 10^{-5}$ Pa (based on data from [Kla13]).	127
6.7	Development of final pressure and maximum applied voltage $\Phi_{A,max}$ during the conditioning phase (based on data from [Kla13]).	127
6.8	Simulations were performed for the illustrated part of the transport section, starting at the exit of the vacuum chamber right behind the post-acceleration gap and ending at the slit of the slit-grid emittance scanner.	129
6.9	Results of the beam transport measurements for a 12.6 keV/u He^+ -beam in comparison with numerical simulations.	130
6.10	Intensity profiles for the y (left) and y' (right) plane as a function of the magnetic confining field.	132
6.11	Measured and calculated normalized rms-emittances (left) and kurtosis (right) as a function of the confining fields.	132
6.12	Mean electron density determined by different diagnostic techniques. . .	133
6.13	Comparison of measured light density distribution and the simulated electron density distribution as well as the emitted spectrum for helium as a function of the lens parameters. The asymmetry of the light density distribution is the result of a light spot on the borosilicate window produced by particle losses.	135

6.14	Symmetry factor (left) and rotational symmetry (right) of the light density distribution as a function of the lens parameters.	136
6.15	Comparison of the expected (plasma diagnostics) and the actual electron density for the beam transport experiments.	136
6.16	Technical assessment of Gabor lens during the measurement campaign. .	137
6.17	Influence of the ion current on the focusing performance of the lens. . .	139
6.18	Superposition of the anode potential, the space charge potential of the electron cloud and the uncompensated beam potential for an 3.1 keV/u, 35 mA Ar ⁺ -beam in longitudinal direction.	139
6.19	Measured emittances and intensity profiles of a 3.1 keV/u Ar ⁺ -beam as a function of the lens parameters.	140
6.20	Intensity profiles for y (left) and y' (right) for the different settings of the prototype lens.	142
6.21	Normalized rms-emittance (left) and kurtosis (right) of the Ar ⁺ -beam as a function of the lens parameters.	142
6.22	Comparison of measured light density distribution and the simulated electron density distribution as well as the emitted spectrum for argon as a function of the lens parameters.	143
6.23	Comparison of measured and calculated electron density as a function of the lens parameters.	144
6.24	Symmetry (left) and rotational symmetry (right) for the discussed measurements series.	144
6.25	Confinement efficiencies as a function of the magnetic field for the emittance dominated beam transport measurements (left) and for the space charge dominated beam transport experiments (right).	145
7.1	Measured phase space distribution of the drifted Ar ⁺ -beam (left) and the transported beam by the Gabor lens (right). Both emittances were measured at the same position behind the lens.	149

LIST OF FIGURES

List of Tables

2.1	Comparison of the beam parameters for different projects.	45
5.1	Helium line transitions and their applicability to the temperature determination by the presented line-ratio technique.	92
6.1	Change in the measured emittance due to a variation in the magnetic confining field of the Gabor lens.	131
6.2	Change in the measured emittance due to the magnetic field of the Gabor lens.	141
6.3	Comparison of confinement efficiency and emission area for different experiments.	145
6.4	Parameters for the emittance dominated beam transport measurements.	146
6.5	Parameters for the space charge dominated beam transport measurements.	146

LIST OF TABLES

Acknowledgements

I would like to offer my most sincere gratitude to all people who encouraged and motivated me throughout my PhD.

First and foremost, I would like to thank my supervisor, Prof. Dr. Ulrich Ratzinger. He motivated me to undertake this challenging project and continuously supported me during the entire process. Without his useful comments and remarks, this work could not have been successfully completed.

Furthermore, I am especially grateful to Prof. Dr. Oliver Kester. Not only did he enable and support the experiments at GSI; moreover, as one of the expert assessors, he also invested much time and effort in reviewing this thesis.

I would like to express my deep gratitude to Dr. Oliver Meusel and Dr. Martin Droba for their excellent guidance, enthusiastic encouragement and tremendous commitment during my research.

My special thanks go to the Ion Source Group of GSI, namely to Dr. Ralph Hollinger, Dr. Aleksey Adonin, Dr. Rustam Berezov and Dr. Jochen Pfister. I would never have been able to finish this thesis without their active support and helpful advice.

I am also indebted to Prof. Dr. Alwin Schempp for his continued support throughout my PhD.

I received generous encouragement from my colleagues, namely Christoph

Wiesner, Stefan Schmidt, Daniel Noll, Christopher Wagner, Dr. Hermine Reichau, Hannes Dinter, Stephan Klaproth, Dr. Giuliano Franchetti, Dr. Marcus Iberler, Fips Schneider, Joschka Wagner, Heiko Niebuhr, Adem Ates, Onur Payir, Tobias Nowotnick and many more. Many thanks for good advice, interesting discussions and pleasant cooperation during the last years.

For their technical support and the close cooperation, I would like to express my gratitude to Daniel Bäsch, Thomas Metz, Joachim Jaitner, Sven Reploeg and the whole workshop team.

Last but not least, I would especially like to thank my loved ones for their encouragement and patience throughout the entire process.

Curriculum Vitae

personal

Name Kathrin Silvana Schulte
Born 17.09.1983
Place of Birth Attendorn

education

1990 – 1991 Grundschule Hützenmert
1991 – 1994 Viktoria Grundschule Kronberg
1994 – 1998 Altkönigschule Kronberg
1998 – 1999 Frankfurt International School Oberursel
1999 – 2003 Altkönigschule Kronberg

academic development

diploma studies in physics

2003 – 2004 at University of Technology Darmstadt
2004 – 2008 at Johann Wolfgang Goethe-University Frankfurt
11/2008 diploma thesis

Title *Research of Diagnostic Techniques on a Nonneutral Plasma*
Supervisor Prof. Dr. Ulrich Ratzinger

doctoral studies in physics

12/2008 admission to doctoral studies in physics

Title *Studies on the Focusing Performance of a Gabor Lens Depending on Nonneutral Plasma Properties*
Supervisor Prof. Dr. Ulrich Ratzinger

academic teachers

physics

- Prof. Dr. W. Aßmus
- Prof. Dr. T. Boller
- Prof. Dr. R. Dörner
- Prof. Dr. R. Feile (TU Darmstadt)
- Prof. Dr. C. Greiner
- Prof. Dr. C. Gros
- Prof. Dr. J. Jacoby
- Prof. Dr. W. Mäntele
- Prof. Dr. J. Maruhn
- Prof. Dr. U. Ratzinger
- PD J. Schaffner-Bielich
- Prof. Dr. A. Schempp
- Prof. Dr. H. Stöcker
- Prof. Dr. T. Walther (TU Darmstadt)

mathematics

- Prof. Dr. J. Baumeister
- Prof. Dr. T. Streicher (TU Darmstadt)
- Prof. Dr. J. Bliedtner
- Prof. Dr. J. Weidmann